Raman spectroscopy in Geobiology –

Advances in detection and interpretation of organic signatures in rocks and minerals

Dissertation

zur Erlangung des mathematisch-naturwissenschaftlichen
Doktorgrades
"Doctor rerum naturalium"
der Georg-August-Universität Göttingen

im Promotionsprogramm Geowissenschaften / Geographie
der Georg-August University School of Science (GAUSS)

vorgelegt von

Nadine Schäfer

aus Göttingen

Göttingen 2013

Betreuungsausschuss:

Prof. Dr. Joachim Reitner, Geowissenschaftliches Zentrum,
Abteilung Geobiologie, Universität Göttingen

Prof. Dr. Volker Thiel, Geowissenschaftliches Zentrum,
Abteilung Geobiologie, Universität Göttingen

Mitglieder der Prüfungskommission:

Referent:
Prof. Dr. Joachim Reitner, Geowissenschaftliches Zentrum,
Abteilung Geobiologie, Universität Göttingen

Korreferent:
Prof. Dr. Volker Thiel, Geowissenschaftliches Zentrum,
Abteilung Geobiologie, Universität Göttingen

weitere Mitglieder der Prüfungskommission:

PD Dr. Alexander Schmidt, Courant-Forschungszentrum Geobiologie,
Arbeitsgruppe „Evolution der Landpflanzen und Entwicklung der terrestrischen Ökosysteme“,
Universität Göttingen

PD Dr. Michael Hoppert, Institut für Mikrobiologie und Genetik,
Abteilung für Allgemeine Mikrobiologie, Universität Göttingen

Dr. Burkhard Schmidt, Geowissenschaftliches Zentrum,
Abteilung Experimentelle und Angewandte Mineralogie, Universität Göttingen

Dr. Martin Blumenberg, Geowissenschaftliches Zentrum,
Abteilung Geobiologie, Universität Göttingen

Tag der mündlichen Prüfung: 12.04.2013

Überall geht ein frühes Ahnen

Dem späteren Wissen voraus.

Alexander von Humboldt

Table of contents

Chapter 1: Introduction

1.1 Main goals of the work

In geobiology the use of Raman spectroscopy is a relatively new field. The great advantages of almost destruction free analyzing of mineralogical (inorganic) and organic phases at the same time are complicated by the fact that in many samples vibrations of disordered carbon are the only detectable signal. The interpretation of these signals is not straight forward, as the similarity between kerogenous and graphitic material is very high and also thermal maturity influences the carbon signature (Wopenka & Pasteris, 1993; Pasteris & Wopenka, 2002; Marshall et al., 2010). Therefore, the aim of this study is to detect and interpret organic signatures obtained with Raman spectroscopy in different rocks, demonstrating the benefits but also the constraints of this technique for analyzing geobiological samples.

In **chapter 1** Raman spectroscopy is introduced and the problem of interpreting carbon signals is discussed. As most organic traces in the lithosphere trace back to the growth of assemblages of microorganisms, resulting in the formation of biofilms or microbial mats, a general introduction on the formation of these structures is also given. Another phenomenon for accumulation of organic substances is in the literature referred to as biofouling (cf. Flemming & Ridgway, 2009), describing the formation of conditioning films.

In **chapter 2** organic standard substances from commercial providers (lipids, carbohydrates, amino acids and proteins) where measured in order to create an own database for these substances.

Chapter 3 is focused on the biological important macromolecule melanin. Melanins can be found in microbes, protozoans, animals and plants (Butler & Day, 1998) and serve among others as pigments (Bandaranayake, 2006). This chapter is divided into three parts, where the first part deals with fossilized melanin from ink sacs of Cretaceous and Jurassic coleoid cephalopods (Vampyromorpha). The second part has a greater focus on melanin as a pigment and deals with the occurrence of melanin defining the eye system of a nematomorph worm from the Lower Cambrian Chengjang lagerstätte in China.

The third part is concerned with the detection of fungal melanin, isolated from a 52 Ma old Indian amber piece.

In **chapter 4** the focus is set on fractures of granitic and dioritic rocks from the Äspö Hard Rock Laboratory of the Swedish Nuclear Fuel and Waste Management Company – SKB (HRL, island of Äspö, Sweden). Here the mineralogical content was used for characterizing the samples and at the same time detect organic signals connected to fracture minerals. The organic signals were interpreted to be related to a conditioning film, which could grow inside the fractures due to reactivation events.

In **chapter 5** Raman spectra of a 555 Ma old fossilized microbial mat from the White Sea are discussed. The microbial mat is embedded in the upper part of a siliciclastic matrix with sandy grain size. Here the main organic signatures are those of disordered carbon sometimes associated with minerals (anatase and hematite).

Chapter 6 deals with the occurrence of the so called “yellow calcite” in various cold seep deposits and its possible formation conditions. The characterization of different carbonate facies on the basis of the presence and absence of the carbon signal is crucial. In this regard Raman spectroscopy turned out to be a valuable tool for identifying fossil cold seep sites.

In **chapter 7** so called “round sponge fossils” (RSF) from the lower Cambrian Chengjang Biota were investigated. With Raman spectroscopy a focus was set on the interpretation on carbon film typical for these fossils. As a comparison additional sponge fossils from the Cambrian Xiaoyanxi Formation and putative algal fossil from the Ediacaran Wenghui Biota were analyzed.

In **chapter 8** the results from the previous chapters were summarized and discussed and give concluding remarks on the suitability of Raman spectroscopy for geobiological questions. A special focus hereby is set on the interpretation of carbon signatures.

1.2 Principles of Raman spectroscopy

The birth of Raman spectroscopy dates back into the beginning of the 20th century when Smekal (1923) was the first to postulate the phenomenon of inelastic light scattering. But it took another 5 years before this theory could be

proven experimentally, by Raman and Krishnan (1928). Later on, the phenomenon was named Raman spectroscopy after C.V. Raman, one of the authors.

In general, Raman spectroscopy together with infrared (IR) spectroscopy belongs to the group of vibrational spectroscopy. However, different selection rules are valid for these two techniques. In IR spectroscopy the absorption of infrared radiation by a molecule or crystal lattice vibration, involving a change in dipole moment is observed. Here, the intensity is proportional to the square of the change in dipole moment (eq.1). In contrast Raman spectroscopy is based on inelastic light scattering with a change in polarisability. Here, the intensity is proportional to the square of the change in polarisability (eq.2). The term q represents the normal coordinate of the vibration (cf. Bauer, 2010 and citations therein).

$$I_{IR} \propto \left(\frac{\partial \mu}{\partial q}\right)_0^2 \qquad \text{(eq.1)}$$

$$I_{Raman} \propto \left(\frac{\partial \alpha}{\partial q}\right)_0^2 \qquad \text{(eq.2)}$$

In a Raman experiment the sample is irradiated by laser light of a certain wavelength which can be located in the ultraviolet (UV), visible (VIS) or near infrared (NIR) part of the light spectrum. Most of the light photons (more than 99%) are scattered elastically by the sample without changing energy which is the so-called Rayleigh scattering (Spieß & Klapötke, 1999). But some of the photons (one of 10^6 - 10^8) are at the same time scattered inelastically either to a higher wavelength, which is the so-called Stokes Raman scattering or to a lower wavelength which is the so-called anti-Stokes Raman scattering (Smith & Dent, 2005). If the molecule is in the basic vibrational state when the interaction with the photon takes place, Stokes Raman scattering will occur, leading to a decrease of photon energy. If the molecule already is in an excited vibrational state anti-Stokes Raman will occur, leading to an increase of photon energy (Fig. 1). At room temperature most molecules will exist in the ground vibrational state which means that the effect of Stokes Raman scattering is much larger and the resulting bands have a higher intensity (Spieß & Klapötke, 1999).

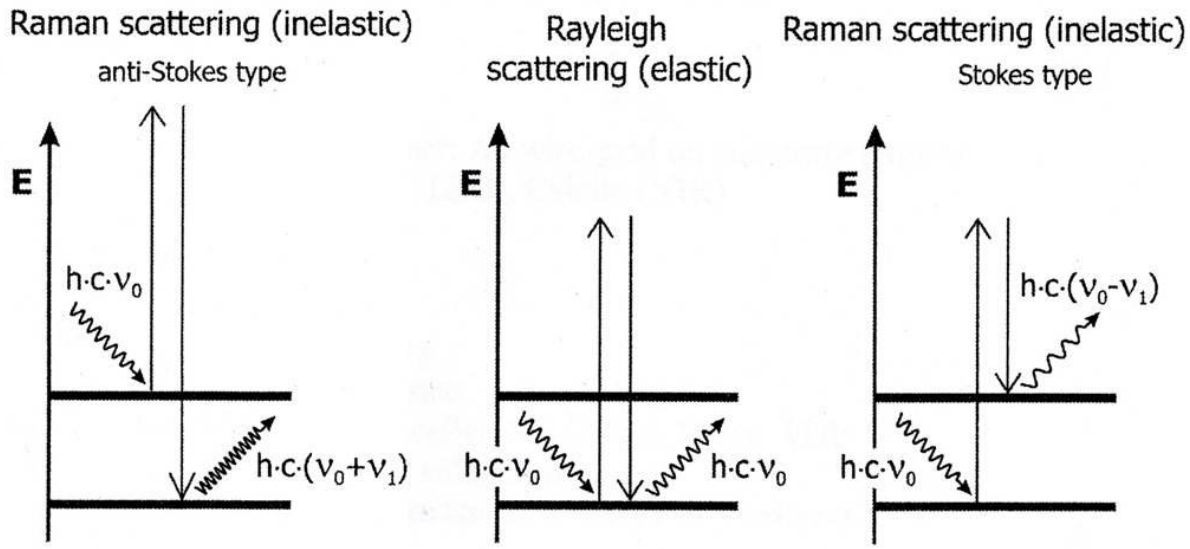

Figure 1: Simplified energy level diagrams, displaying the vibrational state of a molecule before and after interaction with light (after Nasdala et al., 2004). The molecule is excited to a virtual electronic state, from which it will recover immediately. In case of elastic scattering the photon energy of the scattered light has the same value than before the interaction. In contrast for inelastic light scattering the photon energy is either lower (Stokes Raman) or higher (anti-Stokes Raman). The photon energy is displayed by the Planck's constant (h), the speed of light (c) and the frequency (ν).

Therefore, normally only the energy difference between Rayleigh and Stokes Raman scattering is displayed in Raman spectroscopy. The logical plot of a Raman spectrum, therefore, should be light intensity versus the photon energy (Nasdala et al., 2004). But as this is an unusual expression in vibrational spectroscopy, the wavelengths are transformed into wavenumbers ($\tilde{\nu}$), following equation 3 (Nasdala et al., 2004). The range of absolute wavenumbers in which the Raman spectrum is recorded depends on the excitation wavelength. However, the relative Raman spectrum, with Raman shift in wavenumbers, is independent of the excitation wavelength. The Raman shift is characteristic for the molecules, the crystal lattice and the chemical bonds of the sample.

$$\tilde{\nu} = \frac{\nu}{c} = \frac{1}{\lambda} \qquad \text{(eq.3)}$$

The great advantage of Raman spectroscopy is the possibility of almost non-destructive *in situ* analyzing with only little sample preparation. Furthermore, the detection of inorganic and organic substances at the same time is possible (Nasdala et al., 2004). That makes it a very interesting tool for geobiological problems, because the mineralogical (inorganic) contents can be determined

and localized at the same time as the organic ones. The high resolution of the spectrometer makes it possible to localize the obtained spectra on the sample.

Raman spectroscopy already is a well-established technique in mineralogy. The identification of minerals is based on publications describing Raman spectra of known minerals. Furthermore, the existence of public databases on mineral spectra makes identification quite easy. Nasdala et al. (2004) gives an extensive overview about mineralogical applications of Raman spectroscopy in geosciences. One great advantage regarding mineral determination is that polymorphs with equal chemical properties can easily be distinguished (e.g. Etchepare et al., 1974; Etchepare et al., 1978 for SiO_2). Geobiological relevant mineral phases like carbonates (e.g. Rutt & Nicola, 1974; Urmos et al., 1991; Gunasekaran et al., 2006), sulfates (e.g. Jehlička et al., 2009) or sulfides (e.g. Mernagh & Trudu, 1993; McGuire et al., 2001) can also be identified and differentiated without ambiguity. Even in the wide field of biomineralization, Raman spectroscopy is used in a broad range of applications, including studies of hard body, shell and teeth formation of various organisms (e.g. Addadi et al., 2003; Lee et al., 2003; Borzęcka-Prokop et al., 2007), nacre (e.g. Silve et al., 1992; Rousseau et al., 2005) and bones (e.g. Edwards et al., 2001). On the other hand, for organic substances Raman spectroscopy was applied in several fields of interest only in recent years. This is because organic spectra are in general more complex than mineral spectra and therefore, an identification of unknown substances is much harder. In recent years several working groups published reference spectra of biological relevant substances (e.g. Maquelin et al., 2002; De Gelder et al., 2007). These can form a good basis for interpreting Raman spectra of biological origin. But in general, most working groups focus on the detection of one specific substance, like carbohydrates (e.g. Asher, 1984; Maddams & Royaud, 1990; Schrader, 1991; Shinohara et al., 1998), vitamin E (e.g. Beattie et al., 2007) or cellulose (e.g. Cael et al., 1975; Edwards, 2007). These published data are very helpful to identify organic substances. Nevertheless, when coping with several unknown organic substances often a clear assignment is not possible. For special applications like the fingerprinting of bacteria, the signals of normal Raman spectroscopy are too weak in most cases. Therefore, most working groups focusing on bacteria, work with special methods enhancing the Raman effect. The most common method is to use a

tunable laser as excitation source achieving resonance Raman spectra (e.g. Dalterio et al., 1987; Britton et al., 1988; Wu et al., 2001). Another possibility which came up in the last few years, especially when working with bacteria or biologic substances is surface enhanced Raman spectroscopy (SERS) (e.g. Weldon et al., 1998; Zeiri et al., 2004; Jarvis et al., 2006). A good overview about the possibilities of Raman spectroscopy in the field of identifying bacteria is given by Rösch et al. (2005) and citations therein.

One problem which often occurs in Raman spectroscopy with laser excitation in the visible range especially with samples of organic or biological origin is the generation of fluorescence. This signal often is much more intense than the Raman scattering and therefore, can lead to a complete hiding of the Raman signal (Ferraro et al., 2003). One simple method to avoid or reduce fluorescence is to shift excitation wavelength to the NIR or to the UV. In the NIR photon energy is much lower and only few molecules have excited states eliminating electronic transitions (Smith & Dent, 2005). But it has to be taken into account that with higher wavelength the scattering intensity will decrease, and therefore higher integration times are required. When excitation in the UV is used, most energy is already dissipated in the system and even if some energy gets emitted it lies outside of the spectral region used for Raman detection (Smith & Dent, 2005). However, higher energy is impinging on the sample, which can lead to a heating process, affecting or even damaging the sample. Furthermore, due to some technical limitations, the spectral region below 500 cm^{-1} cannot be recorded. This can hinder for example the differentiation between carbonate phases (aragonite and calcite), because the clearest differences can be seen in the lower wavenumber region (e.g.Rutt & Nicola, 1974; Frech et al., 1980; Gunasekaran et al., 2006) (Fig. 2).

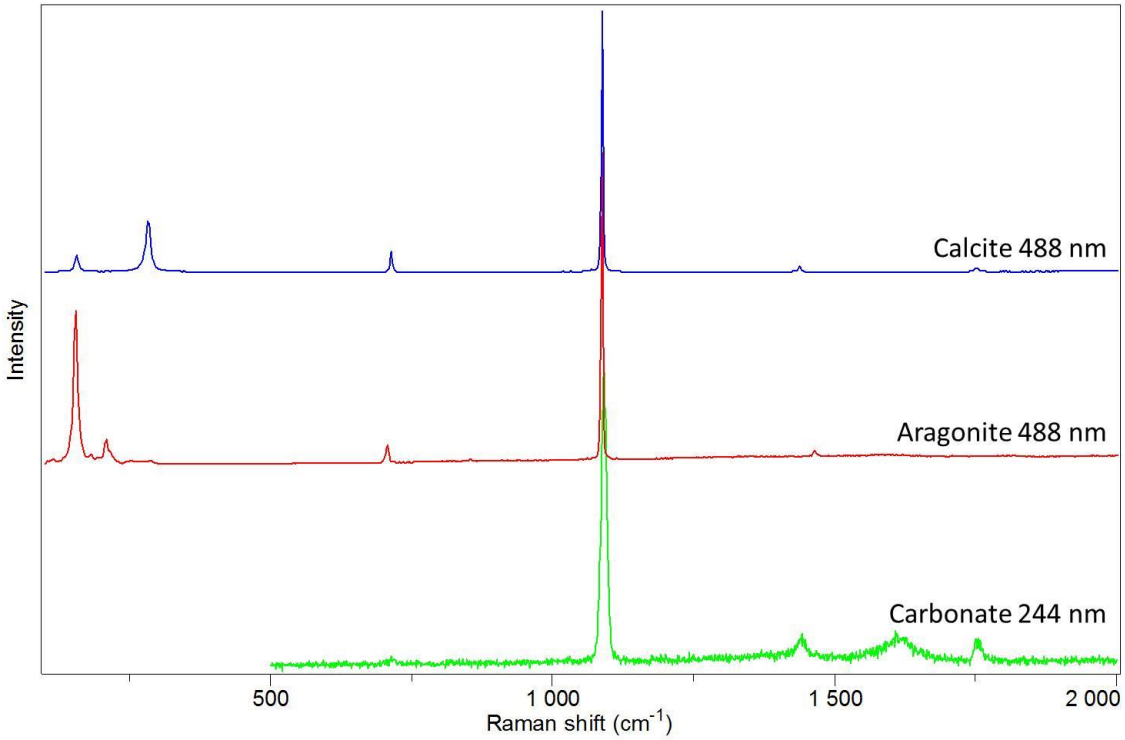

Figure 2: Raman spectra of calcite (blue) and aragonite (red) collected on specimens from the Geoscience Museum of the Georg-August University, Goettingen, recorded with 488 nm excitation. A clear difference in the lower spectral region is obvious. In contrast a carbonate spectrum (green) from a microbialite from the St.Cassian formation, Spain, recorded with 244 nm excitation, where the Raman shift below 500 cm^{-1} cannot be displayed.

1.3 The Raman system

A Raman instrument consists of only four main components: 1) a laser of a specific wavelength as excitation source, 2) optical components for sample illumination and for collecting the Raman scattered light, 3) components for analyzing the spectral properties of light and 4) a device for the detection of light (Ferraro et al., 2003). Nowadays lasers are available with excitation wavelength in the UV, visible or NIR range and also tunable lasers which provide excitation in a larger range (Ferraro et al., 2003). Modern bench top Raman systems use microscope optics for focusing the laser on the sample, yielding a spectral resolution in the order of one micron in all three directions (Ferraro et al., 2003). The Raman spectrometer used in this work (Fig. 3) is equipped with four different lasers with excitation wavelength in the UV (244 nm), the visible (488 nm and 633 nm) and the NIR (785 nm). This gives some possibilities for avoiding fluorescence. The laser light is focused through a microscope optic onto the sample and the scattered light is reflected back through the

microscope into the Raman system. There, the Rayleigh scattered light is separated from the Raman scattered light by a notch filter, which absorbs all light with the same frequency as the incident light. The residual radiation is than dispersed by a grating and focused onto a charge coupled device (CCD) detector (Fig. 3).

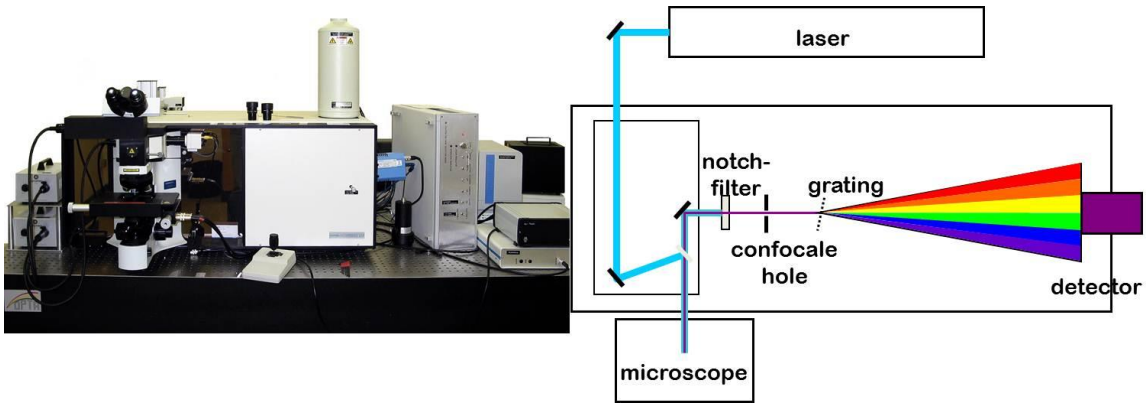

Figure 3: On the left side is a photograph of the Raman spectrometer used in this work. On the right side a simplified illustration of the main components and the pathway of the incident and the scattered light are displayed.

During this work in most of the cases an excitation wavelength of 488 nm with a laser power of 20 mW at the laser exit (ca. 3 mW at the sample) was used. Together with the focal length of the spectrometer of 800 mm and the use of a 600 l/mm grating and a CCD detector with 1024 x 256 pixels, yielded a spectral dispersion of <2 cm^{-1} per pixel. For focusing the laser onto the sample a 100x objective with a numerical aperture of 0.9 was used, which together with closing the confocal hole to 100 µm resulted in a lateral resolution of ca. 1 µm and a depth resolution of ca. 5 µm.

When the excitation wavelength was set to 244 nm, the laser beam was dispersed by a 2400 l/mm grating on a CCD detector with 2048 x 512 pixels, yielding a spectral resolution of ca. 1 cm^{-1} per pixel. For focusing a 40x objective with a numerical aperture of 0.5 was used.

1.4 Interpretation of carbon signatures with Raman spectroscopy

Pioneering work about carbon signatures of graphite and other carbonaceous substances was done by Tuinstra & Koenig (1970). They observed a single Raman band at 1575 cm^{-1} for graphite, whereas other carbonaceous material gave an additional Raman band at 1355 cm^{-1}. Hexagonal sp^2 bonded graphite belongs to the D_{6h}^4 point group, which results into $2E_{2g}$, $2B_{2g}$, E_{1u}, and A_{2u} vibrational modes indicated by the following formula (eq.4) (Tuinstra & Koenig, 1970; Marshall et al., 2010).

$$\Gamma_{vib} = 2B_{2g} + 2E_{2g} + E_{1u} + A_{2u} \qquad \text{(eq.4)}$$

From these possible vibrational modes only the E_{2g} modes are Raman active, whereas the E_{1u} and the A_{2u} modes are IR active (Marshall et al., 2010). The two Raman active E_{2g} modes result in a Raman band at 1582 cm^{-1} and another one in the low frequency range, which is not distinguishable from the Rayleigh line (Wopenka & Pasteris, 1993; Marshall et al., 2010). As this band occurs in all graphitic carbon material it is referred to as G (graphitic) band (e.g. Robertson, 1986; Pasteris & Wopenka, 2003). The additional band observed in other carbonaceous material at 1355 cm^{-1} can be explained by an increased structural disorder of the sp^2 carbon network, which results in an additive Raman active vibrational mode with A_{1g} symmetry (Tuinstra & Koenig, 1970; Marshall et al., 2010). Consequently this band is referred to as D (disorder) band. Raman spectra of carbonaceous material are dominated by these two bands (G and D), representing the first order spectrum (Fig. 4). With increasing disorder of the carbonaceous material the G band is shifted from 1582 cm^{-1} to ca. 1595 cm^{-1} (Marshall et al., 2010), whereby the exact position and width are influenced by the degree of disorder and the size of the crystallites (Pasteris & Wopenka, 2003). The exact position and intensity of the D band is dependent of the excitation wavelength (Vidano et al., 1981; Ferrari, 2002) and is also related to structural disorder (Marshall et al., 2010). The second order spectrum of crystalline hexagonal graphite consists of a doublet at ca. 2695 and 2735 cm^{-1} and weaker bands at ca. 2450 and 3250 cm^{-1}, which are interpreted as overtone and combination bands of the first order spectrum (Vidano et al.,

1981) (Fig. 4). In disordered carbons these bands broaden and additional appear, so that normally bands at ca. 2720, 2950 and 3240 cm^{-1} can be observed (Vidano et al., 1981; Marshall et al., 2010). The second order bands are interpreted as indicating three-dimensional ordering (Lespade et al., 1982).

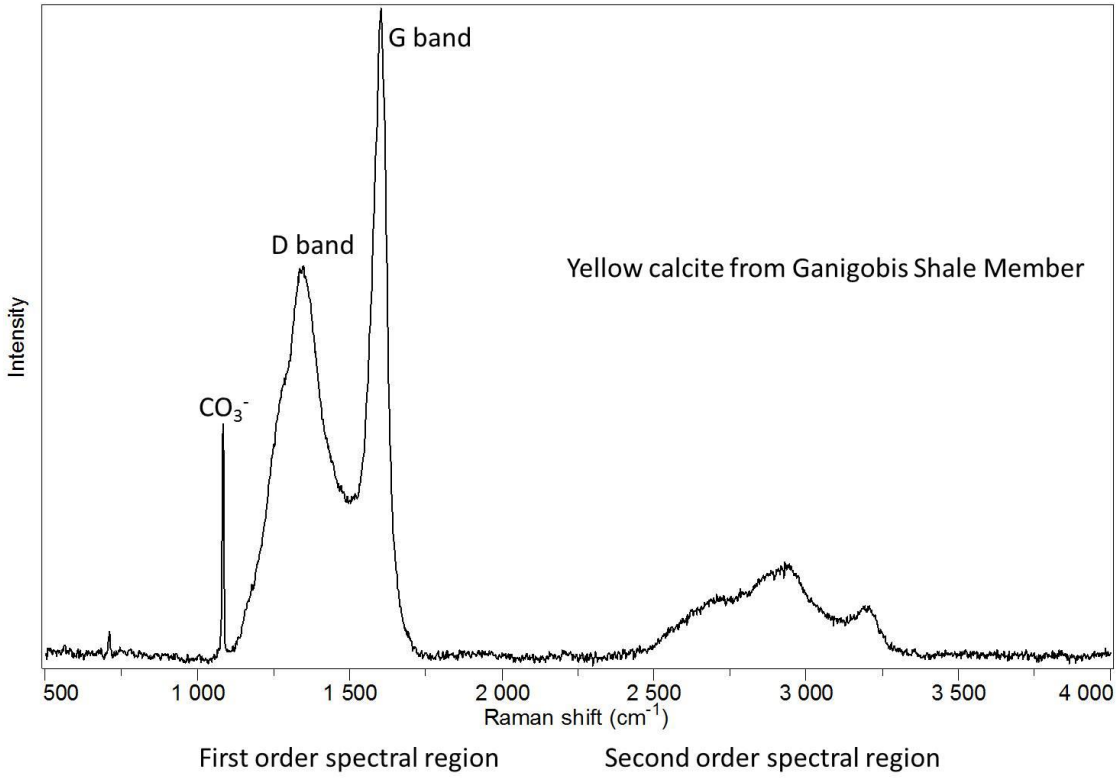

Figure 4: Example for a typical spectrum of disordered carbon. The spectrum was obtained on a Yellow Calcite from the Ganigobis Shale Member, Namibia (compare chapter 6). In the first order spectral region the G and the D band at ca. 1600 cm^{-1} and ca. 1350 cm^{-1} can be observed. The second order bands appear in the higher wavenumber region around 3000 cm^{-1}. An additional band can be seen at 1085 cm^{-1}, which represents vibrations of a CO_3^- molecule.

The difficulties in interpreting carbon signals in ancient rocks lies in the fact that no clear differentiation between carbonaceous matter derived from biological processes and these derived from non-biological processes can be made (cf. Pasteris & Wopenka, 2003). Therefore, especially the proof for ancient life based on carbon signatures is disputable (cf. Brasier et al., 2002; Pasteris & Wopenka, 2002; Schopf et al., 2002). However, it is possible to distinguish between kerogens, that means biological derived material, and disordered graphite, because of increased band widths, displayed band positions and subdued second order bands of the first (Pasteris & Wopenka, 2003). In many metamorphic rocks the carbon content could be used for estimating metamorphic grade temperatures, especially by closely investigating the

average position, intensity and width of both the G and the D band (e.g. Wopenka & Pasteris, 1993; Rahl et al., 2005; Quirico et al., 2009). Only recently Bower et al. (2013) investigated the carbon content of several sedimentary rocks of different ages, together with two different meteorites, in order to improve the understanding of the carbonaceous precursor material. They concluded that a further correlation of the D and G band parameters can be useful for evaluating carbon signatures regarding thermal maturity and a putative biological origin.

This work focuses on various rock types from different locations, as it is crucial for establishing a valuable interpretation of the D and G band parameters to rely on as many different rock types and ages as possible. Thereby the interpretation is mostly focused on the presence and absence of the carbon signal at different parts of the sample. Furthermore, the combination of the carbon signal with mineralogical content at the same spot is from interest. On the other hand, the carbon signals can be used as another step in the line of evidence for samples having a biological origin, together with other information gained with Raman spectroscopy.

1.5 Conditioning film, biofilm, microbial mat

Most organic remains in geobiological samples are connected to the growth of biofilms. A biofilm is defined as an assemblage of microbial cells adhered to each other, irreversibly associated to a surface and enclosed in a matrix of exopolymeric substances (e.g. Costerton et al., 1995; Donlan, 2002). The growth of a biofilm starts in the moment when a solid gets in contact with an aqueous solution. Inorganic and organic molecules present in the liquid move towards the solid surface either by diffusion or turbulent flow (Palmer et al., 2007). Most liquids are not totally neutral in charge due to for example free electrically charged ions (Schneider & Leis, 2003). The same holds true for many surfaces due to unbalanced surface charges. When both phases get in contact some of the free ions get attracted to the charged surface building up an electrostatic boundary (Schneider & Leis, 2003). As bacterial cells in general also have a net negative charge on their cell wall at neutral pH (Rijnaarts et al., 1999; Palmer et al., 2007) a direct attachment of the microbes onto the surface

is prevented due to this hydrodynamic boundary. At the same time diffusion of organic molecules inside an aqueous solution is faster than that of microbes due to their smaller size (Bruinsma et al., 2001). Therefore, it all starts with the adsorption of organic molecules onto the solid surface (Fig. 5A). The molecules form a discontinuous layer with variable thickness. As this layer conditions the surface for the attachment of microbes it is called conditioning film and serves for the microbes as a binding site overcoming the hydrodynamic boundary. An important side effect may be that the conditioning of the surface with organic molecules leads to a concentration of nutrients raising the attractiveness for the microbes to settle there (Knobloch et al., 2001).

Once the conditioning film is formed microbes are able to attach to it (Fig. 5C). This process is initiated by planktonic microbes and proceeds in a reversible and an irreversible step (Petrova & Sauer, 2012). During the reversible attachment stage microbial cells are loosely attached to the surface and to each other and have the ability to return into the planktonic stage (Fig. 5D). This initial attachment is driven by van der Waals forces, electrostatic forces and hydrophobic interactions (Palmer et al., 2007 and citations therein). The irreversible attachment stage is closely related to bacterial adhesins like flagella and pili which allow a permanent binding to each other and to the surface (Palmer et al., 2007). Even more important in that stage is the production of extracellular polymeric substances (EPS) by the microbes (Fig. 5E). In general, EPS consist of mainly polysaccharides, proteins, nucleic acids and lipids (Flemming & Wingender, 2010), has a gelatinous structure and allows the cells to bind and sequester important ions, nutrients and other molecules (Decho, 2011). The composition as well as the function of the different compounds depends on the organisms producing the EPS, and therefore, can vary in a wide range. Furthermore, EPS immobilizes microbial cells and triggers cell interaction including cell-cell communication (Flemming & Wingender, 2010). After the attachment stage the biofilm is fully established and can start to grow and reach a thickness of 10-100 µm (Characklis & Wilderer, 1989) (Fig. 5F).

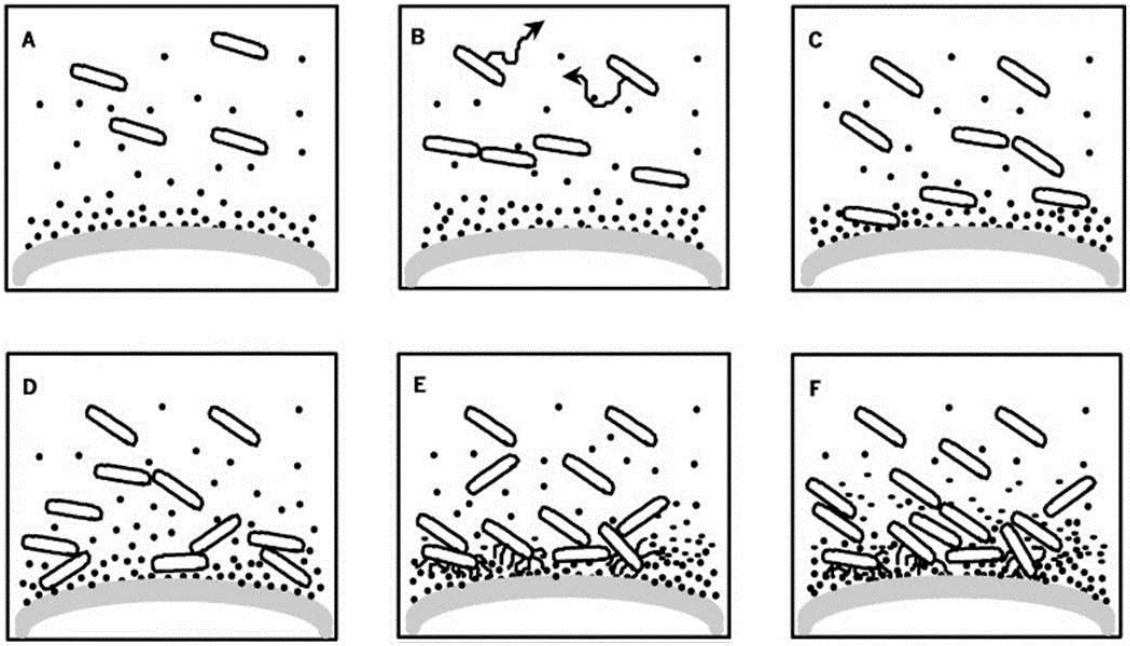

Figure 5: Simplified sketch of biofilm formation (after Bruinsma et al., 2001). (A) Organic molecules adsorb on the surface, building up the conditioning film, while microorganism cannot overcome the electrostatic boundary. (B) Movement of microorganisms towards the conditioned surface. (C) Initial binding of microorganism onto the surface. (D) Loosely attached microorganism on the surface and to each other. Both (C) and (D) represent the reversible part of biofilm formation. (E) Irreversible attachment of microorganism with flagella and pili and the production of EPS. (F) Initial growth of a biofilm.

In contrast to biofilms microbial mats are multi-layered structures of different microorganisms including bacteria, archaea and fungi and can reach a thickness of several cm (Reitner, 2011). They grow in interfaces between different types of material, preferential in moist environments. But they are also reported from extreme environments from deserts to polar regions, like intertidal mud and sand flats, hypersaline lagoons and ponds, polar lakes and soils, hydrothermal vents, cold seeps and alkaline lakes (Friedmann, 1982; Vincent & Howard-Williams, 1989; Stal & Caumette, 1994; Paerl et al., 2000; Van Dover, 2000; Arp et al., 2003; Reitner et al., 2005). The different layers of a microbial mat are dominated by specific microorganisms depending on the respective conditions in that zone. The metabolic activity of the microbes leads to a physico-chemical gradient throughout the mat system (Stal et al., 1985). In photic environments the uppermost layer normally consists of cyanobacteria, whereas the lower most zones are dominated by anaerobic consortia of archaea and sulphate reducing bacteria (Reitner, 2011). Similar as in biofilms EPS is secreted by the microorganisms for stabilizing the mat system. Furthermore, EPS can influence the capability of the microbial mat for sediment

trapping as well as binding of Ca^{2+}-ions and thereby can influence lithification of the mat (Decho et al., 2005; Dupraz & Visscher, 2005). Even more important than the capability of grain trapping is carbonate precipitation, which is initiated by various metabolic processes, including uptake of CO_2 and/or HCO_3^-, ammonification, denitrification and sulphate reduction, leading to an increase in alkalinity (Riding, 2000). Mineralization of microbial mats is quiet common in aquatic environments providing that ionic concentrations are high enough. Mineralized microbial mats are known as stromatolites and thrombolites, and represent the oldest proof of life on Earth.

References

Addadi, L., Raz, S. and Weiner, S. (2003) Taking Advantage of Disorder: Amorphous Calcium Carbonate and Its Roles in Biomineralization. *Advanced Materials* 15: 959-970.

Arp, G., Reimer, A. and Reitner, J. (2003) Microbialite Formation in Seawater of Increased Alkalinity, Satonda Crater Lake, Indonesia. *Journal of Sedimentary Research* 73: 105-127.

Asher, S.A. (1984) Ultraviolet resonance Raman spectrometry for detection and speciation of trace polycyclic aromatic hydrocarbons. *Analytical Chemistry* 56: 720-724.

Bandaranayake, W.M. (2006) The nature and role of pigments of marine invertebrates. *Natural Product Reports* 23: 223-255.

Bauer, M. (2010) Raman spectroscopy of laser induced material alterations. *Dissertation*, Ludwig-Miaximilians-Universität, München, pp. 100.

Beattie, J.R., Maguire, C., Gilchrist, S., Barrett, L.J., Cross, C.E., Possmayer, F., Ennis, M., Elborn, J.S., Curry, W.J., McGarvey, J.J. and Schock, B.C. (2007) The use of Raman microscopy to determine and localize vitamin E in biological samples. *The FASEB Journal* 21: 766-776.

Borzęcka-Prokop, B., Wesełucha-Birczyńska, A. and Koszowska, E. (2007) MicroRaman, PXRD, EDS and microscopic investigation of magnesium calcite biomineral phases. The case of sea urchin biominerals. *Journal of Molecular Structure* 828: 80-90.

Bower, D.M., Steele, A., Fries, M.D. and Kater, L. (2013) Micro Raman spectroscopy of carbonaceous material in microfossils and meteorites: improving a method for life detection. *ASTROBIOLOGY* 13: 103-13.

Brasier, M.D., Green, O.R., Jephcoat, A.P., Kleppe, A.K., Van Kranendonk, M.J., Lindsay, J.F., Steele, A. and Grassineau, N.V. (2002) Questioning the evidence for Earth's oldest fossils. *Nature* 416: 76-81.

Britton, K.A., Dalterio, R.A., Nelson, W.H., Britt, D. and Sperry, J.F. (1988) Ultraviolet Resonance Raman Spectra of Escherichia coli with 222.5-251.0 nm Pulsed Laser Excitation. *Applied Spectroscopy* 42: 782-788.

Bruinsma, G.M., van der Mei, H.C. and Busscher, H.J. (2001) Bacterial adhesion to surface hydrophilic and hydrophobic contact lenses. *Biomaterials* 22: 3217-3224.

Butler, M.J. and Day, A.W. (1998) Fungal melanins: a review. *Canadian Journal of Microbiology* 44: 1115-1136.

Cael, J.J., Gardner, K.H., Koenig, J.L. and Blackwell, J. (1975) Infrared and Raman spectroscopy of carbohydrates. Paper V. Normal coordinate analysis of cellulose I. *The Journal of Chemical Physics* 62: 1145-1153.

Characklis, W. and Wilderer, P. (1989) Structure and Function of Biofilms. *Dahlem Conference Life Science Research Report Nr. 46*, Berlin, Germany, J. Wiley & Sons.

Costerton, J.W., Lewandowski, Z., Caldwell, D.E., Korber, D.R. and Lappin-Scott, H.M. (1995) Microbial biofilms. *Annual Review of Microbiology* 49: 711-745.

Dalterio, R.A., Nelson, W.H., Britt, D. and Sperry, J.F. (1987) An Ultraviolet (242 nm Excitation) Resonance Raman Study of Live Bacteria and Bacterial Components. *Applied Spectroscopy* 41: 417-422.

De Gelder, J., De Gussem, K., Vandenabeele, P. and Moens, L. (2007) Reference database of Raman spectra of biological molecules. *Journal of Raman Spectroscopy* 38: 1133-1147.

Decho, A.W. (2011) Extracellular Polymeric Substances (EPS). In: *Encyclopedia of Geobiology*, edited by J. Reitner and V. Thiel, Springer, Dordrecht, The Netherlands, pp. 359-361.

Decho, A.W., Visscher, P.T. and Reid, R.P. (2005) Production and cycling of natural microbial exopolymers (EPS) within a marine stromatolite. *Palaeogeography, Palaeoclimatology, Palaeoecology* 219: 71-86.

Donlan, R.M. (2002) Biofilms: microbial life on surfaces. *Emerging Infectious Diseases* 8: 881-90.

Dupraz, C. and Visscher, P.T. (2005) Microbial lithification in marine stromatolites and hypersaline mats. *Trends in Microbiology* 13: 429-438.

Edwards, H.G. (2007) Raman spectroscopy in the forensic conservation of a unique marine artefact: The HMS Victory Trafalgar sail. *Spectroscopy Europe* 19: 7-12.

Edwards, H.G.M., Farwell, D.W., Faria, D.L.A.d., Monteiro, A.M.F., Afonso, M.C., Blasis, P.D. and Eggers, S. (2001) Raman spectroscopic study of 3000-year-old human skeletal remains from a sambaqui, Santa Catarina, Brazil. *Journal of Raman Spectroscopy* 32: 17-22.

Etchepare, J., Merian, M. and Kaplan, P. (1978) Vibrational normal modes of SiO_2. II. Cristobalite and tridymite. *The Journal of Chemical Physics* 68: 1531-1537.

Etchepare, J., Merian, M. and Smetankine, L. (1974) Vibrational normal modes of SiO_2. I. alpha and beta quartz. *The Journal of Chemical Physics* 60: 1873-1876.

Ferrari, A.C. (2002) Determination of bonding in diamond-like carbon by Raman spectroscopy. *Diamond and Related Materials* 11: 1053-1061.

Ferraro, J.R., Nakamoto, K. and Brown, C.W. (2003) *Introductory Raman Spectroscopy*. Academic Press, Elsevier, San Diego, CA, USA, pp. 434.

Flemming, H.-C. and Wingender, J. (2010) The biofilm matrix. *Nature Reviews Microbiology* 8: 623-633.

Flemming, H.C. and Ridgway, H. (2009) Biofilm Control: Conventional and Alternative Approaches. In: *Marine and Industrial Biofouling, Springer*

Series on Biofilms Vol.4, edited by H.-C. Flemming, P.S. Murthy, R. Venkatesan and K. Cooksey, Springer Berlin, Heidelberg, Germany, pp. 103-117.

Frech, R., Wang, E.C. and Bates, J. (1980) I. R. and Raman Spectra of $CaCO_3$ (Aragonite). *Spectrochimica Acta Part A: Molecular Spectroscopy* 36: 915-920.

Friedmann, E.I. (1982) Endolithic microorganisms in the antarctic cold desert. *Science* 215: 1045-1053.

Gunasekaran, S., Anbalagan, G. and Pandi, S. (2006) Raman and infrared spectra of carbonates of calcite structure. *Journal of Raman Spectroscopy* 37: 892-899.

Jarvis, R.M., Brookerb, A. and Goodacre, R. (2006) Surface-enhanced Raman scattering for the rapid discrimination of bacteria. *Faraday Discussions* 132: 281-292.

Jehlička, J., Vítek, P., Edwards, H.G.M., Hargreaves, M.D. and Čapoun, T. (2009) Fast detection of sulphate minerals (gypsum, anglesite, baryte) by a portable Raman spectrometer. *Journal of Raman Spectroscopy* 40: 1082-1086.

Knobloch, J.K.-M., Bartscht, K., Sabottke, A., Rohde, H., Feucht, H.-H. and Mack, D. (2001) Biofilm Formation by Staphylococcus epidermidis Depends on Functional RsbU, an Activator of thesigB Operon: Differential Activation Mechanisms Due to Ethanol and Salt Stress. *Journal of Bacteriology* 183: 2624-2633.

Lee, A., Brooker, L., Macey, D., Webb, J. and Bronswijk, W. (2003) A new biomineral identified in the cores of teeth from the chiton Plaxiphora albida. *Journal of Biological Inorganic Chemistry* 8: 256-262.

Lespade, P., Al-Jishi, R. and Dresselhaus, M.S. (1982) Model for Raman scattering from incompletely graphitized carbons. *Carbon* 20: 427-431.

Maddams, W.F. and Royaud, I.A.M. (1990) The characterization of polycyclic aromatic hydrocarbons by Raman spectroscopy. *Spectrochimica Acta Part A: Molecular Spectroscopy* 46: 309-314.

Maquelin, K., Kirschner, C., Choo-Smith, L.P., van den Braak, N., Endtz, H.P., Naumann, D. and Puppels, G.J. (2002) Identification of medically relevant microorganisms by vibrational spectroscopy. *Journal of Microbiological Methods* 51: 255-271.

Marshall, C.P., Edwards, H.G. and Jehlicka, J. (2010) Understanding the application of Raman spectroscopy to the detection of traces of life. *ASTROBIOLOGY* 10: 229-43.

McGuire, M.M., Edwards, K.J., Banfield, J.F. and Hamers, R.J. (2001) Kinetics, surface chemistry, and structural evolution of microbially mediated sulfide mineral dissolution. *Geochimica et Cosmochimica Acta* 65: 1243-1258.

Mernagh, T.P. and Trudu, A.G. (1993) A laser Raman microprobe study of some geologically important sulphide minerals. *Chemical Geology* 103: 113-127.

Nasdala, L., Smith, D.C., Kaindl, R. and Ziemann, M.A. (2004) Raman spectroscopy: Analytical perspectives in mineralogical research. In: *European Mineralogical Union Notes in Mineralogy, Spectroscopic Methods in Mineralogy Vol.6*, edited by A. Beran and E. Libowitzky, Eötvös University Press, Budapest, Hungary, pp. 281-343.

Paerl, H.W., Pinckney, J.L. and Steppe, T.F. (2000) Cyanobacterial–bacterial mat consortia: examining the functional unit of microbial survival and growth in extreme environments. *Environmental Microbiology* 2: 11-26.

Palmer, J., Flint, S. and Brooks, J. (2007) Bacterial cell attachment, the beginning of a biofilm. *Journal of Industrial Microbiology & Biotechnology* 34: 577-588.

Pasteris, J.D. and Wopenka, B. (2002) Laser-Raman spectroscopy (Communication arising): Images of the Earth's earliest fossils? *Nature* 420: 476-477.

Pasteris, J.D. and Wopenka, B. (2003) Necessary, but not sufficient: Raman identification of disordered carbon as a signature of ancient life. *ASTROBIOLOGY* 3: 727-38.

Petrova, O.E. and Sauer, K. (2012) Sticky Situations: Key Components That Control Bacterial Surface Attachment. *Journal of Bacteriology* 194: 2413-2425.

Quirico, E., Montagnac, G., Rouzaud, J.N., Bonal, L., Bourot-Denise, M., Duber, S. and Reynard, B. (2009) Precursor and metamorphic condition effects on Raman spectra of poorly ordered carbonaceous matter in chondrites and coals. *Earth and Planetary Science Letters* 287: 185-193.

Rahl, J.M., Anderson, K.M., Brandon, M.T. and Fassoulas, C. (2005) Raman spectroscopic carbonaceous material thermometry of low-grade metamorphic rocks: Calibration and application to tectonic exhumation in Crete, Greece. *Earth and Planetary Science Letters* 240: 339-354.

Raman, C.V. and Krishnan, K.S. (1928) A new type of secondary radiation. *Nature* 121: 501-502.

Reitner, J. (2011) Microbial Mats. In: *Encyclopedia of Geobiology*, edited by J. Reitner and V.Thiel, Springer, Dordrecht, The Netherlands, pp. 606-608.

Reitner, J., Peckmann, J., Reimer, A., Schumann, G. and Thiel, V. (2005) Methane-derived carbonate build-ups and associated microbial communities at cold seeps on the lower Crimean shelf (Black Sea). *Facies* 51: 66-79.

Riding, R. (2000) Microbial carbonates: the geological record of calcified bacterial–algal mats and biofilms. *Sedimentology* 47: 179-214.

Rijnaarts, H.H.M., Norde, W., Lyklema, J. and Zehnder, A.J.B. (1999) DLVO and steric contributions to bacterial deposition in media of different ionic strengths. *Colloids and Surfaces B: Biointerfaces* 14: 179-195.

Robertson, J. (1986) Amorphous carbon. *Advances in Physics* 35: 317-374.

Rösch, P., Harz, M., Schmitt, M., Peschke, K.-D., Ronneberger, O., Burkhardt, H., Motzkus, H.-W., Lankers, M., Hofer, S., Thiele, H. and Popp, J. (2005) Chemotaxonomic Identification of Single Bacteria by Micro-Raman Spectroscopy: Application to Clean-Room-Relevant Biological Contaminations. *Applied and Environmental Microbiology* 71: 1626-1637.

Rousseau, M., Lopez, E., Couté, A., Mascarel, G., Smith, D.C. and Bourrat, X. (2005) Voronoi Growth model of sheet nacre. *9th International Symposium on Biomineralization*, Pucón,Chile.

Rutt, H.N. and Nicola, J.H. (1974) Raman spectra of carbonates of calcite structure. *Journal of Physics C: Solid State Physics* 7: 4522-4528.

Schneider, R.P. and Leis, A. (2003) Conditioning Films in Aquatic Environments. In: *Encyclopedia of Environmental Microbiology*, edited by, John Wiley & Sons, Inc.

Schopf, J.W., Kudryavtsev, A.B., Agresti, D.G., Wdowiak, T.J. and Czaja, A.D. (2002) Laser-Raman imagery of Earth's earliest fossils. *Nature* 416: 73-76.

Schrader, B. (1991) Raman Spectroscopy of Mineral Oil Products. Part I: NIR/FT-Raman Spectra of Polycyclic Aromatic Hydrocarbons. *Applied Spectroscopy* 45: 1230-1232.

Shinohara, H., Yamakita, Y. and Ohno, K. (1998) Raman spectra of polycyclic aromatic hydrocarbons. Comparison of calculated Raman intensity distributions with observed spectra for naphthalene, anthracene, pyrene, and perylene. *Journal of Molecular Structure* 442: 221-234.

Silve, C., Lopez, E., Vidal, B., Smith, D., Camprasse, S., Camprasse, G. and Couly, G. (1992) Nacre initiates biomineralization by human osteoblasts maintained In Vitro. *Calcified Tissue International* 51: 363-369.

Smekal, A. (1923) Zur Quantentheorie der Dispersion. *Naturwissenschaften* 11: 873-875.

Smith, E. and Dent, G. (2005) *Modern Raman spectroscopy - A practical approach*. John Wiley & Sons Ltd, West Sussex, England, pp. 210.

Spieß, G. and Klapötke, T.M. (1999) *Eine einfache Einführung in die Raman-Spektroskopie*. Ludwig-Maximilians-Universität, München, pp. 17.

Stal, L.J. and Caumette, P. (1994) Microbial mats. Structure, development and environmental significance. In: *NATO ASI Series G: Ecological Sciences, Vol.35*, edited by L.J. Stal and P. Caumette, Springer, Berlin, Germany, pp. 263-263.

Stal, L.J., van Gemerden, H. and Krumbein, W.E. (1985) Structure and development of a benthic marine microbial mat. *FEMS Microbiology Letters* 31: 111-125.

Tuinstra, F. and Koenig, J.L. (1970) Raman Spectrum of Graphite. *The Journal of Chemical Physics* 53: 1126-1130.

Urmos, J., Sharma, S.K. and Mackenzie, F.T. (1991) Characterization of some biogenic carbonates with Raman spectroscopy. *American Mineralogist* 76: 641-646.

Van Dover, C.L. (2000) *The ecology of deep-sea hydrothermal vents*. Princeton University Press, Princeton, USA.

Vidano, R.P., Fischbach, D.B., Willis, L.J. and Loehr, T.M. (1981) Observation of Raman band shifting with excitation wavelength for carbons and graphites. *Solid State Communications* 39: 341-344.

Vincent, W. and Howard-Williams, C. (1989) Microbial communities in southern Victoria Land streams (Antarctica) II. The effects of low temperature. *Hydrobiologia* 172: 39-49.

Weldon, M.K., Zhelyaskov, V.R. and Morris, M.D. (1998) Surface-Enhanced Raman Spectroscopy of Lipids on Silver Microprobes. *Applied Spectroscopy* 52: 265-269.

Wopenka, B. and Pasteris, J.D. (1993) Structural characterization of kerogens to granulite-facies graphite: applicability of Raman microprobe spectroscopy. *American Mineralogist* 78: 533-557.

Wu, Q., Hamilton, T., Nelson, W.H., Elliott, S., Sperry, J.F. and Wu, M. (2001) UV Raman Spectral Intensities of E. Coli and Other Bacteria Excited at 228.9, 244.0, and 248.2 nm. *Analytical Chemistry* 73: 3432-3440.

Zeiri, L., Bronk, B.V., Shabtai, Y., Eichler, J. and Efrima, S. (2004) Surface-Enhanced Raman Spectroscopy as a Tool for Probing Specific Biochemical Components in Bacteria. *Applied Spectroscopy* 58: 33-40.

Chapter 2: Standard substances

In order to create an own database several natural and synthetic standard organic substances were measured. The samples include amino acids, sugars, fatty acids and lipids. Most of the samples were powdered and synthesized by commercial manufacturers (Table 1).

Table 1: List of standard organic substances

Substance class	Substance	Manufacturer	Molecular formula	Appearance
Amino acids	2,6-Diaminopimelic acid	Sigma-Aldrich	$C_7H_{14}N_2O_4$	powder
	L-Glutamic acid	Merck	$C_5H_9NO_4$	powder
	L-Leucine	Sigma-Aldrich	$C_6H_{13}NO_2$	powder
	L-Lysine monohydrochloride	Sigma-Aldrich	$C_6H_{14}N_2O_2$ *HCl	powder
Lipids	5α-Cholestan	Sigma-Aldrich	$C_{27}H_{48}$	powder
	Cholesterol	Matreya	$C_{27}H_{46}O$	powder
	Ergosterol, minimum	Sigma-Aldrich	$C_{28}H_{44}O$	powder
Saccharides	D-(-)-Fructose	Sigma-Aldrich	$C_6H_{12}O_6$	powder
	D-(+)-Galactose	Sigma-Aldrich	$C_6H_{12}O_6$	powder
	D-(+)-Glucose	Sigma-Aldrich	$C_6H_{12}O_6$	powder
	L-(-)-Fucose	Fluka	$C_6H_{12}O_5$	powder
Fatty acids	Linoleic acid	Matreya	$C_{18}H_{32}O_2$	liquid
	Oleic acid	Matreya	$C_{18}H_{34}O_2$	liquid
	Stearic acid	Matreya	$C_{18}H_{36}O_2$	solid

In general the differentiation between various organic substances is very complex, since all organic molecules mainly consist of bonds of carbon atoms with hydrogen, oxygen, nitrogen or carbon itself. Nevertheless, distinct substance classes like amino acids, saccharides, lipids and fatty acids can clearly be distinguished. For example, the spectra of amino acids are influenced by the occurrence of proteins which is represented by the amide I and amide III

bands around 1300 and 1655 cm^{-1}. Fatty acids have their characteristic bands around 1300 and 1440 cm^{-1}. Saccharides show main bands in the regions 1000-1200 cm^{-1} and 1300-1500 cm^{-1}. Lipids are characterized by intense bands around 1400 and between 1600 and 1700 cm^{-1}. What all organic spectra have in common is that each substance has a representative spectrum which can only differ slightly from a spectrum of a very similar substance. This fingerprinting property permits to distinguish between chemical similar substances, especially in the lower wavenumber region. Therefore, the following spectra of standard substances are only displayed from 100-2000 cm^{-1}. In the higher wavenumbers stretching of C-H and O-H occurs at 2800-3000 cm^{-1} and 3100-3600 cm^{-1}, respectively. As these bands normally are much more intense and the variation is quiet small, this region is excluded in the spectra.

The vibrations of saccharides (Fig. 6) can be divided into four different regions (Bell et al., 1994; Yang & Zhang, 2009). The low wavenumber region from 300-600 cm^{-1} is characterized by skeletal vibrations from the pyranose ring structure (Yang & Zhang, 2009). These vibrations are dominated by exo- and endocyclic deformations of the ring structure (De Gelder et al., 2007). In the above examples the most prominent band occurs around 400 cm^{-1} and can be assigned as endocyclic vibration (De Gelder et al., 2007), but between fucose, glucose and galactose a shifting of this vibration is obvious. For fructose that region is much less intense, which probably is related to only four carbon atoms bonded to another molecule in that ring structure. The exocyclic deformations appear around 500 cm^{-1} and also vary in position as well as intensity. In the second region between 600 and 950 cm^{-1} anomeric vibrations occur, that means vibrations of the side groups coupled to the pyranose ring (Bell et al., 1994). Prominent bands can occur between 700 and 800 cm^{-1} which can be assigned to bending vibrations of heavy atoms in the glycosidic link (Bell et al., 1994). In the above examples galactose shows an intense band at around 700 cm^{-1}. Between 800 and 950 cm^{-1} several side group deformations occur (De Gelder et al., 2007). That means for glucose and fructose bands of COH deformations dominate, whereas for fucose additional bands due to CCH deformations appear. The third region from 950-1200 cm^{-1} is the typical fingerprinting region, where prominent bands appear due to glycosidic

stretching modes of C-O and C-C and also C-O-H deformations have a great influence (Bell et al., 1994; De Gelder et al., 2007; Yang & Zhang, 2009). The last region between 1200 and 1500 cm^{-1} is typical for CH_2 and CH deformations (Bell et al., 1994; De Gelder et al., 2007). For galactose additional bands can be observed in that region because of deformations of the CH_2OH group (De Gelder et al., 2007).

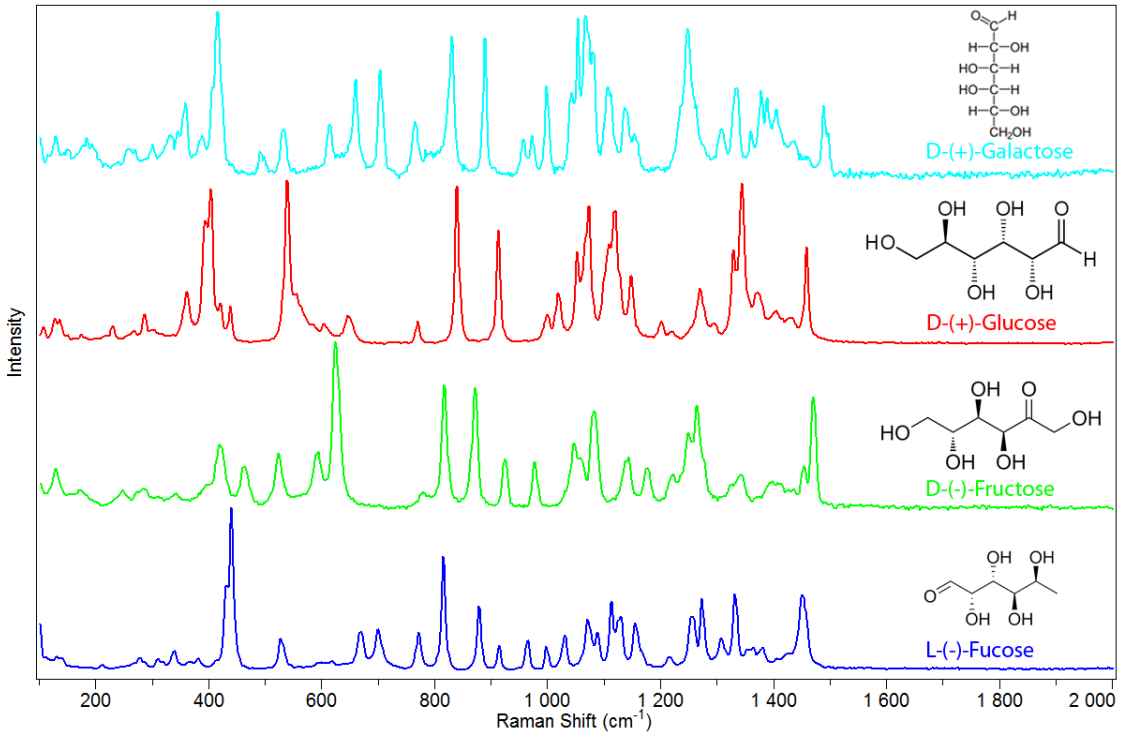

Figure 6: Raman spectrum of L-(-)-Fucose, D-(-)-Fructose, D-(+)-Glucose and D-(+)-Galactose, respectively. The variations of the chemical structures are representative for the difference in the Raman spectrum.

The four analyzed amino acids are characterized by rather simple R side chains. Those of glutamic acid and leucine are simpler and shorter, therefore, their spectra seem not that complex than those of lysine and diaminopimelic acid (Fig. 7). The first prominent bands appear between 800 and 900 cm^{-1} and can be assigned as CNC symmetric stretching vibrations of the amino group (De Gelder et al., 2007). For glutamic acid only one intense band in that region occurs, whereby the other amino acids show more than one band. This is related to the influence of the R group to the position of the C-N stretch band and results in more than one band for more complex and extended R side chains (De Gelder et al., 2007). Lysine and to a smaller degree diaminopimelic acid show various bands around 1000 cm^{-1}, which do not occur for the other

two amino acids. These vibrations can be assigned mainly to stretching vibrations of CH which has the biggest influence on the molecule in lysine. All presented amino acids show intense bands between 1300 and 1500 cm^{-1} which mainly arise due to deformations of CH_2 and CH_3 (e.g. De Gelder et al., 2007). In that region also vibrations of amide bonds can occur, but in most cases these are masked by other vibrations. Only the amide III band can be clearly located for glutamic acid, lysine and leucine between 1620 and 1660 cm^{-1} (Jenkins et al., 2005).

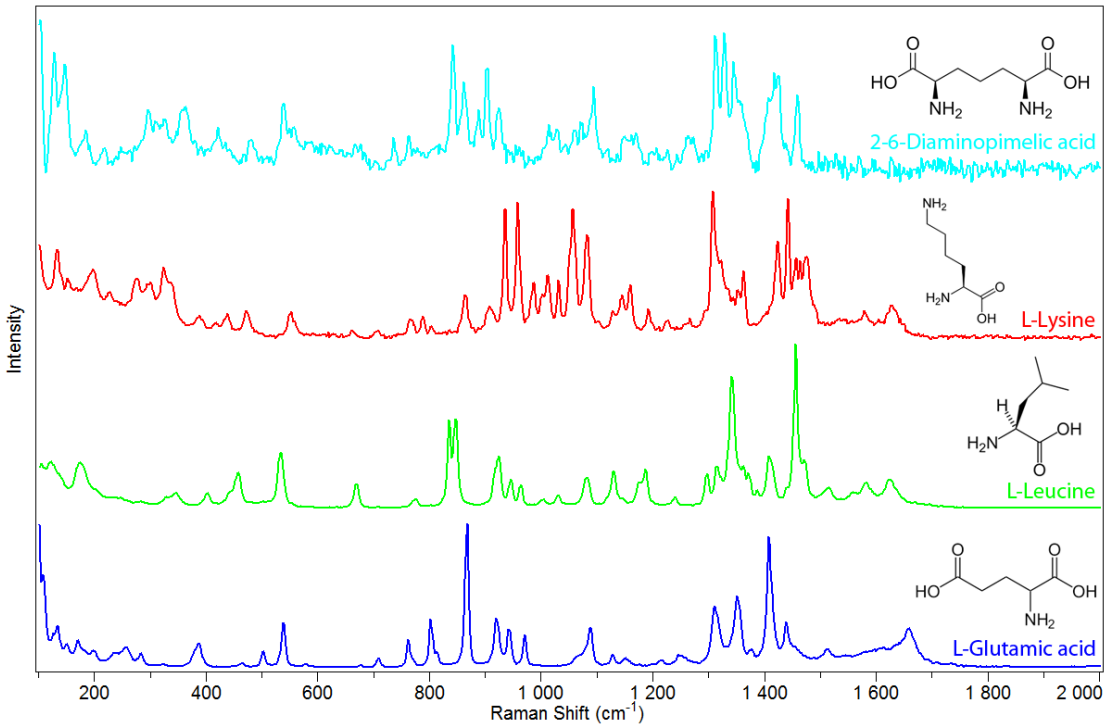

Figure 7: Raman spectrum of L-Glutamic acid, L-Leucine, L-Lysine and 2-6-Daminopimelic acid, respectively. The spectra are highly influenced by vibrations of the amino group. More complex side chains result in a more complex Raman spectrum.

All three shown lipids belong to the group of steroids, whereby cholestan is the simplest and an example for a saturated steroid. The common feature in all three examples is the band between 1440 and 1460 cm^{-1}, which arises due to CH deformations of the aliphatic methyl groups (Steigner & Schrader, 1970; Rösch, 2002; Krafft et al., 2005) (Fig. 8). In cholestan this band is the most intense and no extra bands between 1660 and 1670 cm^{-1} can be seen. In ergosterol the band at 1600 cm^{-1} is the most intense and another around 1665 cm^{-1} occurs. They can be assigned to the C=C in-phase and anti-phase vibrations in the homoannular dien structure (Steigner & Schrader, 1970). In

cholesterol the double bonds are missing, and only an isolated double bond exists. The isolated band around 1700 cm^{-1} in cholestan and cholesterol probably arises due to vibrations of CC and CH groups of the saturated and unsaturated fatty acid chain (Krafft et al., 2005).

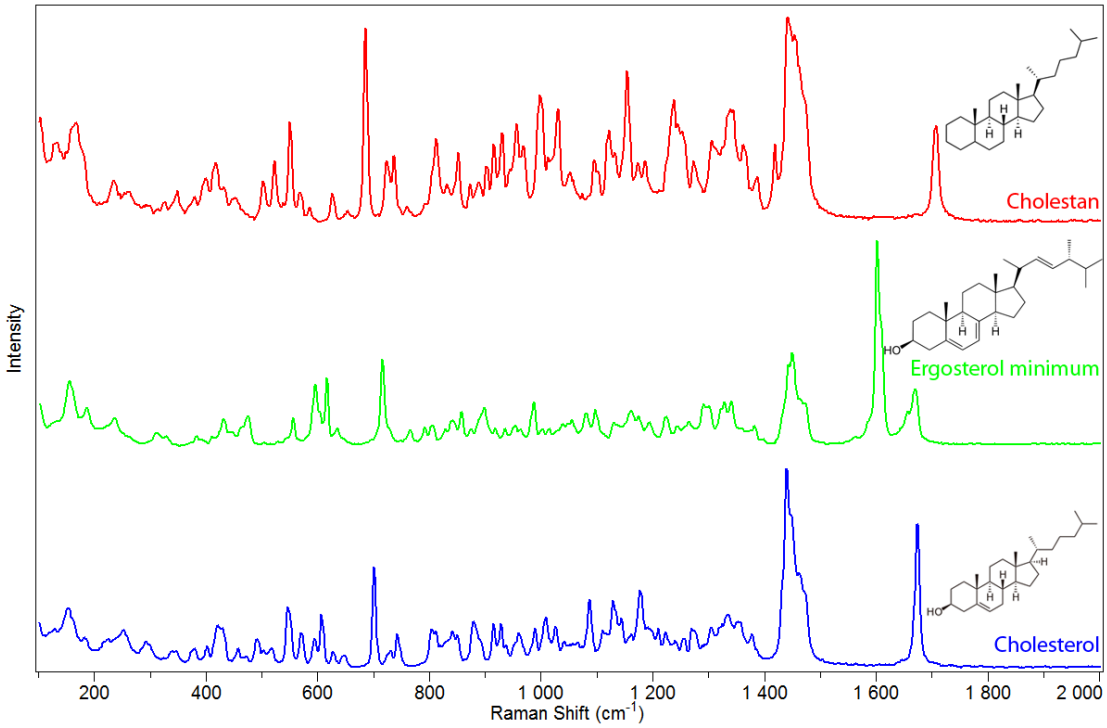

Figure 8: Raman spectrum of Cholesterol, Ergosterol minimum and Cholestan, respectively. The most prominent bands belong to C-H vibrations. Differences in the spectra are mostly related to the number of double bonds.

The most important difference between the three fatty acids is that stearic acid is saturated and therefore has no double bond, whereby oleic and linoleic acid are unsaturated and have one or two double bonds, respectively. Stearic acid is solid at room temperature, whereas oleic acid and linoleic acid are liquid, which can be recognized in the spectra by broadening of the bands (Fig. 9). The saturated stearic acid is characterized by CH_2 deformation bands around 1440 cm^{-1} (Rösch, 2002) as well as several smaller bands between 1000 and 1300 cm^{-1}. The three bands at 1065, 1130 and 1177 cm^{-1} arise due to C-C stretching vibrations in hydrocarbon chains (Chan et al., 2005). The good resolution of these bands are indicative for highly ordered chains in fatty acids (Chan et al., 2005), therefore they cannot be observed for oleic and linoleic acid. In the unsaturated fatty acids bands arise at 1266 cm^{-1} due to =CH in-plane deformations and at 1304 cm^{-1} due to -CH_2 twisting vibrations. These two bands

are indicative for the saturation level in fatty acids, whereby for saturated fatty acids the twisting band is shifted to 1298 cm^{-1} which can be seen in the spectrum for stearic acid (Rösch, 2002). Another important marker for unsaturated fatty acids is the band at 1655 cm^{-1}. The intensity of this band increases with the number of double bonds on cis positions, which is also true for the intensity of the =CH in-plane deformation band, whereas the intensity of the $-CH_2$ twist decreases (Rösch, 2002).

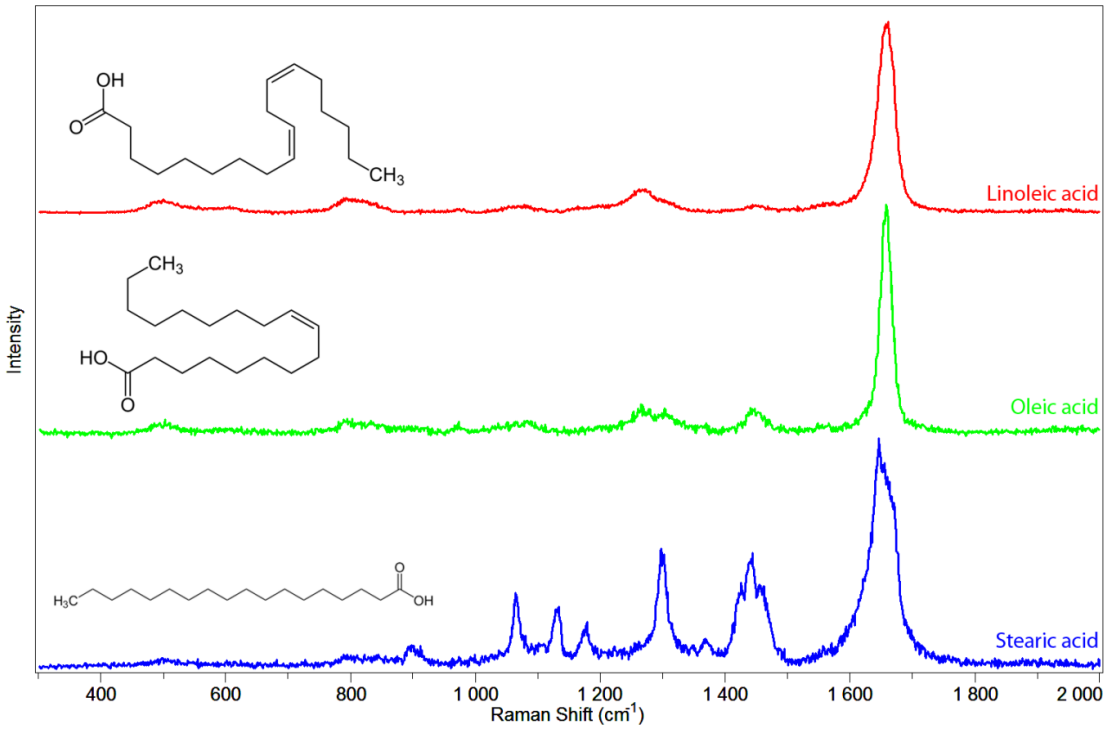

Figure 9: Raman spectrum of Stearic acid, Oleic acid and Linoleic acid, respectively. In the saturated stearic acid bands indicative for highly ordered chains can be observed. The unsaturated fatty acids are dominated by a band at 1655 cm^{-1}, whose intensity varies with number of double bonds on cis positions.

In contrast to the other standard materials, the fatty acids were excited with an UV laser (244 nm). The visible excitation as well as the UV excitation work well for measuring standard substances. However, as already stated in chapter 1, with UV excitation below 500 cm^{-1} no signal can be obtained. Furthermore, the signal to noise ratio for excitation in the visible range is much better.

References

Bell, A.F., Hecht, L. and Barron, L.D. (1994) Disaccharide Solution Stereochemistry from Vibrational Raman Optical Activity. *Journal of the American Chemical Society* 116: 5155-5161.

Chan, J.W., Motton, D., Rutledge, J.C., Keim, N.L. and Huser, T. (2005) Raman Spectroscopic Analysis of Biochemical Changes in Individual Triglyceride-Rich Lipoproteins in the Pre- and Postprandial State. *Analytical Chemistry* 77: 5870-5876.

De Gelder, J., De Gussem, K., Vandenabeele, P. and Moens, L. (2007) Reference database of Raman spectra of biological molecules. *Journal of Raman Spectroscopy* 38: 1133-1147.

Jenkins, A.L., Larsen, R.A. and Williams, T.B. (2005) Characterization of amino acids using Raman spectroscopy. *Spectrochimica Acta Part A: Molecular and Biomolecular Spectroscopy* 61: 1585-1594.

Krafft, C., Neudert, L., Simat, T. and Salzer, R. (2005) Near infrared Raman spectra of human brain lipids. *Spectrochimica acta. Part A, Molecular and biomolecular spectroscopy* 61: 1529-1535.

Rösch, P. (2002) Raman-spektroskopische Untersuchungen an Pflanzen und Mikroorganismen. *Dissertation*, Julius-Maximilians-Universität Würzburg, pp. 195.

Steigner, E. and Schrader, B. (1970) Ramanspektroskopie und Molekülstruktur, II1) Strukturaufklärung von Steroiden mit Hilfe der Ramanspektroskopie. *Justus Liebigs Annalen der Chemie* 735: 15-22.

Yang, L. and Zhang, L.-M. (2009) Chemical structural and chain conformational characterization of some bioactive polysaccharides isolated from natural sources. *Carbohydrate Polymers* 76: 349-361.

Chapter 3 Detection of fossil melanin

3.1 General introduction to melanin

Melanins are macromolecules belonging to the class of pigments and are very widespread in the biosphere. Normally they are classified into eumelanins, which are black in color and contain nitrogen and pheomelanins, which can have a broad range of colors from yellow to red to brownish and additionally contain sulfur (Hackman & Goldberg, 1971; Capozzi et al., 2005). Melanins are synthesized and stored in melanosomes, which are lysosome-related organelles of pigment cells (Raposo & Marks, 2007). During several maturation steps melanosomes can evolve a variety of shapes from ellipsoidal over spherical to almost round, also dependent on the organisms in which they are formed, with a typical size between 500 and 2000 nm (Raposo & Marks, 2007; Lindgren et al., 2012). The research areas regarding melanins are widespread with a medical relevant focus on melanin in tissues (e.g. Watts et al., 1981; Scalia et al., 1990; Wakamatsu & Ito, 2002). Due to the high resistance of the molecule there is some evidence for fossilized melanins, especially in the ink sacs of “Sepia” (Beyermann & Hasenmaier, 1973) and in ammonites (Mathur, 1996), eye systems of lobopods (Schoenemann et al., 2009), fish eyes (Lindgren et al., 2012) and in feathers (Vinther et al., 2008; Li et al., 2010; Barden et al., 2011; Wogelius et al., 2011; Carney et al., 2012). In contrast to other essential biopolymers (carbohydrates, proteins and nucleic acids) melanins are composed of various types of monomers connected by strong carbon-carbon bonds, hindering a clear characterization (Wakamatsu & Ito, 2002). Nevertheless, the basic structure of melanin can be described by covalently linked indoles. Especially for eumelanins the basic building blocks are supposed to be hydroquinone (HQ), indolequinone (IQ) and semiquinone (SQ) (Powell et al., 2004). A good summary of the different properties of melanins is given by Riley (1997), amongst which light absorbance may be is the most important and also is responsible for the difficulties of detecting melanins, especially with spectroscopic methods. The identification of melanin often is based on structural appearance, which can be misleading, because the shape and size of melanosomes corresponds to those of bacteria (Lindgren et

al., 2012). Therefore, it is crucial to be able to distinguish between fossilized melanin residues and structures covered by bacterial biofilms, which indeed can also be responsible for preservation of soft tissue in the fossil record (Wuttke, 1983; Reitner, 2011).

3.2 Melanin in fossil ink sacs of coleoid cephalopods (Vampyromorpha)

In this work various samples from fossilized Vampyromorpha ink sacs were directly measured for characterizing the melanin spectra. The samples originate from the Cenomanian Fish Shale (Fischschiefer) in Lebanon (L1, L2), the Tithonian Solnhofen Plattenkalk (S1, S2) and the Toarcian Posidonienschiefer in Holzmaden, Germany. The color of the melanin in the ink sacs varies from yellowish in the sample from Lebanon, over brownish, red in the samples from the Solnhofen Plattenkalk to black in the samples from the Posidonienschiefer. As melanin is very opaque, spectra were tried to record with all available excitation wavelengths. Thereby, clearest bands could be recorded with excitation in the UV (244 nm), whereas in the NIR (785 nm) no signal could be detected at all. In the low visible range (488 nm) only the main carbon vibrations could be recorded, whereas in the higher visible range (633 nm) the complete spectra were masked by fluorescence. In the following spectra recorded with 244 nm excitation will be shown from Lebanon (L1), and the Solnhofen Plattenkalk (S1), as well as from the Posidonienschiefer (M1, M2) with additional spectra recorded with 488 nm excitation. Due to technical limitations spectra in the UV can only be recorded with a minimum Raman shift of 500 cm^{-1}, whereas the spectra in the visible range already start at a Raman shift of 200 cm^{-1}.

In most of the spectra additional bands due to the carbonate matrix can be observed. Especially in the range around 1085 cm^{-1} the main CO_3^- vibration is visible. The most prominent bands for melanin arise around 1600 cm^{-1} due to C-C stretching of aromatic units and around 1400 cm^{-1} due to aromatic C-N bonds (Horiba, application note: http://www.horiba.com/fileadmin/uploads/Scientific/Documents/Raman/bands.pdf; Socrates, 2001; Smith & Dent, 2005). Furthermore, bands or shoulders can be recognized around 1330 and 1200 cm^{-1}.

In the Fish Shale sample from Lebanon always a very strong carbonate signal (1085, 1413 and 1749 cm^{-1}) from the surrounding rock was visible (Fig. 10). The melanin signal mainly was concentrated on the 1600 cm^{-1} region. The aromatic C-N bonds are only visible in a very weak shoulder around 1400 cm^{-1}, whereas the stronger band at 1433 cm^{-1} belongs to the carbonate stretching vibrations. Around 700 cm^{-1} a broad band appears probably due to additional sulfur in the melanin structure. In this range stretching vibrations of aliphatic C-S bonds occur (Smith & Dent, 2005).

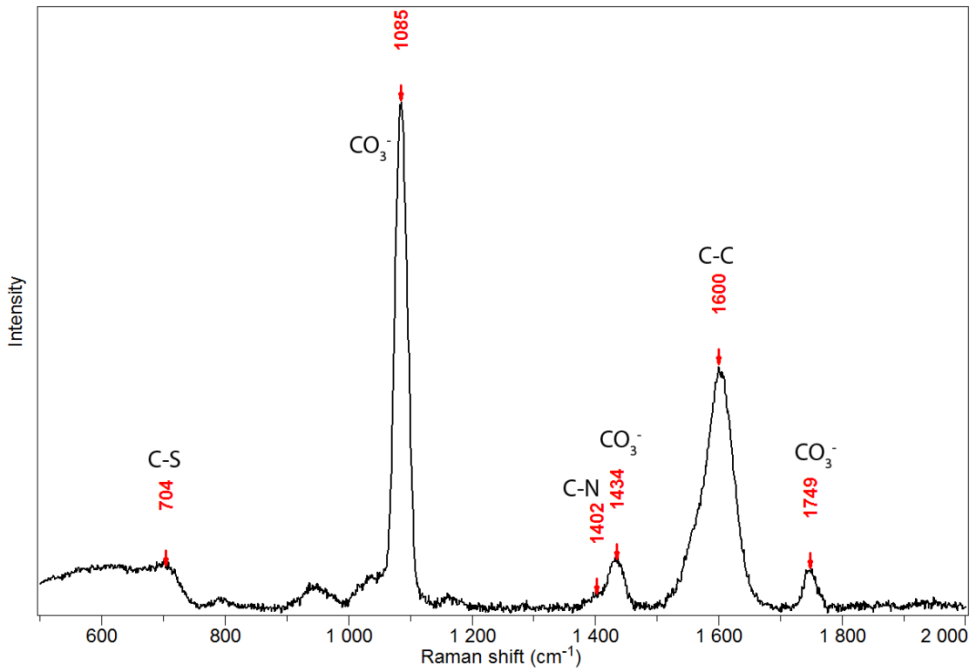

Figure 10: Melanin spectrum from the fossil ink sac of Vampyromorpha from the Cenomanian Fish Shale (Lebanon). High signals from the background carbonate are prominent. Main melanin signals occur due to C-C vibrations at 1600 cm^{-1}, C-N vibrations at 1402 cm^{-1} and C-S vibrations at 704 cm^{-1}.

The melanin spectra from the Solnhofen Plattenkalk (Fig. 11) are dominated by broad bands centered at 1602 cm^{-1} and 1420 cm^{-1}, which belong to C-C and C-H vibrations, respectively (Socrates, 2001; Smith & Dent, 2005). According to Powell et al. (2004) vibrations of hydroquinone would be expected at 1425 cm^{-1}, and could also account to the broad band at 1420 cm^{-1}. Significant band also arise at 963 cm^{-1} and 1075 cm^{-1}. Bands between 950 and 980 cm^{-1} were also observed by Samokhvalov et al. (2004) and are supposed to represent ring modes of the phenyl group. However, this assignment is not quite clear. The band at 1075 cm^{-1} is predicted to occur in semiquinone (Powell et al., 2004), but

also C-S aromatic stretching vibrations appear in that area (Smith & Dent, 2005).

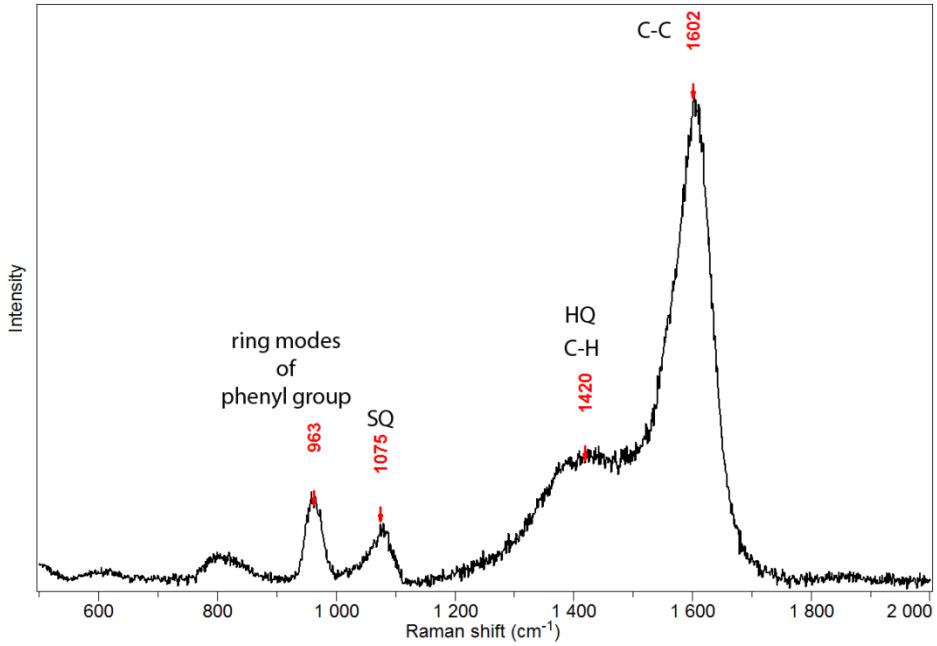

Figure 11: Melanin spectrum from the fossil ink sac of Vampyromorpha of the Tithonian Solnhofen Plattenkalk. Main signals belong to vibrations of C-C and C-H molecules. But also vibrations of the key monomers hydroquinone (HQ) and semiquinone (SQ) can be assigned. Additionally, ring modes of the phenyl group can be observed.

In the spectra from the Posidonienschiefer from Holzmaden clear differences can be seen between excitation with 244 nm and with 488 nm (Fig. 12). With 244 nm almost only the main carbon stretching vibrations centered at 1600 cm^{-1} are visible. In the sample M2 additionally signals from the carbonate matrix appear. On the other hand the spectra recorded with 488 nm excitation show aside to the C-C vibrations another dominant area between 1300 and 1400 cm^{-1}, which is only slightly denoted when excited with 244 nm. This pattern was observed by several working groups as the typical melanin spectrum, whereby an analysis of the broad band areas with Gaussian functions reveals several different bands which can be assigned to vibrations of the key monomers of eumelanin (see Capozzi et al., 2005). Another interesting area again is again more obvious in the spectra recorded with 488 nm excitation wavelength. The broad band between 550 and 600 cm^{-1} can be interpreted as an enrichment of Fe (III) in the melanin. This phenomenon is described by Samokhvalov et al. (2004) who observed an increase of a band centered at 570 cm^{-1} with increasing Fe (III) content.

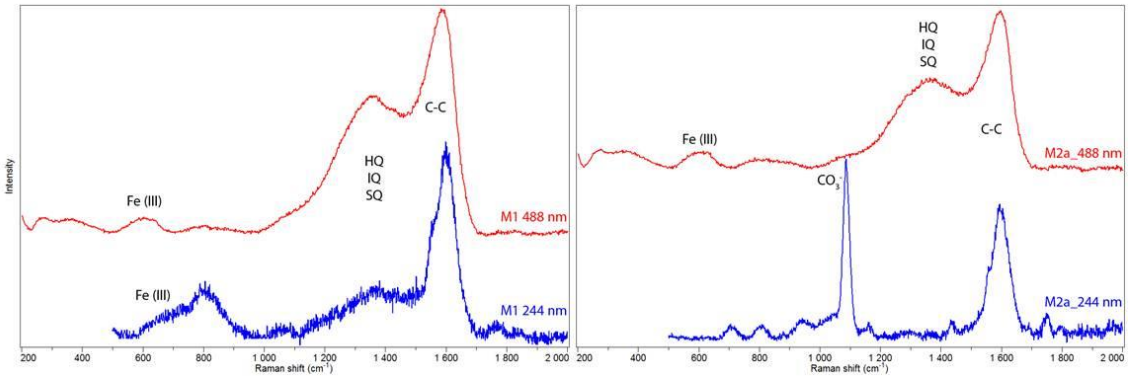

Figure 12: Melanin spectra of the fossil ink sac of Vampyromorpha from the Toarcian Posidonienschiefer in Holzmaden. Clear differences can be seen between excitation with 244 nm and with 488 nm wavelength. HQ, IQ and SQ stand for the key melanin monomers hydroquinone, indolequinone and semiquinone.

The results of those Mesozoic fossils show that vibrations which can be assigned to melanin can be reproduced. However, Raman spectra of melanin are much more unspecific (cf. Samokhvalov et al., 2004; Capozzi et al., 2005; Perna et al., 2005) as spectra of standard materials as shown in chapter 2. Nevertheless, differences between the sampled specimens can be related to their different color, which is influenced by the occurrence of sulfur in the melanin structure (Hackman & Goldberg, 1971). Therefore, the melanin spectra from the yellowish Fish Shale sample from Lebanon show bands related to C-S vibrations and the black samples from the Posidonienschiefer are influenced by higher Fe content.

The comparison of the results with 244 nm and 488 nm excitation has shown that with 488 nm excitation the signal to noise ratio of the spectra is much better. Additionally, a better analogy to the predicted key monomers (HQ, IQ, SQ) of melanin reported by Powell et al. (2004) could be found with an excitation wavelength of 488 nm. Therefore, in the following the detection of melanin was only performed with this excitation wavelength.

3.3 Melanin in fossil eye systems

Based on these findings further approaches were made for detecting melanin in fossils. It is well known that melanins are responsible for the color of hair and eyes in mammals (Riley, 1997). They are also expected to already have an important role on simple early eye systems (Schoenemann et al., 2009).

Therefore a fossil sample of a nematomorph worm from the Chengjang lagerstätte, China provided by Brigitte Schoenemann was analyzed with Raman spectroscopy in order to detect traces of melanin. The worm has an almost identical appearance to the nematomorph *Cricocosmia jinningensis* described by Hou & Sun (1988), differing only by two conspicuous spot eyes, identified by their typical morphological position in the head region (Schoenemann, 2012; unpublished). The spectrum was recorded with 488 nm excitation wavelength and it was concentrated only on the region with the most intense bands between 1200 and 1600 cm^{-1} (Fig. 13). As these bands are very broad it is probable that they reflect various overlaying vibrations. Therefore, after baseline subtraction a peak fitting with a Gauss Lorentz function was performed via the spectrometer software.

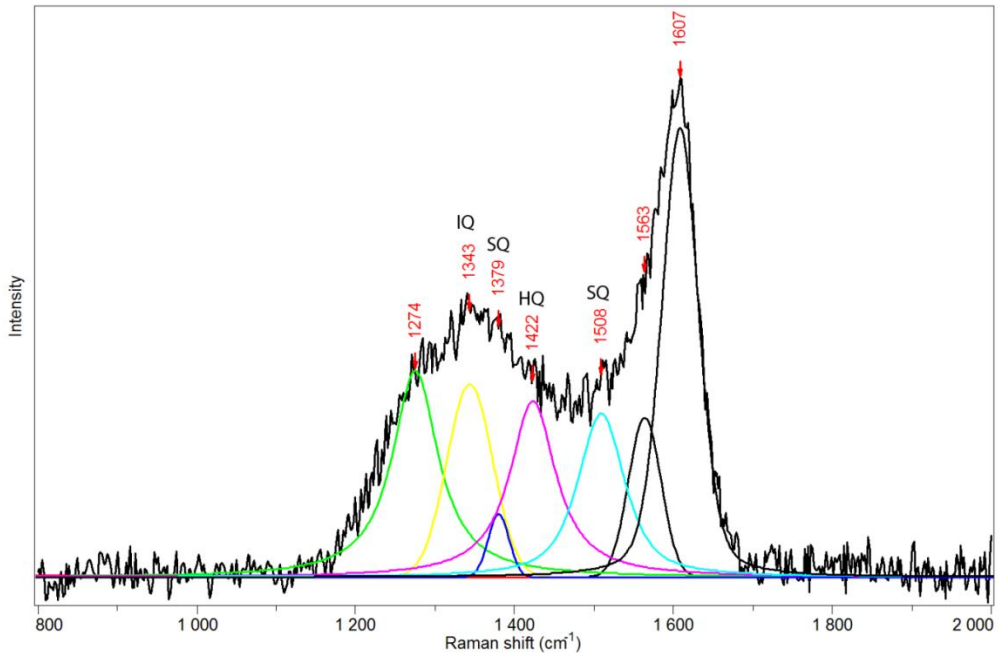

Figure 13: Raman spectrum of the eye spot of a nematomorph worm consisting of melanin. The irregular shape of the bands indicates several underlying bands which are displayed by the colored bands underneath the spectrum. The position of these bands represents a Gauss-Lorentz function which was calculated via the spectrometer software. The assignment refers to the expected bands of the key monomers of melanin hydroquinone (HQ), indolequinone (IQ) and semiquinone (SQ) after Powell et al. (2004).

The main band centered at 1607 cm^{-1} belongs to carbon vibrations. Based on the predicted bands for the key melanin monomers by Powell et al. (2004) bands could be assigned to IQ (1343 cm^{-1}), HQ (1422 cm^{-1}) and SQ (1379 and 1508 cm^{-1}). Also Capozzi et al. (2005) assign bands at 1510 cm^{-1} to stretching

vibrations of C=N as they occur in SQ, but also an influence of N-H bending is possible. In this case, Raman spectroscopy is a valuable tool for providing a good argument that melanin already occurred in early developed eye systems. As discussed by Schoenemann et al. (2009) eye systems in especially small fossils can only be described due to their size and their general appearance as well as the localization in the fossil itself. With Raman spectroscopy additional evidence can be supplied by identifying the typical melanin bands on dark areas in fossils which are suspected to belong to eye systems, in contrast to any other randomly dark region.

References

Barden, H.E., Wogelius, R.A., Li, D., Manning, P.L., Edwards, N.P. and van Dongen, B.E. (2011) Morphological and Geochemical Evidence of Eumelanin Preservation in the Feathers of the Early Cretaceous Bird, *Gansus yumenensis*. *PLoS ONE* 6: e25494.

Beyermann, K. and Hasenmaier, D. (1973) Identifizierung 180 Millionen Jahre alten, wahrscheinlich unverändert erhaltenen Melanins. *Fresenius' Zeitschrift für analytische Chemie* 266: 202-205.

Capozzi, V., Perna, G., Gallone, A., Biagi, P.F., Carmone, P., Fratello, A., Guida, G., Zanna, P. and Cicero, R. (2005) Raman and optical spectroscopy of eumelanin films. *Journal of Molecular Structure* 744–747: 717-721.

Carney, R.M., Vinther, J., Shawkey, M.D., D'Alba, L. and Ackermann, J. (2012) New evidence on the colour and nature of the isolated Archaeopteryx feather. *Nature Communications* 3: 637.

Hackman, R.H. and Goldberg, M. (1971) Microchemical detection of melanins. *Analytical Biochemistry* 41: 279-285.

Horiba *Raman Application Note. Raman Data and Analysis: Raman spectroscopy for analysis and monitoring*. http://www.horiba.com/fileadmin/uploads/Scientific/Documents/Raman/bands.pdf

Hou, X. and Sun, W. (1988) Discovery of Chengjiang fauna at Meishucun, Jinning, Yunnan. *Acta Palaeontologica Sinica* 27: 1-112.

Li, Q., Gao, K.-Q., Vinther, J., Shawkey, M.D., Clarke, J.A., D'Alba, L., Meng, Q., Briggs, D.E.G. and Prum, R.O. (2010) Plumage Color Patterns of an Extinct Dinosaur. *Science* 327: 1369-1372.

Lindgren, J., Uvdal, P., Sjövall, P., Nilsson, D.E., Engdahl, A., Schultz, B.P. and Thiel, V. (2012) Molecular preservation of the pigment melanin in fossil melanosomes. *Nature Communications* 3: 824.

Mathur, A. (1996) Über Ammoniten der Kössener Schichten und den Nachweis der Tintenbeutel-Substanz Melanin bei ihnen. *Documenta Naturae* 102: 1-161.

Perna, G., Gallone, A., Capozzi, V., Biagi, P.F., Fratello, A., Guida, G., Zanna, P., Argenzio, E. and Cicero, R. (2005) Optical Spectra of Melanin Films Extracted from Rana esculenta L. *Physica Scripta* 2005: 89.

Powell, B.J., Baruah, T., Bernstein, N., Brake, K., McKenzie, R.H., Meredith, P. and Pederson, M.R. (2004) A First Principles Density-Functional Calculation of the Electronic and Vibrational Structure of the Key Melanin Monomers. *Journal of Chemical Physics* 120: 8608-8615.

Raposo, G. and Marks, M.S. (2007) Melanosomes [mdash] dark organelles enlighten endosomal membrane transport. *Nature Reviews Molecular Cell Biology* 8: 786-797.

Reitner, J. (2011) Biofilms and Fossilization. In: *Encyclopedia of Geobiology*, edited by J. Reitner and V.Thiel, Springer, Dordrecht, The Netherlands, pp. 136-137.

Riley, P.A. (1997) Melanin. *The International Journal of Biochemistry & Cell Biology* 29: 1235-1239.

Samokhvalov, A., Liu, Y. and Simon, J.D. (2004) Characterization of the Fe(III)-binding Site in Sepia Eumelanin by Resonance Raman Confocal Microspectroscopy. *Photochemistry and Photobiology* 80: 84-88.

Scalia, M., Geremia, E., Corsaro, C., Santoro, C., Baratta, D. and Sichel, G. (1990) Lipid Peroxidation in Pigmented and Unpigmented Liver Tissues: Protective Role of Melanin. *Pigment Cell Research* 3: 115-119.

Schoenemann, B. (2012) Analysis of fossilized eye systems. An approach to describe internal structures and functions of fossilised visual systems and their relevance in palaeocological contexts and evolution. *Habilitation treatise*, unpublished, pp. 89.

Schoenemann, B., Liu, J.-N., Shu, D.-G., Han, J. and Zhang, Z.-F. (2009) A miniscule optimized visual system in the Lower Cambrian. *Lethaia* 42: 265-273.

Smith, E. and Dent, G. (2005) *Modern Raman spectroscopy - A practical approach*. John Wiley & Sons Ltd, West Sussex, England, pp. 210.

Socrates, G. (2001) *Infrared and Raman Characteristic Group Frequencies: Tables and Charts.* John Wiley and Sons, Chichester, West Sussex, England.

Vinther, J., Briggs, D.E.G., Prum, R.O. and Saranathan, V. (2008) The colour of fossil feathers. *Biology Letters* 4: 522-525.

Wakamatsu, K. and Ito, S. (2002) Advanced Chemical Methods in Melanin Determination. *Pigment Cell Research* 15: 174-183.

Watts, K.P., Fairchild, R.G., Slatkin, D.N., Greenberg, D., Packer, S., Atkins, H.L. and Hannon, S.J. (1981) Melanin Content of Hamster Tissues, Human Tissues, and Various Melanomas. *Cancer Research* 41: 467-472.

Wogelius, R.A., Manning, P.L., Barden, H.E., Edwards, N.P., Webb, S.M., Sellers, W.I., Taylor, K.G., Larson, P.L., Dodson, P., You, H., Da-qing, L. and Bergmann, U. (2011) Trace Metals as Biomarkers for Eumelanin Pigment in the Fossil Record. *Science* 333: 1622-1626.

Wuttke, M. (1983) Weichteil-Erhaltung'durch lithifizierte Mikroorganismen bei mittel-eozänen Vertebraten aus den Ölschiefern der 'Grube Messel'bei Darmstadt. *Senckenbergiana lethaea* 64: 509-527.

3.4 General introduction to fungal melanin

Another group of interest regarding melanin analysis is fungi. Many of them are known to produce them, whereby research is very much concentrated on dihydroxy-naphtalene (DHN) melanin, because it is produced by a wide range of plant pathogenic fungi (Butler & Day, 1998). The most important difference between fungal melanin and eumelanin is that they originate from different monomers, most of which do not contain nitrogen (Butler & Day, 1998). Nevertheless spectroscopic analyzes of the different melanin types do not show significant differences (Cappitelli et al., 2005). The fungal melanin analyzed in this work belongs to *Eomelanomyces cenococcoides*, which develops ectomycorrhizas on the surface of absorbing roots of the host.

3.4.1

Ectomycorrhizas from a Lower Eocene angiosperm forest

Christina Beimforde[1], Nadine Schäfer[1], Heinrich Dörfelt[2], Paul C. Nascimbene[3], Hukam Singh[4], Jochen Heinrichs[5], Joachim Reitner[1], Rajendra S. Rana[6] and Alexander R. Schmidt[1]

Published in New Phytologist (2011) 192: 988–996

[1]Courant Research Centre Geobiology, Georg-August-Universität Göttingen, Goldschmidtstraße 3, 37077 Göttingen, Germany;

[2]Mikrobielle Phytopathologie, Friedrich-Schiller-Universität Jena, Neugasse 25, 07743 Jena, Germany;

[3]Division of Invertebrate Zoology, American Museum of Natural History, 79th Street at Central Park West, New York, NY 10024, USA;

[4]Birbal Sahni Institute of Palaeobotany, 53 University Road, Lucknow 226007, India;

[5]Albrecht-von-Haller-Institut für Pflanzenwissenschaften, Abteilung Systematische Botanik, Georg-August-Universität Göttingen, Untere Karspüle 2, 37073 Göttingen, Germany;

[6]Department of Geology, Hemwati Nandan Bahuguna Garhwal University, Srinagar 246174, India

Summary

• The development of mycorrhizal associations is considered a key innovation that enabled vascular plants to extensively colonize terrestrial habitats. Here, we present the first known fossil ectomycorrhizas from an angiosperm forest.

• Our fossils are preserved in a 52 million-yr-old piece of amber from the Tadkeshwar Lignite Mine of Gujarat State, western India. The amber was produced by representatives of Dipterocarpaceae in an early tropical broadleaf forest. The ectomycorrhizas were investigated using light microscopy and field emission scanning electron microscopy. Dissolving the amber surrounding one of the fossils allowed ultrastructural analyses and Raman spectroscopy.

• Approx. 20 unramified, cruciform and monopodial-pinnate ectomycorrhizas are fossilized adjacent to rootlets, and different developmental stages of the fossil mycorrhizas are delicately preserved in the ancient resin. Compounds of melanins were detectable in the dark hyphae.

• The mycobiont, *Eomelanomyces cenococcoides* gen. et spec. nov., is considered to be an ascomycete; the host is most likely a dipterocarp representative. An early ectomycorrhizal association may have conferred an evolutionary advantage on dipterocarps. Our find indicates that ectomycorrhizas occurred contemporaneously within both gymnosperms (Pinaceae) and angiosperms (Dipterocarpaceae) by the Lower Eocene.

3.4.1.1 Introduction

Mycorrhizas are ubiquitous in terrestrial ecosystems. Up to 90% of all vascular plants live in a mutualistic association with fungi (Malloch et al., 1980). One selective advantage of mycorrhizal symbioses is an increase in the plant's uptake of phosphorus and nitrogen. Additionally, some fungal partners protect plants against droughts and diseases such as microbial soilborne pathogens. At the same time, the fungus gets a relatively constant and direct access to carbohydrates. This symbiotic relationship is considered to be a key innovation of early land plants that enabled them to extensively colonize terrestrial habitats (Cairney, 2000; Wang et al., 2010).

Various classes of mycorrhizas have evolved over the course of time (Brundrett, 2002). Arbuscular endomycorrhizas are the oldest and most abundant ones (Cairney, 2000) and are recorded since the Early Devonian (Remy et al., 1994). Presently, > 70% of all angiosperms build such endomycorrhizal associations, while only 2% build ectomycorrhizal ones (Brundrett, 2009). Within the gymnosperms, ectomycorrhizas are only known from Pinaceae and from the genus *Gnetum* (Brundrett, 2009).

The evolution of different classes of mycorrhizas was influenced not only by changing environmental conditions, but also by the appearance of possible new fungal symbionts (Cairney, 2000; Hibbett & Matheny, 2009). Genes required for the formation of arbuscular mycorrhizas have been found in all embryophyte lineages (Wang et al., 2010). This suggests that early land plants had the potential to form arbuscular endomycorrhizas, and that extant plants that do not form this kind of mycorrhiza have either lost or suppressed the genes involved.

Several studies suggest that various ectomycorrhizas evolved independently, at least once in the Pinaceae, and additionally in several disparate lineages of angiosperms (Fitter & Moyersoen, 1996; Hibbett & Matheny, 2009). However, the geographic origins and subsequent spread of ectomycorrhizal associations are still unclear. Since ectomycorrhizas are most widespread today in boreal and temperate forests, Alexander (2006) addressed the question of whether ectomycorrhizal associations arose in these environments, and only later moved into tropical latitudes, or whether ectomycorrhizas arose independently in the tropics. Until now, the only fossil evidence for ectomycorrhizas had been reported from the roots of Eocene Pinaceae on Vancouver Island (LePage et al., 1997), and these fossils may suggest an origin for ectomycorrhizas in the northern latitudes.

Here, we present the first fossil evidence of ectomycorrhizas from an early tropical rainforest that has Gondwanan affinities. The fossil ectomycorrhizas are enclosed in Early Eocene (52 million yr old) Indian amber that was produced by a tropical angiosperm tree of the family Dipterocarpaceae (Rust et al., 2010). The Indian amber's chemistry is quite distinct from that of most other fossil resins, and it is weakly cross-linked by comparison (Dutta et al., 2009; Mallick et al., 2009; Dutta et al., 2011). For this reason, we were able to dissolve the amber surrounding one mycorrhizal system and apply ultrastructural analyses

to the ectomycorrhiza's surface. Raman spectroscopy revealed compounds of melanins in the dark hyphae.

3.4.1.2 Materials and Methods

Amber piece no. TAD 248 was found *in situ* in the Tadkeshwar Lignite Mine of Gujarat State, western India, which outcrops Early Eocene shallow marine sediments. The amber-bearing strata have been assigned to the Ypresian (52 million yr old) based on shark teeth, foraminiferans and dinoflagellates (Rust et al., 2010).

The original 4 x 3 x 2 cm piece of amber was divided into two smaller pieces (TAD 248 a and b) in order to better access the inclusions. The amber pieces were ground and polished manually using a series of wet silicon carbide papers (grit from FEPA P 600 to 4000 (25.8–5 µm particle size), firm Struers) and examined under incident (Carl Zeiss Stemi 2000) and transmitted light microscopes (Carl Zeiss AxioScope A1) equipped with Canon 450D digital cameras. Sometimes incident and transmitted light were used simultaneously. Some images were obtained from several optical sections using the software package HeliconFocus 5.0 (Kharkov, Ukraine) for a better illustration of the three-dimensional inclusions.

For scanning electron microscopy, a *c.* 20 mm^3 block containing an ectomycorrhizal system was removed from amber piece TAD 258a using a dental drill. The tiny amber block was placed on a microscopic slide and dissolved using several drops of a mixture of toluene and 70% ethanol (10 : 1) as described by Rust et al. (2010). The remaining microfossils were washed several times with a few drops of 70% ethanol. The obtained fragments of the hyphal mantle were then placed on a carbon-covered scanning electron microscope mount using a wet hair from a superfine brush, sputtered by gold／palladium (2 X 120 s at 20 mA, 10 nm coat thickness) using an Automatic Sputter Coater (Canemco Inc., Quebec, Canada) and examined under a field emission scanning electron microscope (Carl Zeiss LEO 1530).

Raman spectra were recorded from extracted dark hyphae using a Horiba Jobin Yvon LabRam-HR 800 UV micro-Raman spectrometer. The spectrometer has a focal length of 800 mm. For excitation, the 488 nm line of an Argon Ion Laser

(IMA 106020B0S, Melles Griot, Carlsbad, CA, USA) with a laser power of 20 mW was used. The laser was dispersed by a 600 l mm^{-1} grating on a CCD detector with 1024 x 256 pixels, yielding a spectral resolution of 0.43 cm^{-1}. An Olympus BX41 microscope equipped with an Olympus LMPlanFl 100 x objective with a numerical aperture of 0.8 focused the laser light onto the sample. The confocal hole diameter was set to 100 µm. The acquisition time was varied between 10 and 300 s for a spectral range of 100–5000 cm^{-1}. By using different filters, the power of the laser was reduced to 0.1, 10 and 50% of its original power at the laser exit. For calibration of the spectrometer, a silicon standard with a major peak at 520.4 cm^{-1} was used. All spectra were recorded and processed using LabSpec™ version 5.19.17 (Jobin-Yvon, Villeneuve d'Ascq, France).

For permanent preparation, the pieces of amber were fully embedded in a high-grade epoxy (Buehler Epoxicure, Lake Bluff, IL, USA) under vacuum (see Nascimbene & Silverstein, 2001 for protocols). After curing, the resultant epoxy plugs surrounding each sample were cut and polished to create clear flat surfaces close to the amber and its inclusions. Both amber fragments are currently housed in the amber collection of the Division of Invertebrate Zoology of the American Museum of Natural History, New York. All Indian amber pieces will finally be deposited in the amber collection of the INSA Project Geology at the University of Lucknow, India.

3.4.1.3 Results

3.4.1.3.1 Description of the fossil ectomycorrhizas

Approximately 20 unramified, cruciform and monopodialpinnate ectomycorrhizas are fossilized adjacent to rootlets of up to 180 µm in diameter (Fig. 14a–e). The nonmycorrhizal parts of the absorbing roots are 300 µm to 8 mm in length and 60–130 µm in diameter. Unbranched mycorrhizas are 320 µm to 1.9 mm long and 90–140 µm in diameter (Fig. 14b). Cruciform ectomycorrhizal systems (Fig. 14c) are 200–310 µm (rarely up to 700 µm) long, and their two branches are 120–220 µm (rarely 500 µm) long and 70–100 µm in diameter. Monopodial-pinnate ectomycorrhizal systems (Fig. 14a,d,e) mostly

range between 350 and 550 µm in length, and their finger-like branches are 100–300 µm (rarely up to 530 µm) long and 60–90 µm wide. The monopodial-pinnate system in amber fragment TAD 248b (Fig. 14e) is 1.3 mm in length and bears five finger-like branches, in which both of the most basal branches are bifurcated.

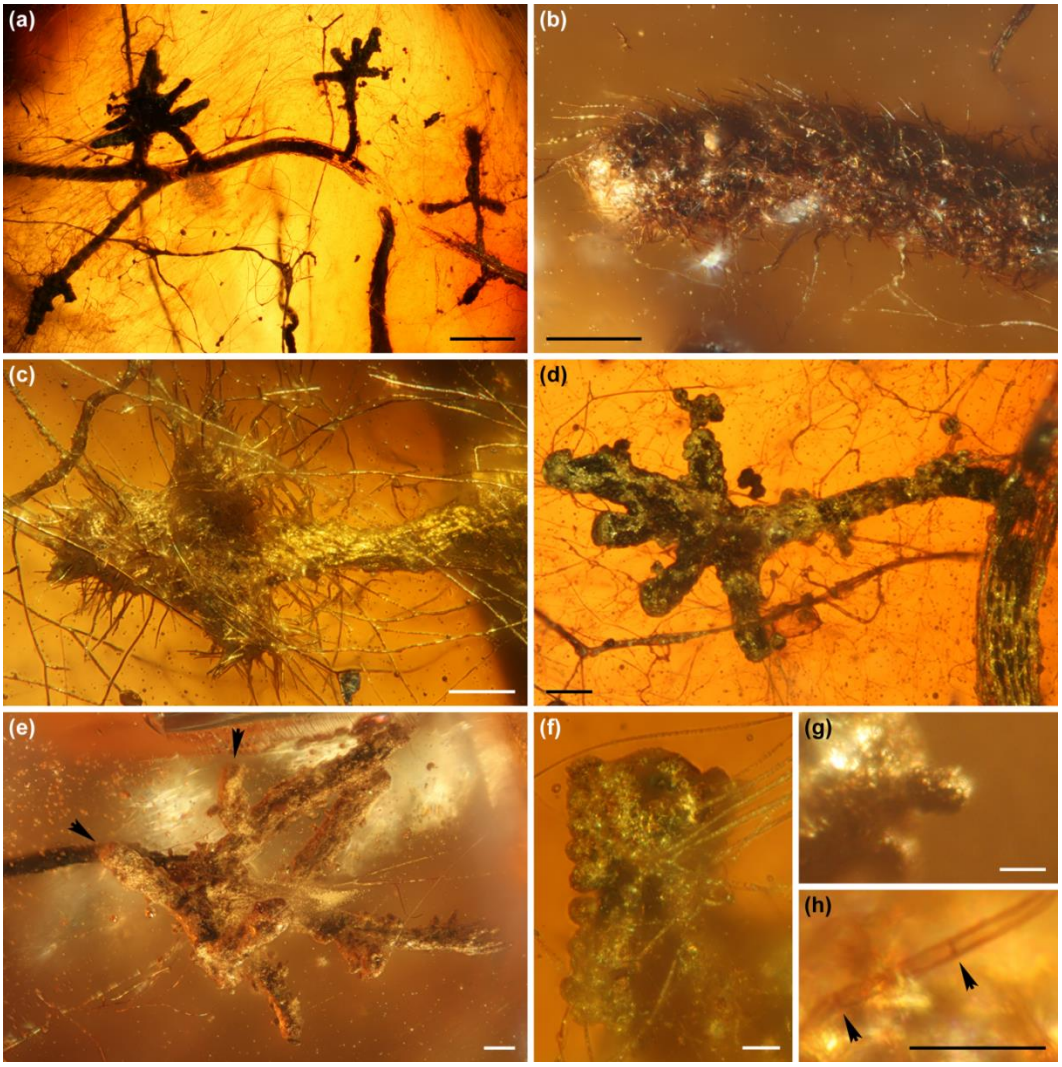

Figure 14: Light-microscopic photomicrographs of the ectomycorrhizal systems of *Eomelanomyces cenococcoides* gen. et spec. nov. from Eocene amber of India. (a) Overview of a rootlet with three monopodial-pinnate ectomycorrhizal systems and one cruciform system (located on the right) with surrounding mycelium (TAD 248a). The system in the middle right represents the holotype (shown in greater detail in Fig. 14(d)). (b) An unramified ectomycorrhiza which has been later removed from the amber for ultrastructural and Raman analyses (see Figs. 15 and 16; TAD 248a). (c) Cruciform ectomycorrhizal system (TAD 248a). (d) Monopodial-pinnate ectomycorrhizal system forming microsclerotia. This system represents the holotype of *E. cenococcoides* gen. et spec. nov. (TAD 248a). (e) Large monopodialpinnate ectomycorrhizal system with five finger-like branches forming microsclerotia. The arrowheads show additional furcation of the basal branches (TAD 248b). (f) Microsclerotia formed at the surface of the basal branch of the system shown in the lower left of Fig. 14(a) (TAD 248a). (g) Large microsclerotium exposed at the surface of the system shown in Fig. 14(e) (TAD 248b). (h) Dark hypha with two septa (arrowheads) extending from the system shown in Fig. 14(b) (TAD 248a). Bars, 500 µm (a); 100 µm (b–e); 20 µm (f–h).

Different developmental stages of the ectomycorrhizas are preserved in the piece of amber. Young ectomycorrhizas show dark pseudoparenchymatous mantles from which numerous irregularly septate dark pigmented hyphae of 1.2– 3.3 µm in diameter extend (Figs. 14b,c,h, 15a–c,). Their walls are 0.2–0.3 µm thick, and iris diaphragms are possessed at the septa (Fig. 15g) whereas clamp connections are absent. Compounds of melanins were detectable in these dark hyphae using Raman spectroscopy. Some of the peaks were assignable to the key monomers of eumelanin: hydroquinone, indolequinone and semiquinone (Fig. 16). Some of these hyphae form chlamydospore-like inflated distal hyphal ends which are clavate or broad fusiform to lemon-shaped and 12–16 µm long and 6.5–9.7 µm wide (Fig. 15c,d). Short forked flat hyphae 7–15 µm long, 2.4–5 µm wide and *c.* 0.5 µm thick (Fig. 2e), as well as short young hyphae 2.5–3 µm in diameter, are sometimes visible at the surface of the pseudoparenchymatous mantle. Dense hyphal systems extend in all directions into the clear translucent amber (Fig. 14a,c), suggesting that some ectomycorrhizas were still alive when initially embedded. Sometimes several hyphae form simple rhizomorphs that are mostly *c.* 10 µm in diameter or thinner, seldom reaching 75 µm (Fig. 17a,b). Generally, hyphae exhibit thick cell walls (Fig. 15f,g) and are frequently coated by a tolueneinsoluble substance. Single hyphae within the rhizomorphs are 1–3 µm wide. The dark hyphae of the mycelium are often coated by light circular structures possessing a rough surface. Hyphae are absent around older ectomycorrhizal systems; instead, numerous spherical to ovoid microsclerotia (hardened mycelia serving as dormant stages) are formed at their surface (Fig. 14d–g). The microsclerotia are mostly 35–40 µm long and 25–30 µm wide, sometimes reaching 55–60 µm in length and 50 µm in width. Small ones are only 15–20 µm in size. Microsclerotia are also formed in the nearby hyphal systems (Fig. 17d,). Clavate short hyphal ends 15–43 µm long and 5.5–6.5 µm wide are regularly formed in the mycelium (Fig. 17c). Sometimes they appear at regular distances of *c.* 450–550 µm apart at the supporting hyphae. The otherwise thick walls of the hyphae become thinner and almost disappear in these branches (Fig. 17c).

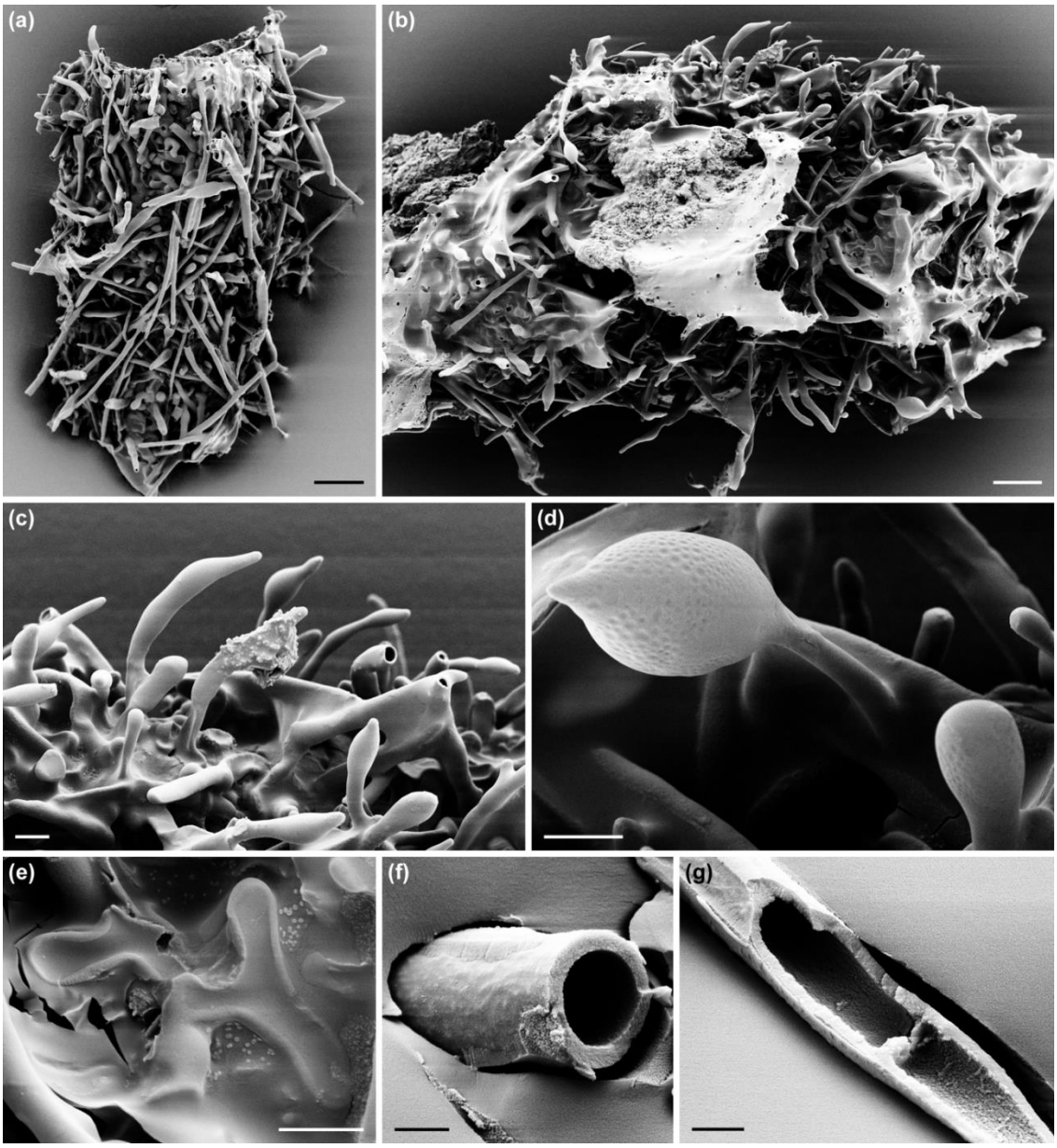

Figure 15: Scanning electron micrographs of *Eomelanomyces cenococcoides* gen. et spec. nov. from Eocene amber of India (TAD 248a). (a,b) Fragments of the pseudoparenchymatous mantle of the ectomycorrhiza shown in Fig. 14(b). (c) Surface of the pseudoparenchymatous mantle showing extending hyphae with initial formation of chlamydospore-like inflated distal hyphal ends. (d) Lemon-shaped inflated distal hyphal end of a short hypha extending from the mantle. (e) Surface of the pseudoparenchymatous mantle with short forked flat hyphae. (f) Hypha showing thick walls at cross-break. (g) Broken hypha exposing a septum with an iris diaphragm. Bars, 20 µm (a,b); 5 µm (c–e); 1 µm (f,g).

Preservation of the ectomycorrhizas is excellent, allowing description of the mycobiont as *Eomelanomyces cenococcoides* gen. et spec. nov. (see the next section, 'Taxonomic summary'). *E. cenococcoides* is a fungus containing melanin and developing ectomycorrhizas as black pseudoparenchymatous mantles on the surface of absorbing roots of the host. Hyphae with iris diaphragms at the septa extend outward from this mantle. In this regard, the

fossil is similar to the recent anamorphic genus *Cenococcum*, but distinguished by the high variability in the branching of the ectomycorrhizal systems and by the regular formation of microsclerotia.

3.4.1.3.2 Taxonomic summary

Eomelanomyces cenococcoides Beimforde, Dörfelt et A. R. Schmidt gen. et spec. nov. (Figs. 14, 15 and 17).

Descriptio: Fungus anamorphus cum substantia ‘melanin’ et ectomycorrhizam formans in plantis. Systema mycorrhizas non ramosa vel cruciformis aut monopodialiter pinnata. Rami frequenter situ in dextero angulo. Tunica mycorrhizae in superficie est pseudoparenchymatica cum cellulis planis, 60–140 µm in diametro, frequenter cum hyphis ramosis, coloratis, non regularibus septis, 1.2–3.3 µm in diametro. Ex tunica pseudoparenchymaticae hyphae eminentes cum septis. Septa cum simplicibus centralibus cavis ut in genere recentem *Cenococcum*. Nonnullae hyphae apices formantes ad similitudinem chlamydosporibus, usque ad 8 x 5 µm in diametro. Hyphae conjunctae in chordam myceliae ut in simplicibus rhizomorphis. In aetate mycorrhizae sine vividis ramosis hyphis eminentibus autem cum multis microsclerotiis ovoideis, *c.* 35–50 x 25–35 µm in diametro.

Typus: In resina fossile ex India, collectio numerous AMNH TAD 248; Systema ectomycorrhizae est spectata in Fig. 14(d) est holotypus.

Etymologia: Eo, eos: Eocaen; melanos: nigrum. Epitheton speciei propter similitudinem cum recenti genere anamorpho *Cenococcum*.

3.4.1.4 Discussion

3.4.1.4.1 Assignment of the mycobiont

Although the fungal mantle is excellently preserved, the root tissue of the host plant decayed in the amber (likely as a result of taphonomic conditions affecting the preservation of woody tissues). Consequently, we could not document the

Hartig net in which the mycobiont penetrates the intercellular spaces of the host.

We assign the ectomycorrhizas of amber piece no. TAD 248 to a single fossil species because all (including different developmental stages) are arranged close to each other on the rootlets. Some photomicrographs of Fig. 14 and S1 may suggest variation in color of the ectomycorrhizas and adjacent hyphae because different intensities of transmitted and incident light were used. Lighter color is also caused by a refractive nanometer-sized space that sometimes appears between the amber inclusion and the surrounding resin. This gas-filled space probably originated by shrinkage of solidifying resin and desiccation of the inclusion during fossilization.

We consider *E. cenococcoides* to belong to the Dothidiomycetes (Ascomycota) because of its dark melanized hyphae, the formation of a mycorrhizal mantle, the regular formation of microsclerotia, and the similarity of this fossil to the extant anamorphic genus *Cenococcum*.

The septal porus is an iris diaphragm, which is not swollen like the dolipore of the Agaricomycotina (see Fig. 15g). Furthermore, clamp connections are absent. The dark color of the pseudoparenchymatous mantle's surface and of the hyphae is similar to the extant anamorphic genus *Cenococcum*, whose teleomorph is a species of the Dothideomycetes. The only extant species of this genus, *Cenococcum geophilum* Fr., forms mostly unbranched mycorrhizas with modern hosts of the Spermatophyta.

A particular feature of the mycelium surrounding the ectomycorrhizal systems is the regular occurrence of clavate short hyphal ends with very thin walls (Fig. 17c). It remains unclear if these structures were for nutrient uptake.

3.4.1.4.2 Search for fossil melanin in *E. cenococcoides*

Raman studies of melanin from modern samples are reported by several research groups for different melanin-containing substances (Samokhvalov et al., 2004), as well as density-functional calculations of the three melanin monomers (Powell et al., 2004).

The Raman spectrum of the dark hyphae of *E. cenococcoides* revealed two very broad bands which are centered at 1354 and 1576 cm^{-1} (Fig. 16). This

spectrum has a great similarity to the typical spectrum of amorphous carbon, with peaks at 1350 and 1550 cm^{-1} (Robertson, 1986). These two peaks are caused by vibrations of carbon atoms arranged in a graphitic-like structure. However, owing to the molecular structure of melanin, other vibrational modes involving oxygen, hydrogen and nitrogen should be visible. When analyzing the spectrum with a Gauss Lorentz function, several underlying peaks could be identified between 1000 and 1600 cm^{-1}. Based on the work of Powell et al. (2004), we were able to assign several of these peaks to hydroquinone, indolequinone and semiquinone, the key monomers of eumelanin. In the calculated spectrum of Powell et al. (2004) the peaks are very narrow, whereas our spectra, as well as those of Capozzi et al. (2005), show broad bands. This may be caused by the high fluorescence background, and by the degradation of the melanin molecules as a result of the Eocene age of our sample. Although eumelanins are not identical to fungal melanins (Butler & Day, 1998), the vibrational modes detectable with Raman spectroscopy likely do not show essential differences (see Cappitelli et al., 2005).

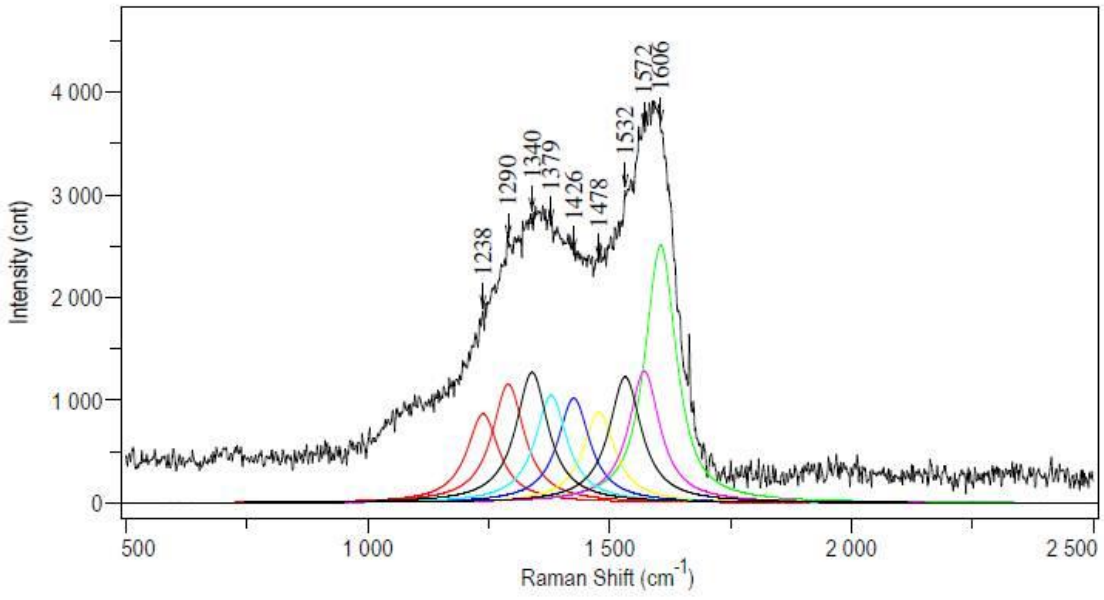

Figure 16: Raman spectrum of a single hypha of the ectomycorrhiza shown in Fig. 14(b). The colored pattern underneath the spectrum represents the peaks analyzed by Gauss–Lorentz function. The peak at 1426 cm^{-1} can be assigned to hydroquinone, those at 1340, 1532 and 1572 cm^{-1} to indolequinone, and the one at 1290 cm^{-1} to semiquinone. The main peak at 1606 cm^{-1} represents carbon bonding.

Previous studies exclusively report fossil melanins or melanosomes from animals, for example, melanin from Triassic ammonites (Mathur, 1996), and fossil melanosomes from Jurassic to Eocene feathers (Vinther et al., 2008; Li et al., 2010). Thus, our Raman spectrum provides the first indication of fossil fungal melanins in amber, and in fact the first record of melanin in a fossil fungus.

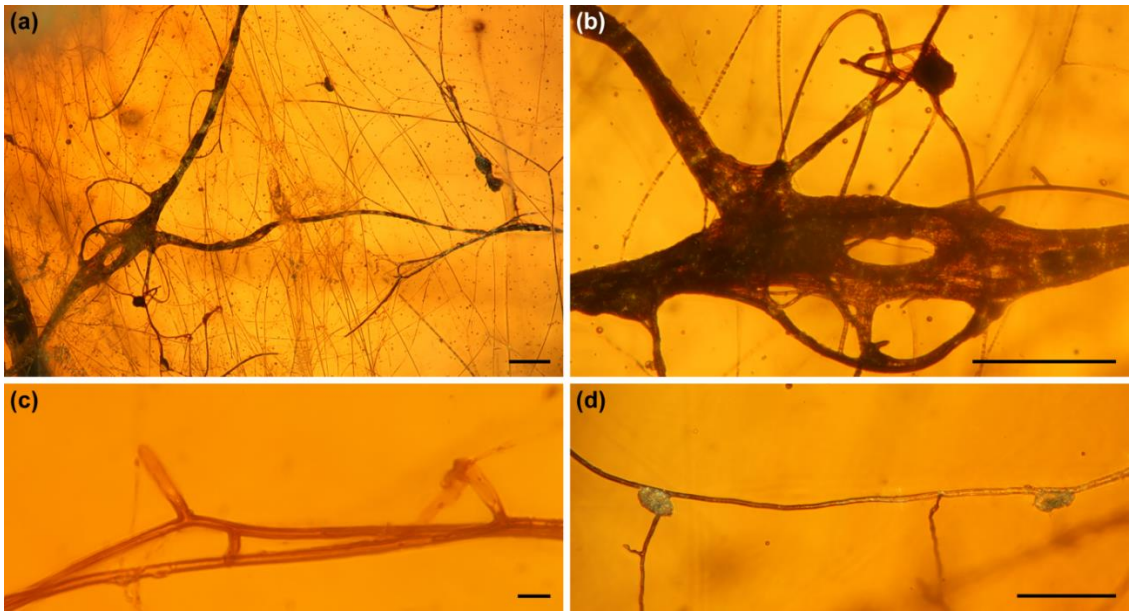

Figure 17: Light-microscopic photomicrographs of the mycelium of *Eomelanomyces cenococcoides* gen. et spec. nov. surrounding rootlets and ectomycorrhizal systems from Eocene amber of India (TAD 248a). (a) Branched rhizomorphs. (b) Detail of Fig. 17(a). Numerous hyphae composing the rhizomorph are visible. (c) Two hyphae each forming a clavate short hyphal end. The walls of the hyphae thin and almost disappear in these branches. (d) Two microsclerotia formed at a branched hypha. Bars, 100 µm (a, b, d); 10 µm (c).

3.4.1.4.3 Probable assignment of the host tree

The ectomycorrhizas reported here were fossilized in a single piece of clear translucent amber. The only syninclusions of the fossil ectomycorrhizas are several lepidopteran scales. We assume that the resin originally filled a small hole inside the litter or soil horizon of the forest floor that contained vital ectomycorrhizas. The resin may have been released by the roots or dropped from above by one of the trees.

Today, arbuscular endomycorrhizas typically predominate in tropical forests (Janos, 1983; McGuire, 2007). However, several ecologically important tropical plant families, notably the amber-producing Dipterocarpaceae, are

ectomycorrhizal (Lee, 1998). If present, ectomycorrhizal angiosperm trees generally make up a large portion of the total forest area, and can sometimes even dominate tropical rainforests (Connell & Lowman, 1989; McGuire, 2007), as dipterocarps do today in parts of Southeast Asia. The chemical analysis of the amber from the Tadkeshwar Mine revealed a class II or dammar-type resin (Dutta et al., 2009; Mallick et al., 2009; Rust et al., 2010; Dutta et al., 2011), a cadinene-based polymer, which is produced primarily by trees in the Dipterocarpaceae (Van Aarssen et al., 1994; Anderson & Muntean, 2000). Independent evidence for the presence of Lower Eocene Dipterocarpaceae was recently obtained from fossil pollen grains that were found in the same sediments (Dutta et al., 2011). In addition, fossil wood samples attached to amber pieces showed microanatomical affinity to Dipterocarpaceae, including amber-filled resin canals, further substantiating the botanical source of this amber (Nascimbene et al., 2010; Rust et al., 2010).

The Gujarat region of India during the Lower Eocene was characterized by a strong occurrence of evergreen angiosperms (Sahni & Kumar, 1974; Willis & McElwain, 2001). Gymnosperms occurred rarely, and only a few fossils from the families Araucariaceae, Podocarpaceae and Ginkgoaceae have ever been recovered (Salujha et al., 1967) – their extant representatives are all characterized by arbuscular mycorrhizas, like most other gymnosperms. Based on direct fossil evidence, the Cambay amber and associated sediments provide one of the earliest unequivocal Asian records of a diverse, broadleaf tropical angiosperm forest (Rust et al., 2010).

We consider the host of *E. cenococcoides* to be an angiosperm, because representatives of the family Pinaceae and the genus *Gnetum*, the only known extant gymnosperms forming ectomycorrhizas (Brundrett, 2002), have not been observed in the Eocene of India. Furthermore, besides dipterocarps, no other angiosperms with known ectomycorrhizal associations, past or present, have been identified from this deposit. We therefore propose that the amber-producing Dipterocarp is the probable host of *E. cenococcoides*.

3.4.1.4.4 Palaeobiogeographical implications

The palaeogeographic and temporal origin of Dipterocarpaceae and their association with ectomycorrhizal fungi have frequently been discussed. It is typically suggested that dipterocarps originated in eastern Africa or Madagascar and drifted northward on the Indian platform, reached Asia during the Eocene and spread (Dutta et al., 2011). Alternatively, an origin in Southeast Asia has been proposed and taken into account (Lakhanpal, 1970; Sasaki, 2006). However, the monophyly of the three subfamilies of Dipterocarpaceae and of the Sarcolaenaceae, along with their consistent association with ectomycorrhizal fungi, suggest that the potential to form ectomycorrhizas is an ancestral character of the Dipterocarpaceae family (Ducousso et al., 2004; Moyersoen, 2006). Ectomycorrhizal symbioses may have conferred a selective advantage for some tropical tree species (McGuire, 2007), even in early tropical broadleaf rainforests, and the high diversity and abundance of Dipterocarpaceae in Asia might be based on their potential to associate with ectomycorrhizal fungi.

Ectomycorrhizal associations are considered to be unstable evolutionarily dynamic associations that evolved independently in several major clades of fungi (Hibbett & Matheny, 2009) as well as several times within the angiosperm clade that includes Rosids and Asterids and within the Pinaceae (Fitter & Moyersoen, 1996; Hibbett & Matheny, 2009). Consequently, *E. cenococcoides* itself is not necessarily an ancestral mycobiont of its host. The only previously reported fossil record of ectomycorrhizas is actually from the roots of Eocene (*c.* 50 million yr old) Pinaceae from Vancouver Island (LePage et al., 1997). Our find provides evidence that angiospermous ectomycorrhizal associations in the Paleogene tropics occurred contemporaneously with gymnospermous ectomycorrhizal associations in the Nearctic.

Acknowledgements

The authors would like to thank David A. Grimaldi (New York), Matthias Gube (Jena), Heike Heklau (Halle), Jouko Rikkinen (Helsinki), Kerstin Schmidt (Jena) and Gerhard Wagenitz (Göttingen) for their helpful comments; Jes Rust (Bonn) for advice; and

Wolfgang Dröse (Göttingen) and Dorothea Hause-Reitner (Göttingen) for assistance with histology and the field emission microscope. We are grateful to the anonymous reviewers for their constructive suggestions. H.S. and R.S.R. thank Ashok Sahni (Lucknow) for his unfailing encouragement and kind advice. H.S. would like to recognize Naresh Chandra Mehrotra, the director of the Birbal Sahni Institute of Palaeobotany (Lucknow), for his support of laboratory and field work. R.S.R. thanks the Department of Science and Technology, Government of India. This is publication number 65 from the Courant Research Centre Geobiology, funded by the German Initiative of Excellence.

References

Alexander, I.J. (2006) Ectomycorrhizas – out of Africa? *New Phytologist* 172: 589-591.

Anderson, K.B. and Muntean, J.V. (2000) The nature and fate of natural resins in the geosphere. Part X. Structural characteristics of the macromolecular constituents of modern Dammar resin and Class II ambers. *Geochemical Transactions* 7.

Brundrett, M. (2009) Mycorrhizal associations and other means of nutrition of vascular plants: understanding the global diversity of host plants by resolving conflicting information and developing reliable means of diagnosis. *Plant and Soil* 320: 37-77.

Brundrett, M.C. (2002) Coevolution of roots and mycorrhizas of land plants. *New Phytologist* 154: 275-304.

Butler, M.J. and Day, A.W. (1998) Fungal melanins: a review. *Canadian Journal of Microbiology* 44: 1115-1136.

Cairney, J.W.G. (2000) Evolution of mycorrhiza systems. *Naturwissenschaften* 87: 467-475.

Capozzi, V., Perna, G., Gallone, A., Biagi, P.F., Carmone, P., Fratello, A., Guida, G., Zanna, P. and Cicero, R. (2005) Raman and optical spectroscopy of eumelanin films. *Journal of Molecular Structure* 744–747: 717-721.

Cappitelli, F., Vicin, i.S., Piaggio, P., Abbruscato, P., Princi, E., Casadevall, A., Nosanchuk, J.D. and Zanardini, E. (2005) Investigations of fungal deterioration of synthetic paint binders using vibrational spectroscopic techniques. *Macromolecular Bioscience* 5: 49-57.

Connell, J.H. and Lowman, M.D. (1989) Low-diversity tropical rain forests: some possible mechanisms for their existence. *American Naturalist* 134: 88-119.

Ducousso, M., Béna, G., Bourgeois, C., Buyck, B., Eyssartier, G., Vincelette, M., Rabevohitra, R., Randrihasipara, L., Dreyfus, B. and Prin, Y. (2004) The last common ancestor of Sarcolaenaceae and Asian dipterocarp trees was ectomycorrhizal before the India–Madagascar separation, about 88 million years ago. *Molecular Ecology* 13: 231-236.

Dutta, S., Mallick, M., Bertram, N., Greenwood, P.F. and Mathews, R.P. (2009) Terpenoid composition and class of Tertiary resins from India. *International Journal of Coal Geology* 80: 44-50.

Dutta, S., Tripathi, S.M., Mallick, M., Mathews, R.P., Greenwood, P.F., Rao, M.R. and Summons, R.E. (2011) Eocene out-of-India dispersal of Asian dipterocarps. *Review of Palaeobotany and Palynology* 166: 63-68.

Fitter, A.H. and Moyersoen, B. (1996) Evolutionary Trends in Root-Microbe Symbioses. *Philosophical Transactions of the Royal Society of London. Series B: Biological Sciences* 351: 1367-1375.

Hibbett, D. and Matheny, P.B. (2009) The relative ages of ectomycorrhizal mushrooms and their plant hosts estimated using Bayesian relaxed molecular clock analyses. *BMC Biology* 7: 13.

Janos, D.P. (1983) Tropical mycorrhizas, nutrient cycles and plant growth. In: *Tropical rain forest: ecology and management*, edited by S.L. Sutton, T.C. Whitmore and A.C. Chadwick, Blackwell Scientific Publications, Oxford, UK, pp. 327-345.

Lakhanpal, R.N. (1970) Tertiary floras of India and their bearing on the historical geology of the region. *Taxon* 19: 675-694.

Lee, S.S. (1998) Root symbiosis and nutrition. In: *A review of dipterocarps taxonomy, ecology and silviculture*, edited by A. S. and T. J.M., Center for International Forestry Research, Bogor, Indonesia, pp. 99-114.

LePage, B., Currah, R., Stockey, R. and Rothwell, G. (1997) Fossil ectomycorrhizae from the Middle Eocene. *American Journal of Botany* 84: 410.

Li, Q., Gao, K.-Q., Vinther, J., Shawkey, M.D., Clarke, J.A., D'Alba, L., Meng, Q., Briggs, D.E.G. and Prum, R.O. (2010) Plumage Color Patterns of an Extinct Dinosaur. *Science* 327: 1369-1372.

Mallick, M., Dutta, S., Greenwood, P. and Bertram, N. (2009) Pyrolytic and spectroscopic studies of Eocene resin from Vastan lignite Mine, Cambay basin, Western India. *Journal of the Geological Society of India* 74: 16-22.

Malloch, D.W., Pirozynski, K.A. and Raven, P.H. (1980) Ecological and evolutionary significance of mycorrhizal symbioses in vascular plants (A Review). *Proceedings of the National Academy of Sciences* 77: 2113-2118.

Mathur, A. (1996) Über Ammoniten der Kössener Schichten und den Nachweis der Tintenbeutel-Substanz Melanin bei ihnen. *Documenta Naturae* 102: 1-161.

McGuire, K.L. (2007) Common Ectomycorrhizal Networks May Maintain Monodominance In A Tropical Rain Forest. *Ecology* 88: 567-574.

Moyersoen, B. (2006) Pakaraimaea dipterocarpacea is ectomycorrhizal, indicating an ancient Gondwanaland origin for the ectomycorrhizal habit in Dipterocarpaceae. *New Phytologist* 172: 753-762.

Nascimbene, P. and Silverstein, H. (2001) The preparation of fragile Cretaceous ambers for conservation and study of organismal inclusions. In: *Studies on fossils in amber, with particular reference to the Cretaceous of New Jersey*, edited by D. Grimaldi, Backhuys Publishers, Leiden, The Netherlands, pp. 93-102.

Nascimbene, P.C., Grimaldi, D.A., Anderson, K.B., Schmidt, A.R., Rust, J. and Williams, C.J. (2010) Physicochemical comparisons and implications of new amber deposits from the Lower Eocene of India and the mid

Cretaceous of Ethiopia. *FossilsX3: Insects, Arthropods, Amber*, Capital Normal University, Beijing, China.

Powell, B.J., Baruah, T., Bernstein, N., Brake, K., McKenzie, R.H., Meredith, P. and Pederson, M.R. (2004) A First Principles Density-Functional Calculation of the Electronic and Vibrational Structure of the Key Melanin Monomers. *Journal of Chemical Physics* 120: 8608-8615.

Remy, W., Taylor, T.N., Hass, H. and Kerp, H. (1994) Four hundred-million-year-old vesicular arbuscular mycorrhizae. *Proceedings of the National Academy of Sciences* 91: 11841-11843.

Robertson, J. (1986) Amorphous carbon. *Advances in Physics* 35: 317-374.

Rust, J., Singh, H., Rana, R.S., McCann, T., Singh, L., Anderson, K., Sarkar, N., Nascimbene, P.C., Stebner, F., Thomas, J.C., Solórzano Kraemer, M., Williams, C.J., Engel, M.S., Sahni, A. and Grimaldi, D. (2010) Biogeographic and evolutionary implications of a diverse paleobiota in amber from the early Eocene of India. *Proceedings of the National Academy of Sciences* 107: 18360-18365.

Sahni, A. and Kumar, V. (1974) Palaeogene palaeobiogeography of the Indian subcontinent. *Palaeogeography, Palaeoclimatology, Palaeoecology* 15: 209-226.

Salujha, S., Srivastava, N. and Rawat, M. (1967) Microfloral assemblage from Subathu sediments of Simla Hills. *Journal of the Palaeontological Society of India* 12: 25-40.

Samokhvalov, A., Liu, Y. and Simon, J.D. (2004) Characterization of the Fe(III)-binding Site in Sepia Eumelanin by Resonance Raman Confocal Microspectroscopy. *Photochemistry and Photobiology* 80: 84-88.

Sasaki, S. (2006) Ecology and Physiology of Dipterocarpaceae. In: *Plantation technology in tropical forest science*, edited by K. Suzuki, K. Ishii, S. Sakurai and S. Sasaki, Springer, Tokyo, Japan, pp. 3-22.

Van Aarssen, B.G.K., de Leeuw, J.W., Collinson, M., Boon, J.J. and Goth, K. (1994) Occurrence of polycadinene in fossil and recent resins. *Geochimica et Cosmochimica Acta* 58: 223-229.

Vinther, J., Briggs, D.E.G., Prum, R.O. and Saranathan, V. (2008) The colour of fossil feathers. *Biology Letters* 4: 522-525.

Wang, B., Yeun, L.H., Xue, J.-Y., Liu, Y., Ané, J.-M. and Qiu, Y.-L. (2010) Presence of three mycorrhizal genes in the common ancestor of land plants suggests a key role of mycorrhizas in the colonization of land by plants. *New Phytologist* 186: 514-525.

Willis, K.J. and McElwain, J.C. (2001) *Evolution of plants*. Oxford University Press, Oxford, UK.

Chapter 4: Conditioning films in rock fractures of the Äspö Hard Rock Laboratory (HRL), Sweden

4.1 Introduction to the Äspö HRL

The Äspö Hard Rock Laboratory (HRL) is a ca. 450 m deep tunnel (~400 km South of Stockholm, Sweden) drilled underneath the island of Äspö by the Swedish Nuclear Fuel and Waste Management Company (SKB) as a study site for the disposal of nuclear waste. The igneous rocks in that area belong to the 1.6 - 3.1 Ga old Fennoscandian shield and can be classified as post-orogenic granites to quartz-monzodiorites (Pedersen, 1997; Wahlgren et al., 2006). Due to at least four different orogenies the rocks are heavily fractured (Tullborg et al., 2008). A distinctive aquifer system allows several microorganisms to form biofilms on the tunnel walls and on fracture surfaces (e.g. Pedersen, 1997; Jägevall et al., 2011). Especially Pedersen & Ekendahl (1990) could show that numerous autotrophic microorganisms in the tunnel environment use hydrogen as energy source. Additionally, iron and sulfate reducing bacteria are very common and active in the groundwater (e.g. Laaksoharju et al., 1995; Pedersen & Karlsson, 1995) as well as autotrophic methanogens, acetoclastic methanogens and acetogenic bacteria (Pedersen, 1997). Therefore, the Äspö tunnel can be considered as a window into the deep biosphere and the formation of biofilms in fracture systems can serve as a model for the development of life on the early earth and on other planets.

4.2

Organic compounds and conditioning films within deep rock fractures of the Äspö Hard Rock Laboratory, Sweden

Manuscript

Nadine Schäfer[1], Burkhard C. Schmidt[2], Andreas Reimer[1], Nadia-Valérie Quéric[1], Birgit Röring[1], *Joachim Reitner[1]

[1]Geoscience Centre, University of Goettingen, Geobiology, Goldschmidtstraße 3, 37077 Goettingen, Germany

[2]Geoscience Centre, University of Goettingen, Experimental and Applied Mineralogy, Goldschmidtstraße 1, 37077 Goettingen, Germany

Abstract

The Palaeoproterozoic grano-dioritic rocks of the island of Äspö exhibit numerous mineralized fractures which consist mainly of quartz, calcite, fluorite and/or epidote. Epifluorescence microscopy revealed a concentration of organic matter associated with fine Manganese-rich calcite fractures. Various analyses applied to the organic matter resulted in numerous different signatures of organic molecules. These molecules could be classified mainly as carbohydrates, saccharides and amino acids. It is supposed that most of the preserved organic matter is related with thin conditioning films. Extracted bacterial and fungal DNA from the granite and a second diorite clearly show still active microbial activity in fracture micro-niches.

4.2.1 Introduction

The Äspö Hard Rock Laboratory (HRL) is a tunnel in southeast Sweden excavated as a study site of the Swedish nuclear waste disposal program (SKB Svensk Kärnbränslehantering AB). The tunnel is located underneath the island of Äspö (Fig. 18) which is part of the Precambrian bedrock belonging to the 1.6

– 3.1 Ga old Fennoscandian Shield (Pedersen 1997). The dominating rocks are 1.8 Ga old post-orogenic granites to quartz-monzodiorites (Wahlgren et al. 2006). At the tunnel location prevailing rocks belong to the so-called Äspö diorite and Småland granite (Fig. 18). The Småland granite is strongly foliated and heterogeneous. Due to a complicate shear structure highly fractured zones are alternating with normal fractured rocks. In general, the fractures have a vertical to subvertical orientation (Smellie & Laaksoharju 1992). Formation and reactivation of the fractures, as well as related mineral precipitation are connected to at least four different orogenies between 1.75 Ga and 0.4 Ga (Tullborg et al. 2008). The fracture mineralization consists of six different parageneses, characterized by varying formation temperatures ranging from early hydrothermal conditions to low temperature conditions of recent times (Drake et al. 2009). After an initial oxic period, the fracture zones remained anoxic, which was supposed to be controlled by microbial activity (e.g., Pedersen 1997; Hama et al. 2001). The microbial processes occurring in the fractures included anaerobic respiration coupled to reduction of ferric iron oxides and methanogenesis inducing the precipitation of calcite and secondary iron minerals (Hama et al. 2001). A further common secondary fracture filling is epidote, which is concentrated in discrete zones and occasionally accompanied by hematite (Hama et al. 2001).

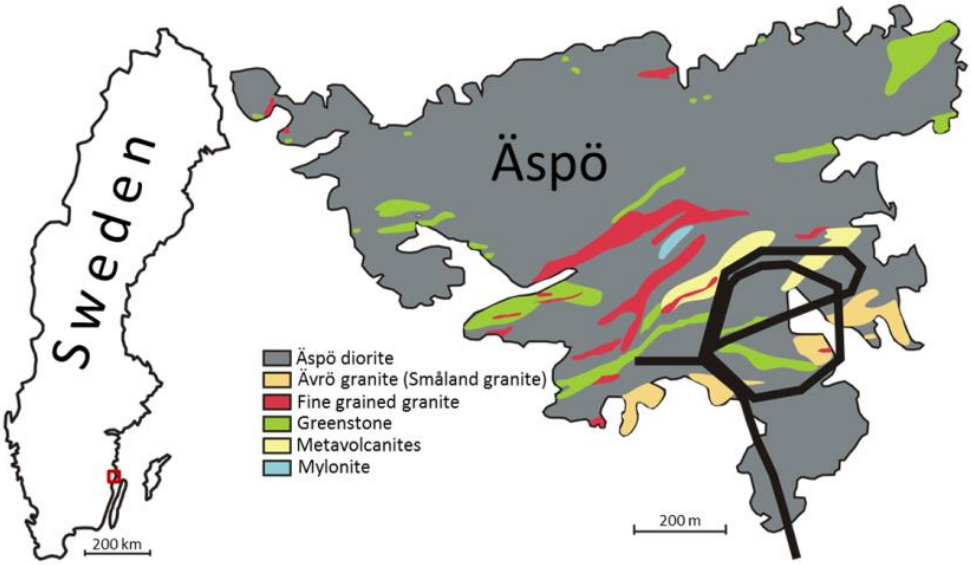

Figure 18: On the left side simplified map of Sweden with the marked location of the island of Äspö (red square). On the right side a simplified geological map of Äspö with the location of the Äspö Hard Rock Laboratory (HRL; black scetch indicating the tunnel shape), modified after Morad et al. (2011).

The presence of microorganisms in the deep biosphere, including igneous rocks (cf. Amend & Teske 2005 and citations therein), is usually suggested to depend on associated aquifer systems (Pedersen & Ekendahl 1990; Ekendahl et al. 1994; Pedersen 1997; Kotelnikova et al. 1998). The contact of the solid rock surfaces with aqueous solutions leads to the formation of conditioning films, needed for balancing negative charges enabling the attachment of microorganisms to the surface (Bhosle & Wagh 1997; Bhosle 2004). During the development of a conditioning film a number of organic compounds, like glycoproteins (Baier 1980), proteins (Compere et al. 2001), lipids, humic acids, nucleic acids, polysaccharides and aromatic amino acids (Taylor et al. 1997) are reported (Bhosle 2004).

Here we present results obtained in fracture fillings of both main rock types of the island of Äspö with Raman spectroscopy, HPLC and HPAE-PAD, demonstrating the presence of a variety of organic compounds, including aromatic amino acids and saccharides. Furthermore, preliminary DNA analyzes emphasize an active inhabitation of bacteria and fungi in the fractures. As the organic content of the fractures is rather low and in most cases unspecific we suggest that the organic material represents the rests of a conditioning film, which arose due to seepage of the overlying sea water.

4.2.2 Materials and Methods

A granitic and a dioritic sample were taken from two different drill cores (KF 0066A01, 10.4 m and KJ 0052F01, 11.6 m) obtained at a depth of 450 m in the Äspö Hard Rock Laboratory (Fig. 19 A1 and B1). For most analyzes crushed core material was used. For Raman analyzes a 4 mm thick section of the granite core was cut. During preparation greatest importance was attached to contamination-free sectioning. Therefore, the saw and saw blade were cleaned with pre-distilled acetone and sterilized de-ionized water.

Organic and carbonate carbon contents of the samples were analyzed with a multiphase carbon determinator (Leco RC 412, St. Joseph, MI, USA), that separates both phases using a heating gradient. To validate the results, about 250 mg of the crushed granite core and diorite core, respectively, were analyzed 5 times and a mean value was calculated. To confirm the very low

amounts total carbon and organic carbon after acidification were also measured with a CNS elemental analyzer (Euro Vector Instruments, Hekatech). This method was also applied in order to determine the concentrations of nitrogen and sulfur.

For the analyzes of enantiomers of chiral amino acids with high pressure liquid chromatography (HPLC) about 1.5 g of the crushed granite and diorite as well as 2 ml of water collected from open fractures in the Äspö tunnel were spiked with 2 ml 6 N HCl and hydrolyzed for 24 hours at 110°C. After hydrolysis the supernatants were collected and the HCl was evaporated in a Speed Vac. Samples were washed twice with HPLC-H_2O, concentrated, and for derivatization reconstituted in HPLC-H_2O. Then sodium borate buffer (0.5 M; pH 7.7) and norvaline (2.5 µM/ml) as an internal standard were added. Derivatization was performed with (+)-1-(9-fluorenyl)-ethylchloroformate (FLEC) followed by 1-Aminoadamantans (ADAM) and after waiting for 45 s eluent (Na-acetate; pH 4.2) was added. After 5 min reaction time 10 µl of the samples were injected on the column (GROM-SIL FLEC-1, 250 x 4.0 mm, flow rate 0.6 ml/min).

Sugars were analyzed using high-performance anion-exchange chromatography with pulsed amperometric detection (HPAE-PAD). 1 mg of crushed core material from both rock types as well as 2 ml free water were spiked with 2 ml 2N trifluoroacetic acid (TFA) and hydrolyzed for 4 hours at 110°C. Hydrolysis was terminated by evaporating the TFA in the Speed Vac. Afterwards samples were washed 3 times with HPLC-H_2O and entered in NaOH adjusting the pH between 5 and 8. Subsequently the samples were injected on the column (Carbo Pac PA10, Dionex).

Raman spectra were recorded using a confocal Horiba Jobin-Yvon LabRam-HR 800 UV Raman spectrometer with attached Olympus BX41 microscope. The excitation wavelength was the 488 nm line of an Argon ion laser (Melles Griot IMA 106020B0S) with a laser power of 25 mW at the laser exit (ca. 3-4 mW at the sample). The focal length of the spectrometer of 800 mm and the use of a 600 l mm^{-1} grating and a CCD detector with 1024 x 256 pixels yielded a spectral dispersion of ≤ 2 cm^{-1} per pixel. Using an Olympus MPlane 100x objective with a numerical aperture of 0.9 and closing the confocal hole to 100 µm resulted in a lateral resolution of ca. 1 µm and a depth resolution of ca. 5 µm. The

acquisition time varied between 15 and 60 s for a spectral range of 100 – 5600 cm^{-1}. For calibration of the spectrometer a silicon standard with a major band at 520.4 cm^{-1} was used. All spectra were recorded and processed using LabSpec™ version 5.19.17 (Horiba Jobin-Yvon, Villeneuve d'Ascq, France). The minerals were identified on the basis of the Horiba Jobin-Yvon database for minerals and reference spectra collected on mineral specimens of the Geoscience Museum of the Georg-August University Goettingen. Identification of organic components was based on the spectral databases distributed by S.T. Japan Europe GmbH.

Cathodoluminescence microscopy (CL) and reflected-light microscopy was performed on the counterpart of the section used for Raman microscopy. The section was glued with epoxy on a glass slide and polished to a petrographic thin section. The instrument is composed of a Citl CCL 8200 Mk3A cathode, combined with a Zeiss Axiolab microscope. This cold-cathode generates a voltage of about 20 kV and was operated with an acceleration voltage of 12-15 kV and an electric current of 250-300 µA. Images were created with a cooled SPOT-CCD camera.

Thin sections used for CL were sputtered with Platinum (Pt) and investigated by FE-SEM using a LEO 1530 Gemini instrument at 4 kV. Energy dispersive X-ray spectrometry (EDX) (Oxford INCAx-51-ADD0011, Peltier cooled Si drift crystal detector) was performed at 20 kV on the same samples. The polished sample surfaces were mapped for 8 hours using the INCA EDX detection software in order to get a high resolution element distribution.

The same sample was studied with an epifluorescence microscope ZEISS Axiophot. The best signals could be achieved with a high performance wide-band pass filter BP 395-440, LP 470 (blue violet, no. 487705).

Deoxyribonucleic acid (DNA) extraction with following polymerase chain reaction (PCR) was performed on a different part of the diorite core and on the granite. In addition to a contamination-free sectioning of the drill core (see above), core sections were first rinsed with 70% ethanol (Rotipuran, Roth) for 3 minutes, then sonicated in sterile deionized water (3 times for 15 seconds with 1 minute between each burst) in order to avoid surface contamination. Prior to DNA extraction (according to Zhou et al. 1996, with slight modifications), core sections were divided into subsamples by use of a sterilized chisel and

grounded into powder with liquid nitrogen by using mortar and pestle, separately sterilized for each section zone.

Amplification of bacterial and archaeal 16S rDNA gene fragments was performed with the bacteria-specific primer 616F (5'-GAGTTTGATCCTGGCTCAG-3') in combination with the universal primer 1525R (5'-AAGGAGGTGWTCCARCC-3'; both Lane 1991), and the archaea-specific primers 20F (5'-TTCCGGTTGATCCYGCCRG-3') and Ar958R (5'-YCCGGCGTTGAMTCCAATT-3'; both DeLong 1992). Samples were amplified by use of an initial denaturation step at 94°C (90 sec), followed by 35 cycles of denaturation at 94°C (15 sec), annealing at 55°C (1 min), and an extension at 72°C (2 min). Cycling was completed by a final extension at 72°C (5 min).

Primers NS1F (5'-GTAGTCATATGCTTGTCTC-3'; White et al. 1990) and NS22R (5'-AATTAAGCAGACAAATCACT-3'; Gargas & Taylor 1992) were used for the amplification of fungal 18S rDNA gene fragments, applying an initial denaturation at 94°C (4 min), 30 cycles of denaturation at 94°C (30 sec), annealing at 47°C for 90 sec, and an extension at 72°C (90 sec) followed by a final extension at 72°C for 10 min.

Each 25 µl PCR reaction contained 0.2 µM of forward and backward primer (all primers synthesized by Metabion International AG, Martinsried, Germany), 200 µM of each dNTP, 1× PCR buffer and 1.2 U of Taq polymerase (both Promega, Mannheim, Germany); all PCRs were carried out on an UnoII Thermocycler (Biometra, Goettingen, Germany).

4.2.3 Results

Reflected-light microscopy in combination with cathodoluminescence (CL) shows a distinct distribution of many small calcite fractures throughout the granite and the diorite (Fig. 19 A2-A3 and B2-B5). The bright orange-red color in the CL images is significant for a high concentration of manganese (Mn) in the calcite within the crystal lattice (Richter et al. 2003) which was additionally analyzed by Laser-Inductively Coupled Plasma-Mass Spectroscopy (LA-ICP-MS; data not shown). Also at the location from where the Raman spectra were obtained, such a calcite fracture is visible.

The images created with EDX on the granite sample are in concordance with the images from CL. Here, the fractures filled with calcite are identified by the calcium (Ca) and the carbon (C) map (Fig. 19 A4-A5). Unfortunately, it is not possible to distinguish between the carbon signal due to carbonate (CO_3^{2-}) in the calcite or due to free organic carbon.

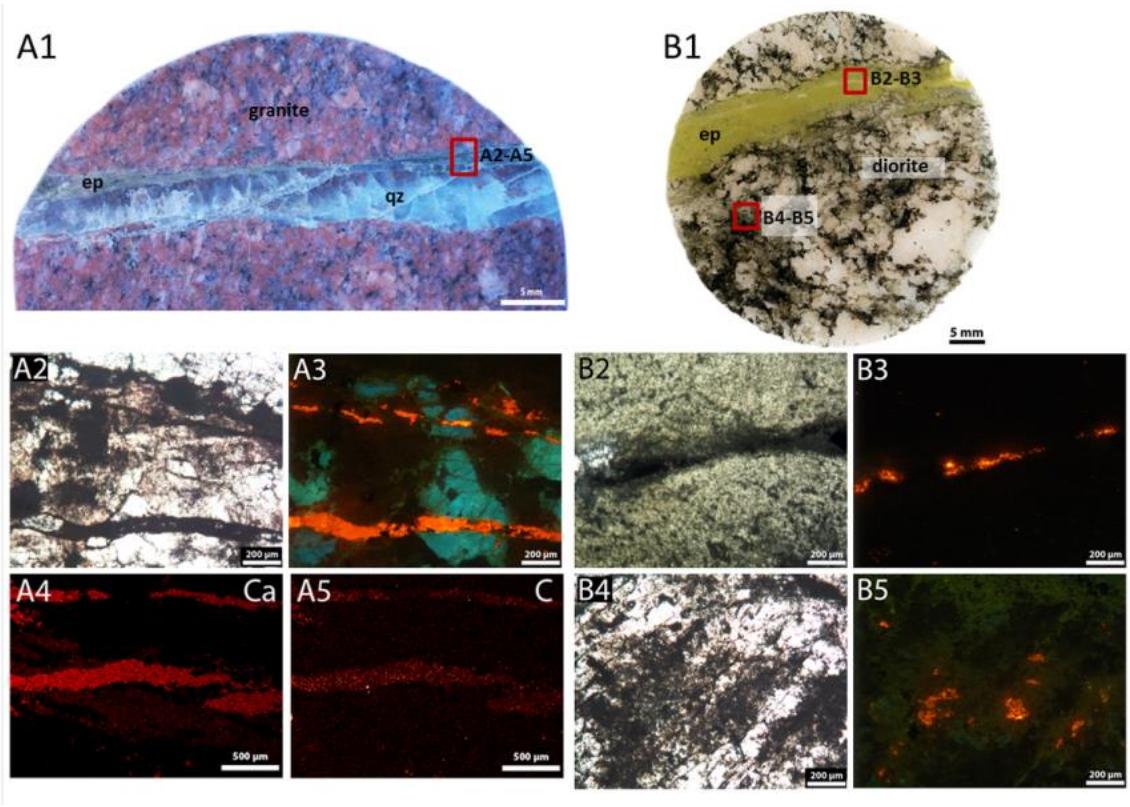

Figure 19: Reflected light image of the granite sample (A1) and the diorite sample (B1). Marked are the main fracture fillings epidote (ep) and quartz (qz). Reflected light images (A2, B2, B4) together with their CL (A3, B3, B5) counterpart help to recognize also very small Mn-rich calcite fillings. EDX mappings of Ca (A4) and (C) identify the fillings as calcite.

A more detailed impression of the calcite fractures could be achieved with epifluorescence microscopy. This technique reveals several micrometer sized areas inside the calcite fractures, which show a brownish fluorescence when excited in the blue range (Fig. 20). To some extent they occur everywhere on the fracture, but the higher concentrations can be found along the rim in direct contact to the granitic matrix (Fig. 20B). Possibly the enrichment of the brownish phase is coupled to phase boundaries and smaller cracks and fissures inside the calcite fracture.

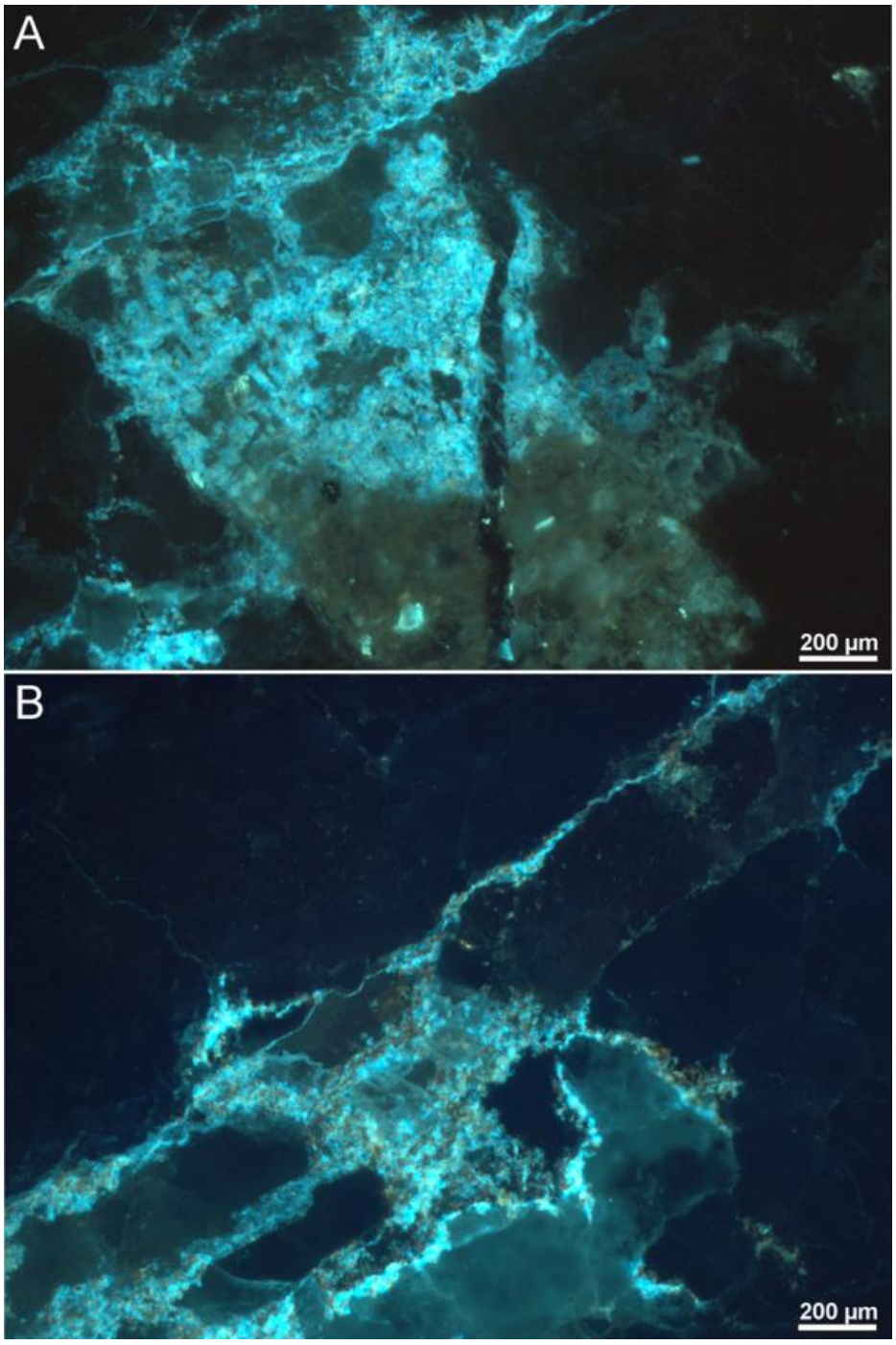

Figure 20: Epifluorescence image of a calcite fracture. In (A) a large area of the fracture is covered by organic matter (brown colored) of a putative conditioning film. (B) In smaller fractures the organic matter is concentrated along the rim in direct contact to the granitic matrix.

The geochemical analyzes revealed a total carbon (TC) content of 0.021 wt% for the granite and 0.078 wt% for the diorite. Due to five single runs of the granite and the diorite, respectively, a total organic carbon (TOC) concentration of 0.002 wt% for the granite and 0.009 wt% for the diorite could be determined. The total inorganic carbon (TIC) concentration was 0.019 wt% for the granite and 0.069 wt% for the diorite. Although the measured concentrations were low,

clear and reproducible peaks could be observed (Fig. 21). In addition, the rather low amounts of TC were confirmed by total carbon determination with the CNS method (0.021 wt% for the granite and 0.078 wt% for the diorite). This method also gave a total nitrogen (TN) concentration of 0.0002 wt% for the granite and 0.0009 wt% for the diorite.

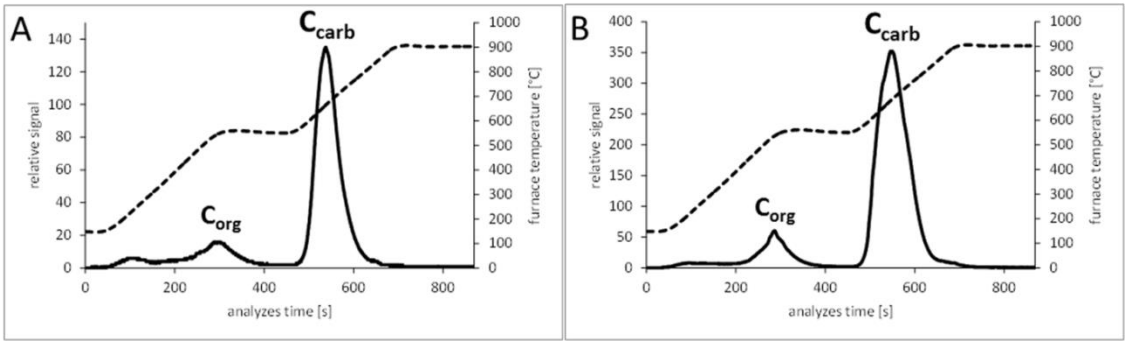

Figure 21: Example of the determination of the total organic carbon (C_{org}) and the total inorganic carbon (C_{carb}) with the multiphase carbon determinator (Leco) of the granite (A) and the diorite (B). The dotted line represents the heating curve for the seperation of C_{org} and C_{carb}.

In order to confirm the macroscopic classification of the sample as granitic, numerous feldspars were measured with Raman spectroscopy. They could be identified as mainly alkali-feldspars (microcline and orthoclase) and albite. Feldspars with a Calcium (Ca) component could not be observed. The specimen also contains quartz as well as mica. Furthermore, small pyrite crystals are embedded in the matrix and also hematite coverings occur. The secondary fracture filling consists of quartz, epidote and calcite.

At the transition zone between the granite and the fracture filled with epidote/calcite, exactly on the areas where the brownish fluorescent phase is concentrated (Fig. 20), several Raman spectra showing significant bands in the spectral range between 100 and 3100 cm^{-1} could be recorded. Some of the spectra are characterized by bands assignable to mineral phases as well as to organic molecules (cf. Fig. 22). In other spectra the signals from minerals can be excluded and only vibrations of organic molecules are detected. Two representative spectra are shown in Figs. 22A and 23. The first has the main bands in the lower spectral range between 800 and 1600 cm^{-1} and also prominent bands between 2800 and 3000 cm^{-1} (Figs. 22A and 23A). The second has the main bands in the lower spectral range between 500 and 1800 cm^{-1} and around 3000 cm^{-1} (Figs. 22A and 23B).

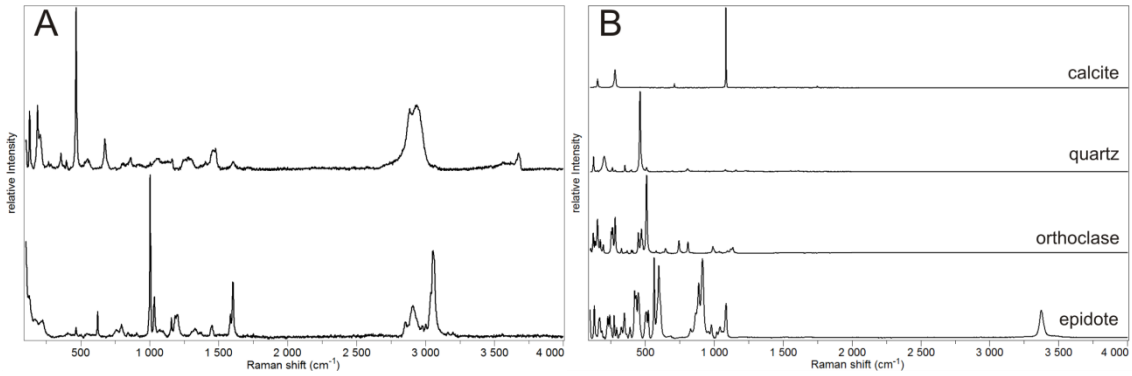

Figure 22: Comparison of Raman spectra obtained on the organic phase (A) with the most abundant minerals (B) occuring in the granite. Note that mineral vibrations are mostly concentrated in the lower wavenumber region.

HPLC analyzes revealed two different amino acids in both rock types and in the water samples (Fig. 25). In the granite 0.102 pmol mg^{-1} D-proline, 0.095 pmol mg^{-1} D-phenylalanine and 0.084 pmol mg^{-1} L-phenylalanine could be detected. In the diorite the same amino acids appear with concentrations of 0.068 pmol mg^{-1} proline and 0.819 pmol mg^{-1} D-phenylalanine. In the water samples the same amino acids occur, with 22.98 pmol ml^{-1} D-proline, 8.69 pmol ml^{-1} D-phenylalanine and 5.019 pmol ml^{-1} L-phenylalanine.

With HPAE-PAD the amount of sugars in the crushed cores of both rock types and from water samples was determined (Fig. 26). In the granite fucose occurs as the main sugar component with a concentration of 1.515 pmol mg^{-1}. Furthermore, 0.999 pmol mg^{-1} galactose, 0.261 pmol mg^{-1} galactosamine and 0.125 pmol mg^{-1} d-glucose could be detected. In the diorite the same sugars were observed, but with galactose as the main component with 5.937 pmol mg^{-1}. In addition, 1.886 pmol mg^{-1} d-glucose, 1.406 pmol mg^{-1} fucose and 0.356 pmol mg^{-1} galactosamine were found. The analyzed water also contained some sugars, but unfortunately the concentration was too low for determination.

For getting a clue on the potential source of the detected organic material, as a first step DNA extraction followed by PCR was performed. Amplification of archaeal 16S rRNA gene fragments did not give PCR products in any of the selected core section zones. While bacteria could be detected in all section zones, fungal 18S rDNA could not be amplified in zone 2 of core section A (Fig. 27).

4.2.4 Discussion

The CNS analyzes together with the determined organic carbon concentration clearly show that there is a small but significant amount of organic substances in both main rock types occurring in the tunnel of Äspö. Contemporaneously with microscopic methods it is noticeable that the granite is crossed by many Mn-rich, luminescent, small calcite fractures which are probably related to the organic matter (Fig 19). Epifluorescence microscopy visualizes the close association of the organic matter with the Mn-rich calcite fracture. The brownish coating of the calcite by organic matter is concentrated along phase boundaries and probably micro fissures of the calcite.

As the macroscopic characterization is not always clear, a mineralogical characterization of the granitic sample was additionally performed with Raman spectroscopy. For this purpose, the different end members (Na, Ca and K) and structural polymorphs of the feldspar group were identified and discriminated (Bendel & Schmidt 2008; Freeman et al. 2008). The specimen analyzed contains K-feldspars (microcline and orthoclase) as a main component as well as albite ($NaAlSi_3O_8$). Besides, relatively high amounts of quartz and minerals belonging to the biotite group could be identified. Hence the characterization of the sample as granite could be confirmed. In addition, Raman spectroscopy has the capability to provide information not only about the mineralogy, but also about organic molecules in the sample. Therefore, additional Raman spectra were gathered in order to characterize the organic matter attached to the calcite fractures. As an enrichment of the organic matter could be observed along the phase boundary towards the granite, Raman analyzes were concentrated at this area.

For the interpretation of the organic Raman spectra it is essential to have comparable spectra of substances presumably occurring in the sample. We assume that in our sample some of the fractures were reactivated and interconnected with an aquatic system causing the formation of conditioning films or even biofilms. In general, organic Raman spectra are very complex and therefore, not easy to interpret. Besides the assignment of single Raman bands, the overall fingerprinting of a spectrum is also important. A detailed overview of Raman spectra of biological molecules is given by De Gelder et al. (2007).

These spectra clearly show that most groups of substances exhibit their main bands in different regions of the spectra. This fingerprinting quality can be used to get a good characterization of the spectra. Other important tools for the interpretation of the spectra are reference databases, which can help to identify signals of specific molecules.

The first spectrum represents a mix of organics with quartz and probably biotite (Fig. 23A; Table 2). The bands in the lower wavenumber region occur due to vibrations of quartz and biotite, whereas the band at 3673 cm^{-1} represents the OH band in biotite. To better differentiate between the organic and the mineral signals, the spectrum of quartz was subtracted from the sample spectrum. As the remaining bands below 780 cm^{-1} could be signals from biotite, as well as the band at 3673 cm^{-1}, these were also removed. The spectrum with the remaining bands is shown in Fig. 24A (upper part). When compared to substances published in databases (S.T. Japan Europe GmbH) the best concordance applies for 3,6,9-trioxaundecane (Fig. 24A; lower part). This substance is a carbohydrate with supplemental oxygen atoms. When examining the bands in more detail, those from 2800-3000 cm^{-1} can be assigned to C-H stretching vibrations and those around 1470 cm^{-1} to CH_2 and CH_3 deformation modes (e.g., Maquelin et al. 2002). The C-C stretching vibrations of the aliphatic chain can be observed between 1240 and 1300 cm^{-1}, whereas C-O-C stretching vibrations occur between 860 and 1150 cm^{-1}.

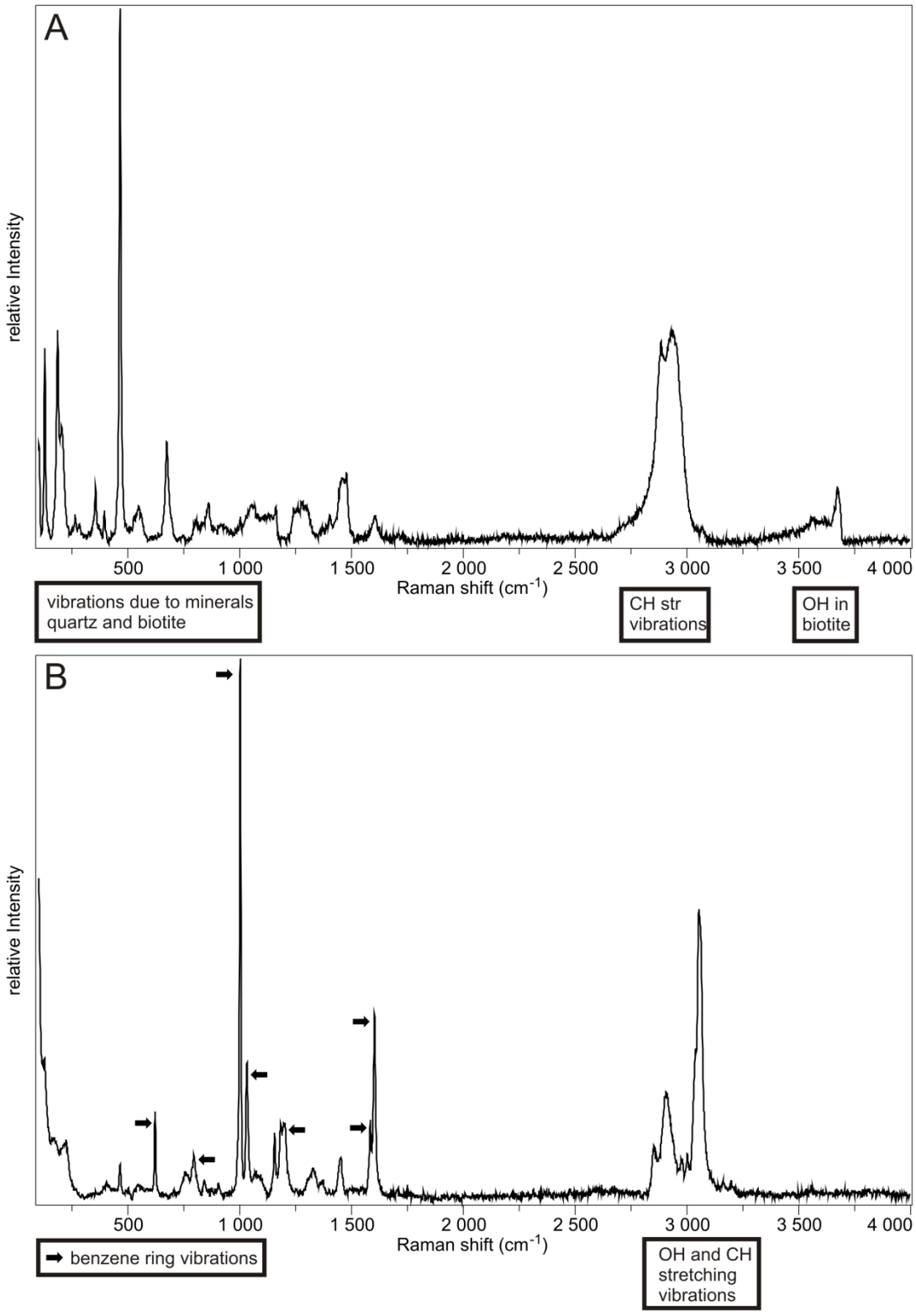

Figure 23: Raman spectra obtained on the organic phase. Spectrum (A) is dominated by mineral vibrations, whereas spectrum (B) is dominated by vibrations of a benzene ring.

Table 2: Assignment of the main Raman bands of the spectrum shown in Fig. 23A.

Raman main bands of the spectrum shown in Fig. 23A [cm^{-1}]	Minerals	Functional groups
129	quartz	
186	biotite	
206	quartz	
356	quartz	
395		
465	quartz	
550		
674	biotite	
860		C-O-C stretching
1003		C-O-C stretching
1058		C-O-C stretching
1162	quartz	
1243		C-C stretching
1276		C-C stretching
1306		C-C stretching
1457		CH_2/CH_3 deformation
1478		CH_2/CH_3 deformation
1604		
2577		
2881		C-H stretching
2944		C-H stretching
3673	biotite	

Table 3: Assignment of the main Raman bands of the spectrum shown in Fig. 23B.

Raman main bands of the spectrum shown in Fig. 23B [cm^{-1}]	Assignment after Maquelin et al., 2002	Assignment after De Gelder et al. 2007	Assignment after Stewart and Fredericks 1999
102			
127			
178			
465		phenylalanine	
622	phenylalanine	phenylalanine	benzene ring
795			
842		phenylalanine	
904			
1002	phenylalanine	phenylalanine	
1033		phenylalanine	benzene ring
1156		phenylalanine	
1183		phenylalanine	
1199			benzene ring
1330		phenylalanine	
1452			
1581		phenylalanine	benzene ring
1603	phenylalanine	phenylalanine	benzene ring
2853			
2910			
2975			
3001			
3056			

The second spectrum only consists of bands assignable to organic molecules and does not include mineral vibrations (Fig. 23B; Table 3). The comparison with spectra from the database (S.T. Japan Europe GmbH) produces a good concordance with a styrene-allyl alcohol copolymer (Fig. 24B). This copolymer consists of a benzene derivative and an allyl alcohol component. Accordingly

bands between 2700 and 3100 cm^{-1} can be assigned to C-H stretching modes (Fig. 23B). Furthermore, after Maquelin et al. (2002) the main bands at 1603, 1002 and 622 cm^{-1} are determined as vibrations of the phenylalanine molecule. This is also in concordance to the spectra published by De Gelder et al. (2007). Here the band pattern is very similar to those of amino acids with a cyclic R side chain, and especially the positions of the main bands are similar to those of L-phenylalanine. The main feature in the chemical structure of phenylalanine is the benzene ring, which vibrations contribute mostly to the Raman spectrum (cf. Stewart & Fredericks 1999 and citations therein). This applies to the main bands at 1003, 1605 and 1584 cm^{-1} as well as to some smaller ones at 622, 1037 and 1203 cm^{-1}. Furthermore, ring breathing modes around 800 cm^{-1} could be detected (after Asher et al. 1986). It can be concluded that this spectrum either represents vibrations of the amino acid phenylalanine, or at least comprises the two main functional groups of this compound, which are a benzene ring and a carboxyl group. It is possible that the carboxyl group is no longer intact, resulting in an alcohol component.

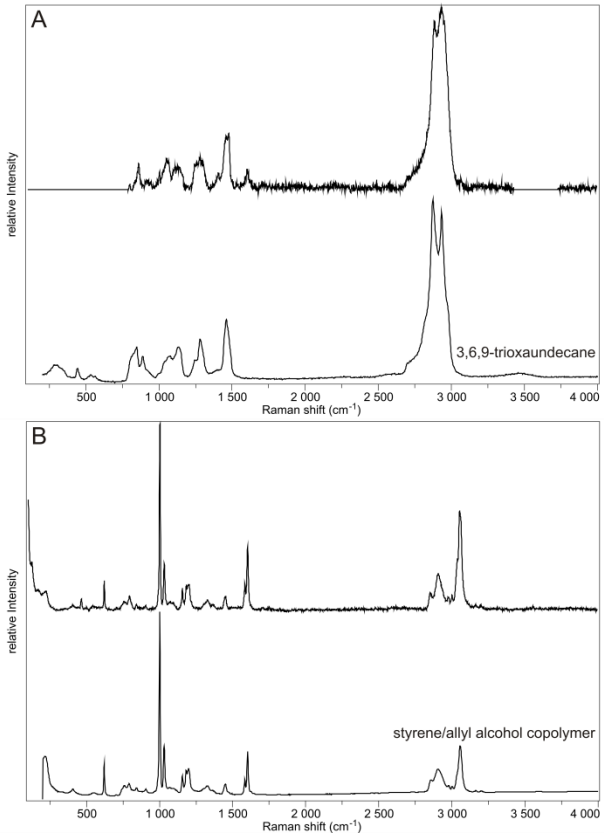

Figure 24: Comparison of Raman spectra obtained on the organic phase with spectral databases (S.T. Japan Europe GmbH). The best fit for spectrum (A) is 3,6,9-trioxaundecane. The best fit for spectrum (B) is a styrene/allyl alcohol copolymer.

Altogether the recorded spectra show a variety of bands which can be assigned to vibrations of different functional groups of organic molecules. Due to the complexity of the spectra it is difficult to distinguish specific substances and normally a spectrum consists of vibrations of different substances.

Nevertheless, putative signals of amino acids, especially phenylalanine, were assignable. To confirm these assignments, we performed HPLC analyzes of the enantiomers of the chiral amino acids of the same sample. This highly sensitive technique allows us to not only confirm the occurrence of amino acids, mainly proline and phenylalanine, but also to distinguish their L- and D- enantiomers (Fig. 25). In living organisms almost exclusively the L-configuration exists. In dead organisms the proteins start to break down, leading to a conversion of the L-configuration into the D-configuration (Robins et al. 2001). This process is called racemization. The analyzed granite sample shows a D/L ratio of 1.13 for phenylalanine, suggesting a racemic mixture which comprises already transferred D-enantiomers. But the D/L ratio greater than 1 also points to different sources of the amino acid which could include the overlying seawater.

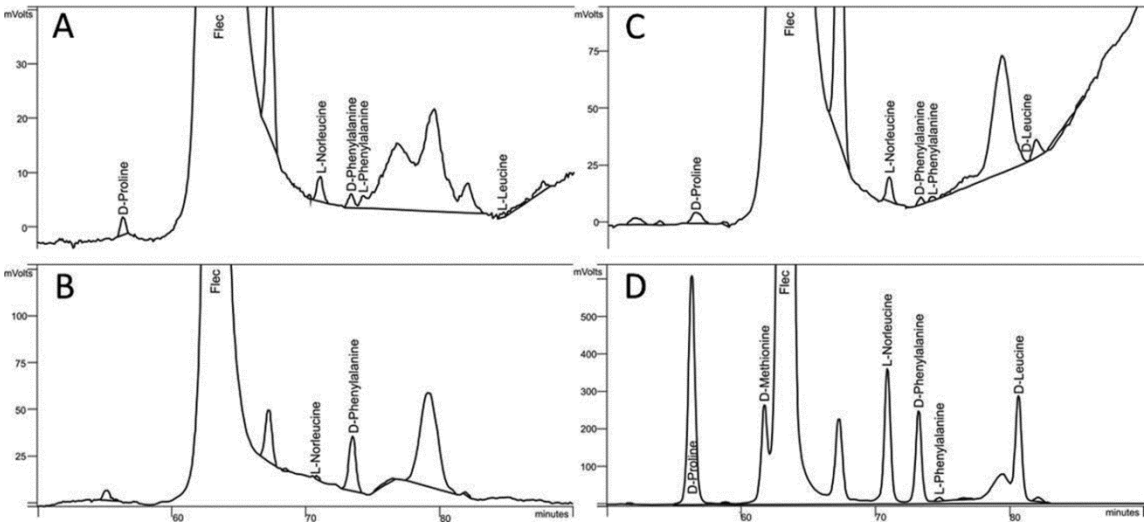

Figure 25: Graphical presentation of the chiral amino acids analyzes of the granite (A), the diorite(B), the water sample (C) and the used standard (D).

Besides some of the proposed band assignments belonging to the group of carbohydrates, small amounts of specific sugars were revealed with HPAE-PAD (Fig. 26). From special interest is the presence of fucose and of amino sugars which are typical remains of EPS structures. Furthermore, fucose is an important constituent in microbial EPS structures (e.g., Reitner 2010) and is

building a sulfated polysaccharide (fucodian) which is formed in brown algae (e.g. *Fucus* sp., *Laminaria* sp.) (Bilan et al. 2002). These algae occur in the overlying seawater and this observation may also support the assumption that seawater seeps inside the hard rocks.

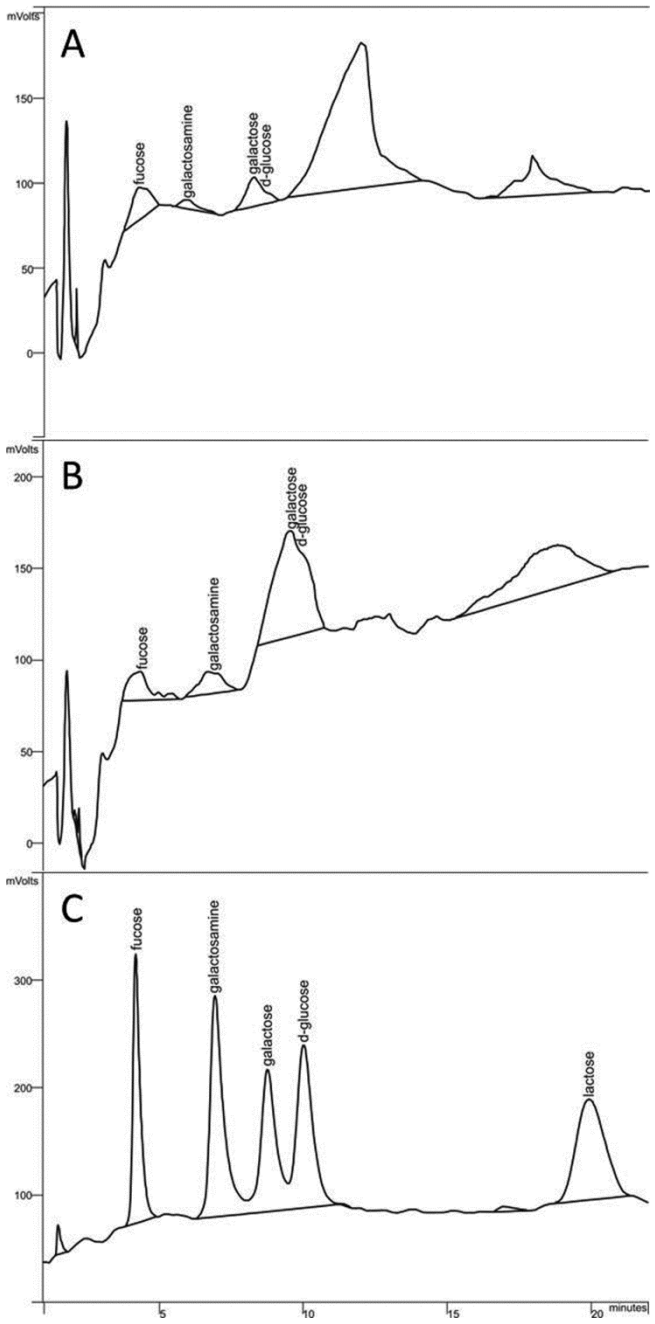

Figure 26: Graphical presentation of the analyzed sugar fraction of the granite (A), the diorite (B) and the standard (C).

Only recently Heim et al. (2012) presented a reconstruction of ancient environmental processes occurring in the tunnel of Äspö. They found organic traces in an Äspö diorite taken from the same depth as the samples described

here. This diorite features four generations of fracture minerals, a Precambrian fluorite, a Palaeozoic Mn-rich calcite, a late Pleistocene permineralized organic-rich amorphous layer and a second calcite phase. Connected to the amorphous layer Heim et al. (2012) found tubular, branched structures of 0.5 to 2 µm in diameter which were interpreted as possibly *Actinomycetes*-like bacteria.

Indeed, preliminary DNA extraction followed by PCR amplification indicates a ubiquitous presence of bacteria throughout the core section, amongst them probably *Actinomycetes*-like bacteria. However, Heim et al. (2012) only observed these structures at the boundary between the fluorite and calcite phase of a fracture filling within the Äspö diorite similar to section B in Fig. 27 (this study). Similarly, earlier studies gave evidence of microfossil biofilm formation along calcite channels, suggesting a fossilization of microorganisms attached to the walls of water-conducting channels in the course of channel clogging and precipitation processes (Pedersen 1997). However, our samples give evidence of a bacterial occurrence also within the granitic rock zones, corroborating the above mentioned hypothesis of an early microbial colonization of the calcitic substrate. Following the idea of a fossilization of water-conducting channels, the evidence of fungal DNA amplification (Fig. 27) corresponds to the detection of several yeast and mold strains within the Äspö HRL groundwater system (Ekendahl et al. 2003). As important components of rock surface microbial communities, fungi and their interactions with mineral chemistry have, however, mainly been studied with respect to biotic weathering processes (Hoffland et al. 2004; Gadd et al. 2011 and references therein). Fossil fungi have already been found within the deep, basaltic earth crust (Schumann et al. 2004), but also as subsurface remains in veins and fractures of continental, crystalline rocks (Reitner et al. 2006). Despite a hydrothermal fluid influence at 1.45 Ga (Kornfält et al. 1997), which would suggest the presence of archaeal fossils (Ventura et al. 2007) and despite the presence of active archaea in the groundwater of this area (Kotelnikova & Pedersen 1998), archaeal gene fragments could not be amplified from the samples discussed in the present study.

The probability of a contamination in terms of recent fungal colonization during core storage can be neglected, as no fungal DNA could be amplified in the raised quartz zone of core section A (Fig. 27). Reports on the long-term survival

of ancient microbial DNA in amber, halite, soft tissue and sediments combined with favorable environmental conditions such as low temperature or arid climate have long been criticized for inadequate experimental setups or insufficient authentication of results (Hebsgaard et al. 2005, and references therein). Nevertheless, it is our strategy to take into account the potential of dormant survival forms and resting stages such as bacterial endospores (Stan-Lotter et al. 2008; Fendrihan 2010) and to apply appropriate methodologies wherever possible (Drancourt & Raoult 2005; Willerslev & Cooper 2005). Hence, final evidence of a possible contamination, a microbial fossilization or later colonization of fractures in these deep granitic hard rock samples will soon be given by the outcomes of presently ongoing phylogenetic studies.

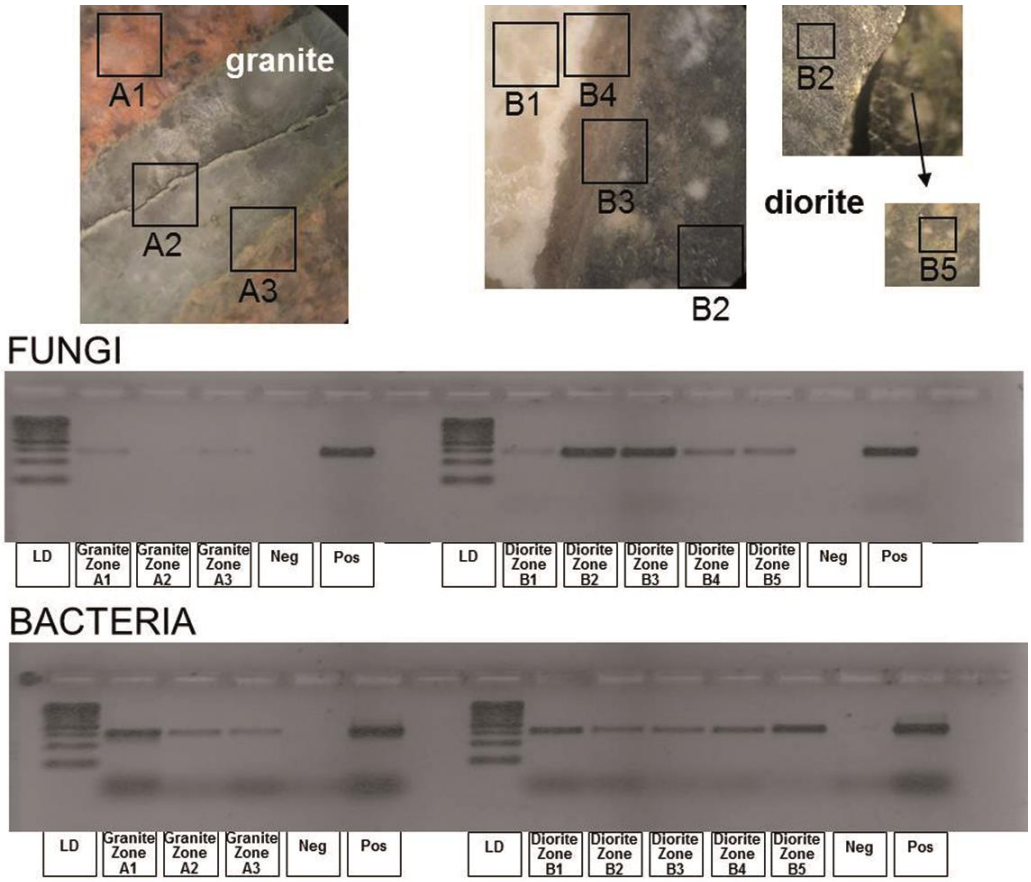

Figure 27: On top core section of the granite with zones A1-A3 and core section of the diorite with zones B1-B5. Underneath visualisation of bacterial and fungal PCR products on a 1,5% Agarose gel by comparing granite core sections with diorite core sections (LD:1kb DNA ladder, Neg: negative and Pos: positive control).

In order to confirm the results obtained from the granite, we also applied CNS, HPLC and HPAE-PAD on a dioritic sample similar to the one described by Heim et al. (2012). To validate the observed data, additional analyzes of water

obtained from open fractures close to the drilling sites were performed. Generally, the data are in good concordance and especially the abundance of amino acids in both rocks and the water sample is significant. As the overlying seawater also contains both enantiomers it can be presumed that the racemic mixture inside the rock fracture is influenced by seepage of the overlying seawater. The detection of fucose in the rock samples is another hint for this influence, because it can be attributed to the occurrence of brown algae.

Based on these findings, we propose that the described organic matter exhibits the remains of a conditioning film. These conditioning films develop as soon as a solid surface gets in contact with an aquatic environment by adsorption of organic and inorganic matter on that surface (Loeb & Neihof 1975; Schneider & Leis 2003). Many different substances are recognizable in a conditioning film including glycoproteins (Baier 1980), humic material (Loeb & Neihof 1975), proteins, lipids, nucleic acids, polysaccharides and aromatic amino acids (Taylor et al. 1997) and/or unspecified macromolecules (Zaidi et al. 1984). Thereby a discontinuous layer with variable thickness is formed (Compere et al. 2001). Already Baier (1980) reported a high abundance of proteins in the conditioning films. This observation could later be confirmed by Compere et al. (2001) who found out that proteins, followed by carbohydrates, are the first compounds adsorbing on stainless steel panels immersed in seawater and also Poleunis et al. (2002, 2003) reported similar results applying Time of flight secondary ion mass spectroscopy (Tof-SIMS). The most important reason for the development of a conditioning film is that due to negative charges microorganisms are not capable of attaching directly to a surface (Bhosle et al. 2005).

After the initial growth of such a conditioning film the surface can be colonized by microorganisms. The production of exopolymeric substances (EPS) and other cellular appendages like flagella and fimbriae is important for the permanent attachment of microorganisms to the surface via the conditioning film. The persisting attachment of microbial cells to the surface triggers the successive formation of a biofilm. A biofilm is defined as an assemblage of surface-associated microbial cells enclosed in a matrix of EPS which primarily consists of polysaccharides (Donlan 2002).

In the samples analyzed in this study the organic matter clearly is associated to Mn-rich calcite fracture fillings. The complex organic molecules revealed by Raman spectroscopy, HPLC and HPAE-PAD fit well into the category of substances which would be expected in a conditioning film. Also the racemic mixture of phenylalanine and the occurrence of fucose suggest seepage of the overlying seawater through the fracture system, enabling the growth of a conditioning film. Additionally, fucose together with the other detected amino sugars could be remains of microbial EPS, already inhabiting the conditioning film

4.2.5 Conclusions

The geochemical analyzes of both rock types occurring in the Äspö tunnel show that they contain little, but significant organic carbon. It has to be noted that the data are referred to the whole rock meaning that such a low concentration of organic carbon as well as nitrogen inside the rocks is conceivable.

Microscopic visualization of the fractures, especially epifluorescence microscopy, revealed a concentration of organic matter inside Mn-rich calcite fractures, especially at the boundary to the rock matrix.

With confocal Raman spectroscopy it is possible to get signatures from inside a sample and thereby minimize contamination effects. In addition, besides mineralogical information, the technique provides information about the organic matter inside the sample. With a good database it is possible to assign specific Raman bands to functional groups or molecules or even specific substances.

However, Raman spectra of organic substances are very complex and therefore, the interpretation of the various bands is not always clear. Nevertheless, when considering the spectra together with additional methods like HPLC and HPAE-PAD an integrated view on the processes occurring inside the granite can be established.

The presence of organic matter, especially carbohydrates (e.g. fucose), amino sugars and amino acids, suggests the existence of a conditioning film. The presence of the amino acid phenylalanine in the L-and the D-configuration occurring in both rock types and the water samples demonstrates the rather

recent formation and an influence of the overlying water seeping through the fracture system.

In addition, the preliminary DNA data suggest a rather active inhabitation of the rocks and the associated fractures by bacteria and fungi.

Acknowledgements

We are grateful to the staff of the Äspö HRL as well as the SKL Nova FoU for technical and logistic support. This study received financial support from the German Research Foundation (DFG – FOR 571, Re 665/27-3). We greatly acknowledge Dr. Christine Heim (Geobiology, Göttingen), Dr. Martin Blumenberg (Geobiology, Göttingen), and Dr. Klaus Simon (Geochemistry, Göttingen) for valuable critical comments and technical support.

References

Amend, J.P. and Teske, A. (2005) Expanding frontiers in deep subsurface microbiology. *Palaeogeography, Palaeoclimatology, Palaeoecology* 219: 131-155.

Asher, S.A., Ludwig, M. and Johnson, C.R. (1986) UV Resonance Raman excitation profiles of the aromatic amino acids. *Journal of the American Chemical Society* 108: 3186-3197.

Baier, R. (1980) Substrate influences on adhesion of microorganisms and their resultant new surface properties. In: *Adsorption of Microorganisms to Surfaces*, edited by G. Bitton and K.C. Marshall, John Wiley & Sons, NY, USA, pp. 59-104.

Bendel, V. and Schmidt, B.C. (2008) Raman spectroscopic characterisation of disordered alkali feldspars along the join $KAlSi_3O_8$–$NaAlSi_3O_8$: application to natural sanidine and anorthoclase. *European Journal of Mineralogy* 20: 1055-1065.

Bhosle, N.B. (2004) Chemical and molecular characterization of biofilm on metal surfaces. In: *Marine Microbiology: Facets & Opportunities*, edited by N. Ramaiah, National Institute of Oceanography, Goa, India, pp. 159-168.

Bhosle, N.B., Garg, A., Fernandes, L. and Citon, P. (2005) Dynamics of amino acids in the conditioning film developed on glass panels immersed in the surface seawaters of Dona Paula Bay. *Biofouling* 21: 99-107.

Bhosle, N.B. and Wagh, A.B. (1997) Amino acids in biofilm material on aluminium panels immersed in marine waters. *Biofouling* 11: 149-166.

Bilan, M.I., Grachev, A.A., Ustuzhanina, N.E., Shashkov, A.S., Nifantiev, N.E. and Usov, A.I. (2002) Structure of a fucoidan from the brown seaweed Fucus evanescens C.Ag. *Carbohydrate research* 337: 719-730.

Compère, C., Bellon-Fontaine, M.N., Bertrand, P., Costa, D., Marcus, P., Poleunis, C., Pradier, C.M., Rondot, B. and Walls, M.G. (2001) Kinetics of conditioning layer formation on stainless steel immersed in seawater. *Biofouling* 17: 129-145.

De Gelder, J., De Gussem, K., Vandenabeele, P. and Moens, L. (2007) Reference database of Raman spectra of biological molecules. *Journal of Raman Spectroscopy* 38: 1133-1147.

DeLong, E.F. (1992) Archaea in coastal marine environments. *Proceedings of the National Academy of Sciences* 89: 5685-5689.

Donlan, R.M. (2002) Biofilms: microbial life on surfaces. *Emerging Infectious Diseases* 8: 881-90.

Drake, H., Tullborg, E.-L. and Page, L. (2009) Distinguished multiple events of fracture mineralisation related to far-field orogenic effects in Paleoproterozoic crystalline rocks, Simpevarp area, SE Sweden. *Lithos* 110: 37-49.

Drancourt, M. and Raoult, D. (2005) Palaeomicrobiology: current issues and perspectives. *Nature Reviews Microbiology* 3: 23-35.

Ekendahl, S., Arlinger, J., Ståhl, F. and Pedersen, K. (1994) Characterization of attached bacterial populations in deep granitic groundwater from the Stripa research mine by 16S rRNA gene sequencing and scanning electron microscopy. *Microbiology* 140: 1575-1583.

Ekendahl, S., O'Neill, A.H., Thomsson, E. and Pedersen, K. (2003) Characterisation of Yeasts Isolated from Deep Igneous Rock Aquifers of the Fennoscandian Shield. *Microbial Ecology* 46: 416-428.

Fendrihan, S. (2010) Microorganisms isolated from subsurface environments and their importance for astrobiology and theoretical biology. *Extreme Life, Biospeology & Astrobiology* 2: 23-36.

Freeman, J.J., Wang, A., Kuebler, K.E., Jolliff, B.L. and Haskin, L.A. (2008) Characterization of natural feldspars by Raman spectroscopy for future planetary exploration. *The Canadian Mineralogist* 46: 1477-1500.

Gadd, G.M., Rhee, Y.J., Stephenson, K. and Wei, Z. (2012) Geomycology: metals, actinides and biominerals. *Environmental Microbiology Reports* 4: 270-296.

Gargas, A. and Taylor, J.W. (1992) Polymerase Chain Reaction (PCR) Primers for Amplifying and Sequencing Nuclear 18s rDNA from Lichenized Fungi. *Mycologia* 84: 589-592.

Hama, K., Bateman, K., Coombs, P., Hards, V.L., Milodowski, A.E., West, J.M., Wetton, P.D., Yoshida, H. and Aoki, K. (2001) Influence of bacteria on rock-water interaction and clay mineral formation in subsurface granitic environments. *Clay Minerals* 36: 599-613.

Hebsgaard, M.B., Phillips, M.J. and Willerslev, E. (2005) Geologically ancient DNA: fact or artefact? *Trends in Microbiology* 13: 212-220.

Heim, C., Lausmaa, J., SjÖVall, P., Toporski, J., Dieing, T., Simon, K., Hansen, B.T., Kronz, A., Arp, G., Reitner, J. and Thiel, V. (2012) Ancient microbial activity recorded in fracture fillings from granitic rocks (Äspö Hard Rock Laboratory, Sweden). *Geobiology* 10: 280-297.

Hoffland, E., Kuyper, T.W., Wallander, H., Plassard, C., Gorbushina, A.A., Haselwandter, K., Holmström, S., Landeweert, R., Lundström, U.S., Rosling, A., Sen, R., Smits, M.M., van Hees, P.A.W. and van Breemen, N. (2004) The role of fungi in weathering. *Frontiers in Ecology and the Environment* 2: 258-264.

Kornfält, K.A., Persson, P.O. and Wikman, H. (1997) Granitoids from the Äspö area, southeastern Sweden - geochemical and geochronological data. *GFF* 119: 109-114.

Kotelnikova, S., Macario, A.J.L. and Pedersen, K. (1998) Methanobacterium subterraneum sp. nov., a new alkaliphilic, eurythermic and halotolerant methanogen isolated from deep granitic groundwater. *International Journal of Systematic Bacteriology* 48: 357-367.

Kotelnikova, S. and Pedersen, K. (1998) Distribution and activity of methanogens and homoacetogens in deep granitic aquifers at Äspö Hard Rock Laboratory, Sweden. *FEMS Microbiology Ecology* 26: 121-134.

Lane, D. (1991) 16S/23S rRNA sequencing. In: *Nucleic acid techniques in bacterial systematics*, edited by E. Stackebrandt and M. Goodfellow, John Wiley & Sons, Chichester, UK, pp. 115-175.

Loeb, G.I. and Neihof, R.A. (1975) Marine Conditioning Films. In: *Applied Chemistry at Protein Interfaces, Advances in Chemistry Vol.145*, edited by, American Chemical Society, pp. 319-335.

Maquelin, K., Kirschner, C., Choo-Smith, L.P., van den Braak, N., Endtz, H.P., Naumann, D. and Puppels, G.J. (2002) Identification of medically relevant microorganisms by vibrational spectroscopy. *Journal of Microbiological Methods* 51: 255-271.

Morad, S., Sirat, M., El-Ghali, M.A.K. and Mansurbeg, H. (2011) Chloritization in Proterozoic granite from the Äspö Laboratory, southeastern Sweden: record of hydrothermal alterations and implications for nuclear waste storage. *Clay Minerals* 46: 495-513.

Pedersen, K. (1997) Microbial life in deep granitic rock. *FEMS Microbiology Reviews* 20: 399-414.

Pedersen, K. and Ekendahl, S. (1990) Distribution and activity of bacteria in deep granitic groundwaters of southeastern Sweden. *Microbial Ecology* 20: 37-52.

Poleunis, C., Compère, C. and Bertrand, P. (2002) Time-of-flight secondary ion mass spectrometry: characterisation of stainless steel surfaces immersed in natural seawater. *Journal of Microbiological Methods* 48: 195-205.

Poleunis, C., Rubio, C., Compère, C. and Bertrand, P. (2003) ToF–SIMS chemical mapping study of protein adsorption onto stainless steel surfaces immersed in saline aqueous solutions. *Applied Surface Science* 203–204: 693-697.

Reitner, J. (2010) Architecture of Archaeal-Dominated Microbial Mats from Cold Seeps in the Black Sea (Dnjepr Canyon, Lower Crimean Shelf). In: *Microbial Mats: Modern and Ancient Microorganisms in Stratified Systems, Springer Science Series Volume 14: Cellular Origin, Life in Extreme Habitats and Astrobiology*, edited by J. Seckbach and A. Oren, Springer Netherlands, pp. 207-220.

Reitner, J., Schumann, G. and Pedersen, K. (2006) Fungi in subterranean environments. In: *Fungi in Biogeochemical Cycles*, edited by G.M. Gadd, Cambridge University Press, Cambridge, UK, pp. 377-403.

Richter, D.K., Götte, T., Götze, J. and Neuser, R.D. (2003) Progress in application of cathodoluminescence (CL) in sedimentary petrology. *Mineralogy and Petrology* 79: 127-166.

Robins, J., Jones, M. and Matisoo-Smith, E. (2001) *Amino Acid Racemization Dating in New Zealand: An overview and Bibliography*. Auckland University, Auckland, New Zealand.

Schneider, R.P. and Leis, A. (2003) Conditioning Films in Aquatic Environments. In: *Encyclopedia of Environmental Microbiology*, edited by, John Wiley & Sons, Inc.

Schumann, G., Manz, W., Reitner, J. and Lustrino, M. (2004) Ancient Fungal Life in North Pacific Eocene Oceanic Crust. *Geomicrobiology Journal* 21: 241-246.

Smellie, J.A. and Laaksoharju, M. (1992) The Äspö Hard Rock Laboratory: Final evaluation of the hydrogeochemical pre-investigations in relation to existing geologic and hydraulic conditions. *SKB Technical Report 92-31*, Swedish Nuclear Fuel and Waste Management Co., Stockholm, Sweden.

Stan-Lotter, H., Fendrihan, S., Dornmayr-Pfaffenhuemer, M., Gerbl, F., Legat, A., Gruber, C. and Weidler, G. (2008) Microorganisms in the Ancient Terrestrial Subsurface – And in Outer Space? In: *From Fossils to Astrobiology, Cellular Origin, Life in Extreme Habitats and Astrobiology Vol. 12*, edited by J. Seckbach and M. Walsh, Springer Netherlands, pp. 233-248.

Stewart, S. and Fredericks, P.M. (1999) Surface-enhanced Raman spectroscopy of amino acids adsorbed on an electrochemically prepared silver surface. *Spectrochimica Acta Part A: Molecular and Biomolecular Spectroscopy* 55: 1641-1660.

Taylor, G.T., Zheng, D., Lee, M., Troy, P.J., Gyananath, G. and Sharma, S.K. (1997) Influence of surface properties on accumulation of conditioning films and marine bacteria on substrata exposed to oligotrophic waters. *Biofouling* 11: 31-57.

Tullborg, E.-L., Drake, H. and Sandström, B. (2008) Palaeohydrogeology: A methodology based on fracture mineral studies. *Applied Geochemistry* 23: 1881-1897.

Ventura, G.T., Kenig, F., Reddy, C.M., Schieber, J., Frysinger, G.S., Nelson, R.K., Dinel, E., Gaines, R.B. and Schaeffer, P. (2007) Molecular evidence of Late Archean archaea and the presence of a subsurface hydrothermal biosphere. *Proceedings of the National Academy of Sciences* 104: 14260-14265.

Wahlgren, C.-H., Hermansson, J., Forssberg, O., Triumf, C.-A., Drake, H. and Tullborg, E.-L. (2006) Geological description of rock domains and deformation zones in the Simpevarp and Laxemar subareas. Preliminary site description Laxemar subarea-version 1.2. *SKB R-05-69*, Swedish Nuclear Fuel and Waste Management Co., Stockholm, Sweden.

White, T., Bruns, T., Lee, S. and J, T. (1990) Amplification and direct sequencing of fungal ribosomal RNA genes for phylogenetics. In: *PCR Protocols. A Guide to Methods and Applications*, edited by M.A. Innis, D.H. Gelfand, J.J. Sninsky and T.J. White, Academic Press San Diego, CA, USA, pp. 315-322.

Willerslev, E. and Cooper, A. (2005) Review Paper. Ancient DNA. *Proceedings of the Royal Society B: Biological Sciences* 272: 3-16.

Zaidi, B.R., Bard, R.F. and Tosteson, T.R. (1984) Microbial Specificity of Metallic Surfaces Exposed to Ambient Seawater. *Applied and Environmental Microbiology* 48: 519-524.

Zhou, J., Bruns, M.A. and Tiedje, J.M. (1996) DNA recovery from soils of diverse composition. *Applied and Environmental Microbiology* 62: 316-22.

Chapter 5: Ediacaran fossil microbial mat, White Sea, Russia

One example for a fossilized microbial mat can be found on samples from the upper part of the Neoproterozoic Ust-Pinega Formation, which was reclassified as the Zimnegory Formation by Grazhdankin (2003), from the Russian White Sea cost. This formation belongs to the 550 m thick Vendian Group (Grazhdankin, 2003; Grazhdankin, 2004), which is characterized by a coarsening upwards succession of shallow marine, fluviomarine and alluvial sedimentary rocks with tuffaceous-siliciclastic properties (Stankovsky et al., 1990). In the White Sea area the Vendian Group crops out along the eastern slope of the Baltic Shield of the East European Craton on a distance of 300 km, whereby the natural outcrops always occur on smaller individual localities (Grazhdankin, 2004). Stratigraphically it is subdivided into four formations, with Lamtsa being the oldest, followed by Verkhovka, Zimnegory and Yorga (Grazhdankin, 2003; Grazhdankin, 2004). In former times the latter three were summarized as Ust-Pinega Formation with diverse subformations (see Solontsov et al., 1970; Stankovsky et al., 1972). For two different tuff layers U-Pb zircon data exist, and give ages of 558 ± 1 Ma for the tuff on the base of the Verkhovka formation (Grazhdankin, 2004), and 555.3 ± 0.3 Ma for the tuff in the Zimnegory formation (Martin et al., 2000). That means, that for the described sample here, a similar age of ca. 555 Ma can be assumed. In the vertical succession of the Vendian Group several lithofacies occur, which include shale, siltstones, sandstones, interstratified sandstones and amalgamated sandstones (Grazhdankin, 2004). These lithofacies can be used for explaining the alternating depositional systems, which range from low-energy lower shoreface to distal braid-delta plain, within a deltaic supersystem (Grazhdankin, 2003). The described sample can be classified into sandy depositions of valley fill. Another important feature of the Vendian Group is that it is famous for the multiple fossil assemblages. Especially the Ediacaran assemblages are remarkable, because they combine elements of otherwise unlike Avalon, Ediacara and Nama biotas found in Newfoundland, South Australia and Namibia, respectively (Fedonkin, 2003). Therefore, this region is very attractive for the research on the Ediacaran fauna and the development of organisms in the Precambrian. Together with the assemblages of the Ediacaran

fossils often microbial mats are observed, which are suspected to play an important role in the preservation process (Steiner & Reitner, 2001; Callow & Brasier, 2009). The microbial mat is characterized by a wrinkle, pustulose appearance, which is referred to as elephant skin (e.g. Gehling, 1999; Steiner & Reitner, 2001). These structures already were recognized as putatively formed under microbial influence for samples of Vendian-Cambrian strata of North America (Hagadorn & Bottjer, 1997), which was confirmed by Steiner & Reitner (2001) for samples of the Vendian Group of the White Sea. Inside this dark microbial mat layer numerous filaments are visible, and were classified as sheaths of possible cyanobacteria or sulfur bacteria (Steiner & Reitner, 2001). As typical for these wrinkle structures the microbial mat is imbedded in the upper part of a siliciclastic matrix with sandy grain size. To get a detailed overview about the described fossilized microbial mat various Raman spectra were recorded. The spectra show siliciclastic signals, like quartz and anatase (TiO_2), as well as iron oxides and pyrite. Many of the spectra additionally show vibrations of organic molecules.

A typical spectrum of anatase obtained in the microbial mat structure is shown in Figure 28. In the lower spectral region typical bands, which occur due to vibrations of TiO_2 can be observed. These bands are in good agreement with the observed and calculated bands described by Oshaka et al. (1978). In the higher spectral region at 1296, 1485 and 1578 cm^{-1} additional bands arise, which can be assigned to vibrations of organic molecules. The bands at 1296 and 1578 cm^{-1} probably belong to vibrations of carbon molecules, whereas the band at 1485 cm^{-1} probably is related to vibrations of C-H molecules (cf. Horiba, application note: http://www.horiba.com/fileadmin/uploads/Scientific/Documents/Raman/bands.pdf; Smith & Dent, 2005).

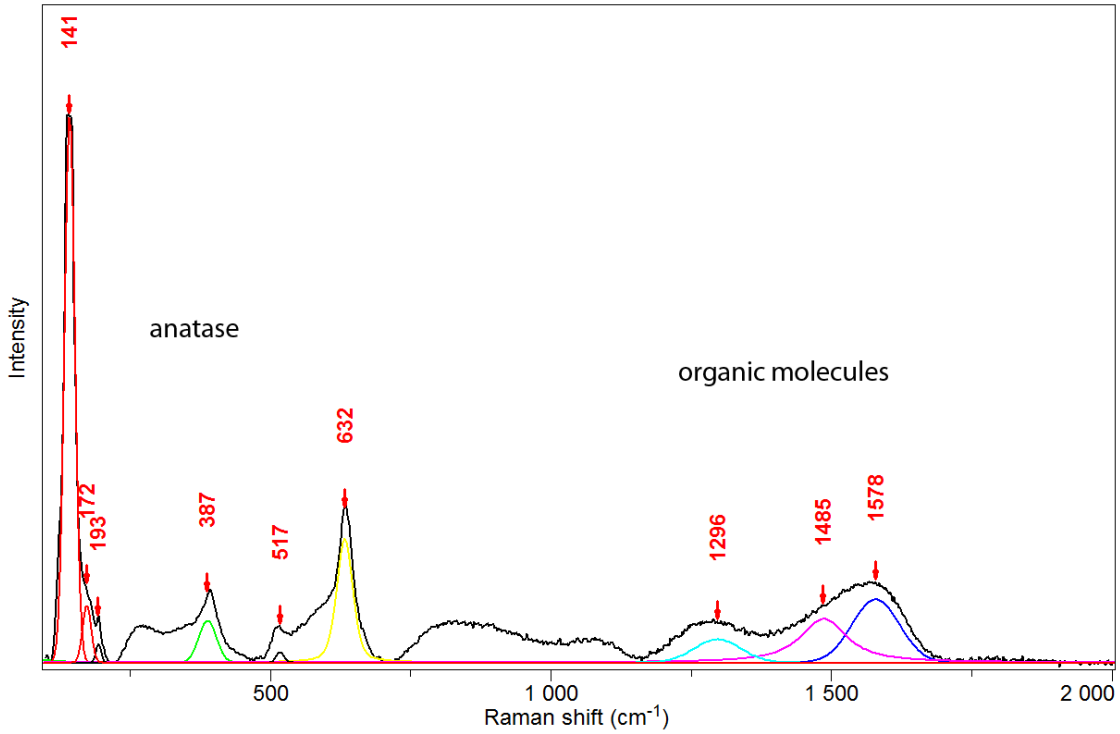

Figure 28: Anatase spectrum obtained in the microbial mat structure. Note the extra bands in the higher wavenumber region, which can be assigned to vibrations of organic molecules (C-C and C-H).

In the literature anatase repeatedly is reported to occur together with carbonaceous material, often also associated with iron oxides or hydroxides. In most of the cases these occurrences could be related to potentially fossilized microbial mats of even Achaean age (Foucher & Westall, 2009; Bower, 2011). Furthermore, bacteria of the *Rhodococcus* strain Gin-1 (NCIMB 40340) were reported to be highly tolerant to TiO_2 and have the capability to adsorb on them (Shabtai & Fleminger, 1994). A more recent example for a likely biogenic origin of anatase rods is given by Glamoclija et al. (2009), who investigated microbial fossils in a pyrite vein of the 35 Ma old Chesapeak Bay impact structure, Virginia, USA. The formation of the supposed anatase permineralized fossils is probably related to a low-temperature hydrothermal event.

The spectra of the iron oxides in the fossilized microbial mat show bands indicating a hematite structure (Fig. 29). However, the band positions are shifted extremely to lower wavenumbers, compared to crystalline hematite (cf. de Faria et al., 1997; Jubb & Allen, 2010). On the one hand this can be a heating effect due to extensive laser power. But on the other hand de Faria et al. (1997) have reported band shifts with a laser power of 7 mW measured on powdered material and a broadening of the bands. In this work the laser power

was at 20 mW but the crystals were bound inside a rock. Furthermore, the bands itself show no extreme broadening as described by de Faria et al. (1997), meaning this more extreme peak shift cannot be the only explanation.

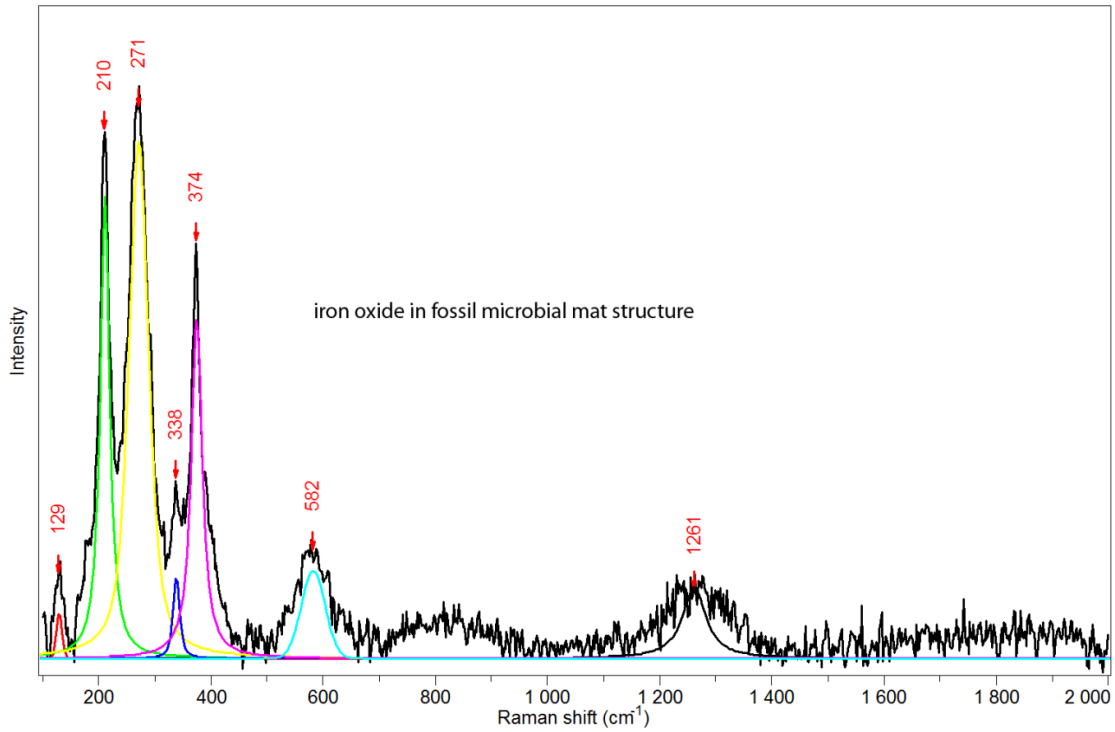

Figure 29: Typical spectrum of iron oxide from the microbial mat structure. The Raman bands indicate a hematite structure, although the band positions are shifted to lower wavenumbers.

Therefore, it is suggested that the formation of the iron oxides is microbial influenced, which leads to band shifts compared to inorganic mineral formation. There exists a recent example of cyanobacterial endoliths colonizing the Antarctic Beacon sandstone reported by Edwards et al. (2004). They could observe a biological geomodification due to the colonization of the sandstone by the endolithic community, which leads to the formation of a mixture between hematite and goethite. They concluded that this process involves mobilization and transportation of iron (III) from the rock by conversion to goethite by the cyanobacteria. The situation in the fossil sample from the White Sea could be similar, especially as shown by Steiner & Reitner (2001) cyanobacteria could be involved. Also the occurrence of the pyritic sheaths inside the fossil microbial mat argue for a microbial related formation of the hematite (cf. Ehrlich, 1999).

The spectra with anatase signal as well as those with iron oxide signal, additionally show bands which can be assigned as amorphous carbon (see

chapter 1.3). They consist of a G band centered around 1580 cm^{-1} and a D band centered around 1300 cm^{-1}. In other spectra from the laminated region this signal is detectable without additional bands from minerals (Fig. 30).

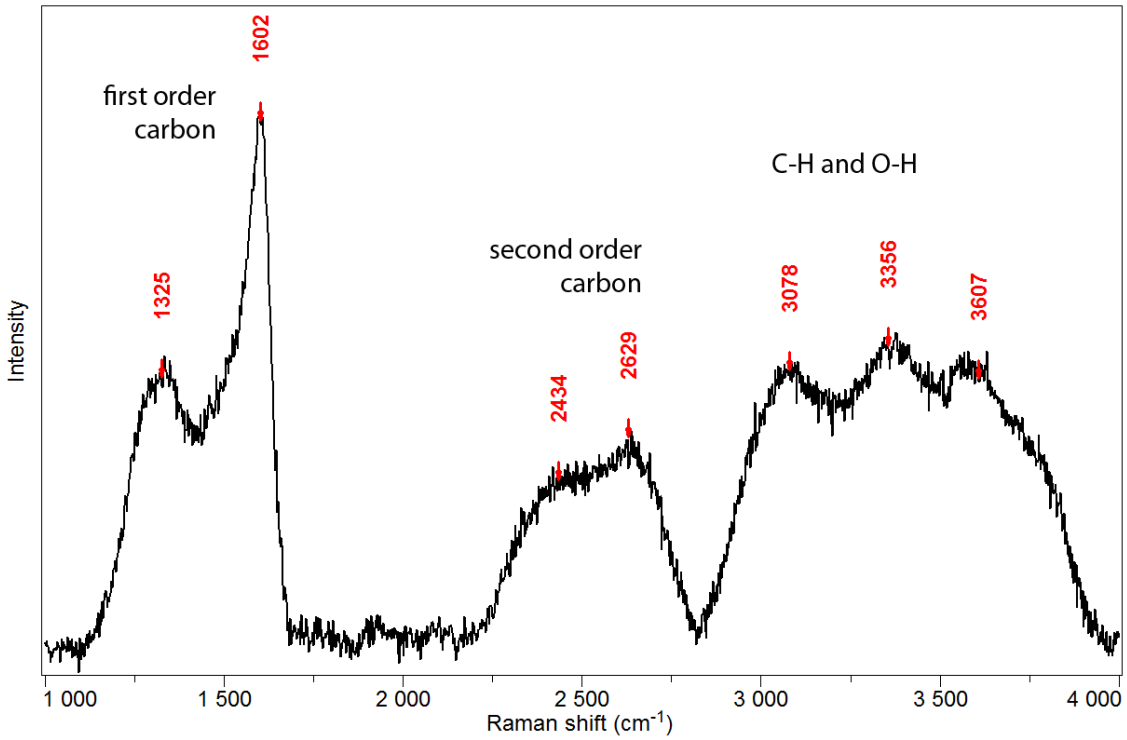

Figure 30: Spectrum of organic compounds from the fossilized microbial mat. Besides the first and the second order bands of amorphous carbon also vibrations of C-H and O-H molecules occur.

In the spectrum above both the first order bands at 1325 cm^{-1} (D band) and 1602 cm^{-1} (G band) as well as second order bands at 2434 and 2629 cm^{-1} are noticeable (cf. Marshall et al., 2010). The strongest band in the second order spectrum for carbonaceous material is reported to appear around 2700 cm^{-1} (Pasteris & Wopenka, 2003), but is not detectable here. The additional bands located at 3078, 3356 and 3607 cm^{-1} are carefully assigned as vibrations of C-H (3078 cm^{-1}) N-H (3356 cm^{-1}) and O-H (3607 cm^{-1}) which can occur in this region (cf. Horiba, application note: http://www.horiba.com/fileadmin/uploads/Scientific/Documents/Raman/bands.pdf; Smith & Dent, 2005).

To get a better impression on how the main mineral phases and the carbon signals are distributed on the sample, a representative area (180 µm times 180 µm) with one datapoint every 10 µm was mapped. Each datapoint gives a single spectrum, which are compiled to a false color images (Fig. 31). The resulting map shows signals for pyrite in red, for quartz in blue and for carbon in

green (Fig. 31A). The mapping area belongs to a pyrite rich zone which is associated to the fossilized biofilm (compare video image Fig. 31C). The signal for quartz arises due to the silicate background. In the black zone on the upper left part signals for epoxy were measured (compare overlain image Fig. 31D). Probably this part was out of focus during the measurement and therefore, only signals from epoxy could be detected. The other darker spots are associated to orthoclase from the sediment matrix and are displayed in the second map in blue (Fig. 31B).

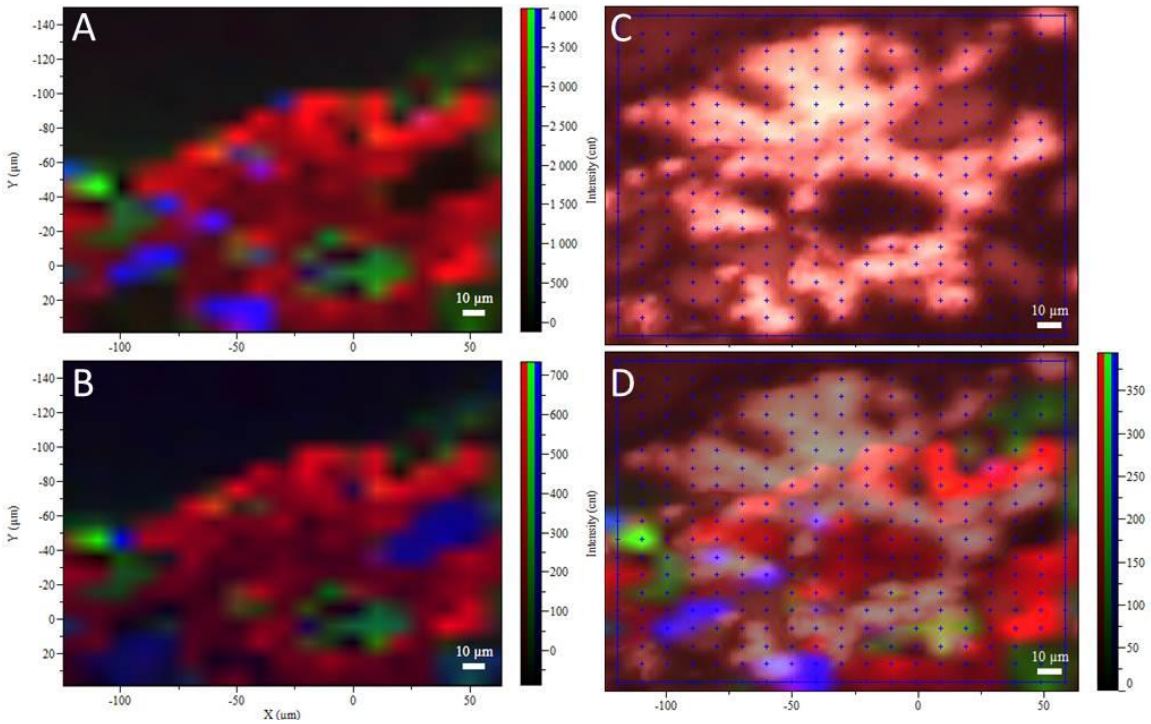

Figure 31: Raman map of a representative, pyrite rich area of the fossilized microbial mat. (A) False color image of the mapped area displaying pyrite in red, quartz in blue and carbon in green. (B) False color image of the mapped area displaying pyrite in red, orthoclase in blue and carbon in green. (C) Video of the mapped area, blue crosses indicate the datapoint position. (D) Stacked image of the video area with indicated datapoint (C) and the false color map (A).

The close association of the carbon matter with the minerals, especially pyrite, confirms the observations of Steiner & Reitner (2001) of a complete pyritization of the microbial mat. They also concluded an early diagenetic sulfide formation induced by bacterial sulfate reduction on the basis of sulfur isotope values. The detection of dolomite with Raman spectroscopy inside the pyrite matrix again confirms the early diagenesis. Dolomite can be distinguished from calcite by a clear band shift of the main carbonate vibration from 1085 cm^{-1} to 1097 cm^{-1}

(Bischoff et al., 1985). Also EDX mappings from a similar area in the pyrite rich layer show comparable patterns with finely dispersed carbon signals (Fig. 32).

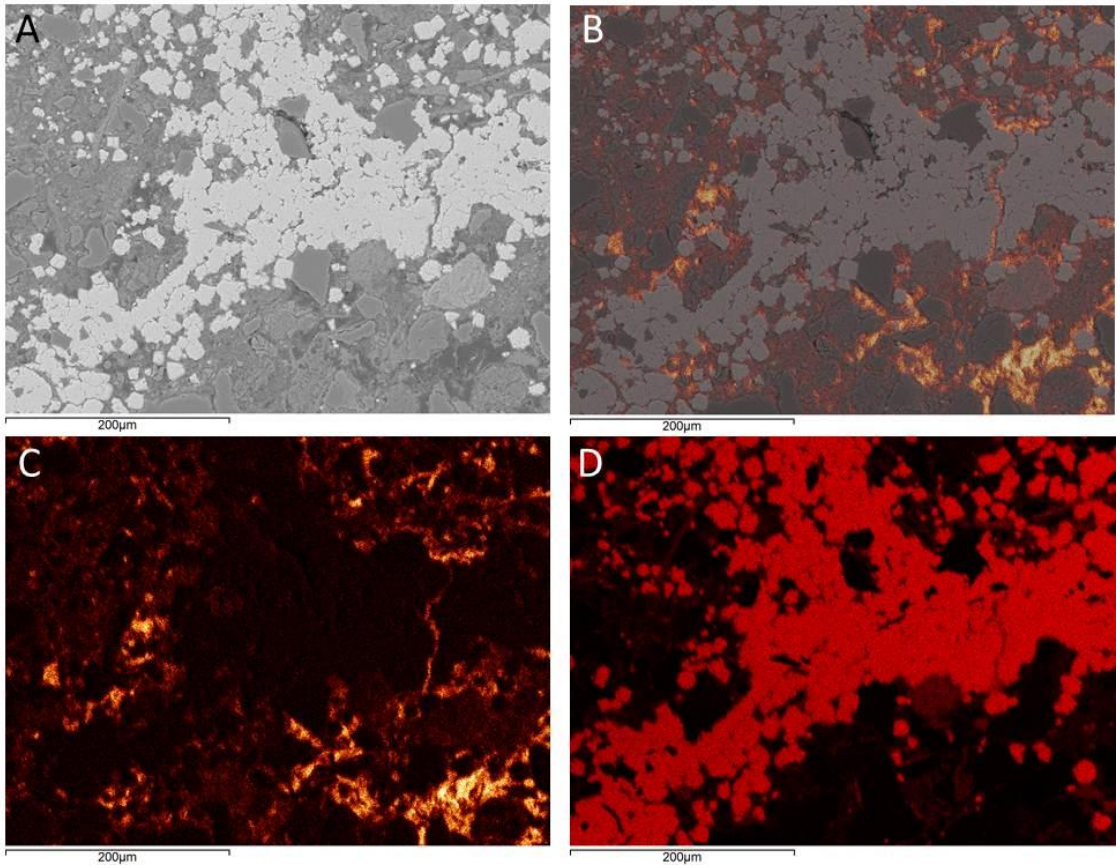

Figure 32: EDX mapping of a representative area of the fossilized microbial mat. (A) Backscatter image showing pyrite in light grey. (B) Combined image of the backscatter image with the carbon signal. Carbon is dispersed inside the microbial mat, but in some areas a high concentration can be noted. (C) EDX mapping of carbon. Some highly concentrated areas of carbonaceous material are displayed. It should be noted that the carbon seems to be associated to the pyrite crystals. (D) EDX mapping of Fe.

For the analysis of the fossil microbial mat described in this chapter, the combined detection of mineral phases and organic molecules was of great importance. The strong association of pyrite with the carbon signal and the probable microbial influence of the hematite formation can serve as an additional support for interpreting the wrinkled elephant skin structure as fossil microbial mats (Hagadorn & Bottjer, 1997; Gehling, 1999).

References

Bischoff, W.D., Sharma, S.K. and MacKenzie, F.T. (1985) Carbonate ion disorder in synthetic and biogenic magnesian calcites; a Raman spectral study. *American Mineralogist* 70: 581-589.

Bower, D.M. (2011) Micro-Raman spectroscopic investigations of mineral assemblages in parallel to bedding laminae in 2.9 Ga sandstones of the Pongola Supergroup, South Africa. *Journal of Raman Spectroscopy* 42: 1626-1633.

Callow, R.H.T. and Brasier, M.D. (2009) Remarkable preservation of microbial mats in Neoproterozoic siliciclastic settings: Implications for Ediacaran taphonomic models. *Earth-Science Reviews* 96: 207-219.

de Faria, D.L.A., Venâncio Silva, S. and de Oliveira, M.T. (1997) Raman microspectroscopy of some iron oxides and oxyhydroxides. *Journal of Raman Spectroscopy* 28: 873-878.

Edwards, H.G.M., Wynn-Williams, D.D. and Villar, S.E.J. (2004) Biological modification of haematite in Antarctic cryptoendolithic communities. *Journal of Raman Spectroscopy* 35: 470-474.

Ehrlich, H.L. (1999) Microbes as Geologic Agents: Their Role in Mineral Formation. *Geomicrobiology Journal* 16: 135-153.

Fedonkin, M.A. (2003) The origin of the Metazoa in the light of the Proterozoic fossil record. *Paleontological Research* 7: 9-41.

Foucher, F. and Westall, F. (2009) Investigating the Oldest Traces of Life by AFM/Confocal Raman Spectroscopy: Applications for the Analysis of Martian Rocks. *AIP Conference Proceedings* 1163: 47-58.

Gehling, J.G. (1999) Microbial mats in terminal Proterozoic siliciclastics; Ediacaran death masks. *PALAIOS* 14: 40-57.

Glamoclija, M., Steele, A., Fries, M., Schieber, J., Voytek, M.A. and Cockell, C.S. (2009) Association of anatase (TiO2) and microbes: Unusual fossilization effect or a potential biosignature? *Geological Society of America Special Papers* 458: 965-975.

Grazhdankin, D. (2004) Patterns of distribution in the Ediacaran biotas: facies versus biogeography and evolution. *Paleobiology* 30: 203-221.

Grazhdankin, D.V. (2003) Structure and Depositional Environment of the Vendian Complex in the Southeastern White Sea Area. *Stratigraphy and Geological Correlation* 11: 313-331.

Hagadorn, J.W. and Bottjer, D.J. (1997) Wrinkle structures: Microbially mediated sedimentary structures common in subtidal siliciclastic settings at the Proterozoic-Phanerozoic transition. *Geology* 25: 1047-1050.

Horiba *Raman Application Note. Raman Data and Analysis: Raman spectroscopy for analysis and monitoring.* http://www.horiba.com/fileadmin/uploads/Scientific/Documents/Raman/bands.pdf

Jubb, A.M. and Allen, H.C. (2010) Vibrational spectroscopic characterization of hematite, maghemite, and magnetite thin films produced by vapor deposition. *ACS Applied Materials and Interfaces* 2: 2804-2812.

Marshall, C.P., Edwards, H.G. and Jehlicka, J. (2010) Understanding the application of Raman spectroscopy to the detection of traces of life. *ASTROBIOLOGY* 10: 229-43.

Martin, M.W., Grazhdankin, D.V., Bowring, S.A., Evans, D.A.D., Fedonkin, M.A. and Kirschvink, J.L. (2000) Age of Neoproterozoic Bilatarian Body and

Trace Fossils, White Sea, Russia: Implications for Metazoan Evolution. *Science* 288: 841-845.

Ohsaka, T., Izumi, F. and Fujiki, Y. (1978) Raman spectrum of anatase, TiO_2. *Journal of Raman Spectroscopy* 7: 321-324.

Pasteris, J.D. and Wopenka, B. (2003) Necessary, but not sufficient: Raman identification of disordered carbon as a signature of ancient life. *ASTROBIOLOGY* 3: 727-38.

Shabtai, Y. and Fleminger, G. (1994) Adsorption of Rhodococcus Strain GIN-1 (NCIMB 40340) on Titanium Dioxide and Coal Fly Ash Particles. *Applied and Environmental Microbiology* 60: 3079-3088.

Smith, E. and Dent, G. (2005) *Modern Raman spectroscopy - A practical approach.* John Wiley & Sons Ltd, West Sussex, England, pp. 210.

Solontsov, L.F., Aksenov, E.M., Andreev, S.P. and Polikarpova, N.T. (1970) To Lithology and Indexation of Sandstone-Siltstone Members and Beds of the Valdai Group in Moscow Syneclise. *Tr. Geol. Inst. (Kazan)* 30: 324-345.

Stankovsky, A., Verichev, J. and Dobeiko, I. (1990) Vendian of the south-eastern White Sea area. In: *The Vendian System, Vol.2*, edited by B. Sokolov and M. Fedonkin, Springer, Berlin, Germany, pp. 76-87.

Stankovsky, A.F., Sinitsin, A.V. and Shinkarev, N.F. (1972) Buried Traps of the Onega peninsula, White Sea Region. *Vestn. Leningr. Univ* 18: 12-20.

Steiner, M. and Reitner, J. (2001) Evidence of organic structures in Ediacara-type fossils and associated microbial mats. *Geology* 29: 1119-1122.

Chapter 6: Cold Seep yellow calcite phases

6.1 General Introduction

In many fossil cold seep carbonates yellow calcite is reported as one of several early diagenetic carbonate cement phases (e.g. Beauchamp & Savard, 1992; Campbell et al., 2002; Peckmann et al., 2002; Barbieri & Cavalazzi, 2005; Himmler et al., 2008). It is always characterized by relatively low $\delta^{13}C$ values between -20 and -40 ‰ (e.g. Campbell et al., 2002; Peckmann et al., 2002; Birgel & Peckmann, 2008; Himmler et al., 2008). In some cases a close association with pyrite is reported (Campbell et al., 2002; Barbieri & Cavalazzi, 2005). Furthermore, these carbonate phases are enriched in lipid biomarkers, compared to other carbonate phases in the respective cold seeps (e.g. Peckmann et al., 2002). Therefore, yellow calcites are regarded to be formed due to microbial activity and can be used among others for recognizing fossil cold seeps. In this regard it is important to have a good method for recognizing the yellow calcites *in situ* before establishing other methods like for example biomarker analyses. For that purpose, several cold seep sites with yellow calcite phases were analyzed with Raman spectroscopy.

6.2 Results and Discussion of the Carboniferous Ganigobis Shale Member

The Ganigobis Shale Member belongs to Dwyka Group sediments, which represent the lowest stratigraphic unit of the Karoo Supergroup (Bangert et al., 1999; Himmler et al., 2008). Inside the Ganigobis Shale Member 24 ash fall horizons are recorded, from which 2 tuff horizons near Ganigobis (southern Namibia) were used for age determination on juvenile magmatic zircons (Bangert et al., 1999). They yield $^{206}Pb/^{238}U$ ages of 302.0 ± 3.0 Ma to 299.2 ± 3.2 Ma designating the Ganigobis Shale Member as Carboniferous (Bangert et al., 1999). The upper part of the formation is dominated by columnar and lenticular limestone deposits which contain four authigenic carbonate phases, microspar, banded/botryoidal cement, yellow calcite and spheroidal calcite, representing fossil hydrocarbon seep carbonates (Himmler et al., 2008).

Raman spectroscopy can give additional information about the carbonate phase. Mainly 3 different kinds of spectra can be distinguished identifying the respective carbonate phase (Fig. 33). The spheroidal calcite (sc) shows clear spectra of a normal calcite with the main symmetric stretching vibration of the CO_3^- molecule at 1084 cm^{-1}, the translational modes at 153 cm^{-1}, the librational modes at 279 cm^{-1} and the in-plane bend at 710 cm^{-1} (cf. Rutt & Nicola, 1974; Bischoff et al., 1985; Urmos et al., 1991) (Fig. 33A, B). Also the weaker bands of the antisymmetric stretch at 1433 cm^{-1} can be observed.

The yellow calcites show the same bands, but the spectra are dominated by very intense bands of stretching vibrations of carbon bonds, centered at 1600 cm^{-1} (G band) and 1350 cm^{-1} (D band). Remarkable is a clear shoulder on the D band centered at 1270 cm^{-1} (Fig. 33A, C, D). Also the second order bands in the higher wavenumber region at 2690, 2940 and 3195 cm^{-1} appear. Here, it should be noted that the band at 2690 cm^{-1} is not the dominating one. Both, the shoulder on the D band and the only small band at 2690 cm^{-1} can be interpreted as a clear indication that these signals are derived from complex organic molecules (Kudryavtsev et al., 2001).

The other carbonate phases give also spectra with both calcite and carbon signal. But here, either no clear domination of one of the two signals is evident, or vibrational bands of the calcite are dominating (Fig. 33E, F, G, H).

That means the microbial influence during the formation of the yellow calcite phase can be demonstrated by the domination of carbon bonds over the calcite signals in the Raman spectra. In the mixed phases which microscopically cannot be allocated to the pure yellow calcite phases, a similar microbial influence is visible, with both calcite and carbon signals. However, the spheroidal calcite phase obviously is a later phase which formed on top or in cracks between the yellow calcite. This is in concordance to the $\delta^{13}C$ data, which are reported to have higher values for the spheroidal calcite and the lowest values in the yellow calcite (Himmler et al., 2008).

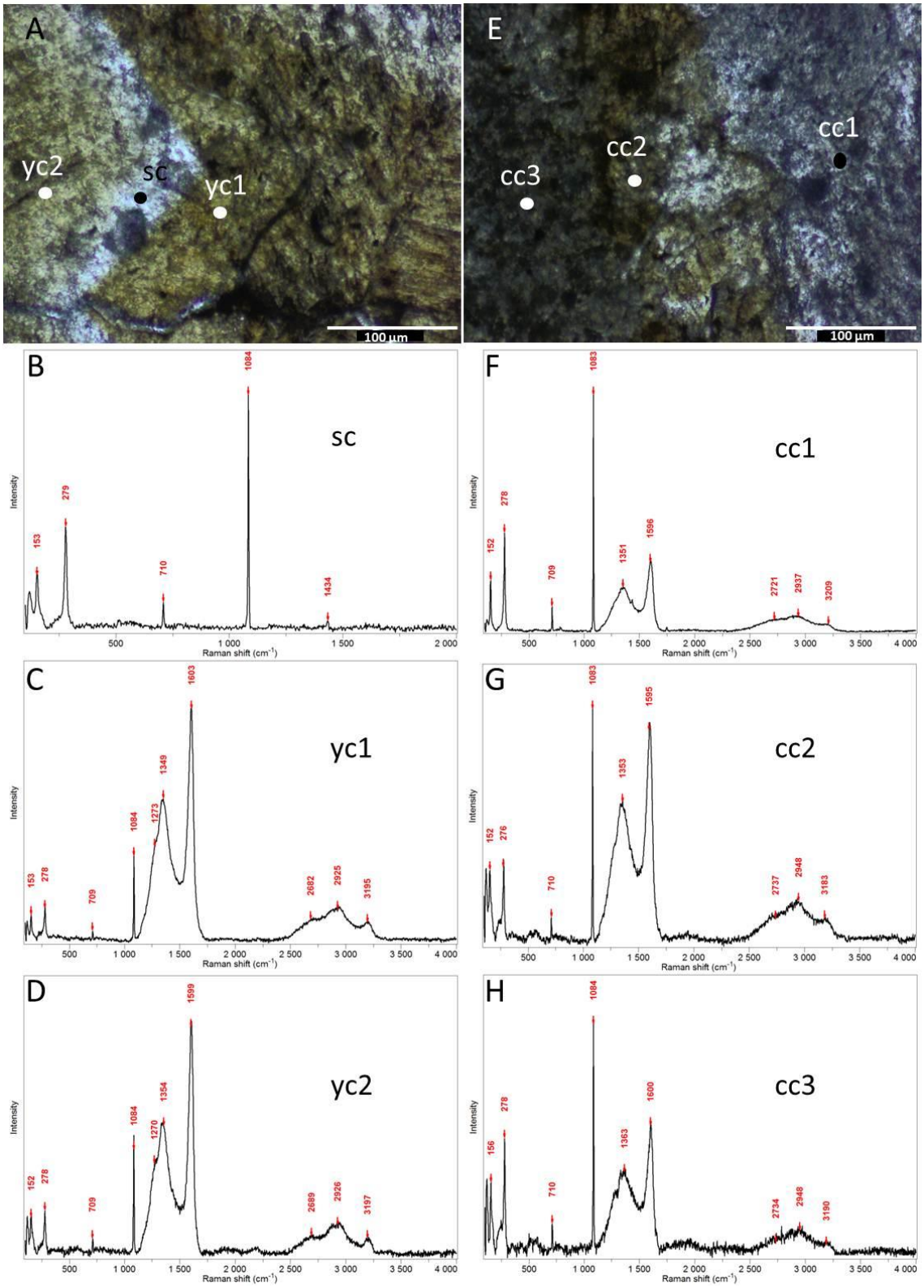

Figure 33: Raman spectra of the different carbonate cements of the Carboniferous Ganigobis Shale Member. In the spheroidal calcite (sc) only calcite vibrations occur. The yellow calcite (yc) is dominated by carbon vibrations, with additional bands of the calcite. In the other carbonate cements (cc) no clear domination of the carbon signal is visible. The marked points in the transmitted light images (A, E) indicate the area where the Raman spectra were recorded.

6.3 Results and Discussion from the Oligocene Lincoln Creek Formation and the Holocene cold seeps from the Black Sea

From the Oligocene cold-seep limestone of the Lincoln Creek Formation (Washington State, USA) similar authigenic carbonate phases are reported as the following common paragenetic sequence: (I) micrite, (II) yellow aragonite and clear aragonite, (III) brownish calcite and (IV) equant calcite spar (Peckmann et al., 2002; Hagemann et al., 2013). Here, the Raman spectra are in many cases highly masked by fluorescence, especially the calcite phases. But most surprisingly the carbonate phases do not show additional carbon bands in their Raman spectra (Fig. 34). In this case that suggests a formation of the carbonate phases due to microbial activity and associated increase of alkalinity. It is likely, that the carbonate phases showing high fluorescence are associated to the microbial activity, which remains are causing the fluorescence itself. Furthermore, small aggregates of framboid pyrite occur, which is partly oxidized to hematite-like iron oxide (Fig. 34C).

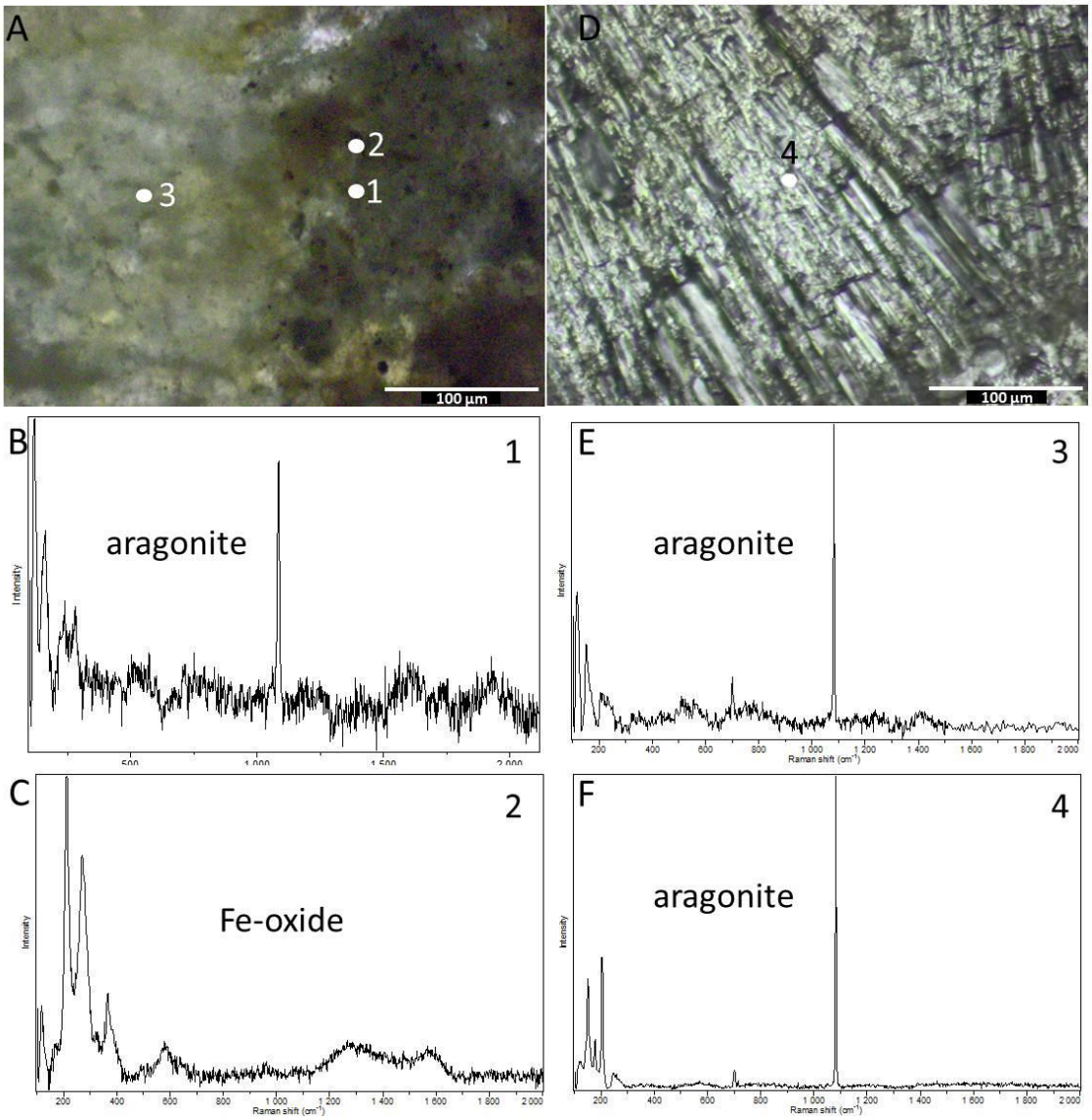

Figure 34: Raman spectra of the cement facies of the Oligocene Lincoln Creek carbonates. Surprisingly no difference between the clear and the yellow phases can be detected. But the spectra are heavily influenced by fluorescence, which can significantly mask the Raman signal. The numbered dots in the transmitted light images (A, D) indicate the area where the Raman spectra were recorded.

Similar results could be obtained for cold-seep carbonates from the Black Sea. The main carbonate phases at this location are: (I) microcrystalline carbonate dominated by High-Mg-calcite and (II) aragonitic cement (Peckmann et al., 2001). Here again only signals from the respective carbonate phase could be observed, or the spectra were completely masked by fluorescence. The strong autofluorescence of the carbonate phases was also reported by Peckmann et al. (2001), even when excited with UV-light. Nevertheless, excitation in this range (244 nm) for Raman spectroscopy could reduce the fluorescent behavior, and even additional carbon and organic bands could be detected (Fig. 35). The

assignment of these bands is not definite, however, it is proposed that the band at 1412 cm^{-1} belongs to vibrations of aromatic units and the bands between 1700 and 1800 cm^{-1} arise due to carboxylic acid (cf. Smith & Dent, 2005). As already mentioned in chapter 1 a differentiation between the carbonate phases (calcite and aragonite) normally is not straightforward with UV excitation. However, the carbonate signal in this example is rather strong and also the band in the higher wavenumber region is clearly visible. As this band occurs at 1462 cm^{-1} and there are two bands visible at 706 and 853 cm^{-1}, it can be assumed that the carbonate phase is aragonite rather than calcite (cf. Frech et al., 1980; Urmos et al., 1991).

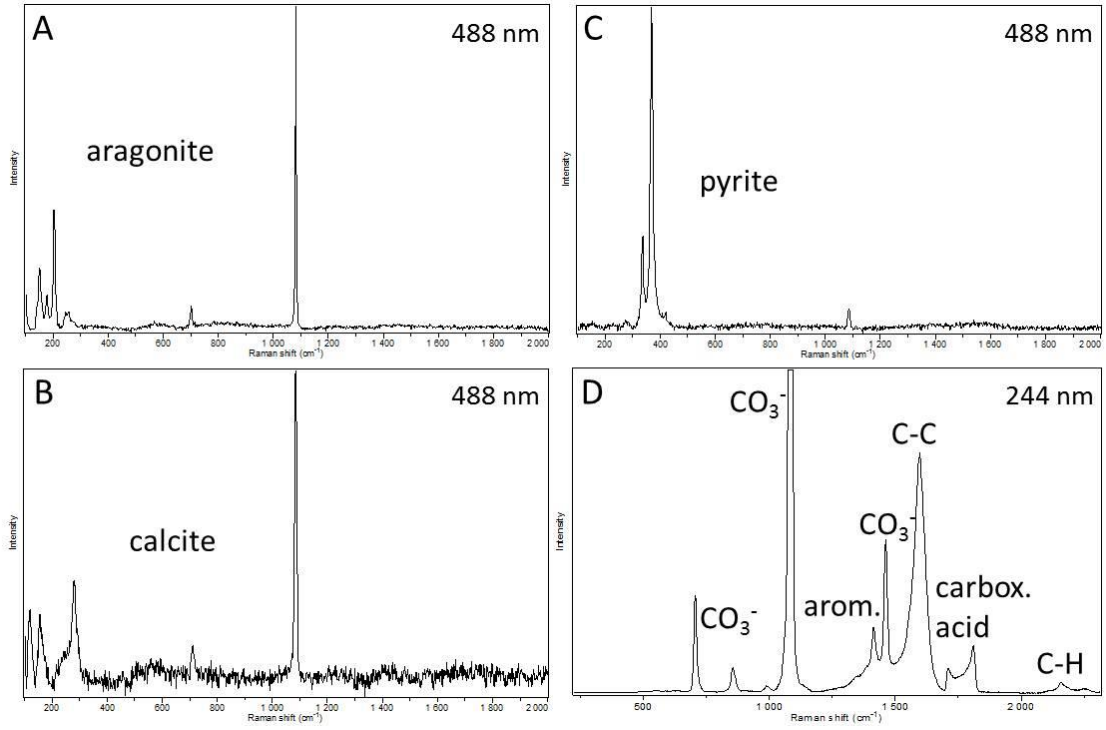

Figure 35: Raman spectra of the cement facies of the Holocene Black Sea cold seep. With 488 nm excitation wavelength aragonite and calcite phases, but no additional carbon could be detected (A, B). Additionally, a typical spectrum of pyrite is shown (C). With excitation in the UV (244 nm) the fluorescence could be reduced and several organic signatures could be detected (D). (arom. = aromatic units; carbox. acid = carboxylic acid).

Interestingly, for the younger cold seep structures of Lincoln Creek and the Black Sea the yellow carbonate phase is aragonite, whereas in older samples it is calcite. Also a much stronger fluorescence behavior can be observed. However, the use of excitation in the UV seems to be a promising tool for gaining additional information on the nature of the organic signatures in the yellow carbonates.

6.4 Results and Discussion for the Ediacaran Doushantou cap carbonates, China

According to the results obtained on the different cement facies of known cold seep carbonates in the following a very similar succession of limestone from the Marionan Doushantuo cap carbonates (South China) was investigated. Cap carbonates are directly related to the severe glaciation processes referred to as “snowball Earth” which have occurred ca. 635 Ma ago (Hoffman et al., 1998; Crowell, 1999; Sohl et al., 1999). The deposition of the carbonates was suspected to be directly linked to the destabilization of methane hydrates during that time on the basis of low $\delta^{13}C$ values (Kennedy et al., 2001; Jiang et al., 2003). However, this hypothesis was questioned by Bristow et al. (2011) on the basis of carbonate clumped isotope data. They came to the conclusion that the deposition of the carbonates was related to hydrothermal fluids more than 1.6 Ma after the deposition of the cap carbonates. However, at least the upper part of the Doushantou cap carbonates is characterized by typical carbonate phases, including yellow calcite, known from other cold seep sides. Additionally, well preserved microbial mats exhibit thrombolytic and stromatolitic structures accompanied by framboid pyrite and phosphate laminae (Reitner et al., 2012). To elucidate the origin of these carbonate phases Raman spectra were recorded in order to compare them with the spectra from the trusted fossil cold seep carbonates (Fig. 36).

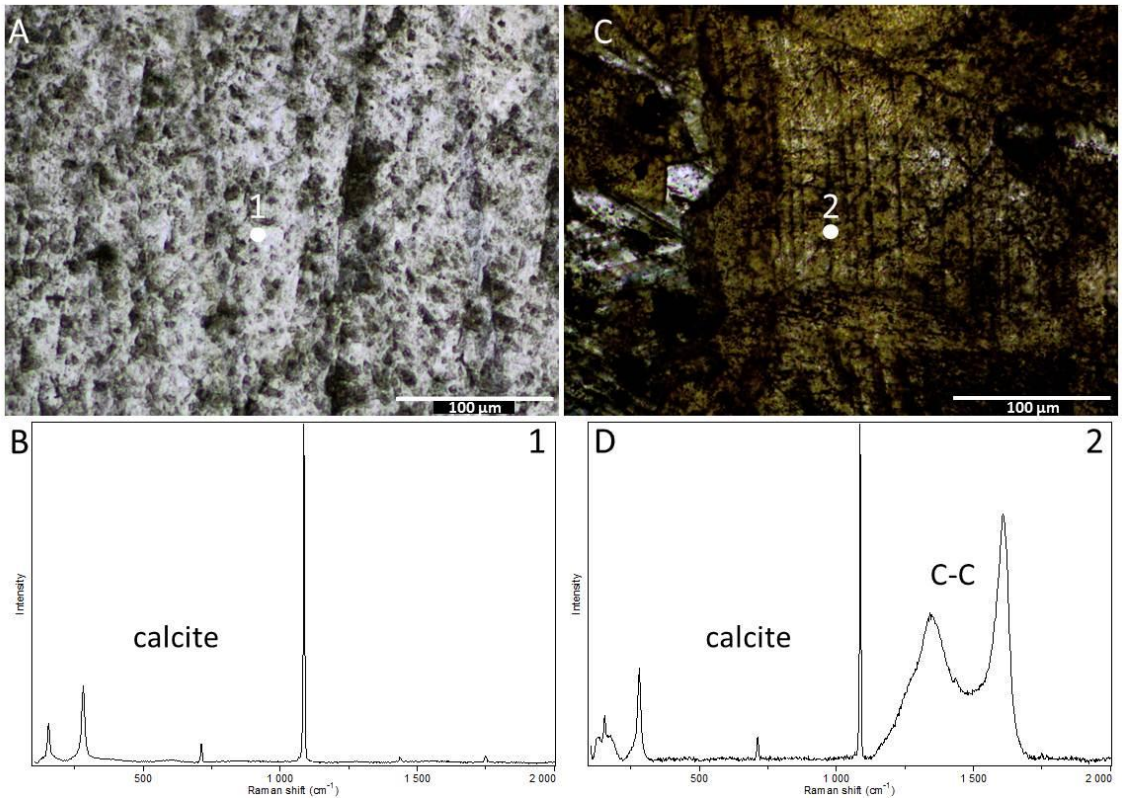

Figure 36: Raman spectra of the Ediacaran cap carbonates. The marked points on the transmitted light images (A,C) indicate the area where the Raman spectra were recorded. A clear differentiation between the clear blocky calcite (A, B) with only calcite signal and the yellow calcite (C, D) with additional carbon bands can be made.

The spectra show a high similarity to the fossil seep sides, with a clear differentiation between the clear, blocky calcite and the yellow calcite. Both phases show typical vibrational modes of calcite with the main band at 1085 cm^{-1}, but only in the yellow calcite additional bands appear. These bands are again typical for disordered carbon centered at 1350 and 1600 cm-^{1} (D and G band) and show both the first and the second order bands. Together with $\delta^{13}C$ values, which also show the typical variations between the clear, blocky calcite and the yellow calcite, with much lower values for the yellow calcite (around -40 ‰) (Reitner et al., 2012; Zhu et al., 2012), this is a clear support for the postulated relation of these carbonates with the collapsing of methane hydrates (Kennedy et al., 2001; Jiang et al., 2003). A direct relation to microbial activity as known from fossil cold seeps, however, is not yet assured. For that purpose, additional biomarker analysis revealing signatures of archaea and anaerobic bacteria with low $\delta^{13}C$ values would be needed. Unfortunately so far only appropriate data for the lower parts of the Doushantou cap carbonates were reported (Reitner et al., 2012). Nevertheless, the Raman analysis already

showed a good concordance with other carbonate phases of fossil cold seep sites.

References

Bangert, B., Stollhofen, H., Lorenz, V. and Armstrong, R. (1999) The geochronology and significance of ash-fall tuffs in the glaciogenic Carboniferous-Permian Dwyka Group of Namibia and South Africa. *Journal of African Earth Sciences* 29: 33-49.

Barbieri, R. and Cavalazzi, B. (2005) Microbial fabrics from Neogene cold seep carbonates, Northern Apennine, Italy. *Palaeogeography, Palaeoclimatology, Palaeoecology* 227: 143-155.

Beauchamp, B. and Savard, M. (1992) Cretaceous chemosynthetic carbonate mounds in the Canadian Arctic. *PALAIOS* 7: 434-450.

Birgel, D. and Peckmann, J. (2008) Aerobic methanotrophy at ancient marine methane seeps: A synthesis. *Organic Geochemistry* 39: 1659-1667.

Bischoff, W.D., Sharma, S.K. and MacKenzie, F.T. (1985) Carbonate ion disorder in synthetic and biogenic magnesian calcites; a Raman spectral study. *American Mineralogist* 70: 581-589.

Bristow, T.F., Bonifacie, M., Derkowski, A., Eiler, J.M. and Grotzinger, J.P. (2011) A hydrothermal origin for isotopically anomalous cap dolostone cements from south China. *Nature* 474: 68-71.

Campbell, K.A., Farmer, J.D. and Des Marais, D. (2002) Ancient hydrocarbon seeps from the Mesozoic convergent margin of California: carbonate geochemistry, fluids and palaeoenvironments. *Geofluids* 2: 63-94.

Crowell, J.C. (1999) Pre-Mesozoic Ice Ages: Their Bearing on Understanding the Climate System. *Geological Society of America Memoirs* 192: 1-112.

Frech, R., Wang, E.C. and Bates, J. (1980) I. R. and Raman Spectra of $CaCO_3$ (Aragonite). *Spectrochimica Acta Part A: Molecular Spectroscopy* 36: 915-920.

Hagemann, A., Leefmann, T.I.M., Peckmann, J., Hoffmann, V.-E. and Thiel, V. (2013) Biomarkers from individual carbonate phases of an Oligocene cold-seep deposit, Washington State, USA. *Lethaia* 46: 7-18.

Himmler, T., Freiwald, A., Stollhofen, H. and Peckmann, J. (2008) Late Carboniferous hydrocarbon-seep carbonates from the glaciomarine Dwyka Group, southern Namibia. *Palaeogeography, Palaeoclimatology, Palaeoecology* 257: 185-197.

Hoffman, P.F., Kaufman, A.J., Halverson, G.P. and Schrag, D.P. (1998) A Neoproterozoic Snowball Earth. *Science* 281: 1342-1346.

Jiang, G., Kennedy, M.J. and Christie-Blick, N. (2003) Stable isotopic evidence for methane seeps in Neoproterozoic postglacial cap carbonates. *Nature* 426: 822-826.

Kennedy, M.J., Christie-Blick, N. and Sohl, L.E. (2001) Are Proterozoic cap carbonates and isotopic excursions a record of gas hydrate destabilization following Earth's coldest intervals? *Geology* 29: 443-446.

Kudryavtsev, A.B., Schopf, J.W., Agresti, D.G. and Wdowiak, T.J. (2001) In situ laser-Raman imagery of Precambrian microscopic fossils. *Proceedings of the National Academy of Sciences* 98: 823-826.

Peckmann, J., Goedert, J.L., Thiel, V., Michaelis, W. and Reitner, J. (2002) A comprehensive approach to the study of methane-seep deposits from the Lincoln Creek Formation, western Washington State, USA. *Sedimentology* 49: 855-873.

Peckmann, J., Reimer, A., Luth, U., Luth, C., Hansen, B.T., Heinicke, C., Hoefs, J. and Reitner, J. (2001) Methane-derived carbonates and authigenic pyrite from the northwestern Black Sea. *Marine Geology* 177: 129-150.

Reitner, J., Zhu, M., Lu, M., He, T., Duda, J.P., Schäfer, N., Hansen, B.T. and Blumenberg, M. (2012) Cap carbonate related microbial biosignatures - facts and myths. *29th IAS Meeting of Sedimentology*, Schladming, Austria.

Rutt, H.N. and Nicola, J.H. (1974) Raman spectra of carbonates of calcite structure. *Journal of Physics C: Solid State Physics* 7: 4522-4528.

Smith, E. and Dent, G. (2005) *Modern Raman spectroscopy - A practical approach*. John Wiley & Sons Ltd, West Sussex, England, pp. 210.

Sohl, L.E., Christie-Blick, N. and Kent, D.V. (1999) Paleomagnetic polarity reversals in Marinoan (ca. 600 Ma) glacial deposits of Australia: Implications for the duration of low-latitude glaciation in Neoproterozoic time. *Geological Society of America Bulletin* 111: 1120-1139.

Urmos, J., Sharma, S.K. and Mackenzie, F.T. (1991) Characterization of some biogenic carbonates with Raman spectroscopy. *American Mineralogist* 76: 641-646.

Zhu, M., Lu, M., Reitner, J. and He, T. (2012) The cap carbonate conundrum: timing of the methane seeps and deglaciation of the snowball Earth. *34th International Geological Congress*, Brisbane, Australia.

6.5. Introduction to the Albian pockmark field of the Basque-Cantabrian Basin

In deep-water sediments of the Albian Black Flysch Group in the Basque-Cantabrian Basin (western Pyrenees) a pockmark field and related authigenic carbonates together with fossil fauna were investigated and identified as a fossil methane-seepage site. For this purpose, Raman spectroscopy was again used for discriminating the different authigenic carbonate phases which are: (I) pyrite-rich micrite, (II) yellow calcite, (III) short fibrous calcite, (IV) dolomite and (V) calcite spar (equant calcite). Furthermore, clear distinctions between the carbon signal in the authigenic carbonates and of pyrobitumen could be made.

6.5.1

Outcrop analogues of pockmarks and associated methane-seep carbonates: A case study from the Lower Cretaceous (Albian) of the Basque-Cantabrian Basin, western Pyrenees

Luis M. Agirrezabala[a], Steffen Kiel[b], Martin Blumenberg[b],
Nadine Schäfer[b], Joachim Reitner[b]

In Press in Palaeogeography, Palaeoclimatology, Palaeoecology 2013

a Estratigrafia eta Paleontologia Saila, Euskal Herriko Unibertsitatea UPV/EHU, 644 P.K., 48080 Bilbo, The Basque Country, Spain
b Georg-August University, Göttingen Geoscience Center, Geobiology Group, Goldschmidtstr. 3, 37077 Göttingen, Germany

Abstract

Late Albian deep-water sediments of the Black Flysch Group in the Basque-Cantabrian Basin (western Pyrenees) preserve a fossil pockmark field including methane seep carbonates and associated macrofauna. The geometry of the pockmarks is reconstructed from repeated lens-shaped turbidite deposits with centrally located carbonate bodies. Early diagenetic carbonate phases such as

clotted micrite and yellow calcite with $\delta^{13}C$ values as low as −41.6‰, and hydrocarbon biomarkers (e.g. 2,6,10,15,19-pentamethylicosane) with strong depletions in ^{13}C indicate that the carbonates precipitated due to anaerobic oxidation of methane. The pockmarks probably formed due to subsidence induced by dewatering and degassing of the gas-charged seabed perhaps enhanced by the weight of the carbonate bodies. The macrofauna resembles that of other late Mesozoic deep-water methane-seeps world-wide, and is dominated by large lucinid and Caspiconcha bivalves, and hokkaidoconchid gastropods. During late diagenesis the carbonate $\delta^{18}O$ values were reset to a narrow range of −12 to −10‰, the remaining pore spaces and fissures were filled with pyrobitumen, and additional carbonate phases precipitated, potentially due to thermochemical sulfate reduction processes.

6.5.1.1 Introduction

Methane seepage on the seafloor is often associated with pockmarks: craters resulting from the rapid expulsion of water and/or gas through the seabed. When seepage of methane-rich fluids continues after the initial expulsion it can fuel distinctive communities of chemosymbiotic animals such as siboglinid tube worms, bathymodiolin mussels and vesicomyid clams (Hovland et al., 1987; Dando et al., 1991; Ondréas et al., 2005; Sahling et al., 2008). Furthermore, the anaerobic oxidation of the methane (AOM) mediated by microbial consortia results in the precipitation of carbonates with characteristic petrographic and geochemical features (Hovland et al., 1985; Peckmann et al., 2001; Peckmann & Thiel, 2004) and forms the hardground for the associated macrofauna.

Pockmarks are concave depressions with different sizes, ranging from 1 to 700 m in width and several centimeters to 45 m in depth (Hovland et al., 2002), although larger ones can result from the agglomeration of several pockmarks. They were first discovered on the Scotian shelf (King & MacLean, 1970) and subsequent mapping of the seabed confirmed their occurrences in most oceans and seas (Judd & Hovland, 2007). They occur on both passive and active continental margins at various depths and geodynamic contexts, where fluids discharge upward through muddy seabed sediments (Hovland & Judd, 1988). Many pockmarks are related to methane cold seepage, but pockmarks formed

by hydrothermal fluid flows have also been described in volcanic areas (Pickrill, 1993).

Fossil methane seep communities range back into Devonian time and have been reported from ancient forearc, backarc, and continental shelf settings (Goedert & Squires, 1990; Gaillard et al., 1992; Peckmann et al., 1999; Majima et al., 2005; Campbell, 2006; Metz, 2010). Although ancient pockmarks have been recorded in seismic profiles from different continental margins (Hovland, 1982; Cole et al., 2000; Gemmer et al., 2002; Andresen et al., 2008), there is only one example of cropping ancient pockmarks (Hovland, 1989). In this paper we present a multidisciplinary study (sedimentology, petrology, paleontology and geochemistry) of Cretaceous pockmarks and related authigenic carbonates and fossil fauna cropping out in the northern margin of the Basque-Cantabrian Basin. The excellent exposure of these ancient pockmarks on a present-day wave-cut platform and adjacent seacliffs allowed examination of the entire seep system, including the sub-seabottom plumbing system, on a lamina by lamina resolution that is 2 to 3 orders of magnitude better than state-of-the-art seismic profiles.

6.5.1.2 Geological setting

The studied paleo-pockmarks and lenticular authigenic carbonate bodies crop out within Albian rocks of the northern margin of the Mesozoic Basque-Cantabrian Basin between the villages of Ispaster and Ea (Fig. 37). The Basque-Cantabrian Basin originated by rifting related to the Cretaceous opening of the Bay of Biscay and the eastward drift of the Iberian microplate (Montadert et al., 1974). During the mid-Cretaceous, the basin was affected by an extensional phase in the context of oblique to strike-slip tectonics (Reitner, 1987; García-Mondéjar et al., 1996). This extension led to crustal thinning below the basin (Pedreira et al., 2003), low pressure/high temperature metamorphism associated to main faults (e.g. Montigny et al., 1986), intrusive and effusive magmatism (Rossy, 1988; Castañares et al., 2001) and the formation of hydrothermal deposits (Aranburu et al., 2002; Agirrezabala, 2009). Coeval extensional tectonics created numerous fault-bordered, confined sub-basins filled with deep-water slope deposits (Agirrezabala & García-Mondéjar,

1994; Agirrezabala, 1996). These deposits constitute the Black Flysch Group (Middle Albian–Early Cenomanian), a thick and widespread organic-rich unit cropping out along the Pyrenean domain (Souquet et al., 1985).

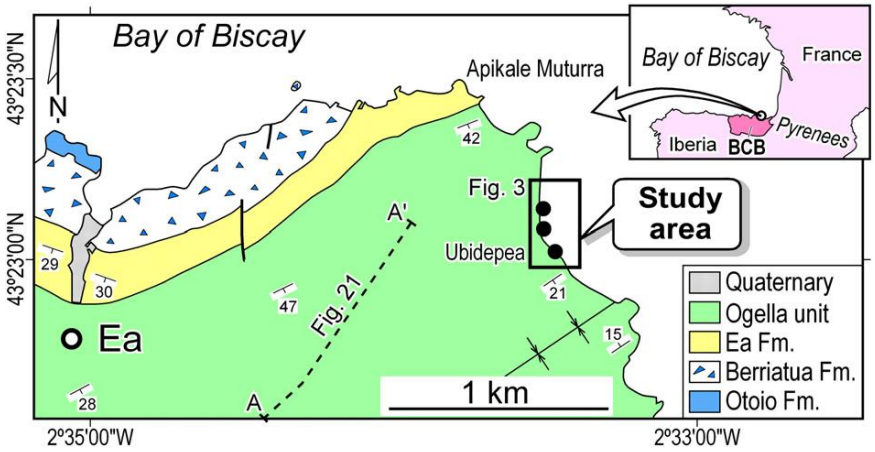

Figure 37: Locality map with generalized geology of the study area; paleo-pockmark and seep carbonate outcrops indicated by black dots. BCB: Basque-Cantabrian Basin.

In the Ispaster area, the Black Flysch Group is underlain by the Otoio Formation (Figs. 37 and 38), which is composed of deltaic siliciclastic deposits as well as shallow-water carbonates rich in fossils (orbitolinids, rudists, algae, corals, etc., cf., Agirrezabala, 1996). The Black Flysch Group itself is subdivided into three lithostratigraphic units and the uppermost of these, the Ogella unit, includes the paleo-pockmarks and carbonates reported here (Figs. 37 and 38). The Ogella unit is composed mainly of alternating mudstones and thin-bedded sandstones deposited in a southwest-facing distal turbiditic slope (Agirrezabala, 1996). The authigenic carbonate bodies occur in a 43 m thick informal sub-unit, named Ubidepea mudstone, where they are concentrated in two discrete intervals (A and B in Figs. 38 and 39) separated by carbonate-free intervening deposits. The intervals A and B are much richer in mudstone (mudstone to sandstone ratio >8:1) than the underlying, overlying and intervening deposits (approximate ratio 3:1) (Fig. 38). The Ubidepea mudstone is dated as Late Albian *Callihoplites auritus–Hysteroceras varicosum* ammonite Subzones (*Mortoniceras inflatum* Zone of the European province zonation), based on the occurrence of the ammonites *Elobiceras* (*Craginites*), *Elobiceras* sp., *Hysteroceras* cf. *choffati* Spath, *Hysteroceras* cf. *bucklandi* Spath, *Mortoniceras* (*Mortoniceras*) gr. *inflatum*, *Mortoniceras* (*Mortoniceras*), *Hysteroceras* sp. and *Hemiptychoceras* sp.

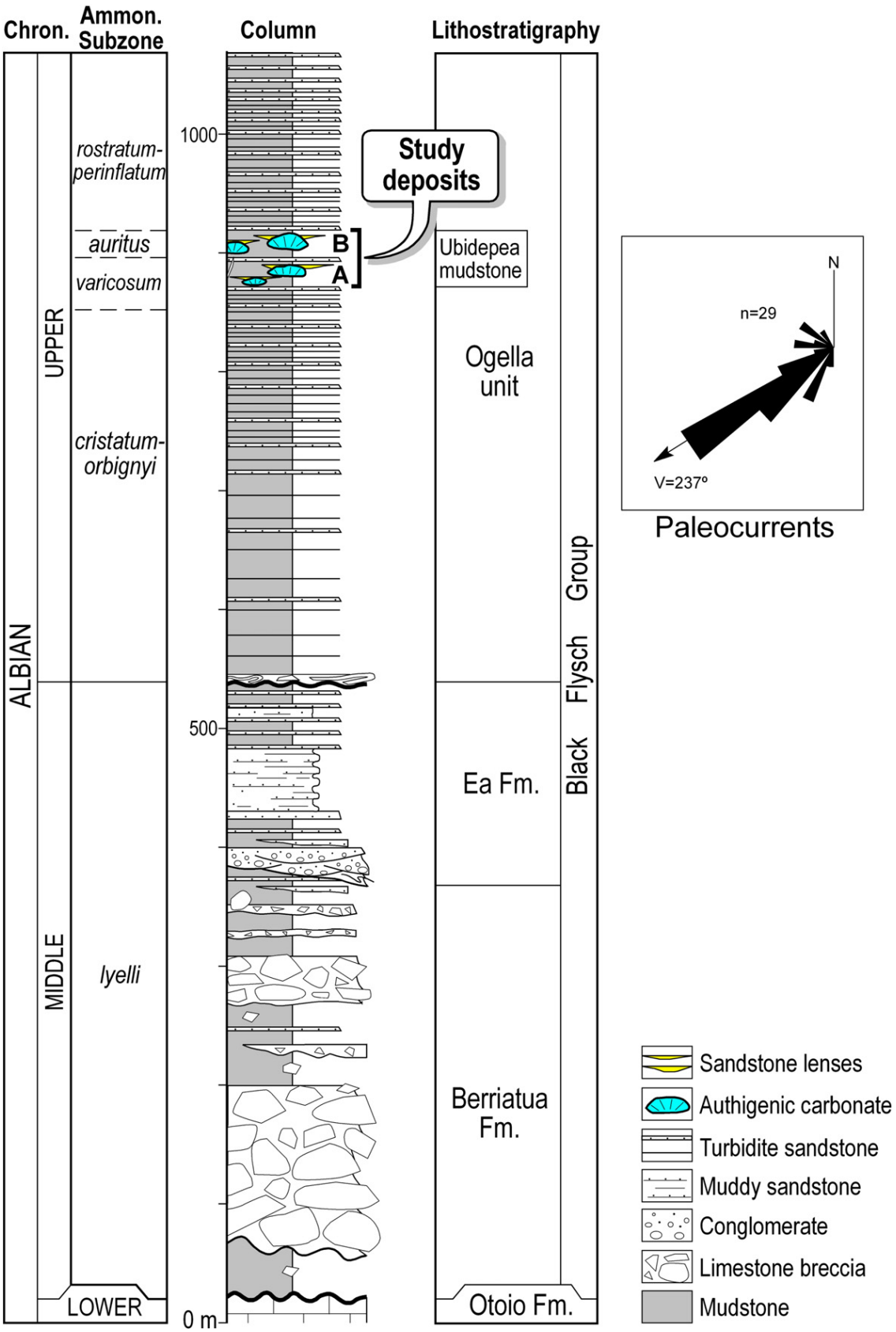

Figure 38: Stratigraphy and lithology in the Ispaster-Ea area; inset on the right shows paleocurrents measured in the Ogella unit.

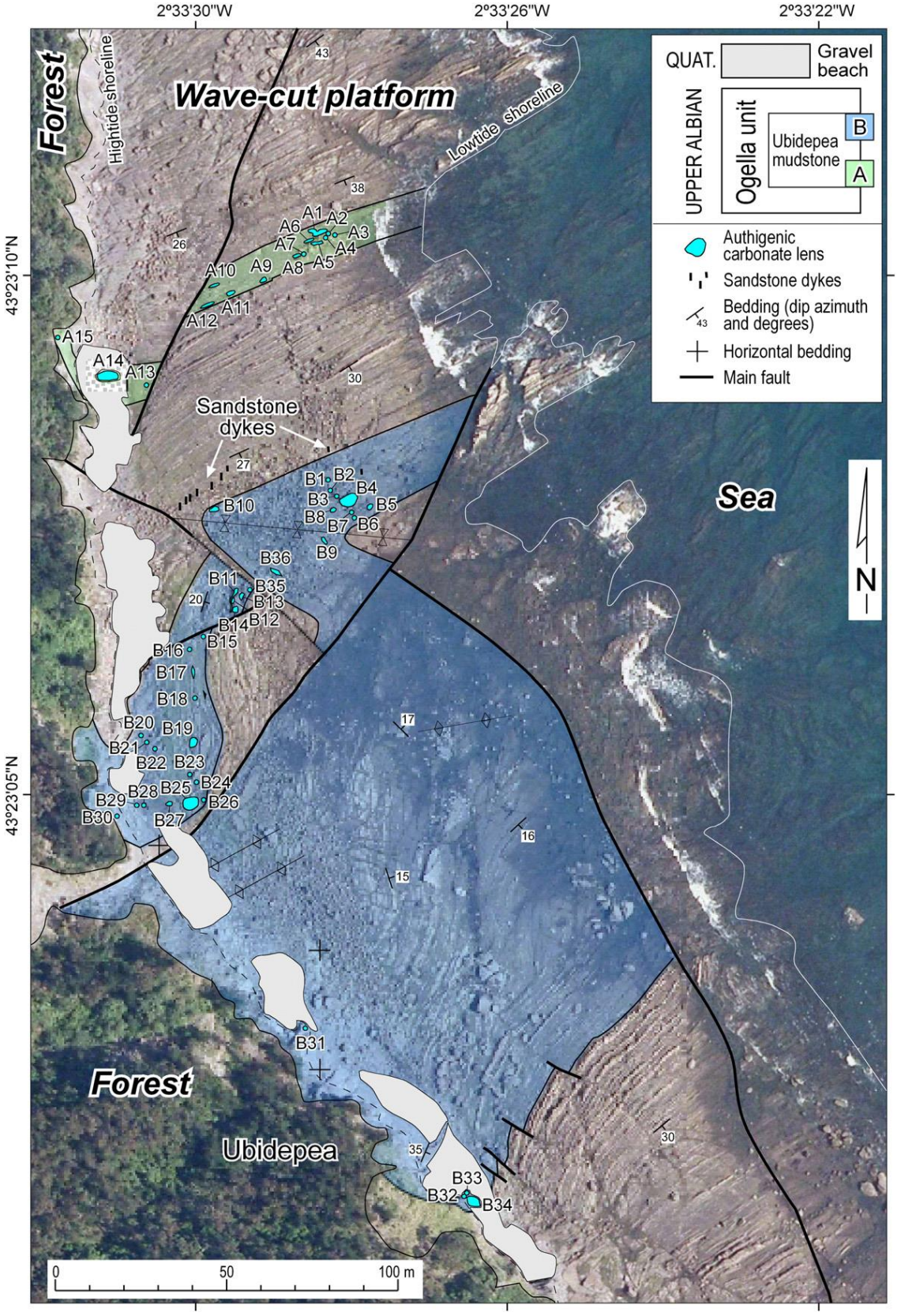

Figure 39: Combined aerial photo and geological map of the studied sea-cliffs and wave-cut platform of Apikale Muturra; this area is indicated on Fig. 37. Mapped are the A and B intervals, individual authigenic carbonate lenses (A1–15 and B1–36) and sandstone dykes. Orthophoto source: PNOA©Instituto Geográfico Nacional de España (Eusko Jaurlaritza).

6.5.1.3 Methods

The study area has been mapped on a 1:1000 orthophoto map. Field descriptions of authigenic carbonates and hosting deposits have been carried out. Elaboration of very detailed stratigraphic columns and their high-resolution (lamina-by-lamina) correlations allowed constructing detailed stratigraphic cross-sections of selected areas in order to characterize geometric relationships between authigenic carbonates and host deposits. Measurements of palaeocurrents and attitudes of sandstone dykes were plotted with the Stereonet v.6.x Program (Allmendinger, 2002). A non-migrated commercial seismic profile (ENIEPSA Company, line BR-51) with static corrections (topographic elevation) has been used to illustrate the subsurface geology of the area. Applied seismic velocities for time-to-depth conversion were obtained from a nearby commercial well (Gaviota field; Huedo-Cuesta et al., 2009).

6.5.1.3.1 Petrography and stable isotopes

A total of 79 thin sections were examined under plane-polarized, cross-polarized, reflected, cathodoluminescence and ultraviolet light microscopy. We observed thin sections using a white background and reflected light in order to distinguish carbonates containing pyrite from those containing organic matter, each of which shows a characteristic reflection pattern (Folk, 1987). 20 thin sections were also stained with potassium ferricyanide and alizarin red to differentiate between carbonate mineral phases. X-ray diffraction (XRD) of six powdered mineral samples was carried out using an automated PANalytical Xpert PRO diffractometer (PANalytical, Eindhoven, The Netherlands) at the Euskal Herriko Unibertsitatea. Semi-quantitative estimates were made from peak areas on XRD patterns (Schultz, 1964). 37 samples of volumetrically major carbonate cements were selected for oxygen and carbon isotope analyses. They were taken from polished blocks using a hand-held microdrill under a binocular microscope. Extraction of CO_2 from each sample followed standard techniques (McCrea, 1950; Craig, 1957) and was performed by reaction with orthophosphoric acid (90 °C), and analyzed in an ISOCARB device attached to a VG-Isotech SIRA-II™ mass spectrometer (both VG Isogas

Co., Middlewich, United Kingdom) at the Universidad de Salamanca. Accuracy was monitored by repeated analysis of both internal and international (NBS-19) carbonate standards under identical analytical conditions. Isotope results are given in the delta notation relative to the Vienna Pee Dee Belemnite (VPDB) standard. Additionally, eleven carbonates samples were analyzed for $\delta^{18}O$ and $\delta^{13}C$ at the University of Göttingen. Details about the analytical procedure can be found elsewhere (Reitner et al., 2005). For both carbon and oxygen, laboratory precision was better than ± 0.2‰. Organic carbon samples for stable isotope determinations were combusted with a EuroVector elemental analyzer linked to an ISOPRIME (GV Instruments LTD, Manchester, UK). Cathodoluminescence investigations were carried out with a Citl 8200 MK3A cold cathode mounted on a Zeiss Axiolab microscope. Micrographs were recorded at 20 kv voltage using a cooled SPOT-CCD camera (see Reitner et al., 2005 for a more detailed description).

6.5.1.3.2 Raman spectroscopy

Raman spectroscopy was performed on a polished thin section, in order to characterize the mineralogical and organic phases in the sample. Raman spectra were recorded using a confocal Horiba Jobin-Yvon LabRam-HR 800 UV Raman spectrometer with attached Olympus BX41 microscope. The excitation wavelength was the 488 nm line of an Argon Ion Laser (Melles Griot IMA 106020B0S) with a laser power of 20 mW. A detailed description of the spectrometer is given in Beimforde et al. (2011). All spectra were recorded and processed using LabSpec™ version 5.19.17 (Horiba Jobin-Yvon, Villeneuve d'Ascq, France). The minerals were identified on the basis of the Horiba Jobin-Yvon database for minerals and reference spectra collected on mineral specimens of the Geoscience Museum of the Georg-August University Göttingen.

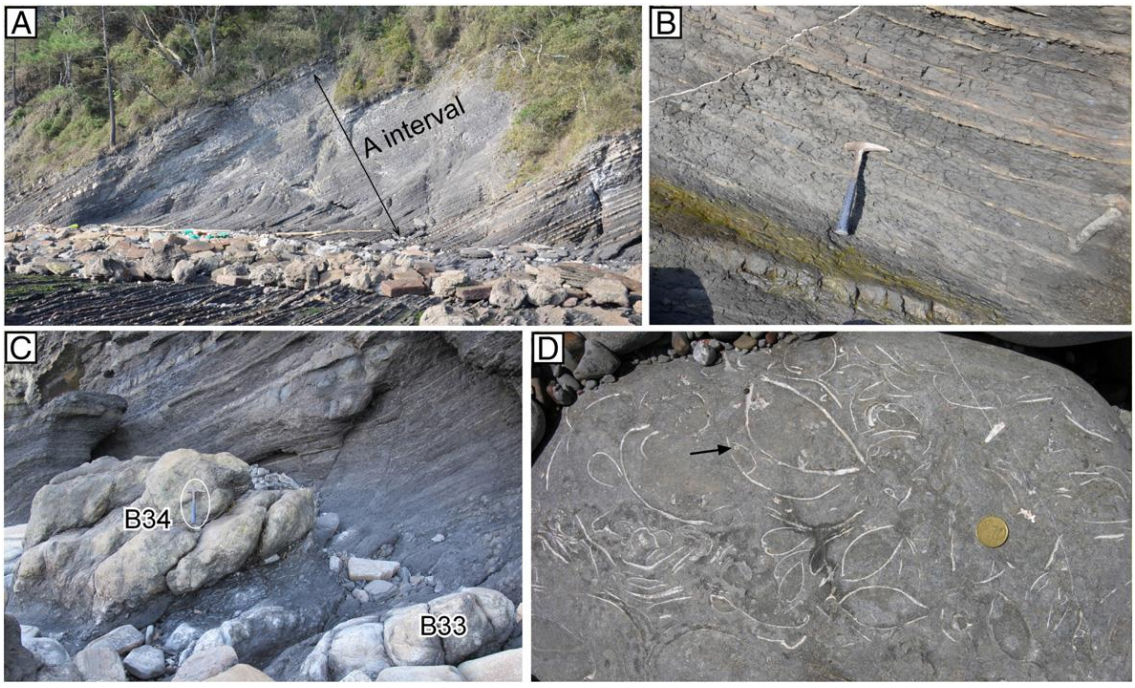

Figure 40: Field photographs of the sedimentary facies. (A) Interval A dominated by mudstone and thin-bedded sandstone facies; note the abundance of mudstone compared to the underlying and overlying deposits. (B) Detail of the mudstone and thin-bedded sandstones; note the tubular carbonate concretion on the right side. (C) Carbonate lenses (B33 and B34) embedded in mudstones (encircled hammer for scale). (D) Detail of carbonate lens enclosing abundant fossils of articulated and disarticulated bivalves and one small coral (arrow); coin for scale (20 mm).

6.5.1.3.3 Biomarker analysis

Two representative carbonates including all major carbonate facies were used for hydrocarbon biomarker studies. For the first, about 100 g carbonate was crushed and powdered using a pebble mill (Retsch MM 301). To reduce the expected yield of pyrobitumen and to enrich intracrystalline hydrocarbons, a second piece (~100 g) was pre-crushed and pre-extracted with dichloromethane (DCM; 2×) before powdering as described above. The grounded samples were extracted with distilled DCM (DCM; 2×; ~100 ml each), DCM/methanol (1/1; v/v; 1×; 100 ml), and methanol (1×; 100 ml) using ultrasonics. Extracts were combined and concentrated in a pre-cleaned rotary evaporator, followed by reduction of the solvent to near dryness in a stream of N_2. The resulting total extracts were separated by column chromatography into a saturated fraction (F1) and an aromatic fraction (F2). Saturated (F1) and aromatic (F2) hydrocarbons were analyzed by combined gas chromatography–mass spectrometry (GC–MS) using a Varian CP-3800 gas chromatograph

coupled to a Varian 1200 L mass spectrometer. Biomarkers were identified by comparing mass spectra and retention times with published data and/or reference compounds. The $\delta^{13}C$-values of hydrocarbons were analyzed (minimum of two replicates) using a Thermo Scientific Trace GC coupled to a Delta Plus isotope-ratio MS (GC-IRMS). The stable carbon isotope compositions are reported in the delta notation ($\delta^{13}C$) vs. the V-PDB standard. Standard deviations for $\delta^{13}C$ analyses were generally less than 1‰ and sometimes higher due to poor peak separation or influences from co-eluting unresolved complex mixtures. Details on column chromatography, GC–MS and GC-IRMS can be found elsewhere (Blumenberg et al., 2012).

6.5.1.4 Sedimentary facies and geometry

6.5.1.4.1 Sedimentary facies description

Four sedimentary facies can be distinguished in the studied section: carbonate lenses, mudstones and thin-bedded sandstones, tephra laminas and sandstone dykes (Fig. 40).

6.5.1.4.1.1 Carbonate lenses

51 carbonate lenses wider and thicker than 50 cm have been mapped in the study area (Fig. 39). They occur as irregular, massive, mainly micritic lenticular bodies hosted in recessive mudstones and thin-bedded sandstones (Fig. 40C). Individual lenses are up to 2.5 m thick and 8 m wide, show an approximate circular shape in planar view, and some lenses constitute clusters composed of up to eight individual bodies. The contact between the carbonate lenses and the embedding rock is mostly sharp, but occasionally there are gradual contacts composed of carbonate concretions. The carbonate lenses will be described in more detail below.

6.5.1.4.1.2 Mudstones and thin-bedded sandstones

This facies is composed of dark grey mudstones alternating commonly with very thin to thin fine-grained sandstone beds (Fig. 40A–C). Mudstones may contain scattered carbonate concretions and show TOC values up to 0.95%. Individual sandstone beds are commonly tabular with thicknesses between 0.5 and 2 cm, but show lens-shaped geometries and thicknesses up to 42 cm near the carbonate bodies. The mudstone to sandstone ratio is usually higher than 8:1. Sandstone beds show sharp bases with sole marks and internally display Bouma Tbc and Tc divisions. Measuring of sole marks from beds of the study interval and Ogella unit indicates a mean paleocurrent toward N237E (Fig. 38). Scattered ammonites and belemnites are present, but no benthic macrofossils. These deposits are similar to facies C2.3 of Pickering et al. (1986) and are here considered the deposit of low-density turbidity currents and probably hemipelagic sedimentation.

6.5.1.4.1.3 Tephra laminae

Scarce tephra laminae occur within the mudstones (Agirrezabala, 1996). They are light greenish, tabular lamina composed only of altered volcaniclastic particles of sand to pebble sizes and very angular shapes. They exhibit great extension and sharp bases and tops, show either no internal structure or normal grading, and their tops are commonly bioturbated. The tephra laminae are here interpreted as submarine pyroclastic tephra deposited from the fallout of ash and lapilli. In the case of the largest fragments ballistic trajectories are likely.

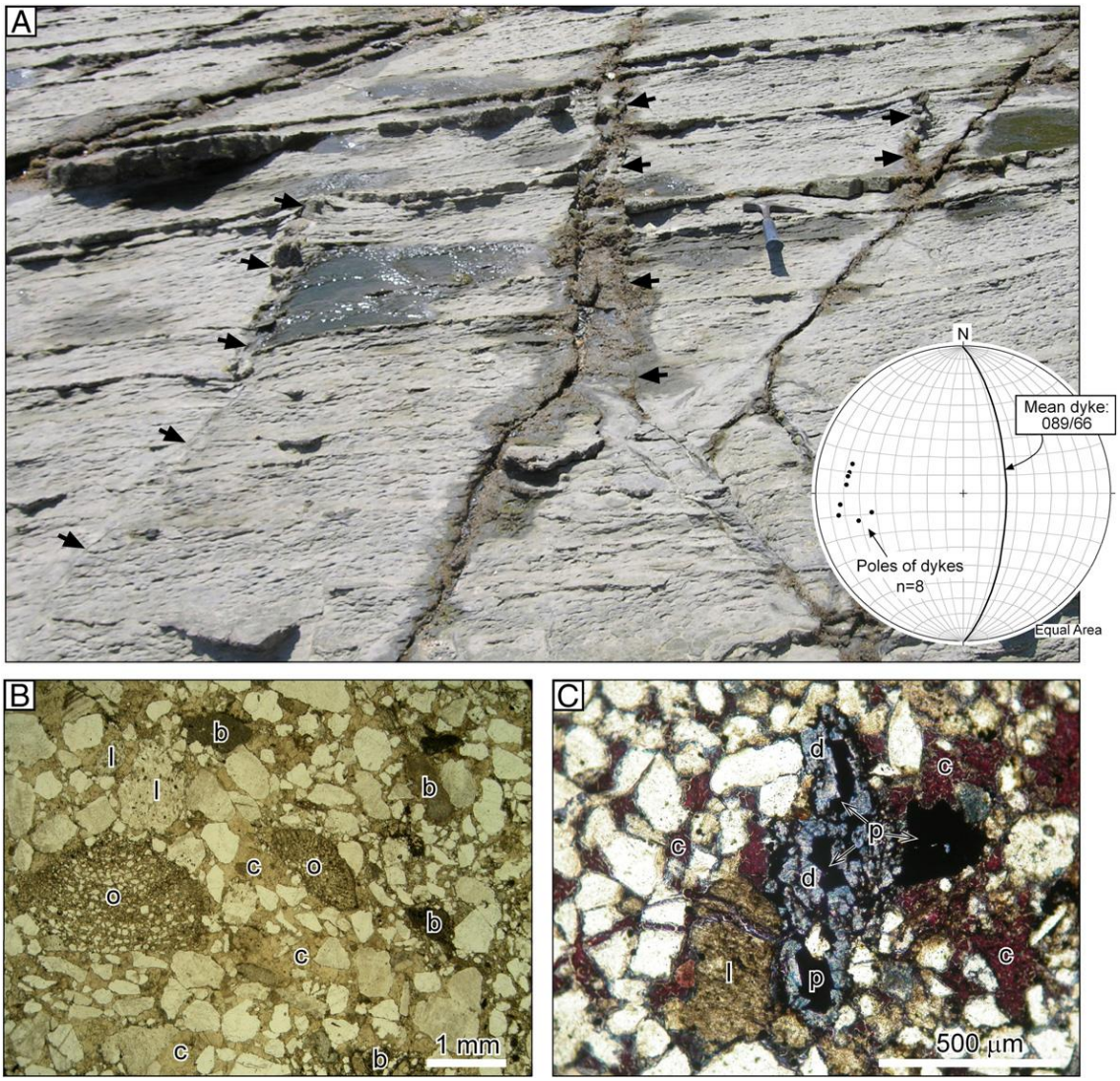

Figure 41: Sandstone dykes. (A) Three parallel sandstone dykes (arrows) cross-cutting stratification. Inset: Equal area stereographic projection of eight dyke poles and resulting mean dyke plane (089/66) after bedding correction. (B) Photomicrograph of a dyke sandstone showing particles of quartz, different bioclasts (b), orbitolines (o) and lithic fragments (l) cemented by sparry calcite (c). (C) Photomicrograph of a stained thin-section of a dyke sandstone showing calcite cement in red (c) and dolomite in blue (d); note pyrobitumen fills (black) and a lithic mudstone fragment (l). (For interpretation of the references to color in this figure legend, the reader is referred to the web version of this article.)

6.5.1.4.1.4 Sandstone dykes

Nine sandstone dykes occur in the uppermost intervening deposits between intervals A and B and also in interval B (Figs. 39 and 41). The dykes are bounded by sharp surfaces highly discordant to the host bedding. Usually, they do not displace crosscut beds, but local displacements up to 2 cm have been measured. The dykes have thicknesses and lengths up to 6 cm and 2 m, respectively, and show planar shapes with local centimeter-scale ptygmatic

folds. Vertically, the dykes end either abruptly or by progressive thinning. In the latter case, dyke traces continue along parallel fractures several meters long (Fig. 41A). Most dyke fills are composed of structureless medium to coarse sublitharenite with common calcite bioclasts, carbonate lithoclasts, and particles of very fine sandstone, mudstone and altered rocks (clay minerals) (Fig. 41A, B). One dyke is composed of pebble-grained quartz conglomerate. Recognized calcite bioclasts are orbitolines, red algae, rudists, oysters, echinoderms, brachiopods and corals, all typical of the Urgonian biofacies (Agirrezabala, 1996). Among the orbitolines are *Orbitolina* (*Mesorbitolina*) *texana* (Roemer) and *Dictyoconus pyrenaicus* Moulade and Peybernès, which indicate an Upper Aptian to Middle Albian age. Sandstone fills are mainly cemented by sparry calcite and, locally, saddle dolomite, and up to 2 mm long pyrobitumen fills occur in pore spaces (Fig. 41B, C). Whole rock XRD analyses on three samples yielded semi-quantitative mean values for quartz, calcite, phyllosilicates (mica, illite and kaolinite) and dolomite of 60%, 33%, 6% and ca. 1%, respectively. Structural measuring of the dykes shows sub-parallel attitudes with a mean dyke trending north and dipping 66° toward east, after bedding correction (Fig. 41A).

The discordant relations with the host beds, tabular geometries, and the presence of exotic fragments are typical of a direct response to subsurface fluid escape and fluidization (Lowe, 1975). Moreover, the great similarity in biofacies and lithofacies between the fragments (calcite bioclasts, carbonate lithoclasts and sandstone particles) present in the dyke fills and the rocks of the underlying Otoio Formation as well as their identical age (Agirrezabala, 1996) suggest that dykes are injectites sourced from that formation. Stratigraphically, the top of the Otoio Formation is 900 m (compacted) below the dykes (Fig. 38), and therefore, a similar minimum upward fluid and sediment migration can be assumed.

6.5.1.4.2 Relations between carbonate lenses and host deposits

Authigenic carbonate lenses are laterally equivalent to mudstones and very thin sandy turbidites (Figs. 40C, 42 and 43). Fig. 42 shows high-resolution stratigraphic cross-sections of three clusters of carbonate lenses and related deposits, in an orientation (NE–SW) parallel to the measured paleocurrents

(Fig. 38). The aim of these cross-sections is to characterize geometric relationships between the authigenic carbonate lenses and the laterally equivalent mudstones and sandy turbidites. Detail photographs of the constructed cross sections are shown in Fig. 43. Although the cross-sections do not show the exact original geometry of the deposits due to post-depositional differential compaction, important geometric results and interpretations can be obtained from their analysis. Geometrically, two kinds of sandy turbidites adjacent to carbonate lenses can be differentiated: lens-shaped sandy turbidites and tabular turbidites.

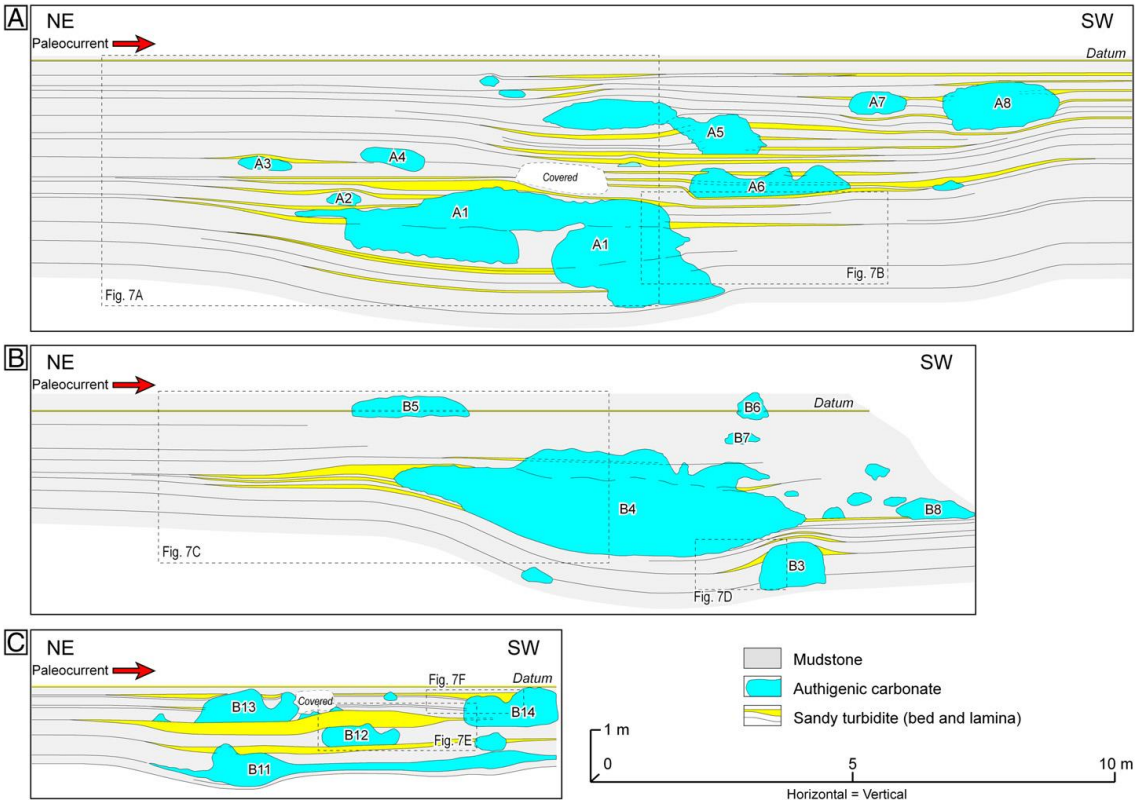

Figure 42: Detailed stratigraphic cross-sections of three clusters of authigenic carbonate bodies and lateral equivalent facies constructed parallel to paleocurrents. (A) Cluster within interval A. (B,C) Clusters within interval B. Note the thickening of most sandy turbidites toward the adjacent or underlying carbonate bodies. Rectangles indicate detail photographs shown in Fig. 43. For location, see Fig. 39. The scale is the same for all three sections.

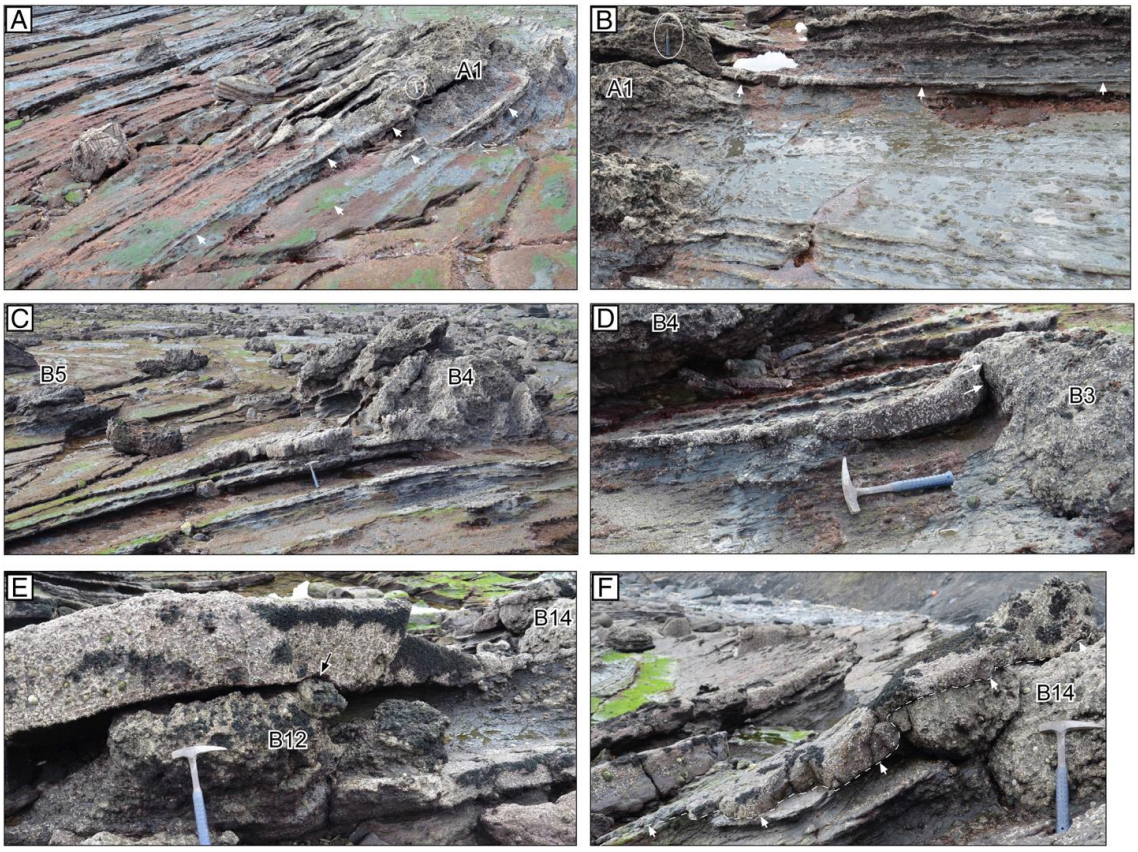

Figure 43: Field images illustrating the geometric relationships between mudstones and sandy turbidites, and the authigenic carbonate bodies shown in Fig. 42. (A) Bedded, lens-shaped sandy turbidites showing almost systematic progressive thickening towards the massive carbonate lens (two beds indicated by arrows). (B) Carbonate body margin and adjacent mudstones with scattered carbonate concretions and sandy turbidites. Upper turbidite (arrow) shows progressive thickening toward the carbonate body, while the lower, very thin turbidites are of tabular shape. (C) Thickening of lens-shaped sandy turbidites (near the hammer) toward the carbonate lens; note that the thin underlying turbidites (lower part) exhibit tabular geometries. (D) A lens-shaped sandy turbidite thickens toward a carbonate body and onlaps it (arrows). Slight deformation of sandstone bed adjacent to the carbonate body is due differential compaction. (E) A lenticular sandy turbidite showing thickening above the underlying authigenic carbonate body; note that the turbidite covers a small protrusion (arrow) from the upper surface of the carbonate body. (F) Lens-shaped sandy turbidite (arrows) onlapping the margin of an authigenic carbonate body and covering its irregular upper surface; note the wedge shape of the turbidite.

6.5.1.4.2.1 Lens-shaped sandy turbidites

These turbidites are very thin (<2 cm) and show tabular shape away from the carbonate bodies, but approaching carbonates they thicken to up to 42 cm (Figs. 42 and 43). This thickening is observed not only upflow and downflow of carbonate bodies, but in all directions. The maximum thickness of individual sandstone lenses is directly adjacent to, or above, the carbonate bodies. In planar view, the carbonate bodies are commonly located approximately in the center of the sandstone lenses, but a few exceptions were also observed. The

contact between the sandy turbidites and the carbonate bodies can be either sharp or gradual. In the case of sharp contacts, the turbidites onlap the carbonates and thin over them (Fig. 43D,F), or lay irregularly on top of the carbonates (Fig. 43E). In the case of gradual contacts, sandy turbidites continue more or less diffusely inside the carbonate bodies as relatively sand-rich intervals (Fig. 42). This type of turbidites occurs more frequently adjacent to the middle and upper part of the carbonate lenses or over them.

6.5.1.4.2.2 Tabular sandy turbidites

These very thin (<2 cm) turbidites have tabular shapes and do not exhibit thickness variation near the carbonate bodies. They show gradual contacts with, and continue through, the carbonates as relatively rich sandy intervals. This type of turbidite is more frequent adjacent to the lowermost part of the carbonate lenses. Commonly, stacked turbidites exhibit an inward dipping pattern toward the carbonate lenses, with gentle higher dips in the deeper beds (Fig. 42).

6.5.1.5 The carbonate lenses

6.5.1.5.1 Petrography

The most common paragenetic sequence of the Ispaster authigenic carbonates is: (i) dark pyrite-rich micrite; (ii) yellow/brown calcite “yellow calcite”; (iii) short fibrous calcite; (iv) dolomite; and (v) calcite spar (equant calcite). Also, pore-filling pyrobitumen and barite crystals occur as minor components. Micrite constitutes volumetrically the main phase of the Ispaster carbonates and hosts porous-filling coarse carbonate cements (Figs. 44 and 45). XRD analysis indicates a composition of microcrystalline calcite (80%), with disseminated framboidal pyrite (4%), clays (7%) and silt to fine sand-sized quartz particles (8%). The micrite embeds abundant sub-spherical fecal peloids, test of radiolaria, planktonic and benthic foraminifera, sponge spicules, ammonites and

scattered wood fragments (Fig. 44A–D, G), as well as an abundant macrofauna (mainly bivalves, gastropods and arthropods) (Fig. 40D).

The diagenetic parasequence is here outlined based on a high-resolution study of several void-fills (Figs. 46 and 47). Such small stromatactis-like voids and V-shaped pores within the micrite are common throughout the Ispaster seep carbonates. The voids are surrounded by dark, thrombolitic micrite (M), have $\delta^{13}C$ values ranging from −37‰ to −27‰, show a very strong luminescent CL behavior (Fig. 46A, B), and their Raman bands indicate calcite and carbonaceous material (sample point C on Fig. 47). The voids are often rimmed by a relatively thick veneer of pyrite framboids with an intermediate layer that is dark under a combination of transmitted and reflected light (Fig. 46A). The Raman bands of the first two layers are quite similar, although the carbon signal is more distinguished in the second, dark layer (sample points D and E on Fig. 47). The inner layer of this pyrite veneer shows Raman bands for pyrite coupled to hematite, as well as for carbon (sample point F on Fig. 47). Often a small, highly cathodoluminescent gap is visible between the pyrite veneer and the non-luminescent ‘yellow calcite’ (Fig. 46B). In transmitted light this gap is often dark and represents an organic- and pyrite-rich clotted micrite (Fig. 46D).

The so-called ‘yellow calcite’ is brownish to slightly yellow, and sometimes exhibits a short fibrous relic structure indicating former high-Mg calcites. The yellow calcite exhibits now a clear scalenoedric fabric which forms semi-spherulitic, bush-like clusters (Fig. 46). The scalenoedric crystals exhibit a strong epitaxial growth pattern indicated by growth bands and their distal ends have sharp crystal planes indicating an undisturbed growth. The Raman spectra show as dominating bands a very narrow carbon signal (sample point G on Fig. 47). In the higher wave number region also smaller and broader bands appear which are interpreted as vibrations from C-H bonds (Socrates, 2001). The yellow calcite exhibits the most depleted $\delta^{13}C$ values (as low as −41.7‰) measured within these cold seep carbonates. Dark clotted micrite either co-occurs with, or subsequent to, the yellow calcite and shows $\delta^{13}C$ values ranging from −37.5‰ to −29‰ (Fig. 46D). The innermost cements within the voids are Mg-poor equant calcites which demonstrate a dull CL behavior in the center of the crystals, but a bright red CL behavior at the margins (Fig. 46A,B). Potassium ferricyanide dye stains the red CL portions blue, indicating Fe-calcite

(Fig. 46C). The non-ferroan calcites exhibit relative high amounts of Mn, whereas the ferroan calcitic portions are poor in Mn and have relatively heavy $\delta^{13}C$ values around −7.6‰ (Fig. 46E,F). This observation is valid for the entire carbonate rock and indicates that strong CL is related to high Mn contents, except for the ferroan calcite areas.

Other late diagenetic components include dolomite which locally forms irregular masses of fine-grained, anhedral crystals with nonplanar, equigranular, mosaic fabrics that are up to several centimeter wide (Figs. 44A and 45F,G). Local corrosion surfaces (C2) and fractures cross-cut previous carbonate cements (Figs. 44C,G and 45A). The remaining porosity can be filled partially or completely with sparry calcite, which constitutes irregular masses of siliciclastic-free, clear to turbid dentate crystals (Figs. 44B–D,G and 45A–G). Locally, sparry calcite exhibits dedolomite fabric lining pore spaces. It consists of coarse (up to 2.2 mm), brown to yellow, euhedral crystals of calcified dolomite which show curved faces characteristic of saddle dolomite (Fig. 45E, F). The originally thin shell of large bivalves is commonly dissolved and subsequently the generated space was filled with up to 2.5 cm thick, coarse sparry calcite, giving them a very thick-shelled appearance. Locally, anhedral, poikilotopic sparry calcite including siliciclastic particles results from recrystallization of micrite (Fig. 45I).

Pyrobitumen and barite crystals occur in close association with late diagenetic dolomite and sparry calcite. It constitutes black solid bitumen, commonly fills the intercrystalline porosity of both dolomite and sparry calcite (Figs. 44D and 45H), is opaque in transmitted light, black under incident light, non-fluorescent under ultraviolet light, and exhibits very low solubility. As shown in Fig. 48 the pyrobitumen is concentrated inside the equant calcite (L-EC), which is surrounded by the thrombolytic micrite (M). The associated Raman spectrum shows only bands of amorphous carbon, without appearance of additional mineral bands and no visible shoulder in the ‘D’-band. This suggests a migration of the pyrobitumen along crystal boundaries of the blocky calcite together with an agglomeration inside the porous texture of the calcite. Barite constitutes prismatic, poikilotopic crystals up to 3.5 mm long with planar to very irregular crystal boundaries (Fig. 45I).

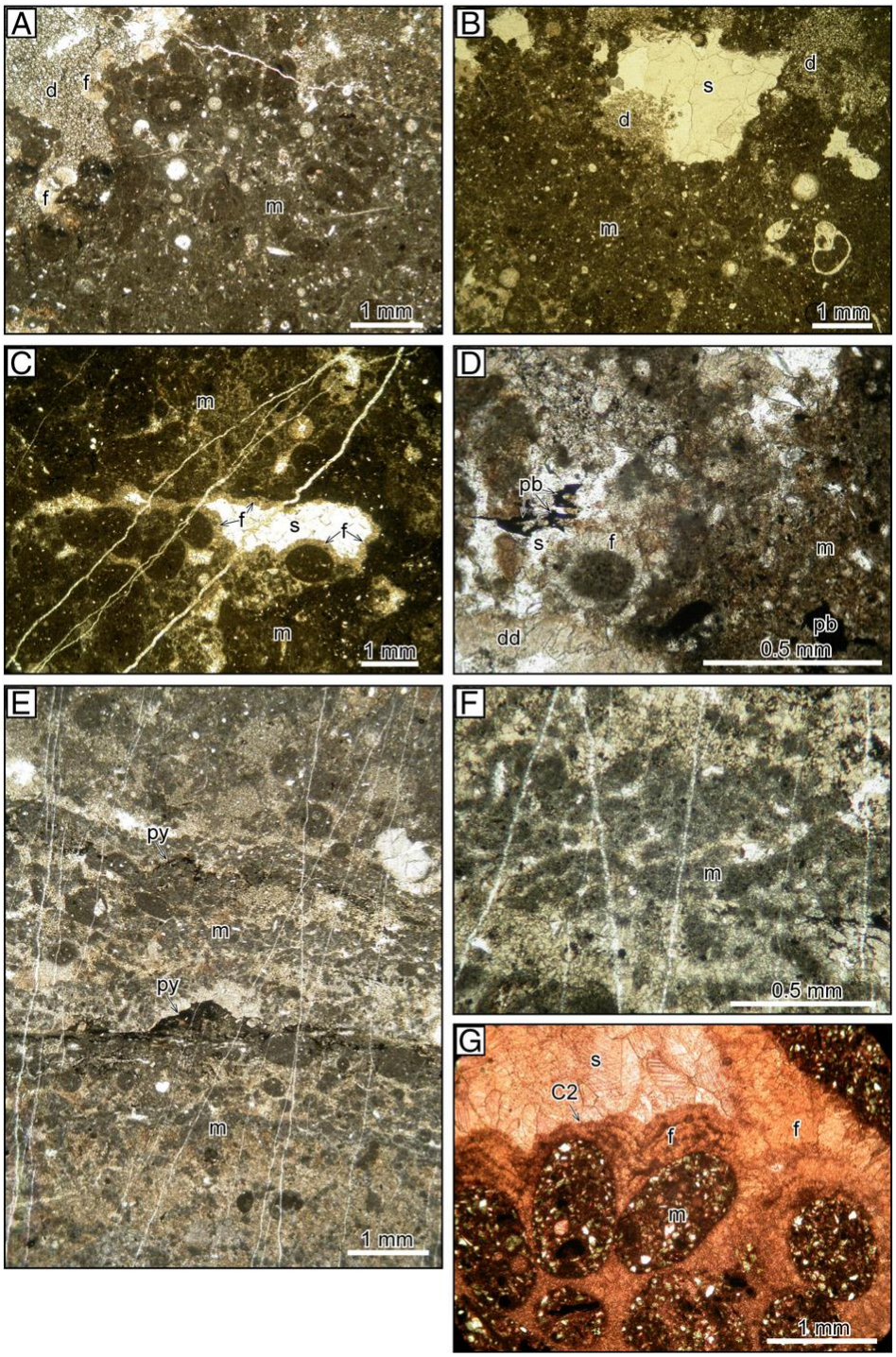

Figure 44: Thin-section microphotographs of the Ispaster seep carbonates. (A) Micrite (m) with disseminated framboidal pyrite (black dots), fecal peloids, siliciclastic particles and microfossils (radiolaria, sponge spicule and planktonic foraminifera). In the upper left, fibrous calcite (f) and dolomite. (B) Micrite (m) hosting microfossils (gastropod, bivalve and radiolaria) (lower right), fine-grained dolomite (d) and pore-filling sparry calcite (s). (C) Peloidal micrite (m), isopachous fibrous calcite (f) lining a pore-space filled with sparry calcite (s), and cross-cutting fracture-filling sparry calcite. (D) Pyrite-rich micrite (m), fibrous calcite (f) lining a fecal pellet, sparry calcite (s) with saddle dedolomite (dd), and pore-filling pyrobitumen (pb). (E) Detail of stromatolitic laminated micrite (m) composed of alternating fenestral micrite (light) and encrusting pyrite (py) lamina. Note clotted microfabric in some laminae (detail in F). (F) Detail of E (center) showing a lamina of clotted micrite. (G) Vug filled with siliciclastic-rich fecal pellets, lining fibrous calcite showing several growth phases (f), and sparry calcite (s). Note corrosion surface (C2) cross-cutting fibrous calcite laminae. All photographs with transmitted light, and (G) is stained with alizarin red.

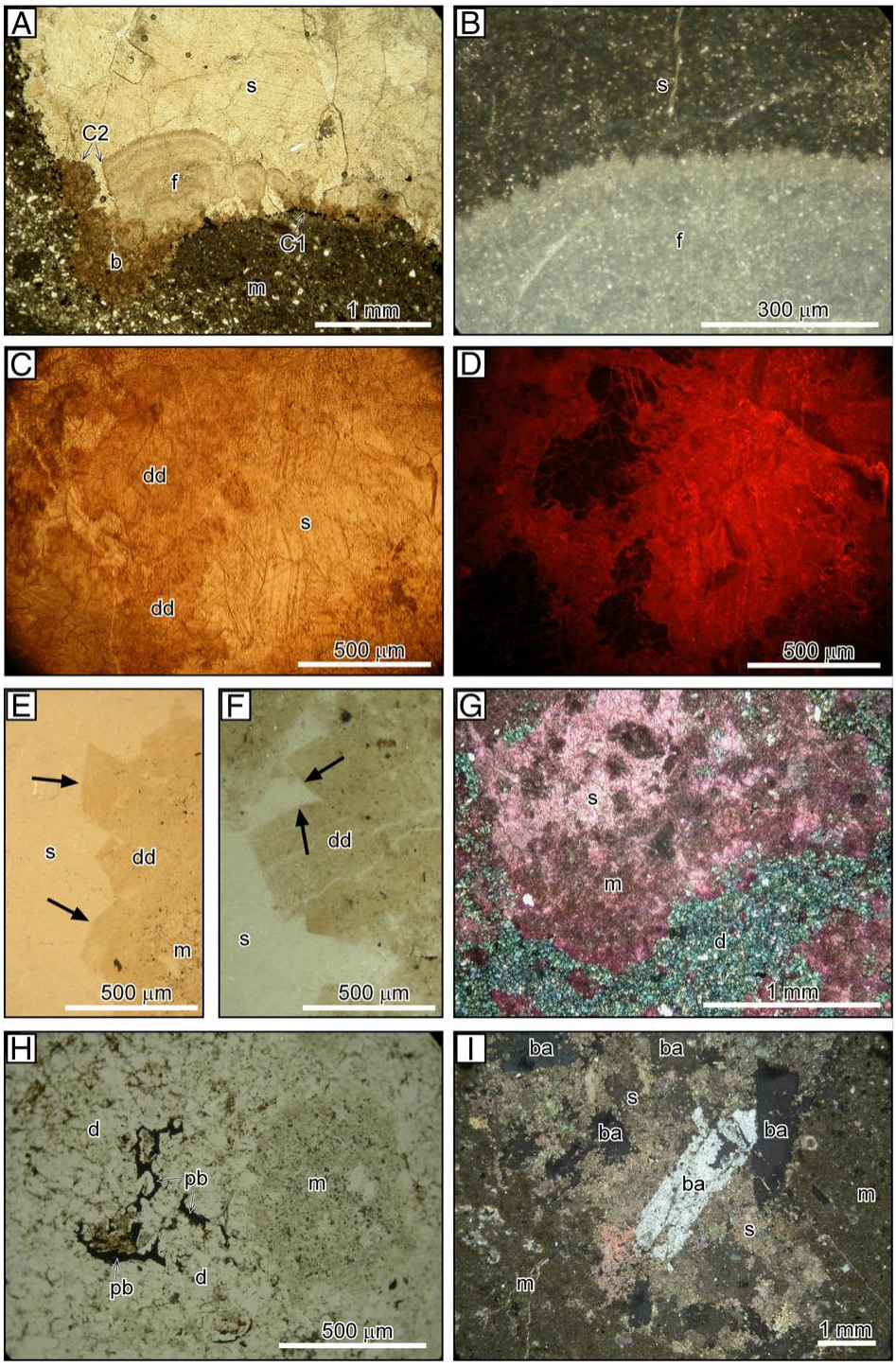

Figure 45: Thin-section microphotographs of the Ispaster seep carbonates. (A) Micrite (m), brown calcite (b), fibrous calcite botryoids (f) and sparry calcite (s). Note corrosion surfaces (C1 and C2), one of which (C1) is encrusted with pyrite. (B) Detail of A, showing rhomb-tip terminations of calcite fibers (f) in a botryoid upper contact. (C) Pore-filling sparry calcite (s) with yellow dedolomite (dd). (D) Detail of C but under cathodoluminescence light. (E,F) Micrite (m) rimmed with brownish saddle dedolomite (dd) and whitish sparry calcite, under reflected light. Note curved faces of dedolomite crystals (arrows). (G) Micrite (m) partially recrystallized, fine-grained replacive dolomite (d) and sparry calcite (s). (H) Micrite (m) with disseminated pyrite (light dots), dolomite (d) and black pyrobitumen (pb) filling intercrystalline porosity, under reflected light. (I) Micrite (m) partially replaced by poikilotopic sparry calcite (s) and barite crystals (ba). (A), (C), and (G) are with transmitted light, and (I) is with plane-polarized light. (B), (E), (F) and (H) are with reflected light, and (D) is with cathodoluminescence light. (For interpretation of the references to color in this figure legend, the reader is referred to the web version of this article.)

6.5.1.5.2 Carbonate stable isotopes

The results of stable carbon and oxygen isotopes analyses of the Ispaster carbonates are plotted in Fig. 49. Analyzed material corresponds to volumetrically major carbonate phases, i.e. micrite, yellow calcite, fibrous calcite and sparry calcite. All samples are depleted in both ^{13}C and ^{18}O compared with Late Albian sea water values, which are about 1.8‰ and −2.3‰ (VPDB), respectively (Wilson & Norris, 2001).

$\delta^{13}C$ data from carbonates present a wide range between −5.1‰ and −41.6‰, showing a marked overlap among the four different carbonate cements. The yellow calcite yielded the most depleted mean value of −39.5‰ (range values between −37.4‰ and −41.6‰). The $\delta^{13}C$ mean values for fibrous calcite, micrite and sparry calcite are −27.0‰ (range values between −16.1‰ and −34.6‰), −25.7‰ (range between −5.1‰ and −33.8‰) and −22.9‰ (range between −7.0‰ and −38.3‰), respectively.

Oxygen isotopic data of the four carbonate cements are very negative and most of them range between −8.0‰ and −12.0‰ exhibiting a significant overlap. The yellow calcite and fibrous calcite yielded similar $\delta^{18}O$ mean values of −8.9‰ (ranges between−6.9‰ and −10.9‰, and between −6.6‰ and −10.0‰, respectively), whereas sparry calcite and micrite present slightly more depleted mean values of −10.7‰ (ranges between −9.3‰ and −13.5‰, and between −9.7‰ and −11.8‰, respectively).

6.5.1.5.3 Organic matter

Twelve samples of mudstones from A and B intervals laterally equivalent to authigenic carbonates have been analyzed (Table 4). They yielded a total organic carbon (TOC) mean value of 0.95% (0.74% to 1.16%). Five of the twelve mudstone samples exhibit a $\delta^{13}C_{org}$ mean value of −25.1‰ (−24.7‰ to −25.3‰). Three samples of pyrobitumen-fills from authigenic carbonates yielded a $\delta^{13}C_{org}$ mean value of −26.9‰ (−26.3‰ to −27.6‰) (Table 4).

6.5.1.5.4 Biomarkers

Biomarker studies revealed that both carbonate samples contain abundant n-alkanes with carbon numbers 16 to 42 (maximum at *n*-C_{23}) as main constituents. Due to pre-extraction of one sample, however, amounts of the most likely pyrobitumen were reduced and other, less concentrated and better protected biomarkers were detected. These include C_{20}-isoprenoids (phytane and/or crocetane), 2,6,10,15,19-pentamethylicosane (PMI), and terminally branched short chained hydrocarbons (iso and anteiso; Fig. 50). Stable carbon isotope signatures of *n*-alkanes in the non-pre-extracted carbonate were between −29.5 and −34.6‰. The same was found for the pre-extracted sample, but in addition terminally branched hydrocarbons, phytane/crocetane and PMI demonstrated strong ^{13}C-depletions (as low as −96.3‰ (for PMI); Table 5). In contrast, a peak including *n*-C_{35} and a $C_{40:0}$ biphytane was slightly enriched in ^{13}C (−25.8‰).

6.5.1.5.5 Macrofauna

The macrofauna of the Ispaster seep deposits consists of nine species; seven molluscs, one shrimp and one coral. The most prominent taxon is a large species of the modiomorphid bivalve genus *Caspiconcha* that reaches 21 cm in length (Figs. 51A, B and 52C, D). They occur mostly in clusters in random orientation, and often two shells are tucked into another (Fig. 51A, B). Second in size and abundance is a lucinid bivalve reaching a length of 13.5 cm (Figs. 51D, 52B). They are scattered throughout the deposits or occasionally found in small clusters. Most specimens are in poor condition and do not preserve hinge teeth, making a classification below family level difficult. However, the lucinid found at the coeval and nearby seep deposit at Mutriku appears to differ by being less inflated and having a more elliptical shell outline than those from Ispaster. Minor components of the bivalve fauna include one small specimen of a solemyid that is about 6 mm long (Fig. 52A), and one specimens of the protobranch *Acila* sp. (family Nuculidae).

Gastropods are found scattered throughout the deposits and show no preferred association with any of the main bivalve taxa or a particular carbonate facies.

Three species were found, including several small (up to 11 mm high), high-spired specimens belonging to the genus abyssochrysoid genus *Hokkaidoconcha* (Fig. 52H). Moderately common is an aporrhaid gastropod, reaching 15 mm in height (Fig. 52I). Lastly, one small (3 mm high) internal mould of a turbiniform gastropod was found (Fig. 52G), which superficially resembles the *Cantrainea* species described by Kaim et al. (2009) from Late Cretaceous seep deposits in northern Japan in general shell shape. Claws of the mud shrimp *Callianassa* reach 12 mm in length (Fig. 52E, F), are abundant in carbonate blocks with tubular structures (Fig. 51C), and are otherwise found as rare specimens throughout the deposits. One small (4 mm diameter) solitary coral has been found in association with a bivalve cluster.

6.5.1.6 Interpretations and discussion

6.5.1.6.1 Primary formation of carbonates

Microfacies, stable carbon isotopes, Raman spectroscopy, and biomarkers clearly show that the carbonate bodies at Ispaster formed, for the most part, due to the anaerobic oxidation of methane, although with a complex thermodiagenetic history. The presence of micrite with stromatolitic lamination, clotted microtexture, and $\delta^{13}C$ values as low as −37.6 ‰ indicates microbial mediated carbonate formation during early diagenesis (Greinert et al., 2002; Peckmann et al., 2002). These micrites include many stromatactis-like voids and v-shaped pores, which were probably formed during a first, fast cementation of micrite. During this phase, voids and pores were often encrusted by microbial biofilms, and filled up with crustacean fecal pellets, other bioclasts and also brecciated material. So-called ‘yellow calcite’ is well developed within such voids and pores and typically shows growth bands with differing CL behavior. Among these growth bands, the non-luminescent ones here are interpreted as primary cement phases. This yellow calcite exhibits the most negative $\delta^{13}C$ values (as low as −41.6‰) measured in Ispaster carbonates. Yellow calcite has been documented from many fossil seep carbonates and are in all cases early carbonate cements (e.g. Beauchamp & Savard, 1992; Campbell et al., 2002; Peckmann & Goedert, 2005). The underlying dark

micritic portions have $\delta^{13}C$ values around −37‰ to −27‰ and the clotted micrites within the stromatactis and V-shaped voids exhibit $\delta^{13}C$ values as low as −37.5‰. These highly depleted stable carbon isotopes signals indicate a strong AOM signal which is in agreement with the related abundant framboid pyrites.

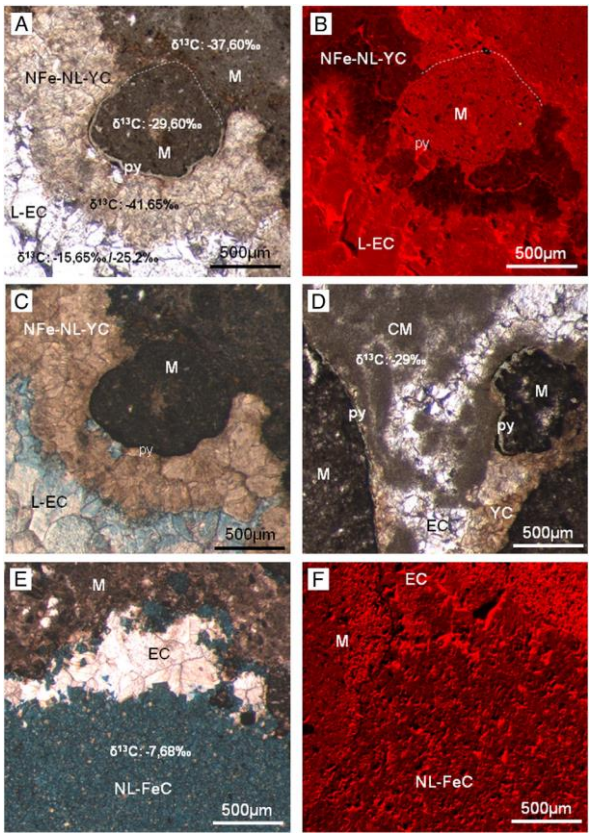

Figure 46: Thin-section microphotographs of the Ispaster seep carbonates. (A) Inner portion of a stromatactis void with a rim of non-ferroan, non-luminescent 'yellow calcite' (NFe-NL-YC) which grows on a mineralized pyrite crust (py) documenting a former AOM microbial film. The micritic core (M) was also formed mediated by microbial activities. The later stage equant calcite (L-EC) is bright. 'yellow calcite' exhibits the lightest $\delta^{13}C$ values and is very probable a product of AOM. The dark micritic facies also demonstrates very light $\delta^{13}C$ values demonstrating a strong AOM influence. The relatively late bright equant low Mg-calcite was formed through later light hydrocarbon rich fluids, evidenced by moderately low $\delta^{13}C$ values. (B) Same thin section as in (A) investigated with a cold cathode luminescence microscope. Note that the 'yellow calcite' is non-luminescent which is related to very low Mn concentrations (LA-ICPMS data, not shown here). All strong luminescence phases are enriched in Mn (L-EC, M). (C) Same thin section as in (A and B) stained with potassium ferricyanide (II) which marks the Fe^{2+}-rich calcites blue. The 'yellow calcite' is non-ferroan in contrast to the later stage L-EC and represents a very early diagenetic growth stage. (D) Often the voids are filled with clotted peloidal micrite (CM) which is also a final product of microbial taphonomic mineralization like the 'yellow calcite' (YC). CM and YC are formed contemporaneously in a very early stage of microbial taphonomy and their low $\delta^{13}C$ values show a clear AOM signal. (E) Late burial Fe-calcite stained intensively blue with potassium ferricyanide (II) due to Fe^{2+}-enriched late diagenetic reduced hot fluids. The unstained crystals are brownish and should not be confused with the early diagenetic 'yellow calcite'. (F) The late burial Fe-calcites are more or less non-luminescent (NL-FeC) due to high concentrations of intracrystalline Fe^{2+} which quenches the Mn-related CL behavior. (For interpretation of the references to color in this figure legend, the reader is referred to the web version of this article.)

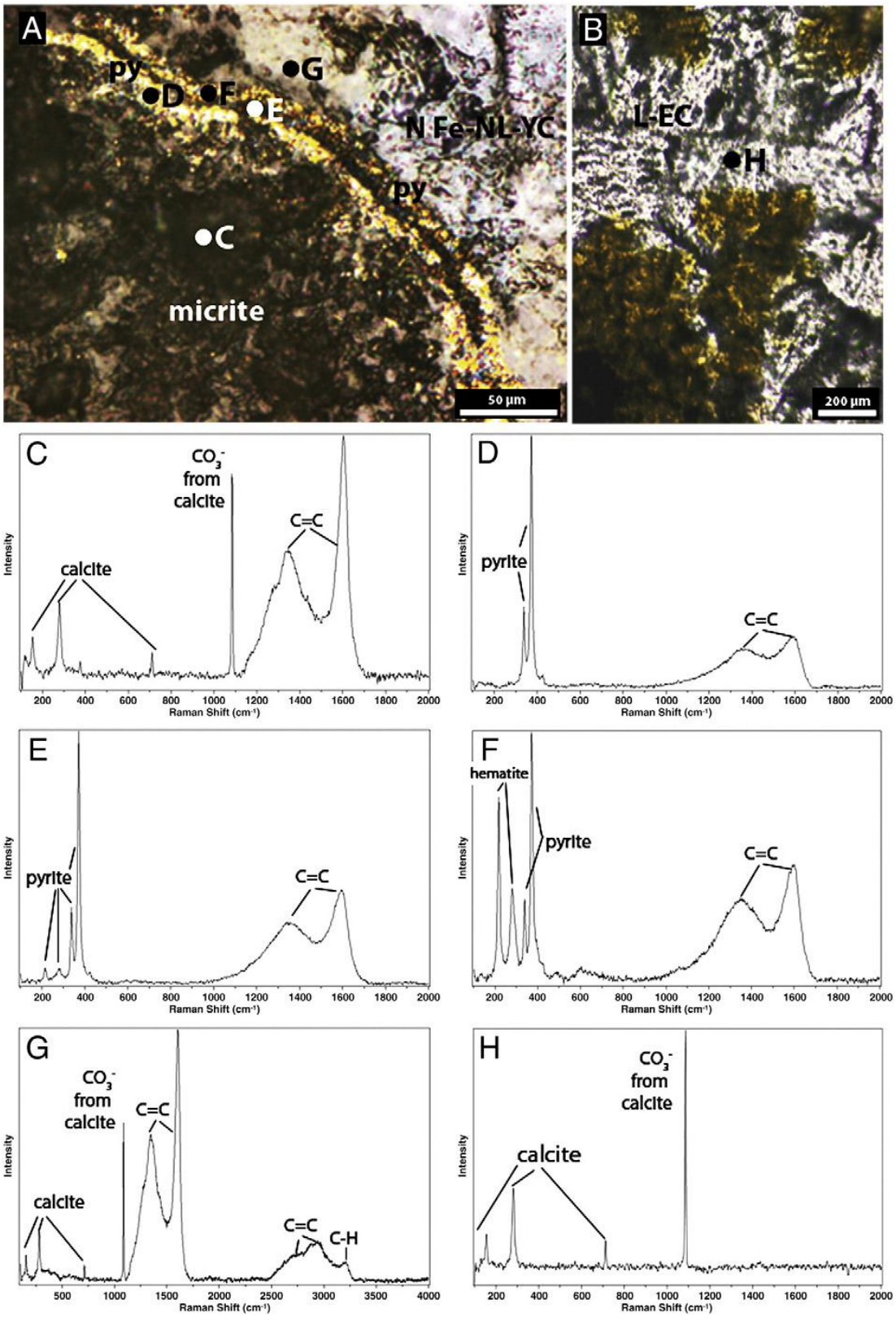

Figure 47: Raman spectra of different zones of a stromatactis void fill (A) and surrounding cement (B) of the Ispaster carbonate. The spectra show mineralogical phases as well as signatures from organic molecules. Spectrum C is generated in the surrounding thrombolytic micrite. Spectra D and F are measured in two different zones of a pyrite layer (py), which are separated by a dark intermediate layer, illustrated in spectrum E. Spectrum G is generated on a 'Yellow Calcite' (N Fe-NL-YC) and spectrum H on blocky calcite cement (L-EC).

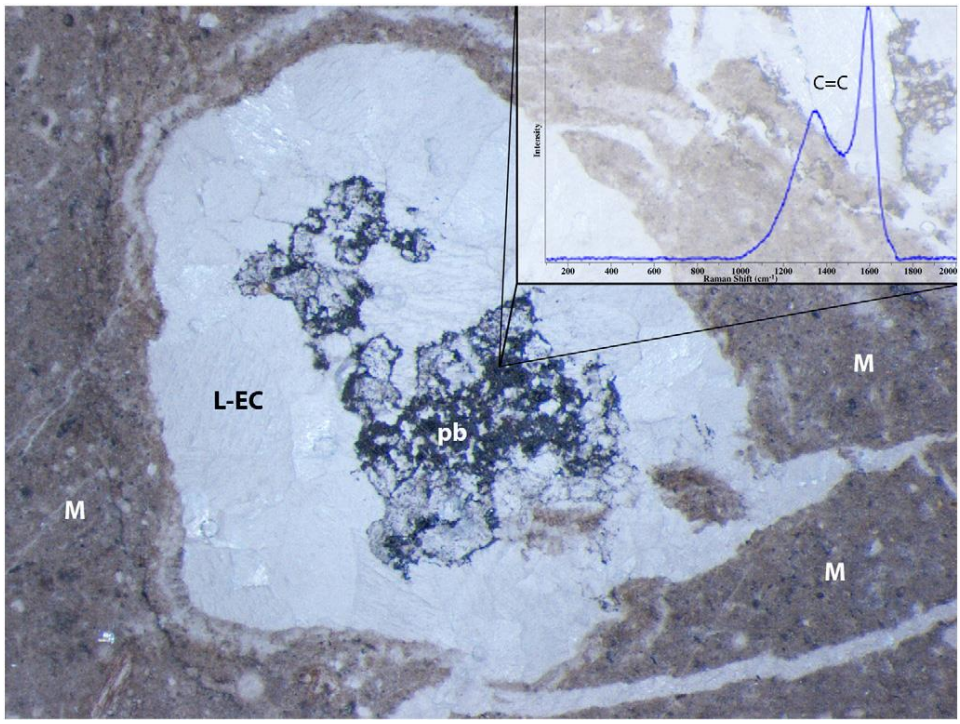

Figure 48: Thin section microphotograph and associated Raman spectrum of pyrobitumen (pb) migrated through crystal boundaries of equant calcite (L-EC). Note that no additional mineral bands appear and more important, no shoulder in the 'D'-band is visible.

Although most biomarkers were obscured by pyrobitumen hydrocarbons, they support that carbonate formation was induced by microorganisms involved in AOM. Biomarkers include PMI and phytane (most likely co-eluting with crocetane) together exhibiting strong depletions in ^{13}C (Table 5). Respective ^{13}C-depleted isoprenoids are suggested to have methanotrophic archaea (ANME) as origin (Elvert et al., 1999; Hinrichs et al., 1999; Thiel et al., 1999). Terminally branched alkanes were also found (e.g., *i*-C_{18} and *ai*-C_{18}). Fatty acids with similar carbon structures are often abundant at cold seep settings, where they are attributed to AOM-related sulfate-reducing bacteria (e.g. Elvert et al., 2003; Blumenberg et al., 2004). The same holds true for ^{13}C-depleted tricosane (*n*-C_{23}), which has a yet unknown AOM-related bacterial source (Thiel et al., 2001; here overlain by *n*-C_{23} from the pyrobitumen). Also found in the sample was a $C_{40:0}$ biphytane, slightly enriched in ^{13}C (−25.8, co-eluting with *n*-C_{35}). Biphytanes are produced by various archaea, but the lack of ^{13}C-depletion in biphytanes in Ispaster excludes methane oxidizing archaea (specifically ANME-1; Blumenberg et al., 2004) as major source. A minor role of ANME-1 archaea in the AOM community at Ispaster — and a favor of ANME-2 — may be linked to the methane seepage intensity, since ANME-1 appear to be

better adapted to low methane partial pressures (Nauhaus et al., 2005). Consequently, relatively high methane seepage can be inferred for the situation at Ispaster during precipitation of the AOM-carbonate. This interpretation is consistent with the high abundance of voids and void-filling authigenic carbonate phases (i.e., yellow calcite) in the Ispaster carbonates; in ancient ANME-1 settings with inferred diffuse seepage such carbonate phases are rare and micrites with less depleted in ^{13}C dominate (Peckmann et al., 2009).

The Raman spectra of the investigated mineral phases provide further evidence for a microbial origin of these carbonates. Vibrational bands at 1350 cm^{-1} and 1600 cm^{-1} are recognized in most mineral phases. They are characteristic for carbonaceous material and are commonly referred to as “D” (disordered) and “G” (graphitic) bands respectively, because of their occurrence in various forms of graphite (Tuinstra & Koenig, 1970). In combination with the other methods used here, these bands can be used to confirm a proposed biological origin. Especially the shoulder occurring in the D-band at around 1250 cm^{-1} suggests a biological origin of these vibrations (Kudryavtsev et al., 2001). As already mentioned in Section 5.4 biomarker analyzes revealed that the carbonates contain a significant amount of hydrocarbons, so that in this case these bands can be simply interpreted as vibrations from carbon molecules, which have their characteristic group frequencies in this spectroscopic range (Socrates, 2001).

In case of the pyrite veneer that lines the stromatactis voids, the combination of bands for carbon and for pyrite coupled to hematite demonstrate coupling of framboid iron sulfides with organic material, supporting the assumption that this pyrite veneer is the product of a former microbial mat. In case of the yellow calcite the Raman spectrum shows several bands indicating organic carbon, both in the lower and the higher wavenumber region (spectrum G in Fig. 47), which together favor an organic origin of the associated phase. This observation supports the assumption that the yellow calcite is genetically linked with the pyrite crust and probably also a product of AOM processes, as indicated by very light C isotope signals. In contrast to the yellow calcite, the calcite with blocky texture (equant calcite-EC) has no carbon signal in its Raman spectrum (spectrum H in Fig. 47), indicating an origin during late burial diagenesis.

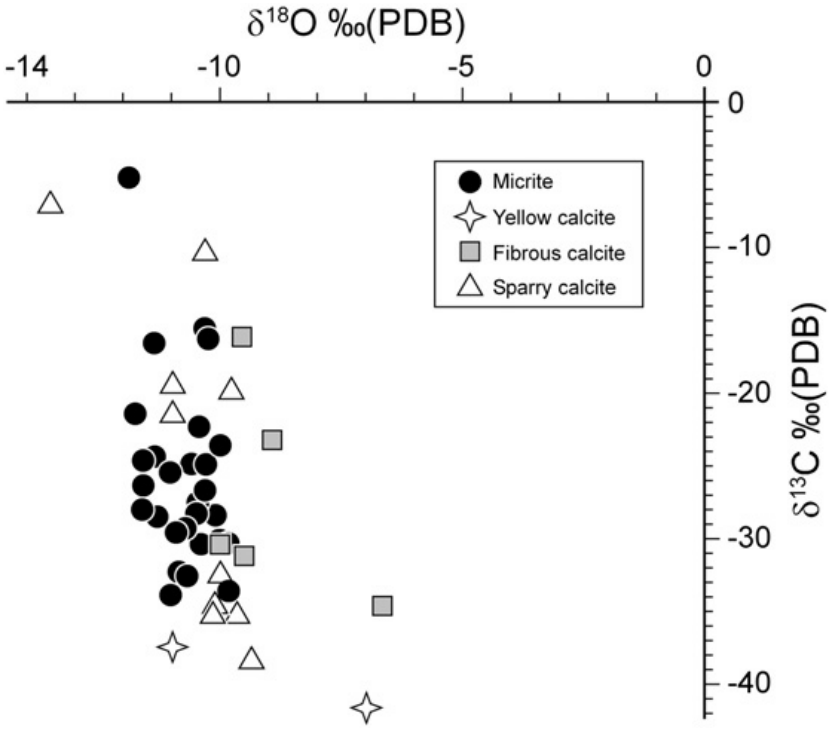

Figure 49: Stable carbon versus oxygen isotopic cross-plot for Ispaster authigenic carbonates.

Table 4: Total organic carbon and stable organic carbon isotope values for host mudstones of the Ogella unit and carbonate pyrobitumen-fills.

Sample ID	TOC (%)	$\delta^{13}C_{org}$‰ (PDB)[a]
Host mudstones		
OGE-l-1	0.79	
OGE-l-2	0.74	
OGE-l-3	0.89	
OGE-l-4	0.90	
OGE-l-5	0.75	
OGE-l-6	1.10	–25.12 ± 0.32
OGE-l-7	1.16	–25.20 ± 0.05
OGE-l-8	1.07	–25.26 ± 0.17
OGE-l-9	1.06	–25.31 ± 0.04
OGE-l-10	1.13	–24.75 ± 0.19
OGE-l-11	0.92	
OGE-l-12	0.96	
Pyrobitumen-fills		
API-12d		-26.91 ± 0.21
API-12e		-27.61 ± 0.24
API-13d		-26.32 ± 0.11

[a] Standard deviation is indicated.

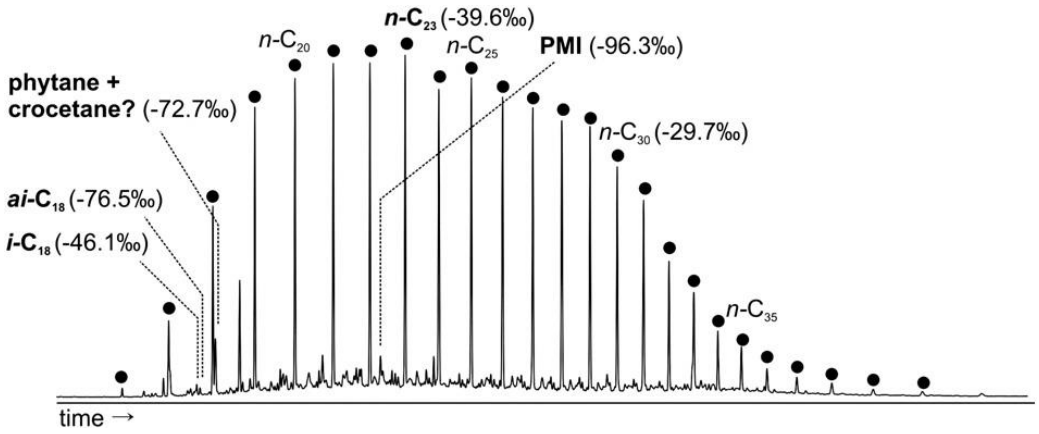

Figure 50: Chromatogram of aliphatic hydrocarbons of the pre-extracted carbonate sample from Ispaster with $\delta^{13}C$ values of selected compounds.

Table 5: Stable carbon isotope signatures of biomarkers from the Ispaster carbonate.

compound	$\delta^{13}C$ vs. VPDB (‰)
2-methyl heptadecane (*i*-C_{18})	-46.1
3-methyl heptadecane (*ai*-C_{18})	-76.5
octadecane (*n*-C_{18})	-36.1
phytane/crocetane	-72.7
2-methyl octadecane (*i*-C_{19})	-43.3
3-methyl octadecane (*ai*-C_{19})	-57.4
nonadecane (*n*-C_{19})	-37.2
eicosane (*n*-C_{20})	-33.2
henicosane (*n*-C_{21})	-34.6
docosane (*n*-C_{22})	-36.9
2,6,10,15,19-pentamethylicosane (PMI)	-96.3
tricosane (*n*-C_{23})	-39.6
tetracosane (*n*-C_{24})	-33.1
pentacosane (*n*-C_{25})	-34.0
hexacosane (*n*-C_{26})	-29.5
heptacosane (*n*-C_{27})	-29.4
octacosane (*n*-C_{28})	-30.9
nonacosane (*n*-C_{29})	-31.3
triacontane (*n*-C_{30})	-29.7
hentriacontane (*n*-C_{31})	-29.5
pentatriacontane (n-C_{35}) + $C_{40:0}$ biphytane	-25.8

6.5.1.6.2 Pockmark geometry

Turbidite lenses are a common architectural element of deep-water deposits (Pickering et al., 1995). They have been interpreted to form through one of three main processes: (i) differential deposition due to an obstacle barrier on an otherwise flat seabed. This seems unlikely for most of the occurrences at Ispaster because it typically results in a sediment ridge upstream from the obstacle and only a thin deposit downstream (Alexander & Morris, 1994), while at Ispaster we observed similar thicknesses upstream and downstream of the carbonate bodies with a maximum adjacent to them. (ii) Differential erosion at the top of sheet sands by by-passing currents. This seems also unlikely because this type of deposit shows sharp and erosive upper contacts (e.g. Mutti & Normark, 1987), while the sandstones at Ispaster have gradual tops, indicating no erosive reshaping of the beds. (iii) Compensation by depositional smoothing of depressions on the seafloor, whereby the resulting beds show concave bases and flat tops (e.g. Mutti et al., 1978; Mutti & Sonnino, 1981; Smith, 1995; Felletti, 2002). This is the configuration we see at Ispaster: flat tops of the turbidite lenses are indicated by the parallel overlying beds, and the bases are concave. Therefore, we interpret the sandstone lenses with the centrally located carbonates as the filling of seabed depressions or pockmarks due to depositional smoothing (Fig. 53). These paleo-pockmarks with authigenic carbonate lenses in their interiors are similar to the “eyed” pockmarks documented by Hovland (2002). The local onlap of sandstone turbidites against some carbonate lenses indicates low positive relieves at their tops. In these cases and since authigenic carbonates are interpreted as precipitated within muddy sediment at or just below the seabed, slight local erosion by the overlying turbidites are inferred.

Shape and dimension of these seabed depressions may be estimated from their sandstone-fills: the diameter of the depression should equal to the length of sandstone-fill, and its depth should be at least (due to compaction) the difference in thickness between the thickest and thinnest part of the lenticular sandstone. The dimensions of 47 of the sandstone lenses at Ispaster are plotted in Fig. 54: diameters range from 0.8 and 24.4 m (mean 6.6 m) and depths range from 2.5 and 42 cm (mean 10 cm). The mean aspect ratio

(diameter:depth) of the lenses is 660:1. These dimensions are at the smaller end of the size range of present-day pockmarks, the so-called unit-pockmarks (Hovland et al., 1984; Hovland, 2002; Hovland et al., 2010).

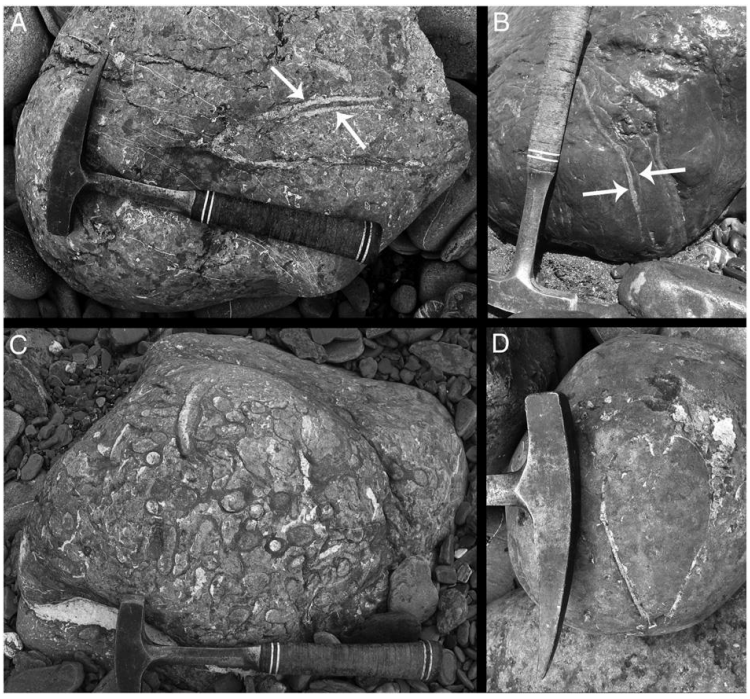

Figure 51: *In situ* macrofossils in the Ispaster seep carbonates. (A, B) Two blocks showing how shells of the elongate modiomorphid bivalve *Caspiconcha* sp. are tucked into another. (C) Block with abundant tubular structures or burrows; when cracked open this block revealed numerous *Callianassa* claws. (D) Cross section of a large lucinid bivalve. Hammer for scale.

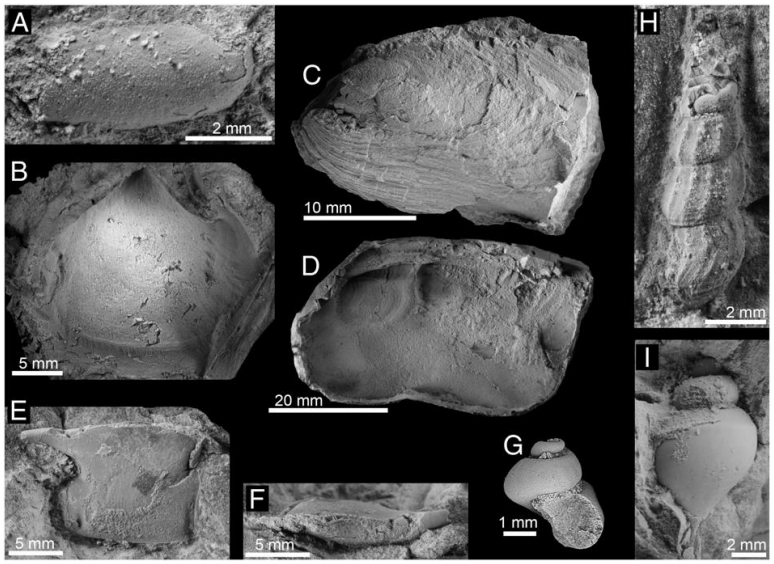

Figure 52: Fossil invertebrates from the Ispaster seep carbonates. (A) Solemyid bivalve. (B) Rubber cast of a lucinid bivalve, showing pallial line and the short but elongate anterior adductor muscle scar. (C, D) The modiomorphid bivalve *Caspiconcha* sp., (C) external view, (D) rubber cast of anterior part of shell, showing anterior adductor and retractor muscle scars. (E, F) Two views on a claw of the crustacean *Callianassa*. (G) Internal mold of an unidentified, trochospiral gastropod. (H) The gastropod *Hokkaidoconcha* sp. (I) Aporrhaid gastropod.

6.5.1.6.3 Mechanism of pockmark formation

The close spatial association of the lenticular sandy turbidites and the methane-seep carbonates suggests a genetic link between them. The mechanisms commonly invoked in pockmark formation include the removal of sediments from the pockmark driven directly or indirectly by sediment fluid flow (reviewed by Paull et al., 1992). The studied pockmarks at Ispaster, however, show little indication for erosion or sediment removal processes. Therefore, we suggest the following mechanisms for their formation: The initial process may have been the degassing and dewatering of methane-rich muddy sediments, and the resulting loss of volume of these sediments. A similar degassing and/or dewatering mechanism has been proposed for some subsidence moats related to present-day mud volcanoes (Camerlenghi et al., 1995; Van Rensbergen et al., 2005; Praeg et al., 2009). The continued flow of methane-rich fluids resulted in carbonate precipitation, which may have caused further subsidence within the pockmark due to the higher density of limestone compared to muddy sediments, especially when the latter are charged with gas (carbonate density 2.1–2.7 g cm^{-3} versus mud density 1.5–1.6 g cm^{-3} (cf. Carmichael, 1984; Emery & Uchupi, 1984). A similar weight-induced enhancement of subsidence has been proposed for some moats of submarine mud volcanoes (e.g. Praeg et al., 2009).

The pockmarks at Ispaster may thus have formed as follows (Fig. 55):

- Stage 1: Methane-rich fluids start seeping into the flat and smooth seabed;
- Stage 2: Degassing and dewatering of the methane-charged mud results in the initial pockmark formation, AOM and carbonate precipitation, and colonization of the seabed by the seep macrofauna (2a); sporadically, turbidity flows deposit sandy sediments which fill the pockmark (2b);
- Stage 3: Continued methane seepage and sedimentation of mud and occasional sandy turbidites results in (i) upward growth of the seep carbonate, (ii) the incorporation of turbidite deposits and faunal remains (i.e., shells, tubular structures or burrows) into the seep-carbonate body, and (iii) possibly further subsidence of the pockmark due to degassing/dewatering of mud and the weight of the carbonate.

• Stage 4: Carbonate precipitation ceases, either because fluid flow comes to a halt, or is blocked or redirected by the sealing of the fluid migration pathway due to carbonate precipitation (the “self-sealing process” of Hovland, 2002), and the pockmark is eventually filled by subsequent sandy turbidites.

This is of course a simplified and idealized model. In reality, the different stages intermingle and overlap temporally and spatially. The carbonate lenses (and stacked pockmark fills) in the Ispaster pockmark fields have a limited thickness up to 2.5 m, and their upper contacts often coincide approximately with the base of an adjacent carbonate body. It indicates that when the growth of a carbonate body (and pockmark) ends, approximately coevally begins the formation of a new adjacent carbonate body (and pockmark). Since carbonate precipitation is indicative of fluid seepage, the observed jumps of the sites of carbonate formation reflect the jump of the fluid pathway. These jumps are interpreted as the consequence of self-sealing process (e.g. Hovland, 2002; Hovland et al., 2010), whereby methane-induced carbonate precipitation causes the clogging or sealing of the fluid plumbing system and its subsequent redirection some meters distant from the original site (Fig. 56).

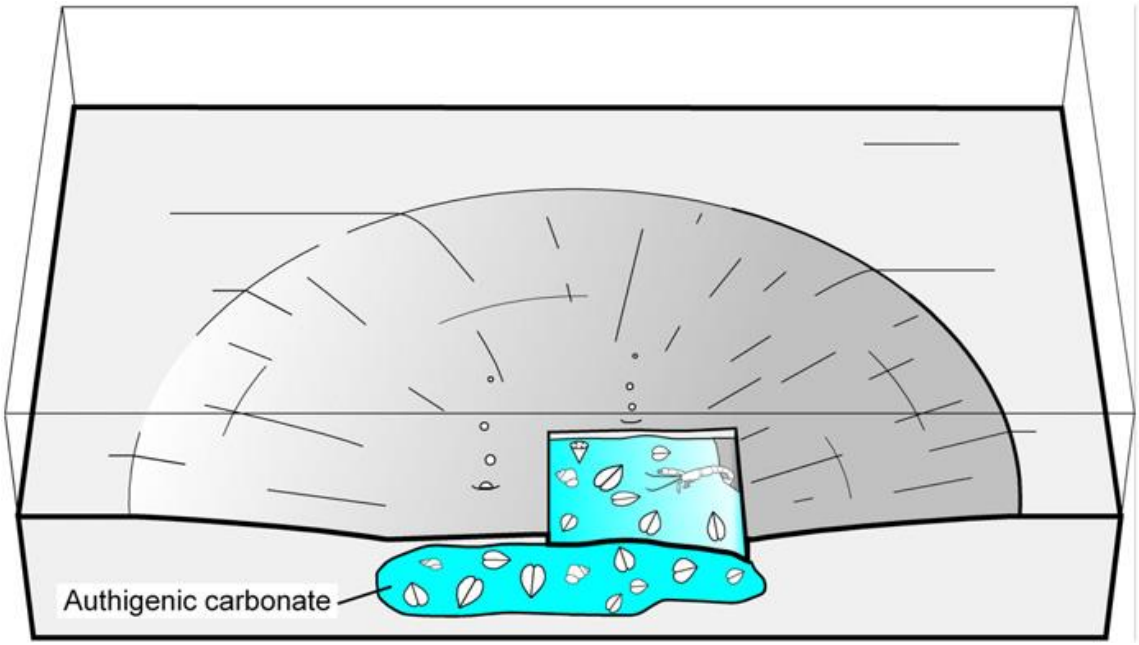

Figure 53: Ispaster seabed depression in which interior methane-derived authigenic carbonates precipitate. A portion of the seabed mud sediment has been removed in order to show dense in fauna (large bivalves, gastropods and shrimps) which inhabits the depression interior. This depression is interpreted as “eyed” unit-pockmark.

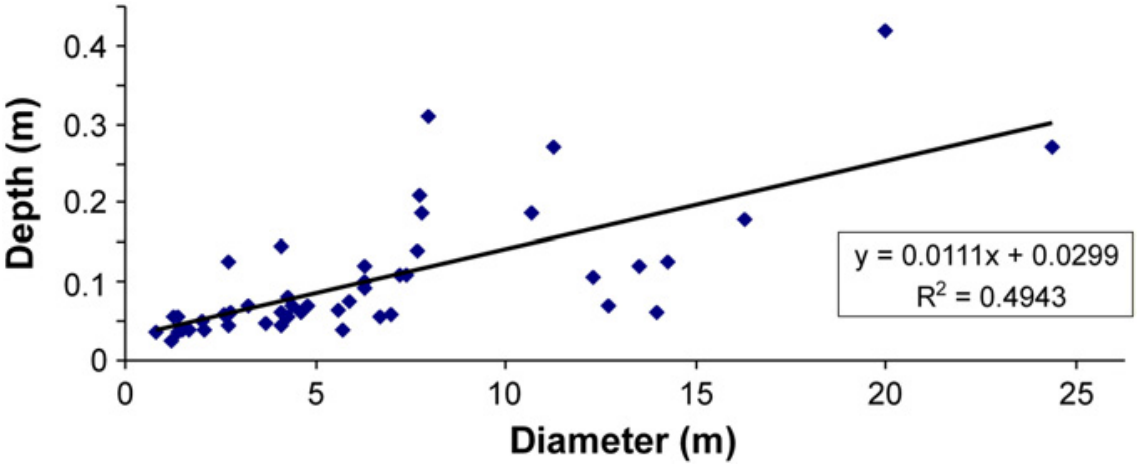

Figure 54: Depression diameter versus depth for 47 depressions measured in the study area. A crude linear correlation is observed.

6.5.1.6.4 Pockmark field formation and controls

Why was the formation of pockmarks and associated methane-seep carbonates in the Ispaster area constrained to two short-lived pulses, the intervals A and B, during the Late Albian? Sea-level and temperature fluctuations are an important control on seep-carbonate formation (Teichert et al., 2003; Kiel, 2009): seep-carbonates are often associated with sea-level fall and/or lowstands, but the Late Albian in general was a period of sea-level rise (Haq et al., 1987). Tectonics and related sediment load was considered a main factor controlling the formation and distribution of seep carbonates (the 'Tepee Buttes') in the Western Interior Seaway of the USA (Metz, 2010). In the case of the Ispaster pockmark field, fluid seepage may have been triggered by the emplacement of magmatic intrusions. Thick volcanic successions and sub-volcanic intrusions formed in the Basque-Cantabrian Basin during Late Albian and Late Cretaceous (Meschede, 1987; Rossy, 1988) which indicate a main phase of volcanic activity roughly during auritus ammonite Subzone (Castañares et al., 2001), and thus contemporaneously with the development of the Ispaster seeps. Although the methane source of the Ispaster seeps is unclear, it seems possible that these magmatic intrusions caused the formation of thermogenic methane in the underlying, organic-rich formations, and provoked fractures that could have acted as conduits for methane-enriched fluids.

A commercial seismic profile across the study area shows at least two highly reflective structures at depths of 0.5 s and 0.75 s (Fig. 57). Although Cenozoic

inversion tectonics could have caused severe modifications in the original geometry of these structures, their high reflectivity, overall concordant character and coarse inverted cone geometry point to possible magmatic sills (e.g. Smallwood & Maresh, 2002). Considering a conservative mean seismic velocity of 4500 ms^{-1}, documented in shallow sedimentary rocks from a nearby commercial well (Gaviota field; Huedo-Cuesta et al., 2009), we estimate that the interpreted intrusions are presently at depths of 1125 m and 1690 m, respectively. Taking into account the regional dip (Fig. 37), they correspond to stratigraphic depths of 800 m and 1190 m below the studied interval. This means that the deepest structure is enclosed within the Otoio Formation, which is in agreement with the abundant rock fragments and fossils derived from that unit present in the dyke fills.

Shallow-depth magmatic intrusions usually cause both forced folding of the overlying deposits and peripheral fracturing above the tips of the intrusions (Pollard & Johnson, 1973; Cosgrove & Hillier, 2000; Thomson, 2007). Although structural evidence for folding in the Albian has not been observed at Ispaster, the significant drop in the proportion of sandy turbidites coincident with the two fluid expulsion events might have been the consequence of gentle positive relief in the seabed due to the emplacement of the magmatic intrusions (Fig. 58). Taking into account that Ispaster pockmark fields are located approximately above the northeastern tip of those structures (Fig. 57), described sandstone dykes could correspond to peripheral fractures, which played as conduits for upward flows of overpressured methane-rich fluids (Fig. 58). A similar role of intrusion-related peripheral fractures has been documented in both subsurface and outcrop examples (e.g. Bell & Butcher, 2002; Jamveit et al., 2004).

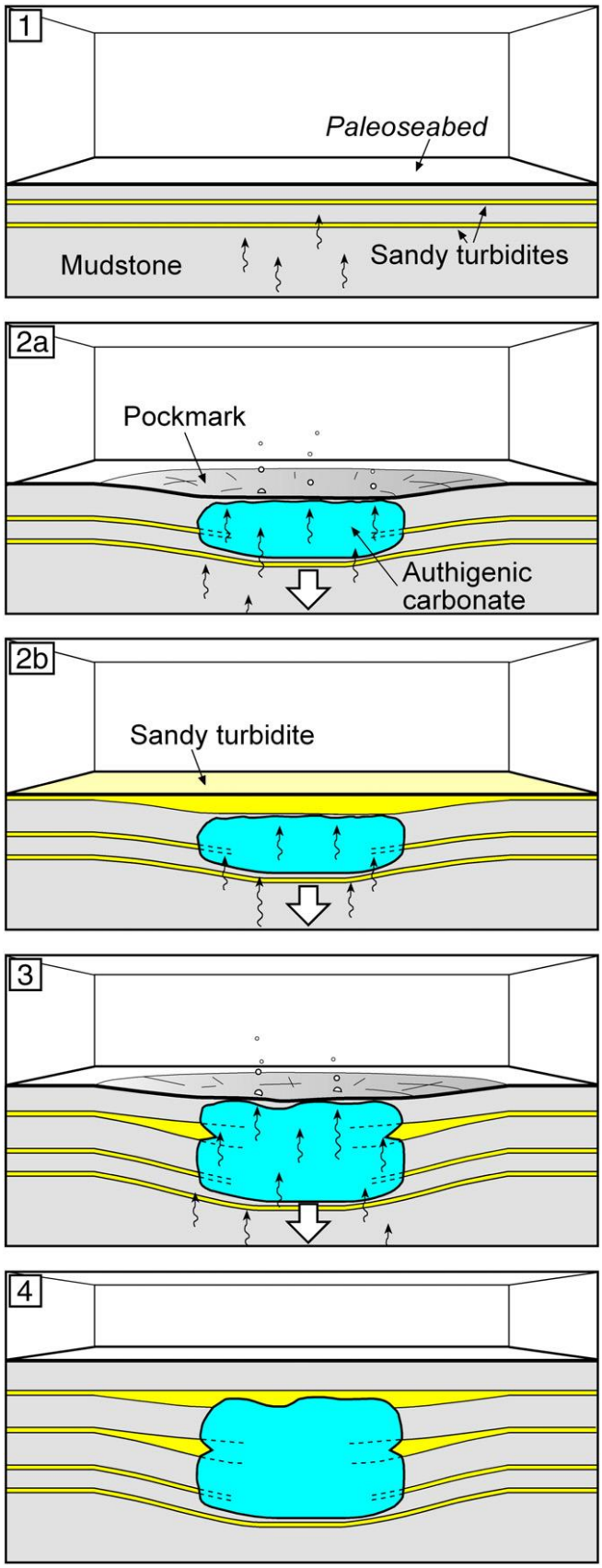

Figure 55: Formation mechanism and evolutionary stages for the Ispaster pockmarks. Degassing and dewatering of sediments aided by the weight of carbonate body trigger local subsidence and pockmark formation. Sandy turbidites fill pockmarks and smooth the seabed relief. Occasionally, turbidity flows can erode thin muddy sediments overlying authigenic carbonates. See explanations in the text.

6.5.1.6.5 Ecology and biogeography of the seep fauna

The macrofauna at the Ispaster seeps resembles that of other Cretaceous deep-water seep deposits. In particular, the large bivalve *Caspiconcha* sp. and the small, high-spired gastropod *Hokkaidoconcha* sp. are members of two genera that are known exclusively from ancient methane-seep deposits and, in the case of *Hokkaidoconcha*, also from other organic- and H_2S-rich environments such as sunken wood or large carcasses on the seafloor (Kelly et al., 2000; Kaim et al., 2008a; Kaim et al., 2008b; Kiel et al., 2008b; Kaim et al., 2009; Kaim & Kelly, 2009; Kiel et al., 2009; Kiel et al., 2010; Jenkins et al., in press.). Other faunal elements such as the shrimp *Callianassa*, the nuculanid bivalve *Acila*, the aporrhaid gastropod and the solitary coral are typically considered as "background fauna"; taxa that inhabit the surrounding seafloor and occasionally venture into the seep environment because of the abundance of organic matter (e.g. Hovland et al., 2012). Ecologically, the fauna is dominated by chemosymbiotic taxa (lucinids, e.g. Taylor & Glover, 2010) and potentially chemosymbiotic taxa (*Caspiconcha*, cf., Jenkins et al., in press.). The gastropods were most likely grazing on bacteria and/or detritus (*Hokkaidoconcha*, aporrhaids, cf., Barnes & Bagenal, 1951; Kaim et al., 2008a). Striking is the difference between the Ispaster fauna and the fauna of the Mutriku seep deposit, which is from the same stratigraphic interval (Late Albian) and only 16 km to the southeast of Ispaster (Agirrezabala, 2009), with which Ispaster shares almost no species. The Mutriku deposit lacks the seep-restricted taxa *Caspiconcha* and *Hokkaidoconcha*, but is instead dominated by a lucinid bivalve that differs morphologically from the lucinid at Ispaster, and includes a rudist bivalve, small solitary corals, and trochid gastropods (Agirrezabala, 2009), taxa that are rare or absent from Ispaster. The only shared species appear to be the nuculid bivalve *Acila* sp. and the solitary coral; taxa considered as "background fauna". This difference between the Ispaster and Mutriku seeps most likely results from the different depositional depths of these localities. In the oceans today, shallow-water seeps are largely inhabited by taxa that are also found on the surrounding seafloor (Dando, 2010), while the typical seep-restricted taxa start to appear in depths around 200–400 m (Sahling et al., 2003). A similar pattern has been observed among Cenozoic

and late Mesozoic seep faunas (Amano et al., 2010; Kiel, 2010a). This interpretation is consistent with sedimentological characteristics and foraminifera associations, which indicate a mesopelagic paleobathymetry for the seep at Mutriku and a deeper upper to middle bathypelagic environment for the Ispaster seeps (Agirrezabala, 1996; García-Mondéjar et al., 2004).

Biogeographically, the Ispaster seep fauna shows links to the Atlantic and Tethyan realm, as well as to the Pacific region. The most prominent species, the elongate, straight-sided *Caspiconcha* sp. is very similar to species at Early Cretaceous seep deposits of the North Atlantic and Tethyan realm: *Caspiconcha whithami* from the Barremian of eastern Greenland (Kelly et al., 2000) and *C. rubani* from the Hauterivian of the Crimean peninsula (Kiel & Peckmann, 2008; Kiel et al., 2010). In contrast, the *Hokkaidoconcha* sp. at Ispaster most closely resembles *H. tanabei* from the late Cretaceous of Japan (Kaim et al., 2008a) and *H. occidentalis* from the early Cretaceous of California (Kiel et al., 2008b). Interestingly, the European species *H. novacula*, of Late Jurassic age (Kiel et al., 2010) has a quite different ornamentation, as has the Late Jurassic Antarctic species *H. hignalli* (Kaim et al., 2009). The large and abundant, but poorly preserved lucinid at Ispaster is more difficult to place in a biogeographic context. Similar in shell outline and adductor muscle scar morphology is *Ezolucina inflata* from the Late Cretaceous of Japan (Amano et al., 2008). Other taxa with similar adductor muscle scars are *Miltha* sp. from a Late Cretaceous methane seep deposit in Japan (Hikida et al., 2003), and *Cubatea asphalitica* from an Oligocene seep deposit in Cuba (Cooke, 1919; Kiel & Peckmann, 2007) but these species have a more elliptical shell outline. The aporrhaid gastropod and the nuculid *Acila* are considered as background fauna here as these taxa were widespread in marine deposits of Mesozoic age; however, related taxa have occasionally been found at Mesozoic and Early Cenozoic seep deposits world-wide (Kaim et al., 2008a; Kiel et al., 2008a; Kiel, 2010b, a; Kiel et al., 2010).

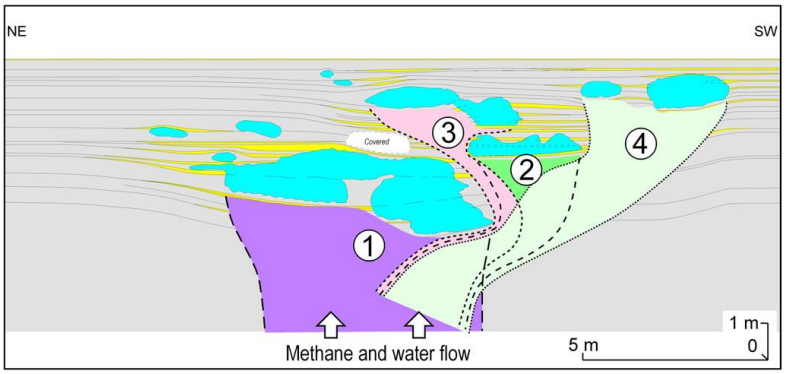

Figure 56: Interpretation of the successive pathways (1–4) of the fluid flow in a cluster of authigenic carbonate lenses and related pockmarks fills (A interval, same that Fig. 42A). Self-sealing of a carbonate body causes the clogging of the plumbing system. It leads contorting of the upward fluid flow pathway avoiding sealed carbonate body. Thus, a second seep form some meters away from the previous locus, where a new pockmark births and carbonate precipitates.

6.5.1.6.6 Late diagenesis

Carbonate precipitation during late diagenesis was restricted to the small remaining pore spaces or the replacement of previous carbonate phases. Crude oil has been part of the late diagenetic fluids. This is evident from (i) its exclusive occurrence as pore infill among late diagenetic dolomite and sparry calcite, and (ii) its Raman spectra that show only bands of amorphous carbon but lacks the shoulder in the 'D'-band, which is distinctly different from Raman spectra of early diagenetic mineral phases. Interesting in this context is that the vast majority of $\delta^{18}O$ values measured at the Ispaster seep carbonates are in a narrow range roughly between −10 and −12‰, regardless of the sampled carbonate phase. This is rather unusual among fossil seep carbonates and strongly suggests a late diagenetic resetting of the oxygen isotope signature. This resetting might result from an influence of meteoric water, which is not unlikely even given the assumed offshore setting of the Ispaster pockmark field, because continental freshwater can occur several tens of kilometers offshore (Kooi & Groen, 2001).

Alternatively, the $\delta^{18}O$ values may be interpreted to reflect ambient pore water temperatures during late diagenesis. In this case, the temperature would have been in the range of 70 to 80 °C and thus within the range of saddle dolomite precipitation (Radke & Mathis, 1980; Warren, 2000). Several characteristics of the late diagenetic phases of the Ispaster seep carbonates, including the precipitation of saddle dolomite and other ^{13}C- and ^{18}O-depleted carbonate

cements together with the formation of pore-filling solid bitumen, are considered to result from the oxidation of hydrocarbons by high-temperature thermochemical sulfate reduction (Machel et al., 1995). This inorganic process occurs under high temperatures (>100 °C) and the oxidation of hydrocarbons takes place by the reduction of sulfate derived from the dissolution of gypsum and/or anhydrite (Machel, 2001). This temperature range is well above that derived from our oxygen isotope ratios; however, our estimated temperatures may be erroneously low because the assumed parent fluid is sea water. Given that saddle dolomite precipitation and thermochemical sulfate reduction typically take place in hypersaline brine fluids enriched in ^{18}O (Spencer, 1987; Davis & Smith Jr., 2006), temperature during saddle dolomite precipitation could be up to several tens degrees higher than calculated for a sea water as parent fluid.

TOC values from mudstones of the Black Flysch Group at Ispaster are 0.95% on average, and, hence, the mudstones constitute a potential source rock for hydrocarbons (Tissot & Welte, 1984). Because oils are commonly ^{13}C-depleted by 1‰ to 3‰ compared to kerogen in their source rocks (Hoefs, 1997), the carbon isotope signature of the pyrobitumen can be used to constrain the source from which it was derived. Accordingly, the close but slightly more depleted mean ^{13}C value of the pyrobitumen (−26.9‰) compared to that of the Black Flysch Group deposits (−25.1‰) suggests that the latter was the source of oil at Ispaster. Other potential source rocks from the basin are Carboniferous coals and Jurassic black shales but their dissimilar isotopic values (Agirrezabala et al., 2008, and references therein) preclude a possible sourcing from those rocks.

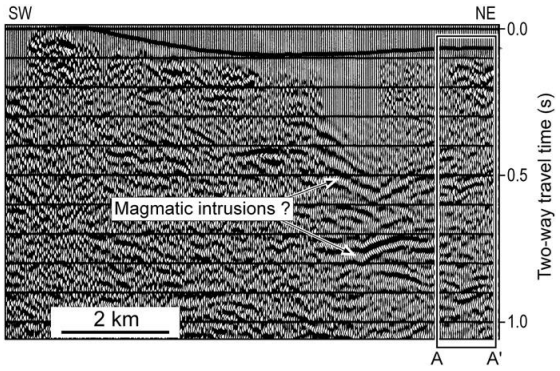

Figure 57: Seismic profile across the study and neighboring areas. At least two highly reflective structures can be distinguished (NE part of the profile), which could correspond to magmatic intrusions. The study area is located at the NE end of these structures. The A–A′ section corresponds to the study area, and its trace is illustrated in Fig. 37.

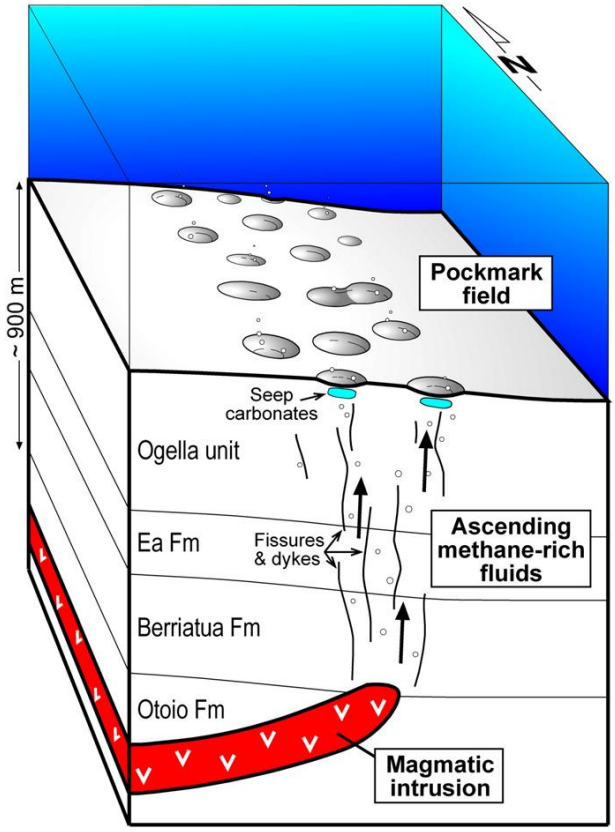

Figure 58: Interpretation of the Ispaster pockmark field. The magmatic intrusion initiated or enhanced thermogenic methane production in the subsurface and may also have produced the fissures that acted as fluid conduits for the hydrocarbon-rich fluids.

6.5.1.7 Conclusions

Our multidisciplinary study of an Albian outcrop of the Black Flysch Group reveals the presence of two fields of paleo-pockmarks in which authigenic carbonate lenses precipitated and rich fossil biota developed. Based on the geometry of the pockmark fills, up to 24.4 m wide and 42 cm deep pockmarks have been determined. Early diagenetic microfacies, stable carbon isotopes with $\delta^{13}C$ values as low as −41.6‰, Raman spectroscopy and hydrocarbon biomarkers (e.g. 2,6,10,15,19-pentamethylicosane) with strong depletions in ^{13}C (−96.3‰) clearly show that they precipitated, for the most part, due to the anaerobic oxidation of methane. The macrofauna resembles that of other late Mesozoic deep-water methane-seeps world-wide, and is dominated by large lucinid and *Caspiconcha* bivalves, and hokkaidoconchid gastropods. Sedimentological analysis suggests that the pockmarks formed due to subsidence induced by dewatering and degassing of the methane-charged

sediment, perhaps enhanced by the weight of the carbonate bodies. The analysis of clusters of pockmarks and associated carbonate bodies indicates the jump and redirection of the subsurface fluid pathway interpreted as the consequence of a self-sealing process. Subsurface and surface data suggest that the formation of the two pockmark fields resulted from methane-rich fluid expulsions triggered by the emplacement of magmatic intrusions. Intrusion-related fractures could have acted as conduits for overpressured fluids sourced from at least 900 m below the paleoseabed. During late diagenesis the carbonate $\delta^{18}O$ values were reset to a narrow range of −12 to −10‰, the remaining pore spaces and fissures were filled with pyrobitumen, and additional carbonate phases precipitated, potentially due to thermochemical sulfate reduction processes.

Acknowledgments

This paper is dedicated to the memory of our wonderful colleague recently deceased Jordi M. de Gibert (Universitat de Barcelona) who generously examined the tubular structures found. We thank H.G. Owen and M. López-Horgue from the Natural History Museum and the Euskal Herriko Unibertsitatea, respectively, for ammonite classification. We also thank P. García-Garmilla from the Euskal Herriko Unibertsitatea for assistance with cathodoluminescence microscopy. Allen Frankovich from the Energiaren Euskal Erakundea kindly supported seismic lines. We are indebted to A. Hackmann (Göttingen) for thin section preparation, J. Germer (Göttingen) for support during biomarker extraction, and J. Dyckmans from the “Centre for Stable Isotope Research and Analysis” at the University of Göttingen for help with compound specific stable carbon isotope analysis. Bas van de Schootbrugge, Barbara Teichert, Martin Hovland and one anonymous reviewer are thanked for their useful and constructive comments. This work was financially supported by the Ministerio de Ciencia e Innovación (project CGL2009-08545 to LMA), the Euskal Herriko Unibertsitatea (project EHU11/42 to LMA), the Deutsche Forschungsgemeinschaft (grants BL971/1-3 to MB and Ki802/6-1 to SK) and the Courant Research Centre Geobiology of the University Göttingen (to JR and MB). This is publication no. 111 of the Courant Research Centre Geobiology of the University Göttingen.

References

Agirrezabala, L.M. (1996) El Aptiense-Albiense del Anticlinorio Nor-Vizcaíno entre Gernika y Azpeitia. *Ph.D thesis*, Euskal Herriko Unibertsitatea, Bilbo, pp. 429.

Agirrezabala, L.M. (2009) Mid-Cretaceous hydrothermal vents and authigenic carbonates in a transform margin, Basque-Cantabrian Basin (western Pyrenees): a multidisciplinary study. *Sedimentology* 56: 969-996.

Agirrezabala, L.M., Dorronsoro, C. and Permanyer, A. (2008) Geochemical correlation of pyrobitumen fills with host mid-Cretaceous Black Flysch Group (Basque-Cantabrian Basin, western Pyrenees). *Organic Geochemistry* 39: 1185-1188.

Agirrezabala, L.M. and García-Mondéjar, J. (1994) A coarse grained turbidite system with morphotectonic control (Middle Albian, Ondarroa, northern Iberia). *Sedimentology* 41: 383-407.

Alexander, J. and Morris, S. (1994) Observation on experimental, nonchannelized, highconcentration turbidity currents and variations in deposits around obstacle. *Journal of Sedimentary Research A* 64: 899-909.

Allmendinger, R.W. (2002) *Stereonet for Macintosh*. pp. 42.

Amano, K., Jenkins, R.G., Aikawa, M. and Nobuhara, T. (2010) A Miocene chemosynthetic community from the Ogaya Formation in Joetsu: Evidence for depth-related ecologic control among fossil seep communities in the Japan Sea back-arc basin. *Palaeogeography, Palaeoclimatology, Palaeoecology* 286: 164-170.

Amano, K., Jenkins, R.G., Kurihara, Y. and Kiel, S. (2008) A new genus for Vesicomya inflate Kanie and Nishida, a lucinid shell convergent with that of vesicomyids, from Cretaceous strata of Hokkaido, Japan. *Veliger* 50: 255-262.

Andresen, K.J., Huuse, M. and Clausen, O.R. (2008) Morphology and distribution of Oligocene and Miocene pockmarks in the Danish North Sea – implications for bottom current activity and fluid migration. *Basin Research* 20: 445-466.

Aranburu, A., Fernández-Mendiola, P.A., López-Horgue, M.A. and García-Mondéjar, J. (2002) Syntectonic hydrothermal calcite in a faulted carbonate platform margin (Albian of Jorrios, northern Spain). *Sedimentology* 49: 875-890.

Barnes, H. and Bagenal, T.B. (1951) Observations on Nephrops norvegicus (L.) and on an epizoic population of Balanus crenatus Brug. *Journal of the Marine Biological Association of the United Kingdom* 30: 369-380.

Beauchamp, B. and Savard, M. (1992) Cretaceous chemosynthetic carbonate mounds in the Canadian Arctic. *PALAIOS* 7: 434-450.

Beimforde, C., Schäfer, N., Dörfelt, H., Nascimbene, P.C., Singh, H., Heinrichs, J., Reitner, J., Rana, R.S. and Schmidt, A.R. (2011) Ectomycorrhizas from a Lower Eocene angiosperm forest. *New Phytologist* 192: 988-996.

Bell, B. and Butcher, H. (2002) On the emplacement of sill complexes: evidence from the Faroe-Shetland Basin. In: *The North Atlantic Igneous Province: Stratigraphy, Tectonic, volcanic and Magmatic Processes, Vol.Special Publications 197*, edited by D.W. Jolley and B.R. Bell, Geological Society, London, UK, pp. 307-329.

Blumenberg, M., Seifert, R., Reitner, J., Pape, T. and Michaelis, W. (2004) Membrane lipid patterns typify distinct anaerobic methanotrophic consortia. *Proceedings of the National Academy of Sciences of the United States of America* 101: 11111-11116.

Blumenberg, M., Thiel, V., Riegel, W., Kah, L.C. and Reitner, J. (2012) Biomarkers of black shales formed by microbial mats, Late Mesoproterozoic (1.1 Ga) Taoudeni Basin, Mauritania. *Precambrian Research* 196–197: 113-127.

Camerlenghi, A., Cita, M.B., Vedova, B.D., Fusi, N., Mirabile, L. and Pellis, G. (1995) Geophysical evidence of mud diapirism on the Mediterranean Ridge accretionary complex. *Marine Geophysical Researches* 17: 115-141.

Campbell, K.A. (2006) Hydrocarbon seep and hydrothermal vent paleoenvironments and paleontology: Past developments and future research directions. *Palaeogeography, Palaeoclimatology, Palaeoecology* 232: 362-407.

Campbell, K.A., Farmer, J.D. and Des Marais, D. (2002) Ancient hydrocarbon seeps from the Mesozoic convergent margin of California: carbonate geochemistry, fluids and palaeoenvironments. *Geofluids* 2: 63-94.

Carmichael, R.S. (1984) *Handbook of Physical Properties of rocks, vol. III*. CRC Press, Boca Raton, FL, pp. 360.

Castañares, L.M., Robles, S., Gimeno, D. and Vicente Bravo, J.C. (2001) The Submarine Volcanic System of the Errigoiti Formation (Albian-Santonian of the Basque-Cantabrian Basin, Northern Spain): Stratigraphic Framework, Facies, and Sequences. *Journal of Sedimentary Research* 71: 318-333.

Cole, D., Stewart, S.A. and Cartwright, J.A. (2000) Giant irregular pockmark craters in the Palaeogene of the Outer Moray Firth Basin, UK North Sea. *Marine and Petroleum Geology* 17: 563-577.

Cooke, C.W. (1919) Contributions to the geology and paleontology of the West Indies IV. *Tertiary mollusks from the leeward islands and Cuba*, Carnegie Institution of Washington Publications 291, pp. 103-156.

Cosgrove, J.W. and Hillier, R.D. (2000) Forced-fold development within Tertiary sediments of the Alba Field, UKCS: evidence of differential compaction and postdepositional sandstone remobilisation. In: *Forced Folds and Fractures, Vol.Special Publications, 169*, edited by J.W. Cosgrove and M.S. Ameen, Geological Society, London, UK, pp. 61-72.

Craig, H. (1957) Isotopic standards for carbon and oxygen and correction factors for mass-spectrometric analysis of carbon dioxide. *Geochimica et Cosmochimica Acta* 12: 133-149.

Dando, P.R. (2010) Biological communities at marine shallow-water seep and vent sites. In: *The Vent and Seep Biota, Topics in Geobiology Vol.33*, edited by S. Kiel, Springer, Heidelberg, pp. 333-378.

Dando, P.R., Austen, M.C., Burke, R.J., Kendall, M.A., Kennicutt, M.C., Judd, A.G., Moore, D.C., O' Hara, S.C.M., Schmaljohann, R. and Southward, A.J. (1991) Ecology of a North Sea pockmark with an active methane seep. *Marine Ecology Progress Series* 70: 49-63.

Davis, G.R. and Smith Jr., L.B. (2006) Structurally controlled hydrothermal dolomite reservoir facies: an overview. *American Association of Petroleum Geologists Bulletin* 90: 1641-1690.

Elvert, M., Boetius, A., Knittel, K. and Jørgensen, B.B. (2003) Characterization of Specific Membrane Fatty Acids as Chemotaxonomic Markers for Sulfate-Reducing Bacteria Involved in Anaerobic Oxidation of Methane. *Geomicrobiology Journal* 20: 403-419.

Elvert, M., Suess, E. and Whiticar, M.J. (1999) Anaerobic methane oxidation associated with marine gas hydrates: superlight C-isotopes from saturated and unsaturated C20 and C25 irregular isoprenoids. *Naturwissenschaften* 86: 295-300.

Emery, K.O. and Uchupi, E. (1984) *The Geology of the Atlantic Ocean*. Springer, Berlin, Germany, pp. 1050.

Felletti, F. (2002) Complex bedding geometries and facies associations of the turbiditic fill of a confined basin in a transpressive setting (Castagnola Fm., Tertiary Piedmont Basin, NW Italy). *Sedimentology* 49: 645-667.

Folk, R.L. (1987) Detection of organic matter in thin-sections of carbonate rocks using a white card. *Sedimentary Geology* 54: 193-200.

Gaillard, C., Rio, M., Rolin, Y. and Roux, M. (1992) Fossil chemosynthetic communities related to vents or seeps in sedimentary basins; the pseudobioherms of southeastern France compared to other world examples. *PALAIOS* 7: 451-465.

García-Mondéjar, J., Agirrezabala, L.M., Aranburu, A., Fernández-Mendiola, P.A., Gómez-Pérez, I., López-Horgue, M. and Rosales, I. (1996) Aptian— Albian tectonic pattern of the Basque— Cantabrian Basin (Northern Spain). *Geological Journal* 31: 13-45.

García-Mondéjar, J., Fernández-Mendiola, P., Agirrezabala, L., Aranburu, A., López-Horgue, M., Iriarte, E. and Martín de Rituerto, S. (2004) El Aptiense–Albiense de la Cuenca Vasco–Cantábrica. Geología de España. *IGME-SGE*: 291-296.

Gemmer, L., Huuse, M., Clausen, O.R. and Nielsen, S.B. (2002) Mid-Palaeocene palaeogeography of the eastern North Sea basin: integrating geological evidence and 3D geodynamic modelling. *Basin Research* 14: 329-346.

Goedert, J.L. and Squires, R.L. (1990) Eocene deep-sea communities in localized limestones formed by subduction-related methane seeps, southwestern Washington. *Geology* 18: 1182-1185.

Greinert, J., Bohrmann, G. and Elvert, M. (2002) Stromatolitic fabric of authigenic carbonate crusts: result of anaerobic methane oxidation at cold seeps in 4,850 m water depth. *International Journal of Earth Sciences* 91: 698-711.

Haq, B.U., Hardenbol, J. and Vail, P.R. (1987) Chronology of fluctuating sea-levels since the Triassic. *Science* 235: 1156-1167.

Hikida, Y., Suzuki, S., Togo, Y. and Ijiri, A. (2003) An exceptionally well-preserved fossil seep community from the Cretaceous Yezo Group in the Nakagawa area, Hokkaido, northern Japan. *Paleontological Research* 7: 329-342.

Hinrichs, K.-U., Hayes, J.M., Sylva, S.P., Brewer, P.G. and DeLong, E.F. (1999) Methane-consuming archaebacteria in marine sediments. *Nature* 398: 802-805.

Hoefs, J. (1997) *Stable Isotope Geochemistry*. Springer, Berlin, Germany, pp. 201.

Hovland, M. (1982) Pockmarks and the Recent geology of the central section of the Norwegian Trench. *Marine Geology* 47: 283-301.

Hovland, M. (1989) Modern analogues to Middle Ordovician sedimentary mounds and washout depressions. *Journal of Sedimentary Research* 59: 585-589.

Hovland, M. (2002) On the self-sealing nature of marine seeps. *Continental Shelf Research* 22: 2387-2394.

Hovland, M., Gardner, J.V. and Judd, A.G. (2002) The significance of pockmarks to understanding fluid flow processes and geohazards. *Geofluids* 2: 127-136.

Hovland, M., Heggland, R., De Vries, M.H. and Tjelta, T.I. (2010) Unit-pockmarks and their potential significance for predicting fluid flow. *Marine and Petroleum Geology* 27: 1190-1199.

Hovland, M., Jensen, S. and Fichler, C. (2012) Methane and minor oil macro-seep systems — Their complexity and environmental significance. *Marine Geology* 332–334: 163-173.

Hovland, M. and Judd, A. (1988) *Seabed Pockmarks and Seepage: Impact on Geology, Biology, and the Marine Environment*. Graham & Trotman, London, UK.

Hovland, M., Judd, A.G. and King, L.H. (1984) Characteristic features of pockmarks on the North Sea Floor and Scotian Shelf. *Sedimentology* 31: 471-480.

Hovland, M., Talbot, M., Olaussen, S. and Aasberg, L. (1985) Recently formed methane-derived carbonates from the North Sea floor. In: *Petroleum Geochemistry in Exploration of the Norwegian Shelf*, edited by B.M. Thomas, Norwegian Petroleum Soc., Graham & Trotman, pp. 263-266.

Hovland, M., Talbot, M.R., Qvale, H., Olaussen, S. and Aasberg, L. (1987) Methane-related carbonate cements in pockmarks of the North Sea. *Journal of Sedimentary Research* 57: 881-892.

Huedo-Cuesta, J.L., Cole, C., Pérez-García, A., Zucconi, V., Clauss, O., Sese-Martínez, V.H. and Muskaj, J.S. (2009) Construcción del modelo de velocidades para el procesado en profundidad de la sísmica de la Fragata 3D (plataforma y talud continentales de Vizcaya). *6th Simposio Margen Ibérico Atlántico MIA09*, pp. 93-96.

Jamveit, B., Svensen, H., Podladchikov, Y.Y. and Planke, S. (2004) Hydrothermal vent complexes associated with sill intrusions in sedimentary basins. In: *Physical Geology of High-Levelmagmatic Systems, Vol.Special Publications 234*, edited by C. Breitkreuz and N. Petford, Geological Society, London, UK, pp. 233-241.

Jenkins, R.G., Kaim, A., Little, C.T., Iba, Y., Tanabe, K. and Campbell, K.A. (in press.) Worldwide distribution of modiomorphid bivalve genus Caspiconcha in late Mesozoic hydrocarbon seeps. *Acta Palaeontologica Polonica*.

Judd, A. and Hovland, M. (2007) *Seabed fluid flow: the impact on geology, biology and the marine environment*. Cambridge University Press, Cambridge, pp. 475.

Kaim, A., Jenkins, R.G. and Hikida, Y. (2009) Gastropods from Late Cretaceous hydrocarbon seep deposits in Omagari and Yasukawa, Nakagawa area, Hokkaido, Japan. *Acta Palaeontologica Polonica* 54: 463-690.

Kaim, A., Jenkins, R.G. and Warén, A. (2008a) Provannid and provannid-like gastropods from Late Cretaceous cold seeps of Hokkaido (Japan) and the fossil record of the Provannidae (Gastropoda: Abyssochrysoidea). *Zoological Journal of the Linnean Society* 154: 421-436.

Kaim, A. and Kelly, S.R.A. (2009) Mass occurrence of hokkaidoconchid gastropods in the Upper Jurassic methane seep carbonate from Alexander Island, Antarctica. *Antarctic Science* 21: 279-284.

Kaim, A., Kobayashi, Y., Echizenya, H., Jenkins, R.G. and Tanabe, K. (2008b) Chemosynthesis-based associations on Cretaceous plesiosaurid carcasses. *Acta Palaeontologica Polonica* 53: 97-104.

Kelly, S.R.A., Blanc, E., Price, S.P. and Withham, A.G. (2000) Early Cretaceous giant bivalves from seep-related limestone mounds, Wollaston Forland, Northeast Greenland. In: *The evolutionary biology of the Bivalvia, Vol.177*, edited by E.M. Harper, J.D. Taylor and J.A. Crame, Geological Society of London, Special Publication, London, pp. 227-246.

Kiel, S. (2009) Global hydrocarbon seep carbonate precipitation correlates with deep-water temperatures and eustatic sea-level fluctuations since the late Jurassic. *Terra Nova* 21: 279-284.

Kiel, S. (2010a) The fossil record of vent and seep mollusks. In: *The Vent and Seep Biota, Topics in Geobiology Vol.33*, edited by S. Kiel, Springer, Heidelberg, pp. 255-278.

Kiel, S. (2010b) On the potential generality of depth-related ecologic structure in cold-seep communities: Cenozoic and Mesozoic examples. *Palaeogeography, Palaeoclimatology, Palaeoecology* 295: 245-257.

Kiel, S., Amano, K., Hikida, Y. and Jenkins, R.G. (2009) Wood-fall associations from Late Cretaceous deep-water sediments of Hokkaido, Japan. *Lethaia* 42: 74-82.

Kiel, S., Amano, K. and Jenkins, R.G. (2008a) Bivalves from Cretaceous cold-seep deposits on Hokkaido, Japan. *Acta Palaeontologica Polonica* 53: 525-537.

Kiel, S., Campbell, K.A., Elder, W.P. and Little, C.T.S. (2008b) Jurassic and Cretaceous gastropods from hydrocarbon-seeps in forearc basin and accretionary prism settings, California. *Acta Palaeontologica Polonica* 53: 679-703.

Kiel, S., Campbell, K.A. and Gaillard, C. (2010) New and little known mollusks from ancient chemosynthetic environments. *Zootaxa* 2390: 26-48.

Kiel, S. and Peckmann, J. (2007) Chemosymbiotic bivalves and stable carbon isotopes indicate hydrocarbon seepage at four unusual Cenozoic fossil localities. *Lethaia* 40: 345-357.

Kiel, S. and Peckmann, J. (2008) Paleoecology and evolutionary significance of an Early Cretaceous Peregrinella-dominated hydrocarbon-seep deposit on the Crimean Peninsula. *PALAIOS* 23: 751-759.

King, L.H. and MacLean, B. (1970) Pockmarks on the Scotian Shelf. *Geological Society of America Bulletin* 81: 3141-3148.

Kooi, H. and Groen, J. (2001) Offshore continuation of coastal groundwater systems; predictions using sharp-interface approximations and variable-density flow modelling. *Journal of Hydrology* 246: 19-35.

Kudryavtsev, A.B., Schopf, J.W., Agresti, D.G. and Wdowiak, T.J. (2001) In situ laser-Raman imagery of Precambrian microscopic fossils. *Proceedings of the National Academy of Sciences* 98: 823-826.

Lowe, D.R. (1975) Water escape structures in coarse-grained sediments. *Sedimentology* 22: 157-204.

Machel, H.G. (2001) Bacterial and thermochemical sulfate reduction in diagenetic settings — old and new insights. *Sedimentary Geology* 140: 143-175.

Machel, H.G., Krouse, H.R. and Sassen, R. (1995) Products and distinguishing criteria of bacterial and thermochemical sulfate reduction. *Applied Geochemistry* 10: 373-389.

Majima, R., Nobuhara, T. and Kitazaki, T. (2005) Review of fossil chemosynthetic assemblages in Japan. *Palaeogeography, Palaeoclimatology, Palaeoecology* 227: 86-123.

McCrea, J.M. (1950) On the Isotopic Chemistry of Carbonates and a Paleotemperature Scale. *The Journal of Chemical Physics* 18: 849-857.

Meschede, M. (1987) The tectonic and sedimentary development of the Biscay synclinorium in Northern Spain. *Geologische Rundschau* 76: 567-577.

Metz, C.L. (2010) Tectonic Controls on the Genesis and Distribution of Late Cretaceous, Western Interior Basin Hydrocarbon-Seep Mounds (Tepee Buttes) of North America. *The Journal of Geology* 118: 201-213.

Montadert, L., Winnock, E., Delteil, J. and Grau, G. (1974) Continental margins of Galicia-Portugal and Bay of Biscay. In: *Geology of Continental Margins*, edited by C.A. Burk and C.L. Drake, Springer, Berlin, Germany, pp. 223-342.

Montigny, R., Azambre, B., Rossy, M. and Thuizat, R. (1986) K-Ar Study of cretaceous magmatism and metamorphism in the pyrenees: Age and length of rotation of the Iiberian Peninsula. *Tectonophysics* 129: 257-273.

Mutti, E., Nilsen, T. and Ricci Lucchi, F. (1978) Outer fan depositional lobes of the Laga Formation (upper Miocene and lower Pliocene), east-central Italy. In: *Sedimentation in Submarine Canyons, Fans, and Trenches*., edited by D.J. Stanley and G. Kelling, Hutchinson & Ross, Strudsburg, PA, pp. 210-223.

Mutti, E. and Normark, W.R. (1987) Comparing examples of modern and ancient turbidite systems: problems and concepts. In: *Deep Water Clastic Deposits: Models and Case Histories*, edited by J.K. Legget and G.G. Zuffa, Graham and Trotman, London, UK, pp. 1-38.

Mutti, E. and Sonnino, M. (1981) Compensation cycles: a diagnostic feature of turbidite sandstone lobes. *IAS European Regional Meeting*, Bologna, Italy, pp. 120-123.

Nauhaus, K., Treude, T., Boetius, A. and Krüger, M. (2005) Environmental regulation of the anaerobic oxidation of methane: a comparison of ANME-I and ANME-II communities. *Environmental Microbiology* 7: 98-106.

Ondréas, H., Olu, K., Fouquet, Y., Charlou, J.L., Gay, A., Dennielou, B., Donval, J.P., Fifis, A., Nadalig, T., Cochonat, P., Cauquil, E., Bourillet, J.F., Moigne, M.L. and Sibuet, M. (2005) ROV study of a giant pockmark on the Gabon continental margin. *Geo-Marine Letters* 25: 281-292.

Paull, C.K., Chanton, J.P., Neumann, A.C., Coston, J.A., Martens, C.S. and Showers, W. (1992) Indicators of methane-derived carbonates and chemosynthetic organic carbon deposits: examples from the Florida Escarpment. *PALAIOS* 7: 361-375.

Peckmann, J., Birgel, D. and Kiel, S. (2009) Molecular fossils reveal fluid composition and flow intensity at a Cretaceous seep. *Geology* 37: 847-850.

Peckmann, J., Gischler, E., Oschmann, W. and Reitner, J. (2001) An Early Carboniferous seep community and hydrocarbon-derived carbonates from the Harz Mountains, Germany. *Geology* 29: 271-274.

Peckmann, J. and Goedert, J.L. (2005) Geobiology of ancient and modern methane-seeps. *Palaeogeography, Palaeoclimatology, Palaeoecology* 227: 1-5.

Peckmann, J., Goedert, J.L., Thiel, V., Michaelis, W. and Reitner, J. (2002) A comprehensive approach to the study of methane-seep deposits from the Lincoln Creek Formation, western Washington State, USA. *Sedimentology* 49: 855-873.

Peckmann, J. and Thiel, V. (2004) Carbon cycling at ancient methane-seeps. *Chemical Geology* 205: 443-467.

Peckmann, J., Walliser, O.H., Riegel, W. and Reitner, J. (1999) Signatures of hydrocarbon venting in a middle Devonian carbonate mound (Hollard Mound) at the Hamar Laghdad (Antiatlas, Morocco). *Facies* 40: 291-296.

Pedreira, D., Pulgar, J., Gallart, J. and Díaz, J. (2003) Seismic evidence of Alpine crustal thickening and wedging from the western Pyrenees to the Cantabrian Mountains (north Iberia). *Journal of Geophysical Research* 108: 2204.

Pickering, K., Clark, J., Smith, R., Hiscott, R., Ricci Lucchi, F. and Kenyon, N. (1995) Architectural element analysis of turbidite systems, and selected topical problems for sand-prone deep-water systems. In: *Atlas of Deep Water Environments*, edited by K.T. Pickering, R.N. Hiscott, N.H. Keynon, F. Ricchi Lucchi and R.D.A. Smith, Chapman and Hall, London, UK, pp. 1-10.

Pickering, K., Stow, D., Watson, M. and Hiscott, R. (1986) Deep-water facies, processes and models: a review and classification scheme for modern and ancient sediments. *Earth-Science Reviews* 23: 75-174.

Pickrill, R.A. (1993) Shallow seismic stratigraphy and pockmarks of a hydrothermally influenced lake, Lake Rotoiti, New Zealand. *Sedimentology* 40: 813-828.

Pollard, D.D. and Johnson, A.M. (1973) Mechanics of growth of some laccolithic intrusions in the Henry mountains, Utah, II: Bending and failure of overburden layers and sill formation. *Tectonophysics* 18: 311-354.

Praeg, D., Ceramicola, S., Barbieri, R., Unnithan, V. and Wardell, N. (2009) Tectonically-driven mud volcanism since the late Pliocene on the Calabrian accretionary prism, central Mediterranean Sea. *Marine and Petroleum Geology* 26: 1849-1865.

Radke, B.M. and Mathis, R.L. (1980) On the formation and occurrence of saddle dolomite. *Journal of Sedimentary Research* 50: 1149-1168.

Reitner, J. (1987) Mikrofazielle, pal kologische und pal ogeographische Analyse ausgewählter Vorkommen flachmariner Karbonate im Basko-Kantabrischen Strike-Slip-Fault-Becken-System (Nordspanien) an der Wende von der Unterkreide zur Oberkreide. *Documenta Naturae* 40: 1-248.

Reitner, J., Peckmann, J., Reimer, A., Schuman, G. and Thiel, V. (2005) Methane-derived carbonate build-ups and associated microbial communities at cold seeps on the lower Crimean shelf (Black Sea). *Facies* 51: 71-84.

Rossy, M. (1988) Contribution a l'étude du magmatisme Mésozoìque du domaine Pyrénéen. *Ph.D. Thesis*, Université de Franche-Comté, France, pp. 368.

Sahling, H., Bohrmann, G., Spiess, V., Bialas, J., Breitzke, M., Ivanov, M., Kasten, S., Krastel, S. and Schneider, R. (2008) Pockmarks in the

Northern Congo Fan area, SW Africa: Complex seafloor features shaped by fluid flow. *Marine Geology* 249: 206-225.

Sahling, H., Galkin, S.V., Salyuk, A., Greinert, J., Foerstel, H., Piepenburg, D. and Suess, E. (2003) Depth-related structure and ecological significance of cold-seep communities - a case study from the Sea of Okhotsk. *Deep-sea Research I* 50: 1391-1409.

Schultz, L.G. (1964) Quantitative interpretation of mineralogical composition from X-ray and chemical data for the Pierre Shale. *US Geological Survey Professional Papers* 391-C: 1-31.

Smallwood, J.R. and Maresh, J. (2002) The properties, morphology and distribution of igneous sills: modelling, borehole data and 3D seismic from the Faroe-Shetland area. In: *The North Atlantic Igneous Province: Stratigraphy, Tectonic, volcanic and Magmatic Processes, Vol.Special Publications197*, edited by D.W. Jolley and B.R. Bell, Geological Society, London, UK, pp. 271-306.

Smith, R. (1995) Complex bedding geometries in proximal deposits of Castelnuovo Member, Rocchetta Formation, Tertiary Piedmont Basin, NW Italy. In: *Atlas of Deep Water Enviroments*, edited by K.T. Pickering, R.N. Hiscott, N.H. Keynon, F. Ricchi Lucchi and R.D.A. Smith, Chapman and Hall, London, UK, pp. 244-248.

Socrates, G. (2001) *Infrared and Raman Characteristic Group Frequencies: Tables and Charts*. John Wiley and Sons, Chichester, West Sussex, England.

Souquet, P., Debroas, E.-J., Boirie, J.-M., Pons, P., Fixari, G., Roux, J., Dol, J., Thieuloy, J.-P., Bonnemaison, M., Manivit, H. and Peybernes, B. (1985) Le Groupe du Flysch Noir (Albo-Cénomanien) dans les Pyrénées. *Bulletin des Centres de Recherche Exploration-Production Elf-Aquitaine* 9: 183-252.

Spencer, R. (1987) Origin of Ca-Cl brines in Devonian formations, western Canada sedimentary basin. *Applied Geochemistry* 2: 373-384.

Taylor, J.D. and Glover, E.A. (2010) Chemosymbiotic bivalves. In: *The Vent and Seep Biota. Topics in Geobiology*, edited by S. Kiel, Springer, Heidelberg, Germany, pp. 107-136.

Teichert, B.M.A., Eisenhauer, A., Bohrmann, G., Haase-Schramm, A., Bock, B. and Linke, P. (2003) U/Th systematics and ages of authigenic carbonates from Hydrate Ridge, Cascadia Margin: recorders of fluid flow variations. *Geochimica et Cosmochimica Acta* 67: 3845-3857.

Thiel, V., Peckmann, J., Schmale, O., Reitner, J. and Michaelis, W. (2001) A new straight-chain hydrocarbon biomarker associated with anaerobic methane cycling. *Organic Geochemistry* 32: 1019-1023.

Thiel, V., Peckmann, J., Seifert, R., Wehrung, P., Reitner, J. and Michaelis, W. (1999) Highly isotopically depleted isoprenoids: molecular markers for ancient methane venting. *Geochimica et Cosmochimica Acta* 63: 3959-3966.

Thomson, K. (2007) Determining magma flow in sills, dykes and laccoliths and their implications for sill emplacement mechanisms. *Bulletin of Volcanology* 70: 183-201.

Tissot, B. and Welte, D. (1984) *Petroleum Formation and Occurrence*. Springer, Berlin, Germany.

Tuinstra, F. and Koenig, J.L. (1970) Raman Spectrum of Graphite. *The Journal of Chemical Physics* 53: 1126-1130.

Van Rensbergen, P., Depreiter, D., Pannemans, B. and Henriet, J.-P. (2005) Seafloor expression of sediment extrusion and intrusion at the El Arraiche mud volcano field, Gulf of Cadiz. *Journal of Geophysical Research: Earth Surface* 110: F02010.

Warren, J. (2000) Dolomite: occurrence, evolution and economically important associations. *Earth-Science Reviews* 52: 1-81.

Wilson, P.A. and Norris, R.D. (2001) Warm tropical ocean surface and global anoxia during the mid-Cretaceous period. *Nature* 412: 425-429.

Chapter 7: A preliminary investigation on the “round sponge fossils” from the Cambrian Chengjiang Biota

Manuscript

Cui Luo[1], Nadine Schäfer[1], Jan-Peter Duda[1], Li-Xia Li[2]

1. Department of Geobiology, Centre of Geosciences of the University of Göttingen, Goldschmidtstraße 3, 37077 Göttingen, Germany

2. School of Earth Sciences and Engineering, Nanjing University, Hankou Road 22, 210093 Nanjing, China

Abstract

The discordance between the expected early origin of sponges and the late appearance of them in the fossil record is probably caused by either the lack of favorable taphonomical windows in the Precambrian times or the missing capability of building mineral skeletons in early sponges. An investigation on the taphonomy and diversity of early fossil aspicular sponges may shed a new light on the secret history of sponge evolution. The so-called “round sponge fossils” (RSF) from the Burgess Shale-type (BST) Chengjiang Lagerstätte are interesting in this regard because they are preserved with explicit organic remains, and some specimens are characterized by an unusual dense carbonaceous film while lacking spicules.

In this paper four specimens with a diameter of 0.6 - 0.8 cm are reexamined. They display a series of increasing thicknesses of the carbon films and at the same time a contemporaneous decreasing significance of spicules. Based on previous and the current observation, the size, paleoecology and diversity of RSF seem not to accord with the former interpretations as sponge gemmules. Instead, at least parts of the RSF may represent adult sponges of various taxa. Their similar shape is probably caused by growing in a similar ecological environment. Specimens like No.42952, which possesses the thickest carbon film without any trace of spicules, may represent primitive keratose sponges. However, No.42952 lacks a distinguishable organic skeletal framework typical

for keratose sponges, which could be a consequence of a unique original body plan and/or diagenetic processes.

The carbonaceous remains of the fossils are also examined with Raman spectroscopy, together with organically preserved sponge fossils from the Cambrian Xiaoyanxi Formation and algal fossils from the Ediacaran Wenghui Biota. All the carbonaceous material emits similar Raman signals of amorphous carbon. However, the relative intensity ratio between the D- and G-band in the spectra does vary between samples, characterize different fossil sites and differentiate between fossil and background material. However, both for sponge fossil research as well as for the Raman spectroscopy method, further investigations based on more material are essential to support or improve the current assumptions.

7.1 Introduction

Porifera is the known most ancient lineage of Metazoa (e.g. Philippe et al., 2009; Sperling et al., 2009) and is now suspected having originated as early as Cryogenian (Peterson et al., 2008; Sperling et al., 2010). However, the generally acknowledged fossil record of this linage is not older than the early Cambrian, although a group of unusual structures from Precambrian strata have been proposed as candidates of early sponges (e.g. Maloof et al., 2010; Brain et al., 2012). This is partly because spicules, the element traditionally regarded as a reliable or even necessary criterion to set up a poriferan affinity, may have not been evolved in Precambrian or the taphonomical windows were not favorable for the spicular material (Sperling et al., 2010). Therefore, an evaluation of the possible fossil record of aspicular sponges and their taphonomical characters may lead to a new understanding on the early evolutionary history of Porifera.

In addition to those preserved in phosphorite nodules and carbonates (e.g. McMenamin, 2008; Reitner et al., 2012), large amounts of Cambrian sponge fossils are preserved in siliciclastic sediments. The Burgess Shale-type (BST) Lagerstätten exhibit abundant sponge fossils together with other exclusively preserved non-mineralized organisms (e.g. Steiner et al., 2005). The earliest reliable record of “keratose” demosponge *Vauxia* was also reported from the

Middle Cambrian Burgess Shale (Rigby & Collins, 2004). Thus, this type of Lagerstätten could serve as a good realm to study early aspicular sponges and their unique taphonomy compared to that of spicular sponges.

The so called “round sponge fossils” (RSF) from the Chengjiang Biota are particularly interesting in this regard. These fossils share a common appearance with a circular to sub-circular shape, small size (3 - 40 mm in diameter, mostly <10 mm) and an apparent continuous carbonaceous film. Although obviously polyphyletic, Wu (2004) first discussed these fossils together and interpreted them as possible sponge gemmules. Spicules, mostly diactinal and a few stauractinal, are preserved as moulds in some of these fossils, but are rare, obscure or even absent in others. Based on an observation on more than 200 specimens, Wu (2004) concluded that with increasing density of the carbonaceous cover the conspicuousness of the spicules decreases. In this study, a few specimens of RSF are reexamined followed by a discussion on their taphonomy and affinity. Raman spectroscopic analysis was also applied to them as well as to other exceptionally preserved carbonaceous fossils to explore the suitability of this method in the research of carbonaceous fossils.

7.2 Materials and Methods

All the specimens studied in this paper are from the collection of Prof. M.-Y.Zhu’s group in the Nanjing Institute of Geology and Palaeontology, Chinese Academy of Sciences, including four RSF from the Cambrian Chengjiang Biota (inventory numbers No. 42436, No. 42446, No. 42952 and No. 42982), one sponge fossil from the Cambrian Xiaoyanxi Formation (XYX) and several algal fossils from the Wenghui Biota (WH). These fossils were observed with ZEISS Stemi 2000-C stereoscope and photographed with a CANON EOS 500D. For Raman spectroscopic analysis a confocal Horiba Jobin-Yvon LabRam-HR 800 UV Raman spectrometer attached to an Olympus BX41 microscope was used. The excitation wavelength for the Raman spectra was the 488 nm line of an Argon Ion Laser (Melles Griot IMA 106020B0S) with a laser power of 20 mW. A detailed description of the spectrometer is given in Beimforde et al. (2011). All spectra were recorded and processed using LabSpec™ version 5.19.17 (Horiba Jobin-Yvon, Villeneuve d'Ascq, France).

Mineral identification was performed on the basis of the Horiba Jobin-Yvon database for minerals.

As stated by Wu (2004), the RSF were collected from fossil sites near Chengjiang County, mainly from Maotianshan and Xiaolantian. The fossils are preserved in the yellowish-green shale from the Maotianshan Shale Member of Yu'anshan Formation (Fig. 59). The age of the fossiliferous layer has been estimated as ca. 520 Ma (Hu, 2005). Previous research distinguished two types of sediments from the Maotianshan Shale: the slowly deposited background beds and the rapidly deposited event beds which probably represent storm-induced distal tempestites (Hu, 2005). Wu (2004) did not designate the exact type of sediments in which the RSF were collected. But, as revealed by quantitative analysis, the two types of beds have similar recurrent and abundant species, as well as similar temporal trends in evenness and richness, indicating the fossils in the two taphonomical facies originating from a single local community, although sponge fossils appear occupying a higher percentage in the background beds (Zhao et al., 2009).

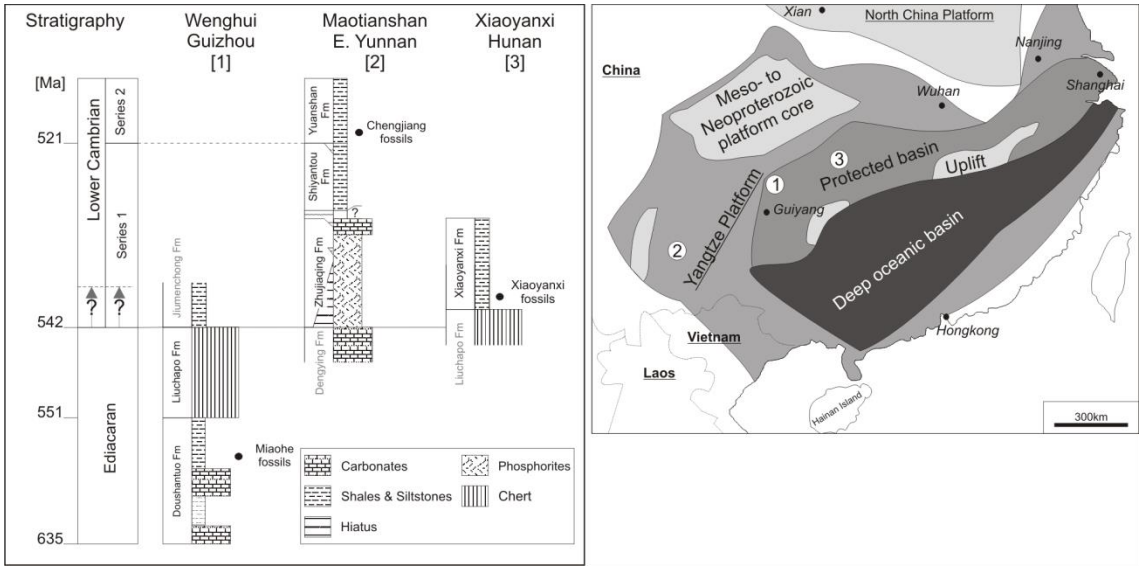

Figure 59: Stratigraphy, locality and depositional environments of the sampled sections. Numbers of sections refer to the marked positions on the map (Stratigraphy based on Steiner et al., 2001; Condon et al., 2005; Guo et al., 2007; Zhu et al., 2007; map based on Steiner et al., 2001).

In order to explore the capability of Raman spectroscopy for distinguishing and investigating organically preserved fossils, additional specimens from two further fossil Lagerstätten were selected. One is a non-described sponge fossil

from the carbonaceous black shale of Xiaoyanxi Formation in Yuanling, Hunan Province (Fig. 59; Fig. 61a). Similar to other Lower Cambrian sequences in South China, the fossiliferous black shale is successively underlain by a layer of Nickel-Molybdenum ore, a phosphorite layer and finally Precambrian sedimentary rocks. The absolute age of the fossil horizon was evaluated as younger than 532 Ma (Jiang et al., 2012). The other selected specimens are algal remains from the Ediacaran Wenghui Biota, Guizhou (Fig. 61b-d). This biota yields abundant algal fossils preserved in the black shale of the upper Doushantuo Formation (Fig. 59). Because the fossil community is dominated by benthic algae which appear to be buried *in situ*, the sedimentary depth was probably below storm wave base but still within the photic zone (Zhu et al., 2012).

7.3 Preservational potential of aspicular sponges in BST Lagerstätten

BST preservation was firstly defined as "*exceptional organic preservation of non-mineralizing organisms in fully marine siliciclastic sediments*", with "*some degree of early diagenetic mineralization*" (Butterfield, 1995). Although the mechanism causing this exceptional preservation are still under debate (e.g. Butterfield, 1990; Petrovich, 2001; Gaines et al., 2005), it is obvious that materials of different taphonomical resistance are preserved in different status in this type of Lagerstätten. As observed by Butterfield (2007), two-dimensional carbonaceous compressions probably derive from relatively recalcitrant extracellular components (e.g. cuticles and chaetae), while former labile soft-tissues may result in three-dimensional mineralization of either carbonates or phosphates, and early diagenetic pyrite is incidentally distributed in all Burgess Shale fossils.

In a short review about the preservation potential of organic matter, collagen, keratin and sclerotin were listed as most recalcitrant organic components in animals (Butterfield, 1990). Sponges possess two types of collagen: fibrillar collagen as a universal skeletal material found in all sponges and spongin as horny fibers and related structures in specific groups of sponges (e.g. keratose sponges) (Bergquist, 1978). These organic skeletal elements are generally believed to have very small chances to be preserved, and the poriferan fossil

record has therefore, a strong bias toward mineral skeletons (Pisera, 2006). However, in BST Lagerstätten many sponges are preserved including carbonaceous remains. For example, the sponge fossils from Cambrian Chengjiang-type fauna studied by Forchielli et al. (2012) still exhibit continuous carbonaceous films, while silica spicules have been resolved or replaced by diagenetic minerals. In the Burgess Shale, the coring fibers of *Vauxia gracilenta* are preserved as carbon remains although partly replaced by limonite (Rigby & Collins, 2004). Li et al. (1998) also mentioned a single specimen of a keratose sponge in their collection from the Chengjiang fauna. However, although sponges also contain large amounts of taphonomically labile organic material, carbonatization and phosphatization are not popular preservation types to record the taxonomically valuable features of sponges in BST Lagerstätten. Hence, besides the spicules record, the carbonaceous remains of the sponge fossils in BST Lagerstätten seem to be a useful archive for early sponges. Consequently, reliable evidence that the organic remains in sponge fossils are most probably derived from taphonomically recalcitrant spongin and/or collagen material will help to interpret the fossils.

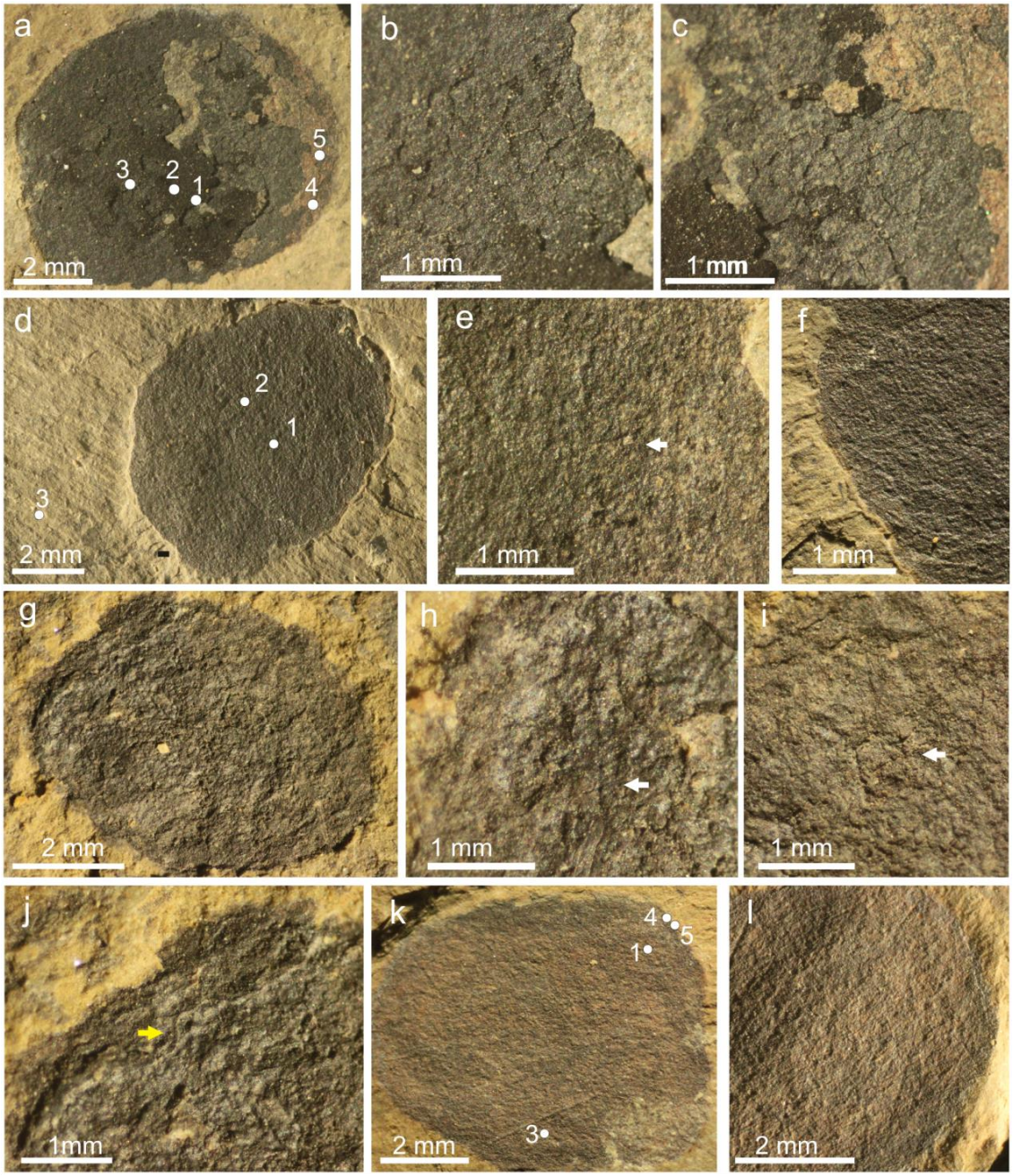

Figure 60: Round sponge fossils (RSF) from Chengjiang Biota. **a-c** No.42952; **b** and **c** show details of the cracks on the surface of the carbonaceous film. **d-f** No.42436; **e** and **f** show details of **d**, the white arrow in **e** points to a possible mark of spicules. **g-j** No.42446; **h-j** show details of **g**. The white arrows point to possible mineral skeleton marks, while the yellow arrow in **j** is to emphasize the two-layered preserved carbonaceous film. **k-l** No.42982; **l** shows apparent spicular structures. The number marks in **a**, **d** and **k** represent the location of Raman spectra sample spots.

7.4 Results & Discussion

7.4.1 Affinity of RSF

The four round sponge fossils studied here have an elliptical shape and a diameter of 0.6 - 0.8 cm. No.42952 maintains the thickest carbonaceous remains but lacks spicules (Fig. 60a-c). Polygonal cracks are developed on the upper surface of the carbonaceous remains (Fig. 60b-c). By comparison, No.42436 (Fig. 60d-f) and No.42446 (Fig. 60g-i) have thinner carbonaceous films. Some small and faint marks, resembling moulds of spicules, are distributed on parts of the fossil surface, but they are not confirmatively of spicular origin (Fig. 60e, h-i). In addition, both No.42952 and No.42446 show features of double-layered carbon films (Fig. 60a, c, g & j), which indicate a former existence of spongocoel. No.42982 is intensively weathered and exhibits weakly preserved but authentic moulds of spicules with only scattered carbonaceous remains (Fig. 60k-l).

Wu (2004) interpreted RSF as sponge gemmules because they possess exceptionally recalcitrant organic matter and a round shape. However, gemmules of modern sponges are normally only 0.2 - 1 mm in diameter (Fell, 1993), much smaller than the RSF. If the amount of totipotent cells and nutrients in millimeter-sized gemmules are adequate for dormancy and later germination, then the production of centimeter-sized gemmules appears not to be economic. And as observed in modern examples, each sponge typically produces hundreds to thousands of gemmules which either attach to the substrate or fill in the sponge body (Fell, 1993). But little is known about the substratum for the gemmule-theory and even the largest sponge in the Chengjiang Biota (*Quadrolaminiella*; Hou et al., 2004) is not big enough to contain hundreds of centimeter-sized gemmules. Furthermore, fossil records of sponge gemmules were mostly reported from fresh water environments, except one possible example of Cretaceous age published recently (Petit & Charbonnier, 2012, and references therein), and all of these fossils have only a size of about 1mm. In contrast to gemmules, buds of sponges have a size ranging from hundreds of micrometers to a few centimeters. They can be reinforced by collagen and spicules and exhibit a more or less spherical shape

in some species (Fell, 1993). However, RSF contribute a large proportion to the Chengjiang sponge fossil record (12.48% of 2252 specimens studied by Wu, 2004), but to our knowledge no budding process has been directly observed in these normal sponge fossils.

Furthermore, some of the spicular RSF fit into the genera *Triticispongia* and *Saetaspongia* erected by Steiner et al. (1993) from another Cambrian fossil Lagerstätte in Sancha (Wu, 2004). While *Saetaspongia* (holotype about 3 x 4 cm large) was treated as normal sponge fossil, *Triticispongia* was originally interpreted as representing juvenile stages because their size hardly exceeds 10 mm. However, Rigby & Hou (1995) were apt to interpret *T. diagonata* as adult precursor of reticulosid sponges based on the well-organized skeletal structures and the absence of larger adult specimens in fossil collections of Chengjiang and Sancha. Later, larger specimens (with diameters of 2.5 - 3 cm) were discovered from Niutitang Formation in Songlin, Guizhou (Zhao et al., 2006). But, their giant sizes are more probably related to a different environment or evolutionary stage than representing the adult form of the analogues from Sancha and Chengjiang, because none of these three fossil sites contain both the big and small specimens at the same time. Furthermore, sorting during carcass transportation seems unlikely considering the same static depositional environment of the black shales in Sancha and Songlin and the different water dynamics between the background beds and event beds in Chengjiang Lagerstätten. For these reasons, we agree with the interpretation of Rigby & Hou (1995) on *T. diagonata*. Since also no reliable adult forms of other RSF are currently known to us, we further propose that at least a part of the RSF in Chengjiang Biota represent adult sponges which belong to various taxa but occupied similar ecological niches. In sponges, the exterior morphology is strongly affected by environment while the skeletal construction is controlled by gene expression. This explains the phenomenon that the RSF have at the same time a variety of skeleton structures but similar shapes and sizes and also occur in similar taphonomical facies. Nonetheless, this argument does not completely exclude the possibility that some of the RSF have gemmule or bud origin, especially for very small specimens.

In the light of the earlier taphonomical review, the continuous transition of RSF from explicit mineral skeletons to completely carbonaceous preservation

resembles the reduction of spongin and/or collagen in the skeletal framework from keratose sponges to other demosponges and hexactinellids. In most keratose sponges, the whole skeletal framework consists of spongin; while in other demosponges the fibrillar collagen is still pervasive and often forms dense bands between spicules whereas in hexactinellids collagen forms a thin sheath wrapping the spicules but does not occur massively (Bergquist, 1978). This clearly underlines that the aspicular specimens with dense carbonaceous remains may represent a kind of primitive keratose sponge. On the other hand, the absence of the typical dendritic or anastomosing network of keratose sponges in the round sponge fossils may hinder this interpretation. However, this could be explained by consolidation of organic material during diagenesis. The continuous carbonaceous films of No.42436, No.42446 and No.42952 could represent the end product of the diagenetic fusing of a fine network composed of dense spongin or collagen material, but not necessarily have to be the result of a continuous organic shall of the gemmule as suggested by Wu (2004). The polygonal fractures on the surface of No.42952 could also be due to diagenetic altering, since similar structures are also observed in the Wenghui fossils where dense organic carbon is preserved (Fig. 61e).

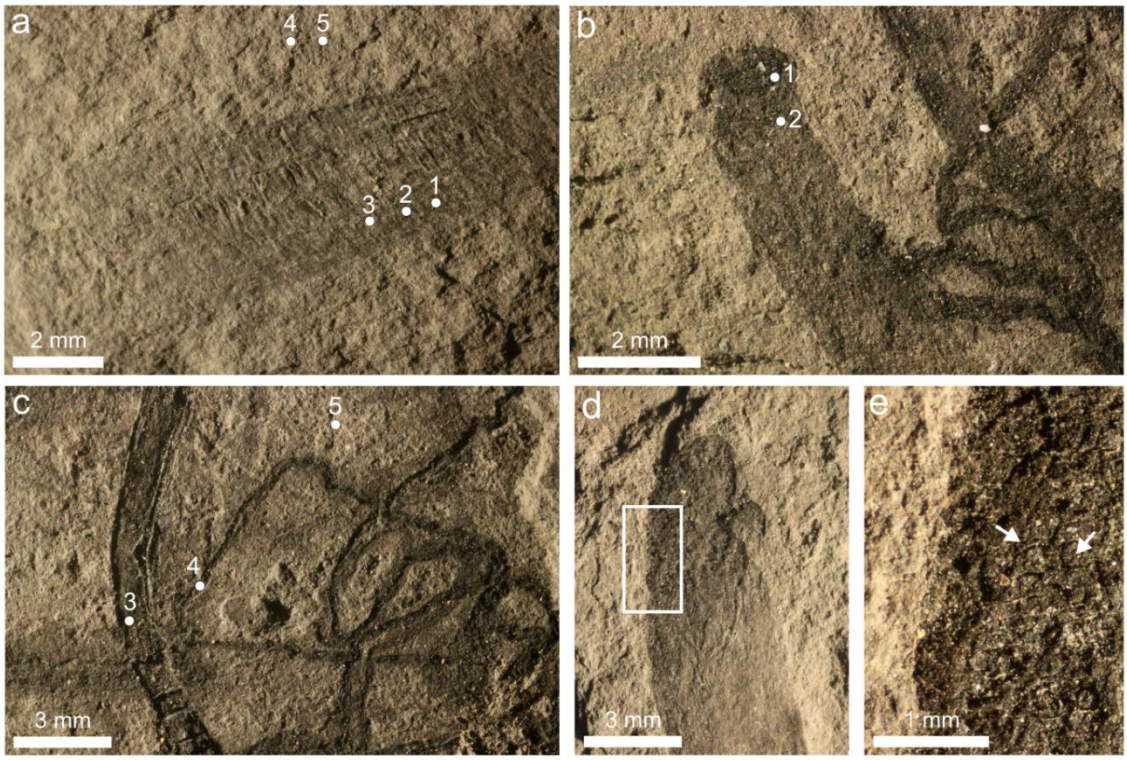

Figure 61: Carbonaceous fossils from Xiaoyanxi Formation and Wenghui Biota. **a** the non-described sponge fossil from Early Cambrian Xiaoyanxi Formation. **b-e** the algal fossils from Ediacaran Wenghui Biota. **e** represents the white rectangle in **d**. white arrows in **e** point to polygonal cracks in the densely preserved carbon film. Number marks in **a**, **b** and **c** represent the location of Raman spectra sample spots.

7.4.2 Raman spectra

Totally 23 Raman spectra have been obtained from three of the Chengjiang fossils, the single specimen of sponge fossil from the Xiaoyanxi Formation and a few algal remains from Wenghui Biota (Fig. 62). The most prominent signals from all of the samples are typical for amorphous carbon, characterized by two prominent bands in the lower wavenumber region around 1600 cm^{-1}(G-band; graphite-band) and around 1350 cm^{-1} (D-band; disorder-band) (cf. Tuinstra & Koenig, 1970; Wopenka & Pasteris, 1993; Quirico et al., 2009). Sometimes additional bands for minerals also occur, which are a good sign for influence of the background material. Furthermore, especially the background shale material exhibits a high fluorescence, which can be caused by the extremely fine grained clay minerals, resulting in a reduction of the Raman signal (Wang & Valentine, 2002). In order to focus on the analysis of the carbon signal, the mineral- and fluorescence-influenced spectra are not shown in this paper.

On first sight, the results for all samples look quite similar, with the exception of XYX (Fig. 62). In the latter, the D-band is always higher than the G-band. The differences between the fossil and background material are also difficult to recognize. However, it is well known that peak intensities of the two bands can vary in a small range due to several independent factors like thermal alteration, the original carbonaceous material, and crystallinity of the carbon (Robertson, 1986; Pasteris & Wopenka, 2003; Busemann et al., 2007; Marshall et al., 2010). Therefore, geologically valuable information was extracted by calculating the relative intensity ratio (R1) between the D- and the G-band (Fig. 62). This ratio seems to be suitable to differentiate between different samples as well as between fossil and background material. The round sponge fossils from the Chengjiang Biota show mean R1 values of 0.79 (No.42982), 0.84 (No.42952) and 0.73 (No.42436). In these samples, the fossil area generally yields lower R1 than the background material. An exception is No.42982, where the ratio shows little variation between the fossil and the background. This is possibly due to weathering of the sample, supported by the pervasive hematite signals in the spectra from this sample. The algal fossils from the Wenghui Biota have a mean R1 of 0.86. In contrast to the Chengjiang material, here R1 on the fossils is higher than that in the background. This discrepancy may reflect either different sedimentary environments (tempestite shale vs. black shale) or different sources of organic carbon (sponge vs. algae). Sample XYX, characterized by signals with higher D-band than G-band, has an average R1 of 1.05. But the ratios measured on different points do not show any special distribution. This is probably caused by the rather thin and discontinuous carbon film over the fossil. However, intensive diagenesis and/or metamorphism might also have contributed to this result, because higher D- than G-band is often reported from samples which experienced a high metamorphic grade (compare Wopenka & Pasteris, 1993; Rahl et al., 2005; Bower et al., 2013; Foucher & Westall, 2013). As in this study only one sample from this fossil site has been analyzed so far, more data are necessary to draw a conclusion on this matter.

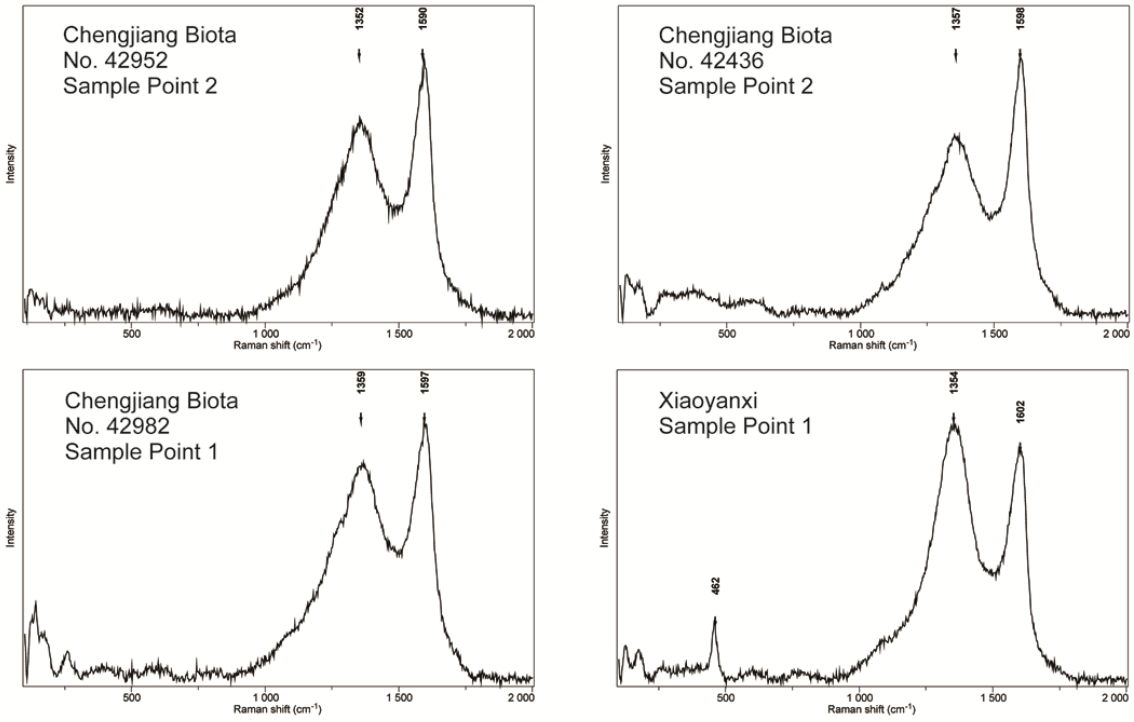

	Sample Point	Description	D-band intensity [1/cm]	G-band intensity [1/cm]	R1
Chengjiang Biota	1	fossil	4375	5830	0.75
No. 42952	2	fossil	1430	1819	0.79
	3	fossil	742	896	0.83
	4	rim	1624	1815	0.89
	5	rim	748	788	0.95
No. 42436	1	fossil + background	1316	1791	0.76
	2	fossil	5460	7904	0.69
	3	background	1015	1339	0.76
No. 42982	1	fossil	5993	7152	0.84
	3	fossil	3031	4042	0.75
	4	background	2690	3450	0.78
	5	background	3694	4766	0.78
Xiaoyanxi	1	fossil	4400	4004	1.01
	2	fossil	4087	3714	1.10
	3	fossil	9839	9444	1.04
	4	background	5805	5581	1.04
	5	background	3759	3588	1.05
Wenghui Biota	1	fossil	1174	1256	0.93
	2	fossil	4310	5267	0.81
	3	fossil	1690	14855	0.91
	4	fossil	1797	1988	0.90
	5	background	5437	6975	0.78

Figure 62: Representative Raman spectra of carbon measured on each of the fossils. The small band centered at 462 cm^{-1} in the Xiaoyanxi spectrum belongs to the main SiO_2 vibration in quartz. The table lists the measured relative intensities of the D- and the G-bands on all of the sample points, as well as the intensity ratio between both bands (R1). The exact sample points on the samples can be viewed in Fig. 60. Sample point 2 of sample No.42982 is missing in this list, because the spectrum contains only vibrations of hematite.

7.5 Conclusions

A short review of the existing theoretical studies and fossil reports implies that the mineral skeleton of sponges tends to be preserved as moulds or to be replaced by diagenetic minerals in BST Lagerstätten, whereas the recalcitrant organic skeletal components like spongin and collagen have prominent potential to become carbonaceous fossils in this taphonomical window. The RST from Chengjiang Biota are interpreted here as various sponge taxa living in similar ecological niches, instead of sponge gemmules as stated before. Partly based

on this assumption, some aspicular specimens like No.42952 may even represent primitive keratose sponges. However, the taxonomically valuable details are missing in these aspicular carbonaceous fossils. This can be attributed to their original skeletal framework structure and the diagenetic processes. Raman spectra obtained from the carbon material of these round sponge fossils are mainly signals of amorphous carbon, similar to those emitted by the fossil material from Xiaoyanxi Formation and Wenghui Biota. However, the R1 ratios of the amorphous carbon spectra do differentiate between samples from different fossil sites and between fossil and background material. If this is repeatable in future experiments, it may provide a new way to evaluate carbonaceous fossils. This work reveals some interesting aspects in both early sponge fossil record and Raman spectroscopy. However, further investigation based on more material is essential to make certain statements.

Acknowledgement

We would like to thank Prof. M.-Y. Zhu for providing the fossil material. Dr. W. Wu, L.-Y. Miao and H. Zeng are greatly acknowledged for collecting literature. We are grateful to the unknown reviewers for their constructive suggestions.

References

Beimforde, C., Schäfer, N., Dörfelt, H., Nascimbene, P.C., Singh, H., Heinrichs, J., Reitner, J., Rana, R.S. and Schmidt, A.R. (2011) Ectomycorrhizas from a Lower Eocene angiosperm forest. *New Phytologist* 192: 988-996.

Bergquist, P.R. (1978) *Sponges*. University of California Press, Berkeley and Los Angeles, pp. 267.

Bower, D.M., Steele, A., Fries, M.D. and Kater, L. (2013) Micro Raman Spectroscopy of Carbonaceous Material in Microfossils and Meteorites: Improving a Method for Life Detection. *ASTROBIOLOGY* 13: 103-113.

Brain, C.K.B., Prave, A.R., Hoffmann, K.-H., Fallick, A.E., Botha, A., Herd, D.A., Sturrock, C., Young, I., Condon, D.J. and Allison, S.G. (2012) The first animals: ca. 760-million-year-old sponge-like fossils from Namibia. *South Africa Journal of Sciences* 108: 658~665.

Busemann, H., Alexander, C.M.O.D. and Nittler, L.R. (2007) Characterization of insoluble organic matter in primitive meteorites by microRaman spectroscopy. *Meteoritics & Planetary Science* 42: 1387-1416.

Butterfield, N.J. (1990) Organic Preservation of Non-Mineralizing Organisms and the Taphonomy of the Burgess Shale. *Paleobiology* 16: 272-286.

Butterfield, N.J. (1995) Secular distribution of Burgess-Shale-type preservation. *Lethaia* 28: 1-13.

Butterfield, N.J., Balthasar, U.W.E. and Wilson, L.A. (2007) Fossil diagenesis in the Burgess Shale. *Palaeontology* 50: 537-543.

Condon, D., Zhu, M., Bowring, S., Wang, W., Yang, A. and Jin, Y. (2005) U-Pb Ages from the Neoproterozoic Doushantuo Formation, China. *Science* 308: 95-98.

Fell, P.E. (1993) Porifera. In: *Asexual propagation and reproductive strategies, Reproductive biology of invertebrates*, edited by K.G. Adiyodi and R.G. Adiyodi, Wiley, Chichester, pp. 1-44.

Forchielli, A., Steiner, M., Hu, S.X. and Keupp, H. (2012) Taphonomy of Cambrian (Stage 3/4) sponges from Yunnan (South China). *Bulletin of Geosciences* 87: 133-142.

Foucher, F. and Westall, F. (2013) Raman Imaging of Metastable Opal in Carbonaceous Microfossils of the 700-800 Ma Old Draken Formation. *ASTROBIOLOGY* 13: 57-67.

Gaines, R.R., Kennedy, M.J. and Droser, M.L. (2005) A new hypothesis for organic preservation of Burgess Shale taxa in the middle Cambrian Wheeler Formation, House Range, Utah. *Palaeogeography, Palaeoclimatology, Palaeoecology* 220: 193-205.

Guo, Q., Shields, G., Liu, C., Strauss, H., Zhu, M., Pi, D., Goldberg, T. and Yang, X. (2007) Trace element chemostratigraphy of two Ediacaran–Cambrian successions in South China: Implications for organosedimentary metal enrichment and silicification in the early Cambrian. *Palaeogeography, Palaeoclimatology, Palaeoecology* 254: 194-216.

Hou, X.-G., Aldridge, R.J., Bergström, J., Siveter, D.J., Siveter, D.J. and Feng, X.-H. (2004) *The Cambrian fossils of Chengjiang, China: the flowering of early animal life*. Blackwell Publishing, Malden, Oxford and Victoria, pp. 233.

Hu, S. (2005) Taphonomy and Palaeoecology of the Early Cambrian Chengjiang Biota from Easter Yunnan. *Berliner Paläobiologische Abhandlungen* 7: 1-197.

Jiang, G., Wang, X., Shi, X., Xiao, S., Zhang, S. and Dong, J. (2012) The origin of decoupled carbonate and organic carbon isotope signatures in the early Cambrian (ca. 542–520 Ma) Yangtze platform. *Earth and Planetary Science Letters* 317–318: 96-110.

Li, C.W., Chen, J.Y. and Hua, T.E. (1998) Precambrian sponges with cellular structures. *Science* 279: 879-882.

Maloof, A.C., Rose, C.V., Beach, R., Samuels, B., Calmet, C.C., Erwin, D.H., Poirier, G.R., Yao, N. and Simons, F.J. (2010) Possible animal-body fossils in pre-Marinoan limestones from South Australia. *Nature Geoscience* 3: 653-659.

Marshall, C.P., Edwards, H.G.M. and Jehlicka, J. (2010) Understanding the Application of Raman Spectroscopy to the Detection of Traces of Life. *ASTROBIOLOGY* 10: 229-243.

McMenamin, M.A.S. (2008) Early Cambrian sponge spicules from the Cerro Clemente and Cerro Rajón, Sonora, México. *Geological Acta* 6: 363-367.

Pasteris, J.D. and Wopenka, B. (2003) Necessary, but Not Sufficient: Raman Identification of Disordered Carbon as a Signature of Ancient Life. *ASTROBIOLOGY* 3: 727-738.

Peterson, K.J., Cotton, J.A., Gehling, J.G. and Pisani, D. (2008) The Ediacaran emergence of bilaterians:congruence between the genetic and the geological fossil records. *Philosophical Transactions of the Royal Society B: Biological Sciences* 363: 1435-1443.

Petit, G. and Charbonnier, S. (2012) Fossil sponge gemmules, epibionts of Carpopenaeus garassinoi n. sp. (Crustacea, Decapoda) from the Sahel Alma Lagerstätte (Late Cretaceous, Lebanon). *Geodiversitas* 34: 359-372.

Petrovich, R. (2001) Mechanisms of fossilization of the soft-bodied and lightly armored faunas of the Burgess Shale and of some other classical localities. *American Journal of Science* 301: 683-726.

Philippe, H., Derelle, R., Lopez, P., Pick, K., Borchiellini, C., Boury-Esnault, N., Vacelet, J., Renard, E., Houliston, E., Quéinnec, E., Da Silva, C., Wincker, P., Le Guyader, H., Leys, S., Jackson, D.J., Schreiber, F., Erpenbeck, D., Morgenstern, B., Wörheide, G. and Manuel, M. (2009) *Phylogenomics Revives Traditional Views on Deep Animal Relationships. Current Biology* 19: 706-712.

Pisera, A. (2006) Palaeontology of sponges - a review. *Canadian Journal of Zoology-Revue Canadienne De Zoologie* 84: 242-261.

Quirico, E., Montagnac, G., Rouzaud, J.N., Bonal, L., Bourot-Denise, M., Duber, S. and Reynard, B. (2009) Precursor and metamorphic condition effects on Raman spectra of poorly ordered carbonaceous matter in chondrites and coals. *Earth and Planetary Science Letters* 287: 185-193.

Rahl, J.M., Anderson, K.M., Brandon, M.T. and Fassoulas, C. (2005) Raman spectroscopic carbonaceous material thermometry of low-grade metamorphic rocks: Calibration and application to tectonic exhumation in Crete, Greece. *Earth and Planetary Science Letters* 240: 339-354.

Reitner, J., Luo, C. and Duda, J.P. (2012) Early Sponge Remains from the Neoproterozoic-Cambrian Phosphate Deposits of the Fontanarejo Area (Central Spain). *Journal of Guizhou University (Natural Sciences)* 29 (Sup. 1): 184-186.

Rigby, J.K. and Collins, D. (2004) Sponges of the Middle Cambrian Burgess Shale and Stephen Formations, British Columbia. *ROM Contributions in Science* 1: 1-155.

Rigby, J.K. and Hou, X.-G. (1995) Lower Cambrian demosponges and hexactinellid sponges from Yunnan, China. *Journal of Paleontology* 69: 1009-1019.

Robertson, J. (1986) Amorphous carbon. *Advances in Physics* 35: 317-374.

Sperling, E.A., Peterson, K.J. and Pisani, D. (2009) Phylogenetic-Signal Dissection of Nuclear Housekeeping Genes Supports the Paraphyly of Sponges and the Monophyly of Eumetazoa. *Molecular Biology and Evolution* 26: 2261-2274.

Sperling, E.A., Robinson, J.M., Pisani, D. and Peterson, K.J. (2010) Where's the glass? Biomarkers, molecular clocks, and microRNAs suggest a 200-Myr missing Precambrian fossil record of siliceous sponge spicules. *Geobiology* 8: 24-36.

Steiner, M., Mehl, D., Reitner, J. and Erdtmann, B.-D. (1993) Oldest entirely preserved sponges and other fossils from the Lowermost Cambrian and a new facies reconstruction of the Yangtze platform (China). *Berliner Geowissenschaftliche Abhandlungen* E: 293-329.

Steiner, M., Wallis, E., Erdtmann, B.-D., Zhao, Y. and Yang, R. (2001) Submarine-hydrothermal exhalative ore layers in black shales from South China and associated fossils — insights into a Lower Cambrian facies and bio-evolution. *Palaeogeography, Palaeoclimatology, Palaeoecology* 169: 165-191.

Steiner, M., Zhu, M., Zhao, Y. and Erdtmann, B.-D. (2005) Lower Cambrian Burgess Shale-type fossil associations of South China. *Palaeogeography, Palaeoclimatology, Palaeoecology* 220: 129-152.

Tuinstra, F. and Koenig, J.L. (1970) Raman Spectrum of Graphite. *The Journal of Chemical Physics* 53: 1126-1130.

Wang, A. and Valentine, R.B. (2002) Seeking and Identifying Phyllosilicates on Mars -- A Simulation Study*. 33rd Annual Lunar and Planetary Science Conference*, Houston, Texas.

Wopenka, B. and Pasteris, J.D. (1993) Structural characterization of kerogens to granulite-facies graphite: applicability of Raman microprobe spectroscopy. *American Mineralogist* 78: 533-557.

Wu, W. (2004) Fossil sponges from the early Cambrian Chengjiang fauna, Yunnan, China. *PhD thesis*, Graduate School of the Chinese Academy of Sciences, Nanjing.

Zhao, F., Caron, J.-B., Hu, S. and Zhu, M. (2009) Quantitative analysis of taphofacies and paleocommunities in the early Cambrian Chengjiang Lagerstätte. *PALAIOS* 24: 826-839.

Zhao, Y., Yang, R., Yang, X. and Mao, Y. (2006) Globular Sponge Fossils from the Lower Cambrian in Songlin, Guizhou Province, China. *Geological Journal of China Universities* 12: 106-110.

Zhu, M., Yang, A., Yang, X., Peng, J., Zhang, J. and Lu, M. (2012) Ediacaran succession and the Wenghui Biota in the deep-water facies of the Tangtze Platform at Wenghui, Jiangkou County, Guizhou. *Journal of Guizhou University (Natural Sciences)* 29 (Sup. 1): 113-138.

Zhu, M., Zhang, J. and Yang, A. (2007) Integrated Ediacaran (Sinian) chronostratigraphy of South China. *Palaeogeography, Palaeoclimatology, Palaeoecology* 254: 7-61.

Chapter 8: Discussion and Conclusion

In the previous chapters many different settings were discussed in which the detection of traces of organic substances in various rock types was described. The best results could be obtained in fractures from the Äspö HRL. Here, the reactivation of the fractures in the Precambrian bedrock provides an ideal environment for the development of a conditioning film. In this case the detected organic remains are relatively young, so that still complex molecules could be detected and determined. However, in most other geobiological contexts this is not the case.

The detection of melanin in different fossils and preserved in amber is a good example for the detection and interpretation of known substances. Although Raman spectra of melanin are unspecific, due to its high light absorbance, a characterization and assignment of its structure were possible. However, the interpretation based on theoretical predictions (cf. Powell et al., 2004) is only possible when dealing with substances which are already known to occur.

In older geologic settings the only prominent signal detectable with Raman spectroscopy are vibrations referred to as amorphous carbon. The general difficulties in interpreting these signals as organic or even biologic provoked an ongoing discussion (cf. Brasier et al., 2002; Pasteris & Wopenka, 2002; Schopf et al., 2002; Pasteris & Wopenka, 2003; Marshall et al., 2010; Bower et al., 2013). Also in this work in many cases the detection of organic remains is limited to the amorphous carbon signature. But nevertheless, differences can be observed which probably are related to different ages and also different thermal maturity.

The identification of cold seep carbonates by the occurrence of organic rich yellow calcite phases is a good example for utilizing Raman spectroscopy to discriminate between chemical identical phases. In these carbonates the presence and absence of additional carbon bands acts as a good indicator for different cement facies. In this regard it is also important to notice that the signals of the disordered carbon related to the yellow calcite are clearly distinguishable from disordered carbon signals related to pyrobitumen which could be also occurring in the vicinity of the carbonates (cf. chapter 6.5.1).

Together with additional information like $\delta^{13}C$ values or biomarkers, this is a valuable tool for identifying fossil methane seepage sites.

The situation gets more complicate when dealing with fossil microbial mats (chapter 5) or even fossils (chapter 7) where more complex organic molecules would be suspected to be detectable. Here, the argument for interpreting the carbon signatures as exclusively organic or even biologic is much weaker. However, in the case of the fossil microbial mat from the Ediacaran of the White Sea (chapter 5) the association of the carbon signal with mineral phases which are suggested to be related to microbial processes (Edwards et al., 2004; Foucher & Westall, 2009; Glamoclija et al., 2009) can serve as additional prove for the microbial origin. In the case of the round sponge fossils (chapter 7) the problematic interpretation of the carbon signal is even more evident. Here at first sight, no difference between the carbon signal of the fossils and of the background shale material is possible. However, when looking more closely at the exact parameters (especially the intensity ratio R1) of the D and the G band a variation between the fossils and the shale background is obvious. This fits into the recently published observations of Bower et al. (2013), who reported a general trend regarding the age of the sample and the thermal maturity. Also data obtained in this work fit in this general trend (cf. Table 6). Similar as in chapter 7 the most prominent differences for the various samples can be seen on the R1 value. The thermal immature examples from Carboniferous Ganigobis yellow calcite, the Ediacaran White Sea microbial mat and the upper Doushantou layer have much lower R1 values, whereas the more mature examples from the Achaean Apex and Strelley Pool chert even have values greater than one. But also the full width at half height (FWHH) of the D band shows great variation. The samples where a microbial influence is probable have a much higher Γ_D value and also the D band position has a tendency to lower wavenumbers. Interestingly a similar trend is visible when comparing carbon signatures of known abiogenic origin from carbonaceous chondrites (Allende and Murchison). The values from the Allende CV chondrite are similar to those observed for the Achaean Apex and Strelley Pool cherts, whereas the R1 value for the Murchison CM chondrite is much lower and the D band is much broader. The two meteorites experienced different degrees of heating, Allende having the higher temperatures (Sears & Dodd, 1988).

Table 6: Comparison of different parameters of the D and the G band in various rocks. The band positions are given in Raman shift (cm^{-1}). The full width at half height is given by Γ_G and Γ_D, respectively. The R1 value represents the intensity ratio of the D and the G band.

Location	Age Ma	G band position	Γ_G	D band position	Γ_D	R1
Ganigobis Yellow Calcite	300	1600	65	1349	214	0.61
White Sea	555	1588	155	1302	126	0.42
Doushantou upper layer	600	1605	41	1335	151	0.48
Apex Chert	3500	1600	54	1353	71	1.25
Strelley Pool	3500	1597	63	1353	70	1.49
Allende meteorite	4600	1584	71	1352	68	1.34
Murchison meteorite	4600	1579	79	1364	144	0.78

As already stated by Bower et al. (2013) the most prominent trend can be seen in the relationship of the Γ_D and the R1 value. It is possible that these values are indicative for more complex precursor material of the carbon signature and thereby can help discriminating between abiogenic and biogenic carbon signatures. The data obtained in this work reflect a very similar trend (Fig. 63). Samples with less compositionally complex carbon precursor material which is possibly thermally overprinted, exhibits higher R1 values and narrow D bands, whereas samples with more complex carbon precursor material exhibit much broader D bands with low R1 values. Also the data from the two chondrites fit into this classification. Allende experienced temperatures up to 1000 °C and is characterized by thermal mature carbon signatures (Krot et al., 2007; Bower et al., 2013 and citations therein) and therefore plots together with the Achaean rocks. On the other hand, Murchison only experiences temperatures around 130 °C and is known for featuring various organic molecules, including amino acids (Cronin & Pizzarello, 1983; Clayton & Mayeda, 1984; Engel & Macko, 1997).

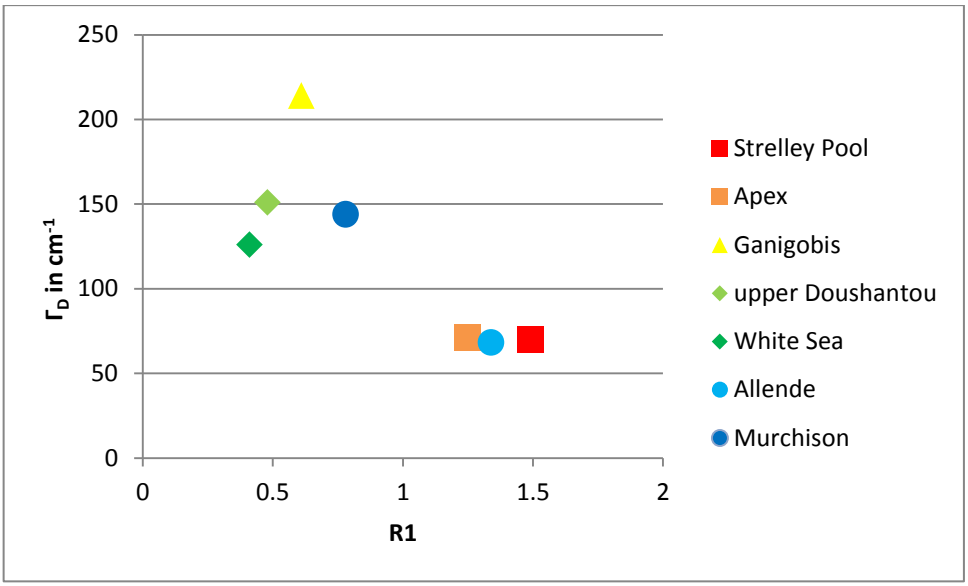

Figure 63: Comparison of the intensity ratio of the D and the G band with the full width at half height of the D band. Note that the Allende meteorite plots together with the Archaic thermal mature rocks of Apex and Strelley Pool, whereas Murchison plots together with the rocks where the carbon signature is probably related to microbial processes.

The recognition of this general trend stated by Bower at al. (2013) with other samples analyzed in this work, suggests a promising field of application in geobiology. However, as the focus of this work was not on the recognition and interpretation of carbon signatures, more data are required before a general assumption can be made. Nevertheless, this work can contribute to evaluate carbon signals obtained with Raman spectroscopy and form an excellent basis for future investigations.

References

Bower, D.M., Steele, A., Fries, M.D. and Kater, L. (2013) Micro Raman spectroscopy of carbonaceous material in microfossils and meteorites: improving a method for life detection. *ASTROBIOLOGY* 13: 103-13.

Brasier, M.D., Green, O.R., Jephcoat, A.P., Kleppe, A.K., Van Kranendonk, M.J., Lindsay, J.F., Steele, A. and Grassineau, N.V. (2002) Questioning the evidence for Earth's oldest fossils. *Nature* 416: 76-81.

Clayton, R.N. and Mayeda, T.K. (1984) The oxygen isotope record in Murchison and other carbonaceous chondrites. *Earth and Planetary Science Letters* 67: 151-161.

Cronin, J.R. and Pizzarello, S. (1983) Amino acids in meteorites. *Advances in Space Research* 3: 5-18.

Edwards, H.G.M., Wynn-Williams, D.D. and Villar, S.E.J. (2004) Biological modification of haematite in Antarctic cryptoendolithic communities. *Journal of Raman Spectroscopy* 35: 470-474.

Engel, M.H. and Macko, S.A. (1997) Isotopic evidence for extraterrestrial non-racemic amino acids in the Murchison meteorite. *Nature* 389: 265-268.

Foucher, F. and Westall, F. (2009) Investigating the Oldest Traces of Life by AFM/Confocal Raman Spectroscopy: Applications for the Analysis of Martian Rocks. *AIP Conference Proceedings* 1163: 47-58.

Glamoclija, M., Steele, A., Fries, M., Schieber, J., Voytek, M.A. and Cockell, C.S. (2009) Association of anatase (TiO_2) and microbes: Unusual fossilization effect or a potential biosignature? *Geological Society of America Special Papers* 458: 965-975.

Krot, A.N., Yurimoto, H., Hutcheon, I.D., Libourel, G., Chaussidon, M., Tissandier, L., Petaev, M.I., MacPherson, G.J., Paque-Heather, J. and Wark, D. (2007) Type C Ca, Al-rich inclusions from Allende: Evidence for multistage formation. *Geochimica et Cosmochimica Acta* 71: 4342-4364.

Marshall, C.P., Edwards, H.G. and Jehlicka, J. (2010) Understanding the application of Raman spectroscopy to the detection of traces of life. *ASTROBIOLOGY* 10: 229-43.

Pasteris, J.D. and Wopenka, B. (2002) Laser-Raman spectroscopy (Communication arising): Images of the Earth's earliest fossils? *Nature* 420: 476-477.

Pasteris, J.D. and Wopenka, B. (2003) Necessary, but not sufficient: Raman identification of disordered carbon as a signature of ancient life. *ASTROBIOLOGY* 3: 727-38.

Powell, B.J., Baruah, T., Bernstein, N., Brake, K., McKenzie, R.H., Meredith, P. and Pederson, M.R. (2004) A First Principles Density-Functional Calculation of the Electronic and Vibrational Structure of the Key Melanin Monomers. *Journal of Chemical Physics* 120: 8608-8615.

Schopf, J.W., Kudryavtsev, A.B., Agresti, D.G., Wdowiak, T.J. and Czaja, A.D. (2002) Laser-Raman imagery of Earth's earliest fossils. *Nature* 416: 73-76.

Sears, D.W. and Dodd, R.T. (1988) Overview and classification of meteorites. In: *Meteorites and the early solar system, Vol.1*, edited by J.F. Kerridge and M.S. Matthews, The University of Arizona Press, Tucson, AZ, pp. 3-34.

Acknowledgements

In the first place I would like to thank Joachim Reitner for giving me the opportunity to join this project and work with so many different samples representing almost the whole Earth history. At the same time I would like to thank Volker Thiel for being a co-advisor who was always interested in my work.
A special thanks to Burkhard Schmidt for explaining the wonders of Raman spectroscopy to me. He always had a helping hand when I had to deal with technical problems.
For analytical support I would like to thank Andreas Reimer and Birgit Röhring. Both of them always were very open in sharing their knowledge.
The work in the Äspö tunnel was only possible due to the constant support of the colleagues from SKB.
Many thanks to the colleagues from the “mensa team” for providing necessary resting periods and ensuring thinking about other important things in life. In this regard a special thanks to Stefan Möller for his helpful hands in many concerns.
I sincerely thank my doctoral student colleagues Christina Heller and Wencke Wegner for manifold theoretical and practical support. Also the numerous shared leisure activities were very much appreciated.
A special thanks to Thomas Bode who had not only always a good advice when dealing with computer problems, but also ensured that we could enjoy a good cup of tea and cake together.
For steady support and encouragement, I am indebted to Konrad Horn and to my family.
This thesis was accomplished as part of the DFG Research Group FOR 571, “geobiology of organo- and biofilms: Coupling of the geosphere and the biosphere by microbial processes”.